



# **ACID DEGRADATION OF ALKALI-ACTIVATED MATERIALS**

A Thesis Submitted

by

**Yanru Wang**

For The Award of  
Doctor of Philosophy

2022

## **Abstract**

Acid corrosion of concrete sewerage pipes arouses both industry and academy concern in recent years due to the high cost of rehabilitation and replacement. Alkali activated materials, also named geopolymers, are recommended as potential alternative materials to Portland cement (PC)-based concrete in sewer environments due to their better resistance to the acid solution.

The reaction products, pore structure, sample curing conditions and acid environment conditions are the influencing parameters that determine the acid resistance of geopolymers. Particularly, the reaction products of geopolymers, i.e., calcium aluminosilicate hydrate (C-A-S-H) gel, calcium (alkali) aluminosilicate hydrate (C-(N)-A-S-H) gel and sodium aluminosilicate hydrate (N-A-S-(H)) gel determine the performance of geopolymers under acidic conditions. However, geopolymers use industrial wastes as raw materials; variations in chemical compositions could induce significant changes in the reaction products and microstructure of geopolymers, leading to different engineering properties and acid resistance behaviour.

The ultimate goal of this research is to investigate the acid degradation mechanism of alkali-activated materials. This lies on a basis of a full understanding of the degradation mechanism of various geopolymers phases under acidic conditions. In this thesis study, instead of using industrial by-products as raw materials, pure precursors were synthesized by organic polymeric steric entrapment solution-polymerisation route. The obtained stoichiometrically controlled powders were activated by alkaline activators to produce 'pure' reaction productions, e.g., N-A-S-(H) gel and C-(N)-A-S-H gel, or blends of C-(N)-A-S-H and N-A-S-(H) gels, with designed Al/Si, Na/Al and Ca/Si ratios. The acid resistance of different reaction products based on the pure precursors was evaluated. The acid degradation of alkali-activated materials derived from fly ash and blast furnace slag were investigated. The innovation and significant contribution to geopolymer chemistry can be summarized as following:

- (1) The synthesized precursors used stoichiometrically controlled routine showed similar chemical properties as the industrial precursors from the TGA, XRD and FTIR results. The non-calcium precursors were mainly amorphous with a

higher surface area and higher hygroscopicity. The calcium promoted the formation of crystalline phases. The synthesized routines could be an effective method for the intrinsic investigation of the acid degradation of AAMs.

- (2) The dealumination dominated the microstructural change of N-A-S-H gel under the sulphuric acid attack, and the dealumination had minor effect on the bulk structure integrity. The C-(N)-A-S-H gel showed both dealumination and decalcification, together with significant and rapid loss of sodium and slow loss of silicon. The dealumination and the loss of sodium continued after decalcification and desiliconization. The Si/Al ratio of non-crosslinked C-(N)-A-S-H gel decreased, while the Si/Al ratio of N-A-S-H gel increased after exposure to sulphuric acid. The silicate polymerization degree ( $Q^4$  concentration) increased, especially for C-(N)-A-S-H gel.
- (3) Low calcium samples showed a higher leaching amount of aluminium than high calcium samples, indicating that the calcium content in the mixture promoted the dealumination resistance when exposed to sulphuric acid. The formation of additional calcium-containing products in Ca-rich, Al-rich sample was decomposed prior to C-(N)-A-S-H/N-A-S-H gels. The Si-O bond strength in N-A-S-H gel appeared weaker than that in the C-(N)-A-S-H gel, due to the calcium prevented the leaching of silicon from samples. The silicon chains length of the C-(N)-A-S-H gel increased with increased Si/Al ratio. However, the chain length of the N-A-S-H gel increased with reduced Si/Al ratio.
- (4) The AAMs derived from fly ash shows more obvious mass loss and volume loss than that derived from slag under sulphuric acid attack, and the lower initial compressive strength was difficult to meet the practical engineering needs. For slag based AAMs, the increased  $SiO_2$  content could greatly improve the initial compressive strength but had less effect on the residual strength under sulphuric acid attack. The hydration products from the paste reacted with sulphuric acid to form expansive calcium sulphates, mainly existing in the weak area between the slurry and fine aggregate, and the expansion stress caused flaking. For low-Ca AAMs derived from fly ash, minor sulphur intruded into the sample, while the high-Ca AAMs derived from slag attracted

more sulphur. The higher calcium content in AAMs attracts more sulphur into the sample due to the high ionic force between  $\text{Ca}^{2+}$  and  $\text{SO}_4^{2-}$ .

**Keywords:** alkali-activated, acid resistance, bio-erosion, slag, sewer, sulphuric acid

## **Certification of Thesis**

This Thesis is the work of (Student name) Yanru Wang except where otherwise acknowledged, with the majority of the authorship of the papers presented as a Thesis by Publication undertaken by the Student. The work is original and has not previously been submitted for any other award, except where acknowledged.

Student: Yanru Wang

Principal Supervisor: Hao Wang

Associate supervisor: Zuhua Zhang

*"Student and supervisors' signatures of endorsement are held at the University."*

## **Acknowledgement**

I would like to thank all the people who have assisted me to make this thesis possible. It is a magical and unusual journey to study at the University of Southern Queensland. The support of the scholarship from USQ is acknowledged.

I want to express my greatest gratitude to my supervisors, Prof. Hao Wang and Prof. Zuhua Zhang, who are strongly supportive of my study and my life. Prof. Hao Wang is very professional in the field of materials engineering. He provided me with indispensable directional guidance for my research project and gave me a lot of assistance in the progress. Prof. Zuhua Zhang is highly experienced in alkali-activated materials. He helped me a lot with project management, results discussions and writing skills. Without their constant trust and support for me, I could not have successfully completed my PhD study.

I would like to thank all group members who give me important advice and suggestions on my study during our group meetings. Dr Yuwei Ma gave me a lot of encouragement and assistance when I encounter difficulties. She was also so helpful in examining my research results and my writing skills. I would like to thank Dr Huajun Zhu and Dr Peng Du who were visiting scholars for their kind support during my study. I specifically thank Prof Peter Schubel for his continuous support. I also want to express my thanks to all my friends and current and former colleagues in the Centre for Future Materials for their friendship, support and discussions these years.

I would like to thank the helpful technicians and colleagues, Wayne Crowell, Martin Geach, Mohan Trada, Susette Eberhard, Adrian Blokland, and Michelle Griffiths, for your kind support during my experiments and study. I would like to thank Ying Yu, Anya Yago, Jen Brown who are from the Centre for Microscopy and Microanalysis (CMM) for their help to do SEM and XRD experiments, and Ekaterina Strounina from the Centre for Advanced Imaging (CAI) for her support in the NMR experiment.

Last but not least, I would like to thank my family for their continuous support and encouragement. They were always my strong backing, inspiring me to overcome difficulties and keep moving forward. I would like to take this opportunity to thank my husband, Yubin Cao, who gave me the confidence to finish PhD study.

## TABLE OF CONTENTS

<b>Abstract</b> .....	I
<b>Certification of Thesis</b> .....	IV
<b>Acknowledgement</b> .....	V
<b>List of Figures</b> .....	IX
Chapter 1. Introduction.....	1
Chapter 2. Literature review .....	4
2.1 Introduction.....	4
2.2 Geopolymer technology.....	7
2.3 Acid corrosion in the cement and concrete structure.....	9
2.3.1 Concrete sewer corrosion and biodeterioration mechanisms.....	9
2.3.2 Acid rain corrosion.....	10
2.3.3 Acid gases corrosion.....	11
2.4 Influencing factors of acid resistance of AAMs.....	12
2.4.1 Effect of precursor.....	12
2.4.2 Type of activator.....	28
2.4.3 Curing program .....	30
2.5 Mechanism of acid corrosion for PC and AAMs .....	32
2.5.1 Sources of acidic environment.....	32
2.5.2 Aggressivity of acid.....	32
2.5.3 Corrosion mechanism of AAM in acid media .....	33
2.6 Summary and outlook.....	37
Chapter 3. Research plan and methodology.....	40
3.1 Introduction.....	40
3.2 Research flow chat.....	40
3.3 Raw materials.....	41
3.4 Characterisation.....	41
3.4.1 Scanning electron microscopy/Energy-dispersive X-ray spectroscopy (SEM-EDX).....	41
3.4.2 X-ray diffraction (XRD).....	42
3.4.3 X-ray fluorescence (XRF).....	42
3.4.4 Combined thermogravimetric analysis (TGA).....	42
3.4.5 Inductively coupled plasma/ atomic emission spectroscopy (ICP-OES)	

3.4.6	Fourier transform infrared spectroscopy (FTIR).....	43
3.4.7	Nuclear magnetic resonance spectroscopy (NMR) .....	43
Chapter 4.	Synthesis of stoichiometrically controlled aluminosilicate precursors and alkali-activated gels.....	44
4.1	Introduction .....	44
4.2	Research method.....	45
4.2.1	Materials preparation for synthesis pure aluminosilicate .....	45
4.2.2	Characterisation .....	46
4.3	Results and discussion .....	47
4.3.1	Chemical compositions .....	48
4.3.2	Thermogravimetric-differential thermogravimetric (TGA-DTG) of precursors.....	49
4.3.3	X-ray diffraction (XRD) analysis.....	54
4.3.4	Fourier transform infrared spectroscopy (FTIR) analysis .....	57
4.4	Concluding remarks.....	58
Chapter 5.	Structural depolymerization of N-A-S-H and C-(N)-A-S-H gels by sulphuric acid attack .....	60
5.1	Introduction .....	60
5.2	Experimental methods .....	62
5.2.1	Geopolymer binder synthesis.....	62
5.2.2	Acid corrosion testing procedures .....	63
5.2.3	Characterisation.....	64
5.3	Results and discussion .....	65
5.3.1	Visual inspection and mass change .....	65
5.3.2	Leaching behaviour .....	67
5.3.3	X-ray diffraction (XRD) analysis.....	73
5.3.4	Thermogravimetric-differential thermogravimetric (TG-DTG) analysis	75
5.3.5	Fourier transform infrared spectroscopy (FTIR) analysis .....	77
5.3.6	Scanning electron microscopy (SEM) and energy dispersive X-ray (EDX) analysis.....	81
5.3.7	Solid-state MAS NMR spectroscopy analysis .....	84
5.4	Concluding remarks.....	93
Chapter 6.	Phase evolution of C-(N)-A-S-H/N-A-S-H gels by sulphuric acid attack	94

6.1	Introduction .....	94
6.2	Materials and methods .....	96
6.2.1	Raw materials and alkali-activated gels manufacture .....	96
6.2.2	Acid corrosion test.....	98
6.2.3	Characterisation analysis.....	98
6.3	Results .....	98
6.3.1	Leaching behavior .....	98
6.3.2	X-ray diffraction (XRD) .....	106
6.3.3	Thermogravimetric analysis (TGA) .....	108
6.3.4	Fourier transform infrared spectroscopy (FTIR).....	113
6.3.5	Solid-state nuclear magnetic resonance spectroscopy .....	117
6.4	Discussions.....	128
6.4.1	The effect of chemical composition on leaching performance .....	128
6.4.2	Corrosion mechanisms of C-(N)-A-S-H and N-A-S-H gels .....	128
6.5	Concluding remarks.....	129
Chapter 7.	Effect of raw materials on the acid resistance of alkali-activated slag/fly ash binders by sulphuric acid attack .....	131
7.1	Introduction .....	131
7.2	Materials and methods .....	133
7.2.1	Materials.....	133
7.2.2	Sample preparation .....	134
7.2.3	Testing procedure .....	135
7.2.4	Characterization.....	136
7.3	Results and discussion .....	138
7.3.1	Physical degradation.....	138
7.3.2	Mineralogical degradation .....	146
7.3.3	Microstructural change .....	152
7.4	Concluding remarks.....	157
Chapter 8.	Conclusions and Recommendations .....	158
8.1	Conclusions .....	158
8.2	Recommendations.....	160
References	.....	162
Publications	.....	177
Appendix	.....	179

## List of Figures

Figure 2-1. Pseudo-ternary plot of binder gel compositions measured by SEM-EDX (van Deventer et al., 2015).....	8
Figure 2-2. Schematic representations of a section of silicon-aluminium chains in C-(N)-A-S-H gel (Provis and Bernal, 2014b), existed in two layers composited by calcium octahedra (Myers et al., 2013).....	9
Figure 2-3. Concrete sewer and biodeterioration mechanisms. The biofilm is composed of sulphur-oxidizing bacteria (SOB) (Chen et al., 2003). Sulphate-reducing bacteria exists in the sludge (Grandclerc et al., 2018). ....	9
Figure 2-4. Stages of corrosion in new concrete with hypothesized microorganism's succession during Microbially Induced Concrete Corrosion (MICC) proposed by (Khan et al., 2019, Islander et al., 1991). ....	10
Figure 2-5. Three-year-average pH values for 2005-2007.....	11
Figure 2-6. Mass and cross-sectional change of OPC, AAS and AAFA mortar cubes exposed to sulphuric acid solutions at different concentrations (1, 3, and 5 wt%) (Aliques-Granero et al., 2017). ....	14
Figure 2-7. Changes of mass and compressive strength of fly ash based geopolymers, data from references listed in Table 2-1.....	15
Figure 2-8. The effect of slag content on compressive strength loss and residual compressive strength, data collect from previous published literatures (Lee and Lee, 2016, Aiken et al., 2018, Koenig et al., 2017, Zhang et al., 2018c). ....	21
Figure 2-9. The effect of slag contents on the reaction products of geopolymers before and after exposed to sulphuric acid solution. GP1 and GP5 were fly ash based, while GP2 to GP4 presenting the slag content in geopolymers were 30%, 70% and 100%, respectively. G-gypsum, M-mullite, Q-quartz, H-hematite, E-ettringite, SC-semicarboxate, CH-calcium hydroxide, CSH-calcium silicate hydrate (Aiken et al., 2018). ....	23
Figure 2-10. Visual analysis and optical microscopy of specimens (a) FA/Slag blend mortar (FA-GPm) and (b) sulphate resistant Portland cement mortar (SRPCm) after exposure to sulphuric acid solution for 6 months (Khan et al., 2020). ....	24

Figure 2-11. SEM images with EDX elemental mapping of fly ash/slag blend mortar (FA-GPm) after exposure to aggressive sewer environment in chamber 1 (high H <sub>2</sub> S content) and 2 (low H <sub>2</sub> S content) for 24 months.(Khan et al., 2020). .....	25
Figure 2-12. SEM images with EDX elemental mapping of sulphate resistant Portland cement mortar (SRPC) after exposure to aggressive sewer environment in chamber 1 (low H <sub>2</sub> S content) and 2 (low H <sub>2</sub> S content) for 24 months.(Khan et al., 2020). .....	26
Figure 2-13. XRD patterns of low kaolinite MKA1 and MKA2 activated by sodium hydroxide, high kaolinite KR activated by potassium hydroxide, respectively Bouguermouh et al. (2017).....	30
Figure 2-14. Schematic diagram of the mechanism of acid attack in 100% fly ash GPs, fly ash/slag GPs and 100% PC mixes. Modified based on Aiken et al. (2018). .....	35
Figure 2-15. Description of relative relationship between properties with CaO content in alkali-activated blenders, no numerical signification (Rafeet et al., 2019). The distances and lines shown in the figure are indicative.....	38
Figure 3-1. Research flow chart of this thesis .....	40
Figure 4-1. Particle size distribution and passing summary of synthesized precursors, metakaolin and GGBFS. ....	48
Figure 4-2. Ternary diagram of the chemical composition (CaO-Al <sub>2</sub> O <sub>3</sub> -SiO <sub>2</sub> ) of solid raw materials, as determined by X-ray fluorescence analysis.....	49
Figure 4-3. TGA-DTG data of the precursors N1, N2 and N3 as marked.....	51
Figure 4-4. TGA-DTG data of the calcium-containing precursors C1, C2, C3 and C4 as marked.....	53
Figure 4-5. TGA-DTG data of the industrial precursors of FA, MK and GGBFS as marked.....	54
Figure 4-6. XRD patterns of each synthesized calcium-free precursors as marked..	56
Figure 4-7. XRD patterns of each synthesized calcium-containing precursors as marked.....	56
Figure 4-8. XRD patterns of fly ash and GGBFS.....	57
Figure 4-9. FTIR patterns of each precursor. ....	58
Figure 5-1. The experimental procedure.....	64
Figure 5-2. The appearance of NASH sample and C(N)ASH sample before and after 28 days exposure to sulphuric acid.....	66

Figure 5-3. The mass change (%) of the NASH sample and C(N)ASH sample after exposure to water and 5% sulphuric acid solution. ....	67
Figure 5-4. pH values of the (a) distilled water and (b) 5% sulphuric acid solution after 56 days of immersion of the NASH sample and C(N)ASH sample. ....	69
Figure 5-5. Cumulative concentrations of aluminium, calcium, sodium, and silicon leached from the NASH sample and C(N)ASH sample exposed to distilled water and 5% sulphuric acid solution for 56 days. ....	72
Figure 5-6. The ratios of (a) Si/Al and (b) Na/Al in the unexposed NASH sample and C(N)ASH sample and their acid leachates. ....	73
Figure 5-7. X-ray diffractions of the (a) NASH sample and (b) C(N)ASH sample before and after 28 days sulphuric acid attack. ....	75
Figure 5-8. Mass change and differential mass change (DTG) of the NASH sample and C(N)ASH sample before and after 28 days of sulphuric acid attack. ....	77
Figure 5-9. FTIR spectra (absorbance) and deconvoluted spectra of the NASH and C(N)ASH samples before and after exposure to sulphuric acid. ....	80
Figure 5-10. SEM images of the NASH and C(N)ASH samples before and after exposure to sulphuric acid. ....	82
Figure 5-11. Atomic ratios Na/Al versus Si/Al for the unexposed and exposed regions of the NASH sample as marked, determined by EDX analysis. A random selection of points evenly distributed across a representative 1000 $\mu\text{m} \times 1000 \mu\text{m}$ section of the sample were used for analysis. The approximate region defined for N-A-S-H refers to (Walkley, 2016). ....	83
Figure 5-12. Atomic ratios Ca/Si versus Al/Si for the unexposed and exposed regions of the C(N)ASH sample as marked, determined by EDX analysis. A random selection of points evenly distributed across a representative 1000 $\mu\text{m} \times 1000 \mu\text{m}$ section of the sample were used for analysis. Approximate regions of C-(N)-A-S-H are determined from (Walkley, 2016). ....	84
Figure 5-13. $^{27}\text{Al}$ MAS NMR data of the NASH sample and C(N)ASH sample before and after exposure to sulphuric acid attack. ....	86
Figure 5-14. $^{29}\text{Si}$ MAS NMR data (black lines) of (a) the unexposed NASH sample and (b) the exposed NASH sample after 28 days of sulphuric acid attack. The fitting line (red) of the spectra for the samples and associated spectral deconvolutions are also shown. ....	90

Figure 5-15. <sup>29</sup> Si MAS NMR data (black lines) of (a) the unexposed C(N)ASH sample and (b) the exposed C(N)ASH sample after 28 days of sulphuric acid attack. The fitting line (red) of the spectra for the samples and associated spectral deconvolutions are also shown. ....	91
Figure 6-1. The pH value of distilled water with immersed samples during 56 days exposure. ....	99
Figure 6-2. The pH value of 3% sulphuric acid solutions with immersed samples during 56 days exposure.....	100
Figure 6-3. Cumulative concentrations of cations (aluminium, calcium, sodium, and silicon) in the distilled water with immersing samples.....	102
Figure 6-4. Cumulative concentrations of cations (aluminium, calcium, sodium, and silicon) in the 3% sulphuric acid with immersing samples.....	105
Figure 6-5. Ca/Al ratios of each sample leaching into the acid and water leachates. ....	106
Figure 6-6. Ca/Si ratios of each sample leaching into the acid and water leachates. ....	106
Figure 6-7. XRD patterns of the samples (a) before and (b) after exposure to 3% sulphuric acid for 28 days of acid corrosion (C-calcite, Z-zeolite, W-wollastonite, Pe-pectolite, Ve-vertumnite, Pw-pseudowollastonite, CAc-calcium aluminium carbonate hydrate, G-gypsum, CSH - amorphous calcium silicate hydrate). ....	108
Figure 6-8. Thermogravimetric data of the samples before and after exposure to 3% sulphuric acid for 1 d, 3 d, 7 d, and 28 d as marked. ....	110
Figure 6-9. Differential thermogravimetric curves for the samples before and after exposure to 3% sulphuric acid for 1 d, 3 d, 7 d, and 28 d as marked. ....	113
Figure 6-10. FTIR spectra of alkali-activated binders before and after exposure to 3% sulphuric acid. The baseline is enclosed in the dashed square. ....	115
Figure 6-11. Magnified FTIR spectra of (a) unexposed samples between 650-1150 cm <sup>-1</sup> and (b) attacked gels between 550-1300 cm <sup>-1</sup> .....	117
Figure 6-12. <sup>27</sup> Al MAS NMR spectrum of samples before and after acid exposure. ....	120
Figure 6-13. <sup>29</sup> Si MAS NMR spectrum and deconvolution spectrum of samples after exposure to distilled water. The tetrahedral coordination of Si is presented by Q.	

Q <sup>n</sup> (mAl) represents that the calculated Si site is connected by n another Si site via oxygen bond and m of them are Al.....	122
Figure 6-14. <sup>29</sup> Si MAS NMR spectrum and deconvolution spectrum of samples after being exposed to 3% sulphuric acid. The tetrahedral coordination of Si is presented by Q. Q <sup>n</sup> (mAl) represents that the calculated Si site is connected by n another Si site via oxygen bond and m of them are Al.....	124
Figure 6-15. The Si coordination characterized in <sup>29</sup> Si MAS NMR spectra of the samples (a) before and (b) after being exposed to sulphuric acid. There is around ±1% of uncertainty for each calculated percentage. ....	125
Figure 6-16. Schematic presentation (two-dimensional) of acid attack on (a) C-(N)-A-S-H and (b) N-A-S-H gels: Ca-O octahedron indicated in green circle, Si-O tetrahedron and Al-O tetrahedron indicated in orange and dark blue triangles, Na cation indicated in pink circle, water indicated in light blue circle. ....	129
Figure 7-1. XRD patterns of fly ash, GGBFS and OPC. ....	134
Figure 7-2. The cross-section photographs of the paste exposed to 3% sulphuric acid solution with clearly outer and inner parts. ....	137
Figure 7-3. The volume of open pores of each sample. ....	138
Figure 7-4. Photographs of cementing mortars after 28 days exposure to water, 3 and 5% solutions of sulphuric acid. ....	140
Figure 7-5. The truncated cross-section of the OPC and AAMs pastes exposed to water and 3% sulphuric acid solution.....	141
Figure 7-6. Mass change of different cementing mortars for 28 days of exposure to (a) water, (b) 3% sulphuric acid and (c) 5% sulphuric acid. ....	143
Figure 7-7. Volume change of different cementing mortars for 28 days of exposure to (a) water, (b) 3% sulphuric acid and (c) 5% sulphuric acid. ....	145
Figure 7-8. Compressive strength of PC, AAFA and AAS mortars during 28 days of exposure to (a) water, (b) 3% sulphuric acid and (c) 5% sulphuric acid. ....	145
Figure 7-9. FTIR spectra of (a) OPC, (b) AAM_1, (c) AAM_2, (d) AAM_3 and (e) AAM_4 pastes exposure to water and sulphuric acid. The inner and outer part are tested separately.....	149
Figure 7-10. The TGA-DTG data of (a) OPC, (b) AAM_1, (c) AAM_2, (d) AAM_3 and (e) AAM_4 pastes exposure to water and sulphuric acid solution.....	152

Figure 7-11. SEM images of the OPC, AAM\_1, AAM\_2, and AAM\_3 pastes after exposed to sulphuric acid for 28 days..... 154

Figure 7-12. BSE images and elemental maps of the (a) OPC, (b) AAM\_2 and (c) AAM\_3 after exposed to sulphuric acid for 28 days. The elemental analysis shows the distribution of calcium (Ca), sulphur (S), silicon (Si), aluminium (Al) and sodium (Na). The red arrow represents the direction of sulphuric acid attack..... 155

Figure 7-13. Chemical analysis of different elements relative content measured by EDX line scan after 28 days of immersion in the sulphuric acid. .... 156

Figure 7-14. BSE images and elemental maps of the high magnification (a) AAM\_2 and (b) AAM\_3 after exposed to sulphuric acid for 28 days. The elemental analysis shows the distribution of calcium (Ca), sulphur (S), silicon (Si), aluminium (Al) and sodium (Na). The red arrow represents the direction of sulphuric acid attack. .... 156

## List of Tables

Table 2-1. Summary of studies investigating durability of alkali-activated fly ash exposed to acid attack. ....	13
Table 2-2. Summary of studies investigating durability of alkali-activated metakaolin exposed to acid attack. ....	17
Table 2-3. Summary of studies investigating durability of alkali-activated slag exposed to acid attack. ....	19
Table 2-4 Summary of studies investigating durability of alkali-activated fly ash/slag exposed to acid attack. ....	20
Table 2-5 Summary of studies investigating durability of alkali-activated other precursors exposed to acid attack. ....	27
Table 3-1. Raw materials used in this thesis. ....	41
Table 4-1. Chemical composition (oxide basis) of fly ash and GGBFS.....	45
Table 4-2. Designed molar ratios for precursor powders.....	45
Table 4-3. The designed and measured physical compositions of synthesized precursor powders. ....	49
Table 5-1. Molar ratios in the precursor powder and the reaction mixture for NASH sample and C(N)ASH sample. ....	63
Table 5-2 Summary of bands in the deconvoluted FTIR spectrum of Si-O-T bands for the NASH and C(N)ASH samples before and after exposed to acid attack in the range of $1300\text{ cm}^{-1} \sim 600\text{ cm}^{-1}$ . Asymmetric stretching vibration ( $\sigma_{as}$ ), symmetric stretching vibration ( $\sigma_s$ ) and bending vibration ( $\delta$ ). * means bands with trace occupation. ....	81
Table 5-3 Deconvolution results of $^{29}\text{Si}$ NMR spectra for the NASH sample and C(N)ASH sample before and after exposed to sulphuric acid. The IA (%) is the normalized relative integral area of each deconvoluted resonance in the spectra.....	92
Table 6-1 Measured formula ( <i>mol %</i> ) by XRF of the precursor powders and each binder. ....	97
Table 6-2 FTIR band assignments of unexposed samples (García Lodeiro et al., 2009). ....	115
Table 6-3 FTIR band assignments of exposed samples (Lee and Lee, 2016, Aiken et al., 2018).....	115

Table 6-4 Summary of the deconvolution results of <sup>29</sup>Si MAS NMR spectra for the unexposed and exposed samples. The mean chain length (MCL) and Si/Al ratios are calculated for non-crosslinked C-A-S-H gel, N-A-S-H gel, and crosslinked C-(N)-A-S-H gels, respectively. .... 127

Table 7-1. Chemical compositions and physical properties of raw materials..... 133

Table 7-2. Mix proportions of the binder mixes (kg/m<sup>3</sup>). The mix proportions of the paste samples were identical to the mortars except they contained no sand..... 135

## CHAPTER 1. INTRODUCTION

Under the concept of sustainable development carbon neutrality, improving the durability of construction buildings is a promising strategic approach in the civil engineering industry. The durability of concrete includes the resistance to permeability, frost damage, corrosion damage, carbonization, and alkali-aggregate reaction etc. The sewerage pipes based on ordinary Portland concrete (PC) have a high potential for acid corrosion due to the presence of carbonation and H<sub>2</sub>S acidification in the sewer environment. The development of alternative more durable materials for sewers application has aroused wide attention and interest in both academia and industry. In the past few years, alkali-activated materials (AAMs) have been recommended as promising alternatives to PC, mainly due to their low CO<sub>2</sub> emission, comparable strength, and superior resistance in acidic environments.

The reaction products of AAMs are important for their acid resistance. However, AAMs normally are derived from industrial by-products like fly ash and slags, which are featured with varied chemical compositions and physical properties. The influence of the impurities from raw materials on the acid resistance of AAMs makes the mechanism of acid corrosion still vague in previous studies.

The aim of this research is as follows:

1. To investigate the acid corrosion mechanism of synthetic AAMs minimizing the effect of raw materials. An organic polymeric steric entrapment solution-polymerisation route will be used to synthesize pure precursors, then alkali solutions will be used to synthesize pure aluminosilicate gels (here 'pure' means containing no other elements such as Fe, S, etc. It does not mean the gels are of a single composition and molecular structure).
2. To explore the acid degradation of the obtained pure gels. Acid corrosion test will be conducted on the obtained pure gels. The dissolution rate, ion concentration, pH value, mass loss, crystallization, microstructure and morphology of AAMs before and after acid attack will be studied.
3. To optimal the materials design of the alali-activated materials according to the real application environment. Finally, optimal mixture of geopolymers concrete in sewer environment will be recommended based on the comparison

of the results from the degradation of the reaction products derived from pure precursors and industrial raw materials.

Chapter 2 shows the critical literature review regarding this research. The acid corrosion that happened in the cement and concrete structures have been discussed in this chapter, including sewer corrosion, acid rain corrosion and acid gases corrosion. The influencing factors including precursors, activators, and curing program on the acid resistance of AAMs have been summarized. The corrosion mechanism for PC and AAMs in different acidic environment is discussed. The exiting problems in the studies regarding to the acid corrosion of PC and AAMs are discussed too, which lead to the research gap of this thesis.

In Chapter 3, the raw materials and the characterization technologies used in this research are summarized. In the following, the specific testing parameters for each test will be given in the respective chapters according to different characterization purposes.

Chapter 4 discusses the details about synthesis of the stoichiometrically controlled aluminosilicate precursors and alkali-activated gels. The chemical and physical properties of the synthesized precursors are described. The comparison between the synthesized precursors and the industrial raw materials is illustrated.

In Chapter 5, the structural depolymerization process of the synthesized N-A-S-H gel vs. C-(N)-A-S-H gel exposed to sulphuric acid attack is investigated. The evolution of the molecular structure of the gels, particularly the bond change after exposure to H<sub>2</sub>SO<sub>4</sub> solution of the designed AAMs is discussed. The C-(N)-A-S-H gel had higher degree of structural order than the N-A-S-H gel, while the N-A-S-H gel showed higher polymerization extent. In N-A-S-H gel, the Al<sup>IV</sup> transferred completely to Al<sup>V</sup> during sulphuric acid attack, while trace amount of Al<sup>IV</sup> was still detected in the exposed C-(N)-A-S-H gels. Both gels had increased silica polymerization degree after exposure to sulphuric acid solution. Due to rapider dealumination of N-A-S-H gel than C-(N)-A-S-H gel, the Si/Al ratio increased much higher in the former. The molecular framework changes of N-A-S-H gel caused by dealumination was found to have less effect on the integrity though than that of C-(N)-A-S-H gel, in which coarse gypsum crystalline grains formed and led to destructive stress in hardened matrix. This paper

provides an insight at microstructure level of the two typical gels, which is essential for the manufacturing and application of alkali-activated materials.

Chapter 6 discusses the phase evolution of the C-(N)-A-S-H/N-A-S-H gels to sulphuric acid attack. Four sodium-containing calcium aluminium-substituted silicate hydrate (C-(N)-A-S-H) and aluminosilicate hydrate (N-A-S-H) gels with designed Ca/Si and Si/Al ratios are produced with synthetic calcium aluminosilicate powders. The C-(N)-A-S-H gels show a higher resistance to leaching than N-A-S-H gel, while the latter has a high resistance to depolymerization under acid attack. The macrostructure damage caused by the presenting of calcium happened in the pure AAMs, however, the calcium hydroxide helps to mitigate the sulphuric acid attack on the reaction gels regarding the phase change. This study provides a basic route to understand the effect of AAMs composition on acid resistance. It further suggests designing the Ca/Al ratios of AAMs in practical applications in compliance with the composition of raw materials and specific exposure conditions to achieve satisfying acid resistance.

In Chapter 7, fly ash and slag used by a local concrete manufacture are used to produce alkali-activated fly ash and slag binders. The binders are exposed to sulphuric acid attack and the effects of raw materials on the acid resistance of alkali-activated materials are investigated via macro analysis and micro analysis. The results are correlated with the previous results in Chapter 5 and Chapter 6. The relationship between the products of synthesised materials and industrial raw materials are established.

Chapter 8 draws the main conclusions of the thesis work and provides perspectives for future research. The main findings of the acid degradation of AAMs derived from synthetic pure materials and the guiding for application of AAMs in practical engineering are shown in this chapter.

## CHAPTER 2. LITERATURE REVIEW

### 2.1 Introduction

Over the past century, ordinary Portland cement (OPC) concrete is the most commonly used construction material as its reliable performance, widespread availability, and low cost. However, as an alkaline material with pH of 12.5-13.5 (Bullard et al., 2011), concrete is susceptible to erosion in acidic environment, leading to performance deterioration and consequently economic loss (Jiang et al., 2014). The economic loss caused by acidic rain (pH < 5.6) corrosion on existing concrete buildings is over 2 million US\$ per annum in Hangzhou, a city in China with around 7 million population (Zhang et al., 2019). Microbial-induced concrete corrosion (MICC), which is complex acid corrosion, that happens in sewer systems reduces the service life of concrete components from 100 years to 30-50 years (Jensen, 2009). Twenty years ago, the maintenance cost in the United States was approximately \$36 billion annually (Koch et al., 2002), including repairing and replacing the concrete components, and it is expected to be more costly.

Alkali-activated materials (AAMs) have been discussed and promoted as an alternative construction material to OPC in particular applications, as their comparable properties and green footprint on the environment (Provis et al., 2015, Provis, 2018, Zhang et al., 2014). AAMs derived from different precursors are also nominalized as AAFA which is produced from fly ash, AAS which is produced from ground blast furnace slag, and AAFS which is produced from fly ash and slag, etc. Several authors reported that AAMs showed an advantage over OPC in terms of acid resistance (Shi and Stegemann, 2000b, Bakharev, 2005, Lloyd et al., 2012b, Ahmad Muhd Izzat, 2013, Izzat et al., 2013b, Aiken et al., 2017, Bernal et al., 2012a, Ariffin et al., 2013). Shi (2003) found that the corrosion depth of OPC was almost twice that of AAS binder when exposed to acid solutions. Moreover, AAFA binder is superior to AAS in appearance change and mass loss when exposed to the sulphuric acid solution (Aiken et al., 2018).

However, there is widespread controversy regarding the evaluation criterion for the acid resistance of AAMs. ASTM C267 (2012) has addressed the standard method for

the chemical resistance of OPC, which indicates four criteria include change of weight and appearance of specimens, test medium, and compressive strength. Some researchers believe that the widespread application of the already-known OPC standards is sufficient for the AAMs, while others disagree. Aiken et al. (2018) reported that the visual appearance and mass loss showed favourable results for the AAMs binders, while the percentage compressive strength loss of OPC mortars was lower than AAFS binders. Furthermore, the residual compressive strength of the AAFA mortar is much lower than the AAFS binders and OPC mortars due to its relatively lower initial compressive strength (Aiken et al., 2018). While this consensus had been raised by more scholars, there is currently no widely accepted test method and evaluation standard. Whether AAMs are more acid resistant than OPC is still unknown.

Due to the diversity of AAMs, it is hard to compare the acid resistance of AAMs and OPC directly. Thus, the present review summarized the state of the art concerning the physical and chemical performance of AAMs exposed to acid attack and discussed the influencing factors responsible for the degradation of materials. The aim of the present review is to provide better understanding of acid resistance of AAMs and also to simulate further research in this topic.

Over the past century, OPC is one of the most commonly used construction materials, due to its versatility, reliable performance, widespread availability and comparatively low cost than most other available building materials. However, concrete is susceptible to erosion in acidic environment as an alkaline system, leading to performance deterioration and economic loss. For example the acidic rain ( $\text{pH} < 5.6$ ) (Likens et al., 1979), a kind of acidic deposition, is a strongly corrosive medium containing not only  $\text{H}^+$  but also other species including  $\text{NH}_4^+$ ,  $\text{Mg}^{2+}$ , and  $\text{SO}_4^{2-}$  (Zeng et al., 2018), which could cause dissolution of alkaline substance in concrete surface and expansion (Zivica and Bajza, 2001b).

According to Chinese government report, about 15.7 billion dollars lost every year due to acidic rain (Xue et al., 2005, Qing and Yanxia, 2009). The sewage produced sulphuric acid dioxide dissolved in water under the decomposition of bacteria, making the sewer environment acidic (Song et al., 2019). This complex reaction made concrete vulnerable to deterioration and reduced the service life of concrete from 100 years to

30 - 50 years (Khan et al., 2019, Jensen, 2009). Approximately \$36 billion were used to maintain, repair and replace concrete component due to sulphide induced corrosion and carbonization (Jiang et al., 2014). Previous research on concrete corrosion caused by climatic environment has mostly focused on carbonation, chloride or sulphate corrosion, and freeze-thaw damage, rarely in acid corrosion (Alexander and Beushausen, 2019, LI and SUN, 2013). On the other hand, the greenhouse gases emission during the manufacture process of Portland cement is becoming perceived as unsustainable for environment, for example generated around 8% of global CO<sub>2</sub> (Provis and Bernal, 2014a, Olivier et al., 2013). Therefore, improving the acid resistance of concrete and developing new alternative acid-resistant construction materials are the motivation of both industry and academia.

Alkali-activated material (AAM) also referred to geopolymer (GP) which is a cementitious construction material prepared with aluminosilicates and alkaline solutions (Davidovits, 1991, Davidovits, 2008). AAM has been discussed and promoted as a supplementary construction material for cement in particular application (Provis et al., 2015, Provis, 2018) as its comparable properties and green footprint for environment. Aluminosilicates major from industrial by-products, particularly like granulated blast furnace slag (GGBFS) and fly ash (Provis et al., 2015, Duxson and Provis, 2008) are used as precursors in the system. Alkali solutions the major source of green gas emission including caustic alkali, silicate, carbonate and sulphate, etc are used as activators. Several authors reported that geopolymers showed out advantage over Portland cement in acidic resistance (Shi and Stegemann, 2000b, Bakharev, 2005). However, there is no standard test procedure classified acid attack of AAM.

The present review summarizes the state of the art concerning the performance of AAM exposed to acid attack and discusses the deterioration mechanisms responsible for the degradation of materials. The state of the art is reviewed from the aspects of the mass change, compressive change and penetration depth of various geopolymers under acidic environment. There is no standard evaluate criteria in published literatures, several factors could influence the value of mass change and compressive change except materials itself, such as kind of acidic solutions, pH value, test period,

etc. By highlighting the advantages and drawbacks of mixtures at different practical application, an outlook for future work will be provided.

## 2.2 Geopolymer technology

Alkali-activated reaction is a different hydration process between aluminosilicate-containing precursor and alkaline solution, unlike directly hydraulic-reaction of Portland cement and water (Chatterji and Rawat, 1965, Palomo et al., 1999b). Solid industrial waste like GBFS, FA, coal gangue, phosphorous slag, steel slag, and red mud which could be activated by alkaline solutions to form hardened cementitious materials are used as precursors (Provis et al., 2015). Metakaolin (MK) possessing intense pozzolanic reactivity is one natural precursor. Precursor is usually divided into two groups according to CaO content: low-calcium precursor, such as class F FA ( $w(\text{CaO}) < 10\%$ ) (ASTM, 2019), metakaolin, coal gangue; high-calcium precursor, like slag and class C FA ( $w(\text{CaO}) = 10 \sim 20\%$ ) (ASTM, 2019). The chemical and physical characteristics of precursors, and the properties of geopolymers derived from them, are well described in the literatures (Provis et al., 2015, Provis, 2014, Shi et al., 2003).

Alkali-activated reaction, also named as geopolymerization is a three-step process (Zhang et al., 2018a): (a). Dissolution. Under the reaction of  $\text{OH}^-$  from activators, the bonds broken of Si-O-Si and Si-O-Al in precursor and converted to ions ( $[\text{SiO}_4]^{4-}$  and  $[\text{AlO}_4]^{4-}$ ) into solution. (b). Conformation of amorphous hydration products. Above ions react with alkali metal cations (i.e.,  $\text{Na}^+$  or  $\text{K}^+$ ) and form hydration product for three-dimensional amorphous polymer structure. Meantime,  $\text{OH}^-$  could react with  $\text{Al}^{3+}$  and  $\text{Si}^{3+}$  at surface of precursors to form  $[\text{OSi}(\text{OH})]^-$ ,  $[\text{OSi}(\text{OH})]^{2-}$ ,  $[\text{OSi}(\text{OH})]^{3-}$  and  $[\text{Al}(\text{OH})_4]^-$  monomer. (c) Above monomers condensation polycondensation. The main alkali-activated products includes low-Ca sodium aluminosilicate hydrate (N-A-S-H) and high-Ca calcium (sodium) aluminosilicate hydrate (C-(N)-A-S-H) (Shi et al., 2011, Lee and Lee, 2016, Garcia-Lodeiro et al., 2011), along with other contaminants, e.g. calcium hydroxide, calcium silicate hydrate (C-S-H), mullite, quartz, hematite, ettringite, semi-carbonate al. (Shi et al., 2018, Bernal et al., 2011a, Bernal et al., 2013a). The composition distribution map is shown in Figure 2-1.

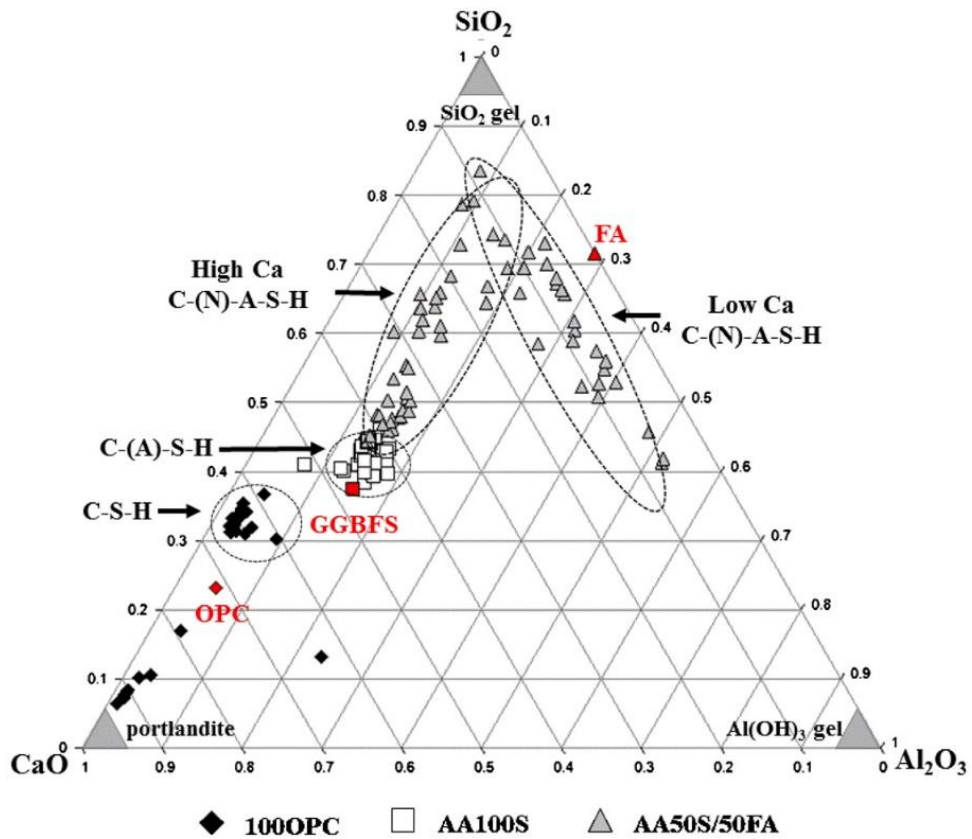


Figure 2-1. Pseudo-ternary plot of binder gel compositions measured by SEM-EDX (van Deventer et al., 2015).

As shown in Figure 2-2, the nanostructure of N-A-S-H gel is a three-dimensional zeolite-like network which contains crosslinked  $\text{AlO}_4$  and  $\text{SiO}_4$  tetrahedra linked via shared oxygen atoms, with terminal hydroxyl groups forming at the gel surface (Davidovits, 1994, Duxson et al., 2007b, Duxson et al., 2005b). C-(N)-A-S-H gel is composed of repeating sets of three silicate tetrahedra in aluminosilicate chains with an interlayer containing liquid  $\text{H}_2\text{O}$ , various cations e.g.  $\text{Ca}^{2+}$ ,  $\text{Na}^+$ , and  $\text{H}^+$ , and a calcium oxide sheet with layered network (Myers et al., 2013, Labbez et al., 2011). Silica presents mainly in one-dimensional chains and tetrahedral coordination (Provis and Van Deventer, 2009, Shi et al., 2003, Provis et al., 2005a, Myers et al., 2013).

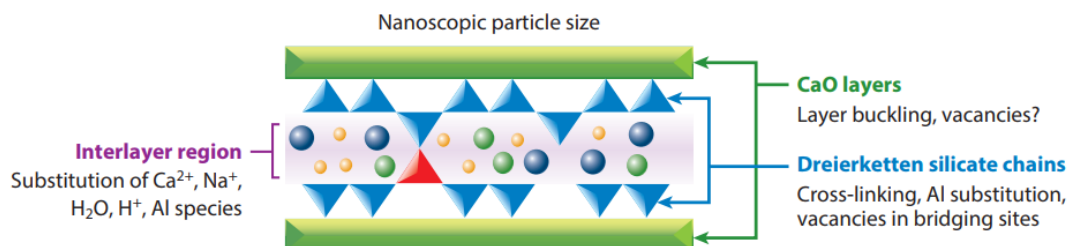


Figure 2-2. Schematic representations of a section of silicon-aluminium chains in C-(N)-A-S-H gel (Provis and Bernal, 2014b), existed in two layers composited by calcium octahedra (Myers et al., 2013).

## 2.3 Acid corrosion in the cement and concrete structure

### 2.3.1 Concrete sewer corrosion and biodeterioration mechanisms

In sewer pipe systems, gaseous hydrogen sulphide ( $H_2S$ ) can cause significant concrete degradation, as shown in Figure 2-3 (Grandclerc et al., 2018). The wastewater is composed of sulphate ions and sulphate-reducing bacteria, and aqueous hydrogen sulfide ( $H_2S$ ) is produced from the sludge under the reaction of bacteria (Shook and Bell, 1998). The gaseous  $H_2S$  escapes into the sewer atmosphere and partitions into the moisture layer present on the surfaces above the water line and dissociates into hydrogen ions ( $H^+$ ) and sulfide ions ( $S^{2-}$ ) in high humidity environment.  $S^{2-}$  could be oxidized into several sulphur species under the reaction of bacterial, then form sulphuric acid ( $H_2SO_4$ ) (Joseph et al., 2012).  $H^+$  could contribute to the reduction of surface pH of cementitious walls and  $SO_4^{2-}$  reacts with diffusion  $Ca^{2+}$  which producing gypsum and ettringite. The expansive reaction products cause severe damage of the sewer system (Alexander and Fourie, 2011).

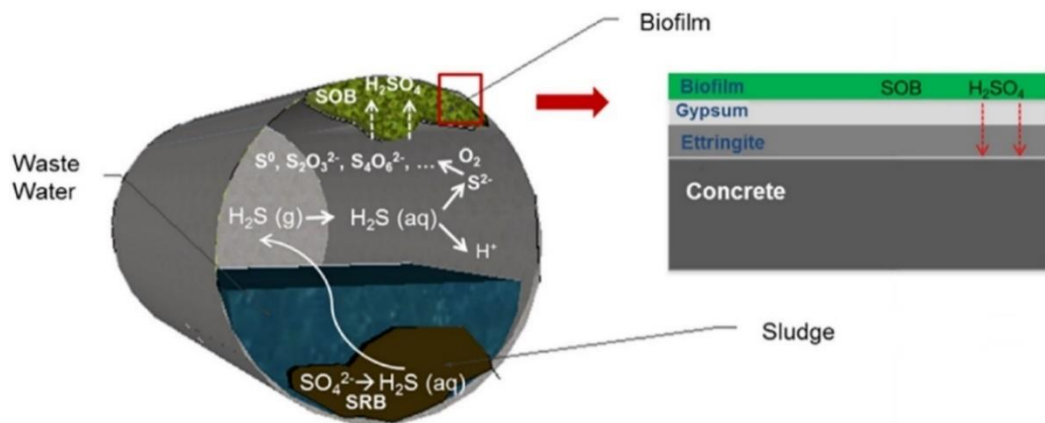


Figure 2-3. Concrete sewer and biodeterioration mechanisms. The biofilm is composed of sulphur-oxidizing bacteria (SOB) (Chen et al., 2003). Sulphate-reducing bacteria exists in the sludge (Grandclerc et al., 2018).

The corrosion process of sewer concrete is summarized in three stages by (Khan et al., 2019, Islander et al., 1991) as shown in Figure 2-4. The freshly placed concretes have a very high pH ranging from 12 to 13. Hence the freshly concrete is not favourable for the growth and colonisation of bacterial species. Firstly, carbonation of carbon oxide

(CO<sub>2</sub>) under humidity atmosphere causes the reduction of concrete surface pH of sewer concrete to 9-10, which is suitable for microbial colonies growth. At the second stage, the neutrophilic sulphur-oxidizing microorganisms (SOM) grows and utilizes the sulphuric compounds from wastewater to produce elemental sulphur and polythionic acid further reducing the pH of the concrete from 9 to around 4. Afterwards, acidophilic SOM starts metabolizing sulphur and thiosulphate into sulphuric acid, reducing the pH of concrete below 2.

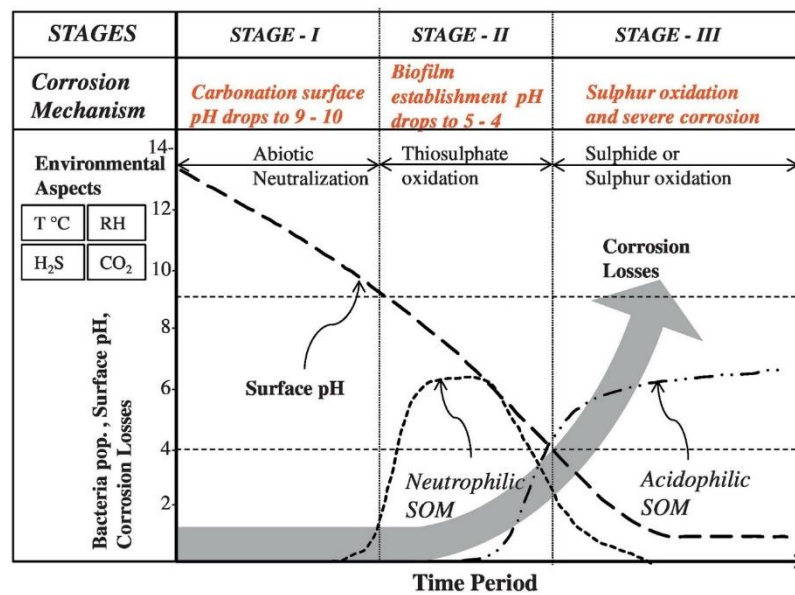


Figure 2-4. Stages of corrosion in new concrete with hypothesized microorganism's succession during Microbially Induced Concrete Corrosion (MICC) proposed by (Khan et al., 2019, Islander et al., 1991).

### 2.3.2 Acid rain corrosion

Sulphur dioxide (SO<sub>2</sub>) and oxides of nitrogen (NO<sub>x</sub>) released into the air when coal and oil are burned can be acidified. In the presence of water, SO<sub>3</sub> is converted rapidly to sulphuric acid (Equation 2-1), and NO<sub>x</sub> reacts with OH<sup>-</sup> to form nitric acid (Equation 2-2). This phenomenon is known as acid rain (Underdal and Hanf, 2019). The pH of acid rain varies by location, ranging from 4.0 to 7.0, as shown in Figure 2-5 (Sharma and Reddy, 2004, Vet et al., 2014). Even if sulphur and nitrogen emissions continue to drop as a consequence of climate protection (Vet et al., 2014), acid rain corrosion on concrete structures cannot be straightway ignored (Fan et al., 2010).

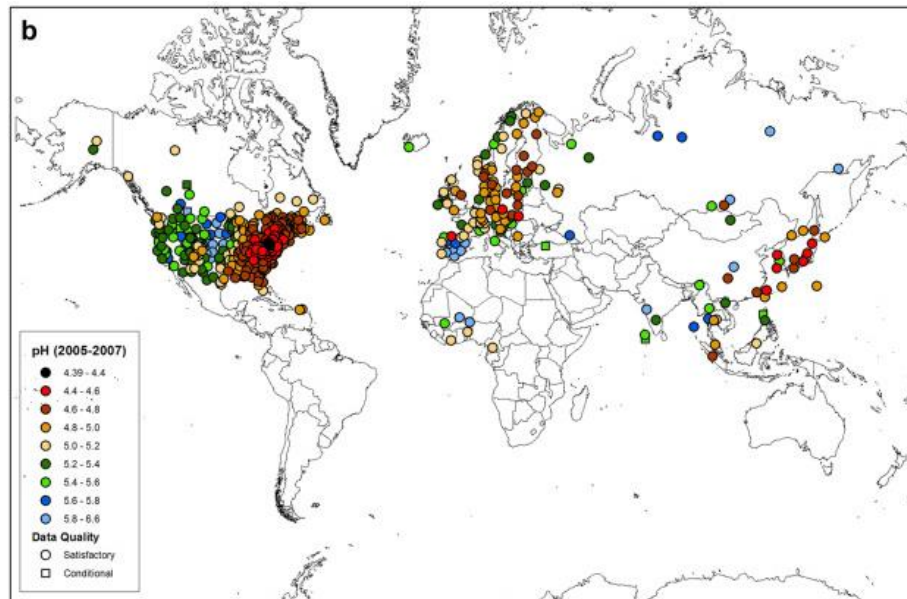


Figure 2-5. Three-year-average pH values for 2005-2007.

### 2.3.3 Acid gases corrosion

As an alternative to reduce CO<sub>2</sub> emission, capture gas from power plants and then store them in suitable geological formations had been proposed by Marchetti in 1977 (Marchetti, 1977). This idea of geological storage of CO<sub>2</sub> was explored further and extended to the treatment of H<sub>2</sub>S (Jacquemet et al., 2012). A large number of gas capture and storage projects have been active around the world (Bachu and Gunter, 2005, Beckwith, 2011). Geological disposal of these acid gases requires drilling and cement wellbores (Lesti et al., 2013). This requires the cement wellbores involved to be corrosion resistant to prevent gas leakage. Acid attack caused by acid gases is the main corrosion that occurs in cement wellbores, as shown in follow equations from Equation 2-3 to Equation 2-7.

$Ca(OH)_2 + CO_{2(aq)} \leftrightarrow CaCO_3 + 2H_2O$	CH carbonation	Equation 2-3
$C_xSH_y(s) + CO_{2(aq)}$	CSH carbonation	Equation 2-4
$\leftrightarrow CaCO_{3(s)} + SiO_2 \cdot yH_2O_{(s)}$ $+ H_2O$		
$H_2S_{(aq)} \leftrightarrow H^+ + HS^-$	H <sub>2</sub> S dissociation	Equation 2-5
$Ca(OH)_2 + 2H^+ \leftrightarrow Ca^{2+} + 2H_2O$	CH leaching	Equation 2-6
$H_2S_{(aq)} + 2H^+ \leftrightarrow Ca^{2+} + 2H_2O + SiO_{2(s)}$	CSH decalcification	Equation 2-7

## 2.4 Influencing factors of acid resistance of AAMs

### 2.4.1 Effect of precursor

Acid resistance of alkali-activated materials depended on the reaction products derived from various precursors (Lee and Lee, 2016, Bernal et al., 2012a, Bakharev, 2005). That main react products of OPC were calcium-silica-hydroxide (C-S-H) gel and calcium hydroxide. Calcium hydroxide could react with sulphuric acid and form expansive gypsum, causing the reduction of pH in cement, further C-S-H gel decomposition. For alkali-activated GGBFS (AAS), C-(A)-S-H gel with low C/Si ratio was formed and showed less solubility compared to C-S-H gel (Bernal et al., 2012a). Conversely, for N-A-S-H gel derived from alkali-activated metakaolin or low calcium fly ash, there was no expansive corrosion product formed and it was much less sensitive to acid solution (Okoye et al., 2017). The detailed results about acid resistance of geopolymers derived from fly ash, GGBFS, or blended precursors were summarized below.

#### 2.4.1.1 Fly ash

Natural pozzolans such as volcanic ashes or various minerals that require calcination like clays or shales were classified as Class N fly ash; low calcium fly ash (CaO ≤ 18%) referred to Class F that produced by burning anthracite or bituminous coal and high calcium fly ash referred to Class C (CaO > 18%) produced from burning lignite or subbituminous coal (ASTM, 2019). Previous studies (listed in

Table 2-1) mainly focused on class F fly ash as its widely source, more unburnt carbon, slower hydration reaction and lower compressive strength than Class C (Hemalatha and Ramaswamy, 2017).

Table 2-1. Summary of studies investigating durability of alkali-activated fly ash exposed to acid attack.

Sample		Curing	Acid solution			Ref.
Precursor	Activator (Na <sub>2</sub> O%/Ms)		Acid	Con. & Tem.	pH	
Class F FA	NaOH	80°C/50% for 72h, 20 ± 1°C/ 50%	H <sub>2</sub> SO <sub>4</sub>	1.0 M, 60 ~ 220°C		(Hashimoto et al., 2017)
	NaOH + Na <sub>2</sub> S	Oven at 85°C/99% for 20h	HCl	0.1 N	1	(Fernandez-Jimenez et al., 2007)
		Oven at 60°C for 24h, room for 3d		12%, 45 °C 30%, 25 °C		(Chaudhary and Liu, 2009)
		70°C for 1d		15%		(Temuujin et al., 2011)
		80 °C for 10 h		1, 2, 4 M		(Nguyen et al., 2013)
		80°C/25% for 12 h, 24°C/50%			1, 2	(Nguyen and Škvára, 2016)
		85°C for 48h	H <sub>2</sub> SO <sub>4</sub>	10%		(Thokchom et al., 2009)
		Mould curing for 1 d, and then water curing for 7 d		3%		(Izzat et al., 2013a)
		oven at 70°C for 24 h, room		3%		(Izzat et al., 2013b)
	oven at 80 °C for 24 h		2%	1	(Mehta and Siddique, 2017)	
	Ambient curing		2%	1	(Ourgessa et al., 2019)	
	Room for 48h, fog room		1%	1	(Gu et al., 2018)	
NaOH/KOH + Na <sub>2</sub> S	Room for 24h, then oven 95°C for 24h.	H <sub>2</sub> SO <sub>4</sub> CH <sub>3</sub> COOH	5%	0.8 2.4	(Bakharev, 2005)	
FA+ calcium aluminate cement	Sodium metasilicate	80°C/100% for 24 h, 300°C for 24 h	H <sub>2</sub> SO <sub>4</sub>	90 °C	2.5	(Pyatina and Sugama, 2016)
FA + red mud	Sodium trisilicate	room at 23°C/40%-50%			3	(Zhang et al., 2016a)
FA + silica fume	NaOH + Na <sub>2</sub> S	oven at 100°C for 72 h, room		2%		(Okoye et al., 2017)
FA + nano-silica		room		3%	3	(Deb et al., 2016)
FA + MK	K <sub>2</sub> S	20°C for 7d, room			4	(Zhuang et al., 2017)

Aliques-Granero et al. (2017) found that alkali-activated fly ash mortar (AAFA) exhibited minor change outer and remained dark grey at the inner region after 196 days 5%-sulphuric acid corrosion. The alkali-activated slag mortar (AAS) had severe expansion from edges to corner and was split into six pyramid-like fragments, corresponding to the cross-sectional change. As a control sample, OPC showed different corrosion process that disintegrated into acid solution from surface until complete dissolution after 196 days. The develop trend of mass change and compressive strength change of OPC, AAS and AAFA was shown in Figure 2-6. From the results, it was clear that AAFA experienced minor mass change and compressive strength. The AAS samples showed increased mass and compressive strength, while OPC sample showed significant decrease in mass and compressive strength.

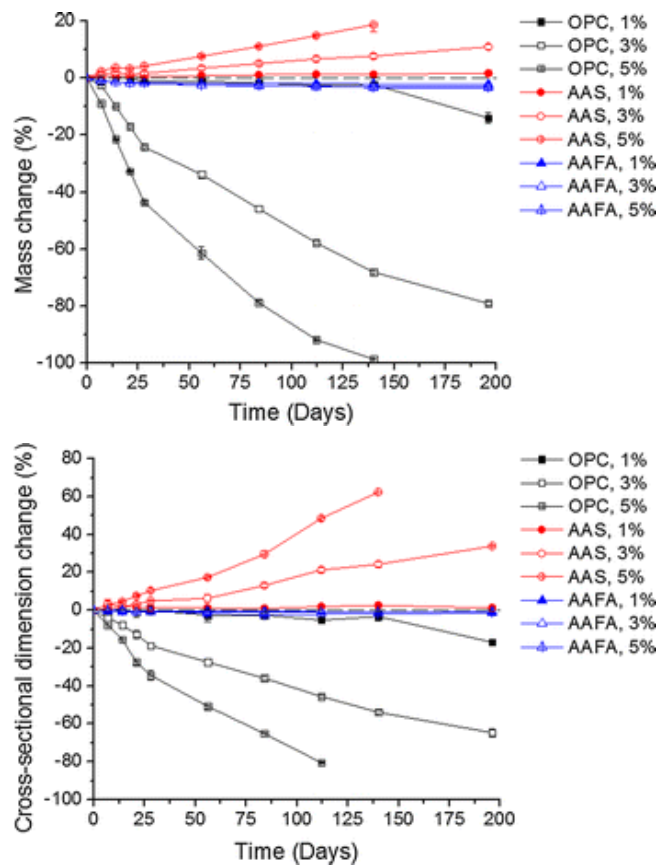


Figure 2-6. Mass and cross-sectional change of OPC, AAS and AAFA mortar cubes exposed to sulphuric acid solutions at different concentrations (1, 3, and 5 wt%) (Aliques-Granero et al., 2017).

Changes of mass and compressive strength of FA-based geopolymer were investigated by most research. It was hard to compare results in a constant variable environment as the inconsistency in experiments and materials. The published results about the mass change and compressive strength of AAFA were summarized in Figure 2-7, the mass

change distributed in the range between -5% and 5%, which meaning that AAMs derived from fly ash experienced minor mass change after exposed to acid. The change of compressive strength varied among studies from around 0% to 50%, which indicated the complexity of each system regarding the acid resistance.

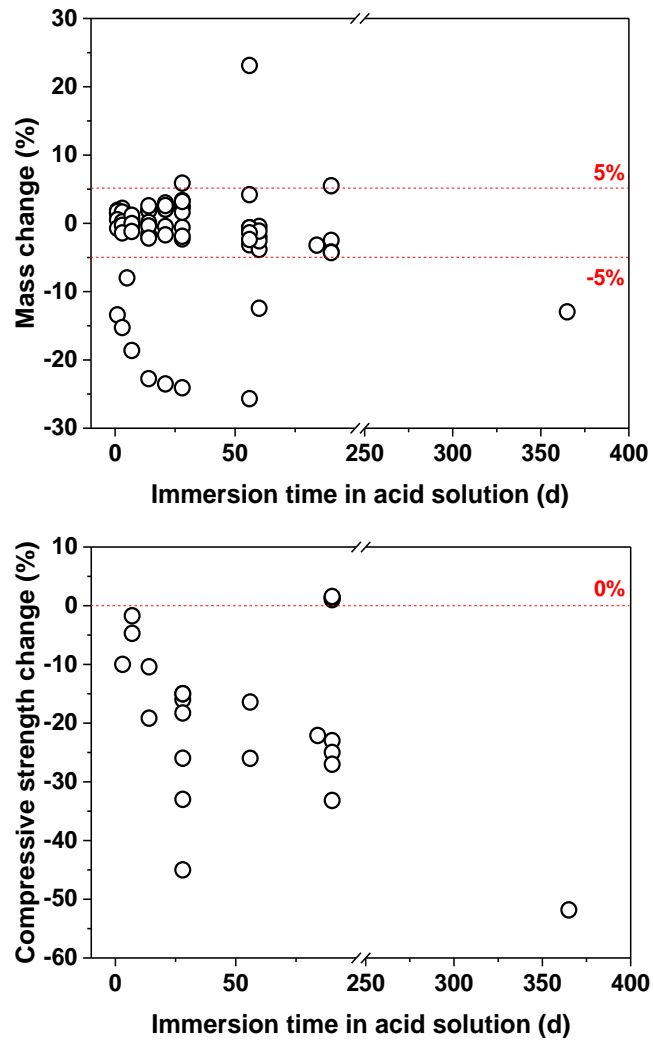


Figure 2-7. Changes of mass and compressive strength of fly ash based geopolymers, data from references listed in

Table 2-1.

For alkali-activated fly ash/metakaolin binders exposed to sulphuric acid solution, Zhuang et al. (2017) found that the flexural strength and compressive strength of binders remained rather stable after 360 days attack, while there was a decrease-increase trend for tensile strength. Compared to OPC, alkali-activated fly ash/metakaolin binders showed better acid resistance. Duan et al. (2015) tested the acid resistance of alkali-activated fluidized bed fly ash/metakaolin blends in sulphuric acid (2%) plus hydrochloric acid (2%) solutions. They consisted of the conclusion that AAMs showed better acid resistance than OPC. The resistance of AAMs derived from metakaolin and municipal solid waste incineration fly ash to acid rain was conducted by Jin et al. (2016), and the compressive strength loss of the samples increased with the pH and acid eluviation volume.

The effects of siliceous supplementary materials, such as silica fume and nano silica, on the acid resistance of fly ash-based AAMs were studied. Chindaprasirt et al. (2014) immersed alkali-activated blends from high calcium ground fluidized bed combustion fly ash and silica fume in 3% sulphuric acid solution for 3 months and found that the silica fume could help to increase the initial compressive strength but had minor effect on the compressive strength loss of blends during acid attack. This was because for high calcium AAMs system, enough silicon could simulate hydrated reaction to a greater degree, producing more C-(A)-S-H gel and developing compressive strength (Guo et al., 2010). In acidic environment, the leaching of calcium and the favourable dissolution of excess silica were responsible for the severe compressive loss. This phenomenon was reversed in the low calcium AAMs system. For low calcium fly ash, silica fume developed the acid resistance of fly ash-based geopolymers with less mass loss and compressive strength loss (Okoye et al., 2017). The calcium content of fly ash was possibly the cause of this difference.

Different to silica fume, nano-silicon had smaller average particle diameter, which could not only provide silicon source for geopolymerisation but also had filling effect to improve the microstructure of matrix under optimum dosage (Belkowitz et al., 2015). Deb et al. (2016) found that 2% corporation of nano-silica in fly ash-based geopolymer reduced the mass loss and compressive strength loss. This was because that increase of SiO<sub>2</sub> under optimum level could develop the density of matrix that

reduced the porosity and permeability and further reduced the ingress of acid. It should be noted that extra nano-silicon could not completely reacted in system which caused excessive self-desiccation and cracking that eventually reduce the acid performance of geopolymers (Belkowitz et al., 2015). A thermal shock resistant cement composed calcium aluminate cement and class F fly ash activated by sodium metasilicate were test the acid resistance to 90 °C sulphuric acid solution (Pyatina and Sugama, 2016). Samples were cured at 85 °C for 1 day followed by cured for another 12 h at 300 °C, simulating the circumstance of geothermal wells. The samples showed less weight loss and a small increase in compressive strength. This was due to that low calcium fly ash continued reacted even at later age. This effect became more obvious with the increase content of fly ash in AAMs.

#### 2.4.1.2 Metakaolin

Metakaolin showed a plate shape which was different from fly ash with sphere. Metakaolin-based AAMs need higher water/solid ratio to reach similar workability to fly ash, due to its shapes and fineness. Kong et al. (2007) illustrated that fly ash based AAMs contained higher proportion of microspores than metakaolin based AAMs which dominantly composed by mesoporous. The research related to the acid resistance of metakaolin-based AAMs was less than fly ash-based, due to its high cost in the production, as listed in Table 2-2.

Table 2-2. Summary of studies investigating durability of alkali-activated metakaolin exposed to acid attack.

Sample	Activator	Curing	Acid solution	Ref.
Precursor	(Na <sub>2</sub> O%/Ms)	(Temperature/Humidity, °C/%)	(pH)	
MK	KOH + PS	oven at 70 °C for 2 h	HCl (2)	(Gao et al., 2013)
MK	NaOH + Na <sub>2</sub> S	oven at 50°C for 17 h	HCl (2)	(Tognonvi et al., 2012)
MK	KOH + K <sub>2</sub> S NaOH + Na <sub>2</sub> S	70°C for 24h	HCl (1.47)	(Bouguermouh et al., 2017)
MK + fluidized bed FA	NaOH + Na <sub>2</sub> S	Microwave for 5min, then 40 °C	H <sub>2</sub> SO <sub>4</sub> HCl	(Duan et al., 2015)
MK + municipal solid waste incineration FA	NaOH + Na <sub>2</sub> S	20°C/60%	Simulated acid rain (3, 4, 5)	(Jin et al., 2016)

Palomo et al. (1999a) found that compression strength of metakaolin-based geopolymers continued increasing after immersion into sulphuric acid solution for 90 days. They claimed that the time spending on the transformation from the amorphous

aluminosilicate network structure into crystallization was responsible for the continuing development of mechanical strength. This was because that small amounts of crystals with faujasite structure were advantaged for the development of strength. Gao et al. (2013) found that the structure of geopolymer derived from metakaolin remained intact after 28 days HCl attack. Bouguermouh et al. (2017) investigated the chemical durability in hydrochloric acid of potassium and sodium activated metakaolin geopolymers and they found that minor changes in the crystalline components and amorphous features of binders.

#### *2.4.1.3 Ground granulated blast-furnace slag (GGBFS)*

Ground granulated blast-furnace slag (GGBFS), sometimes simply referred to as “slag”, is a glassy granular material. Unlike the consistent chemistry and mineralogy of OPC around world or fly ash which completely dependent on the nature and relative proportions of minerals associated with the coal matter being burned, slag lied between these two extremes, with its chemistry dominated by calcium from the limestone and silica from ore. From previous research (as shown in Figure 2-6 and Table 2-3), the mass change and compressive strength change of alkali-activated slag (AAS) blends lied between OPC and alkali-activated fly ash.

Shi and Stegemann (2000c) started the acid corrosion test on activated blast furnace slag cement, compared with PC, lime-fly ash blend and high alumina cement-gypsum and lime (HAC) paste about twenty years ago. Excepted for the rapid dissolution of HAC paste, the corroded depth of alkali-activated slag paste interposed between OPC and lime-fly ash blend. They proposed that the acid resistance of pastes depended on the nature of protective layer which formed after corrosion consisting mainly of silicone gel rather than the permeability porosity. This was because that the calcium was more sensitive to the pH drop than silicon and aluminium. The pastes with higher calcium content corroded more severely. Shi (2003) confirmed the better acid resistance of alkali-activated slag than OPC due to its lower calcium/silicon (Ca/Si) ratio. It was noticed that Ca/Si ratio also determined the corrosion products of materials. A dense protective layer of silica gel formed in alkali-activate slag pastes, while a porous corroded layer left in OPC paste.

Bakharev et al. (2003) compared the compressive strength loss of alkali-activated slag and OPC concrete when exposed to acetic acid solution ( $\text{pH} = 4$ ) for 12 months and found that AAS showed less compressive strength loss than OPC concrete. The decalcification of C-S-H gel and the formation of soluble calcium acetate led to the serious deterioration. Alkali-activated slag composed of less calcium components than OPC, which was verified by Živica and Krizma (2013) and Komljenović et al. (2012). However, Bernal et al. (2012a) found that alkali-activated slag and OPC showed similar compression strength changes when exposed to mineral acids. It was observed that a consistent increase of porosity happened for all samples. But alkali-activated slag showed less increase in porosity compared to OPC. They reiterated the effect of porosity on acid resistance and proposed that alkali-activated slag paste showed better acid resistance than OPC in acetic acid.

Regarding to the mass change, Koenig et al. (2017) found that the OPC samples showed almost twice mass loss than alkali-activated slag when exposed to mixed solution of organic acids. In  $\text{HNO}_3$  acid solution, alkali-activated slag showed around 11.6% mass loss, while around 16.2% of mass loss for OPC (Mellado et al., 2017). Aliques-Granero et al. (2017) found a slightly mass increase in AAS samples when exposed to  $\text{H}_2\text{SO}_4$  solution, and the increase rate increased with the concentration of acid.

Table 2-3. Summary of studies investigating durability of alkali-activated slag exposed to acid attack.

Sample	Precursor	Activator (Na <sub>2</sub> O%/Ms)	Curing (Temperature/Humidity, °C/%)	Acid solution (pH)	Ref.
Slag	Anhydrous sodium metasilicate		moisture chamber at 23°C for 1 year	HNO <sub>3</sub> (3) CH <sub>3</sub> COOH (3) CH <sub>3</sub> COOH (5)	(Shi and Stegemann, 2000c)
			Moist curing (23°C)	HNO <sub>3</sub> (3) CH <sub>3</sub> COOH (3)	(Shi, 2003)
	Anhydrous sodium metasilicate	NaOH + Na <sub>2</sub> S (4%/0.75)	21°C/50%	CH <sub>3</sub> COOH (4)	(Bakharev et al., 2003)
	SS (2.4)		25°C/90%	H <sub>2</sub> SO <sub>4</sub> (3) HCl (3) HNO <sub>3</sub> (3) CH <sub>3</sub> COOH (4.5)	(Bernal et al., 2012a)
	NaOH + Na <sub>2</sub> S		20°C/90%	6 M NH <sub>4</sub> NO <sub>3</sub> (4.95)	(Komljenović et al., 2012)
	NaOH + Silica fume		24 h at 95% RH	1% HCl	(Živica and Krizma, 2013)

#### 2.4.1.4 Fly ash/GGBFS blends

For low calcium systems, geopolymer derived from Class F fly ash set slowly. Curing at high temperature or blended with slag could increase setting speed and improve earlier compressive strength (as listed in Table 2-4). The reaction product of fly ash/slag blends was the coexistence of N-A-S-H, C-A-S-H and C-(N)-A-S-H gels. The C-(N)-A-S-H gel was suggested to possess a higher load-bearing capacity and space-filling effect than N-A-S-H gel (Provis et al., 2012, Zhang et al., 2018c, Lee and Lee, 2016). With the increase of slag content, the compressive strength improved due to the increase content of incorporated calcium and formation of C-(N)-A-S-H gel with denser network. For the acid resistance of blends, except for the difference in raw materials, the fly ash/slag ratio was of significant important influencing factor and was studied by researchers frequently.

Table 2-4 Summary of studies investigating durability of alkali-activated fly ash/slag exposed to acid attack.

Sample		Curing (Temperature/Humidity, °C/%)	Acid solution		Ref.
Precursor	Activator (Na <sub>2</sub> O%/Ms)		Acid (pH)	Con.	
Low calcium FA + slag	NaOH + Na <sub>2</sub> S	23°C/100%	H <sub>2</sub> SO <sub>4</sub>	1%, 3%, 5%	(Aliques- Granero et al., 2017)
		Multi-step curing	H <sub>2</sub> SO <sub>4</sub> (1,2,3)		(Allahverdi and Škvára, 2006)
		23°C	HNO <sub>3</sub> (3)		(Lloyd et al., 2012a)
		75°C for 48h, 20 °C/ 65%	H <sub>2</sub> SO <sub>4</sub> (1~3)		
			HNO <sub>3</sub> (1~3)		
			Mixed Organic acid (3)	acetic propionic lactic acid	(Koenig et al., 2017)
		20°C/50%	H <sub>2</sub> SO <sub>4</sub> (3)	10%	(Lee and Lee, 2016)
20°C/90% for 28d	H <sub>2</sub> SO <sub>4</sub> (1)		(Zhang et al., 2018c)		
70°C for 7d, 20 ± 1°C/50%	H <sub>2</sub> SO <sub>4</sub> (1)	1, 3 and 5%	(Aiken et al., 2018)		
room	H <sub>2</sub> SO <sub>4</sub> (3)	3%	(Deb et al., 2016)		

Figure 2-8 summarized the effect of slag content on the compressive strength change and residual compressive strength of alkali-activated fly ash/slag blends. Lee and Lee (2016) found that the samples with 30% of slag showed the highest decline of the compressive strength. This was possibly due to the formation of N-C-(A)-S-H gel with a certain amount of calcium incorporated in the structure (Ismail et al., 2014), which lower acid resistance than C-(A)-S-H gel. The N-A-S-H gel formed binders with less slag content seemed to have less susceptible to acid than C-(A)-S-H. Aiken et al. (2018) found that the loss rate increased with the acid concentration, but it was hard to judge the effect of slag content on loss rate. Koenig et al. (2017) found that for alkali-activated fly ash binders, a slightly increase of compressive strength was found after 12 weeks immersion in sulphuric acid compared to that curing at water. The alkali-activated fly ash showed barely visible change in visual appearance, while samples started progressively paste loss while with the increasing of slag content. Paradoxically, Lloyd et al. (2012b) calculated the corroded depth by measuring the length change of samples, and found that the corroded depth decreased with the increase of slag content which means samples with higher slag content had less paste off, as shown in Figure 2-8. Although the author claimed that the corrosion depth was the more meaningful indicator than change of mass and compressive strength and had been recognized by some peers (Zhang et al., 2018c), others believed that the claim

could be effective under specific application conditions (Aiken et al., 2018). The peeling depth and remain depth could not represent the corroded depth and uncorroded depth, as not all erosion cause spalling.

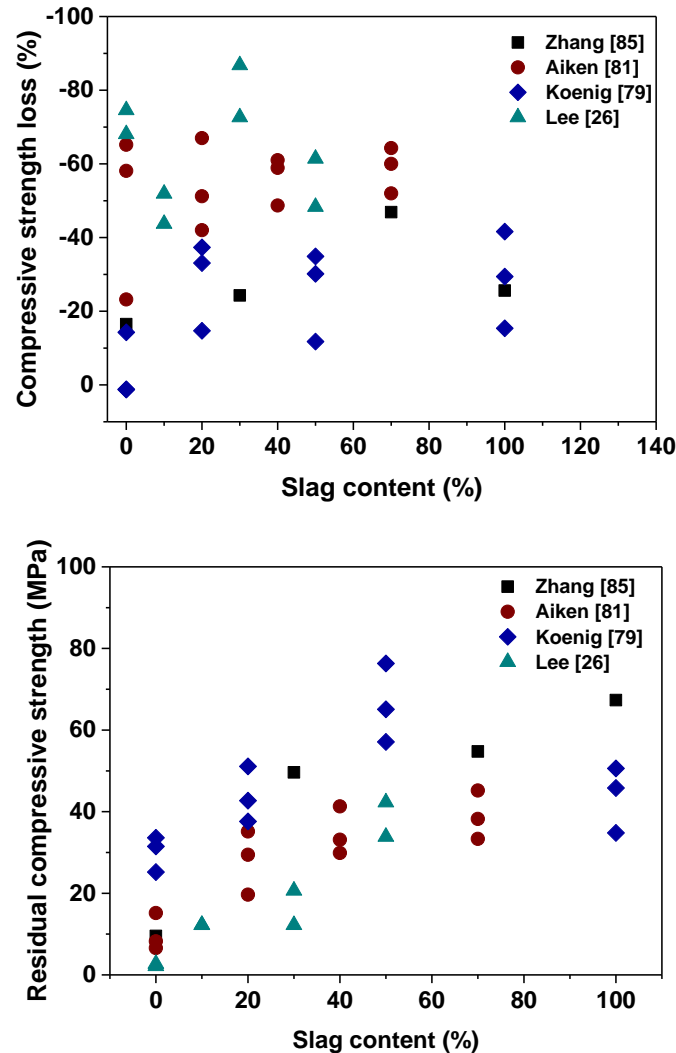


Figure 2-8. The effect of slag content on compressive strength loss and residual compressive strength, data collect from previous published literatures (Lee and Lee, 2016, Aiken et al., 2018, Koenig et al., 2017, Zhang et al., 2018c).

The content of slag appeared different influence trend on the acid resistance based on different evaluate indictors. The compressive loss rate was not a suitable indicator to evaluate the acid resistance of fly ash/slag blends. Neither mass loss, compressive strength loss nor peeling depth could be an effective indictor of acid resistance (Aiken et al., 2018, Lee and Lee, 2016, Gu et al., 2018). There was a need to develop standard test method to evaluate the acid resistance of geopolymers.

The effect of slag content on the change of reaction products of alkali-activated fly ash/slag binders was shown in Figure 2-9. The C-A-S-H and C-N-A-S-H gels formed in high-calcium systems were no longer existent after exposed to sulphuric acid, indicating the gels were vulnerable to sulphuric acid attack. The broad hump indicating N-A-S-H gel in fly ash based geopolymers could still detected in the XRD patterns after sulphuric acid attack.

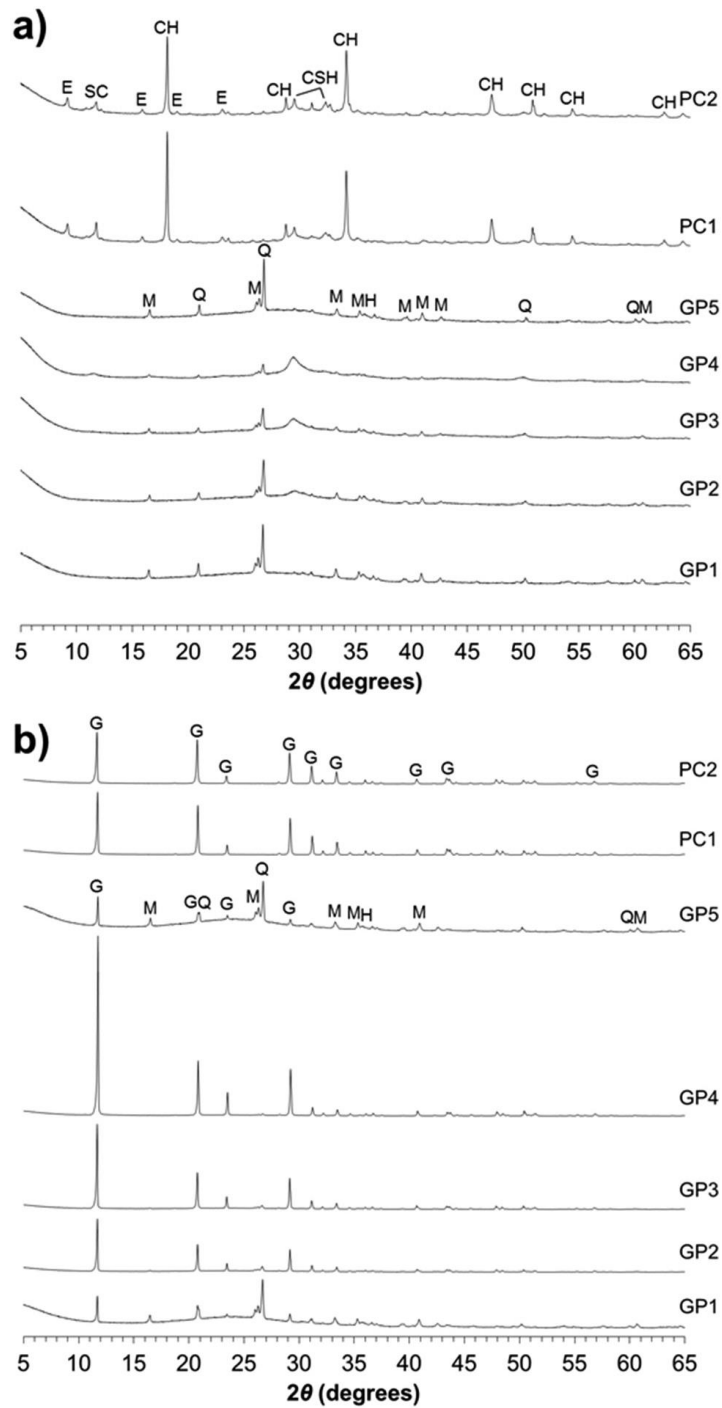


Figure 2-9. The effect of slag contents on the reaction products of geopolymers before and after exposed to sulphuric acid solution. GP1 and GP5 were fly ash based, while GP2 to GP4 presenting the slag content in geopolymers were 30%, 70% and 100%, respectively. G-gypsum, M-mullite, Q-quartz, H-hematite, E-ettringite, SC-semicarbonate, CH-calcium hydroxide, CSH-calcium silicate hydrate (Aiken et al., 2018).

Acid corrosion cause the degraded surface and changes in bromicrostructure of fly ash/slag blends. Signs of physical deterioration such as cracks, gaps and aggregate matrix debonding were observed as shown in **Error! Reference source not found.**. The fly ash and slag based geopolymer mortar (FA-GPm) showed minor crack propagation near edges and minor efflorescence, while the sulphate resistant Portland cement (SRPC) mortar showed major degradation and loss of almost 2-3 mm material from the surface.

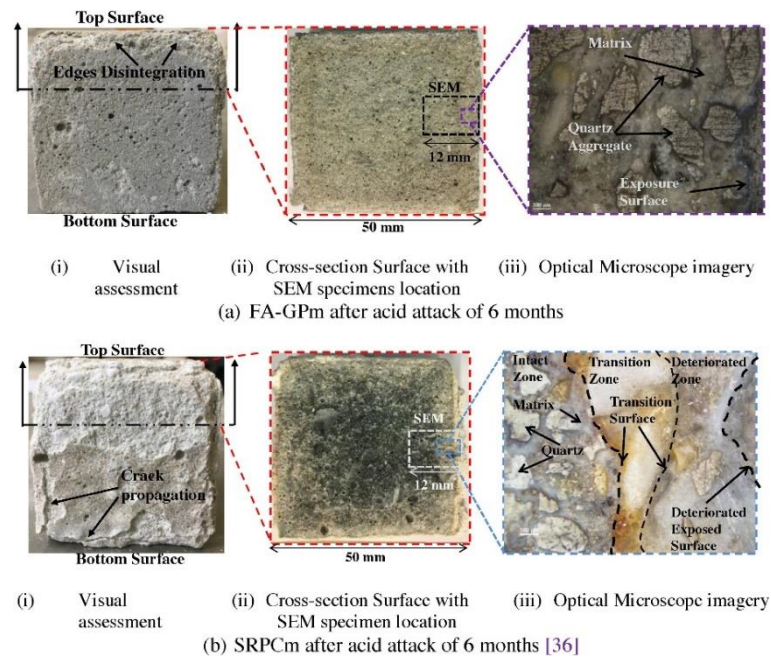


Figure 2-10. Visual analysis and optical microscopy of specimens (a) FA/Slag blend mortar (FA-GPm) and (b) sulphate resistant Portland cement mortar (SRPCm) after exposure to sulphuric acid solution for 6 months (Khan et al., 2020).

The distroation of the crosss-section of the samples after exposure to the sewer attack for 24 months was detected by SEM (as shown in **Error! Reference source not found.**). It was observed that the creation of voids and gaps within the microstructure of FA-GPm near interface with aggregate, which caused the increment of porosity and further the loss of compressive strength and density of the samples. Compbined the EDX images, we could find the precipitation of gypsum. And also we could observe

the loss of alkalinity from the gel matrix, and there was no major dealumination. This indicated that the framework of cross-linked N-A-S-H gel matrix was slightly disoriented with the loss of alkali. But it could be observed of partial dealumination within the matrix which indicating limited transformation of gel framework to amorphous silica gel structure, due to the penetration of acid.

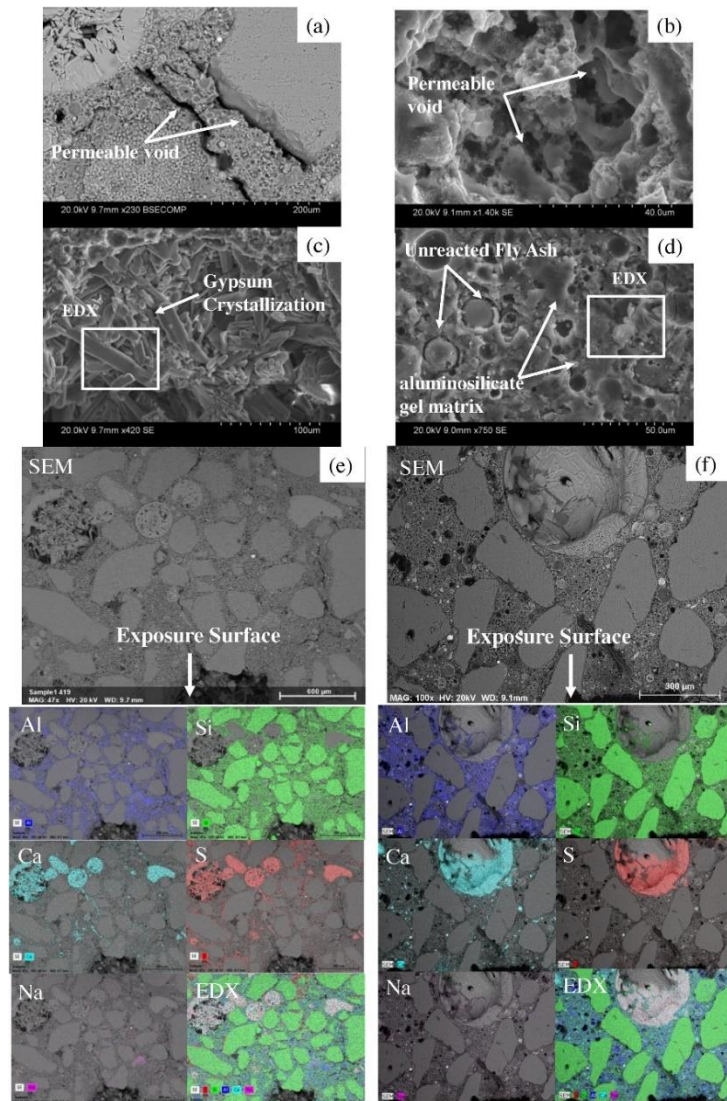


Figure 2-11. SEM images with EDX elemental mapping of fly ash/slag blend mortar (FA-GPm) after exposure to aggressive sewer environment in chamber 1 (high  $H_2S$  content) and 2 (low  $H_2S$  content) for 24 months.(Khan et al., 2020).

The SEM-EDX images of the SRPC mortar which was exposed to sewer attack for 24 months was shown in **Error! Reference source not found.**. From the EDX, it was obvious that extensive sulphur was penetrated into the matrix of the SRPC mortar.

This was led to the disintegration of portlandite and C-S-H matrix, beside the widespread precipitation of gypsum and nucleation of ettringite, while the silicon and aluminum were completely depleted.

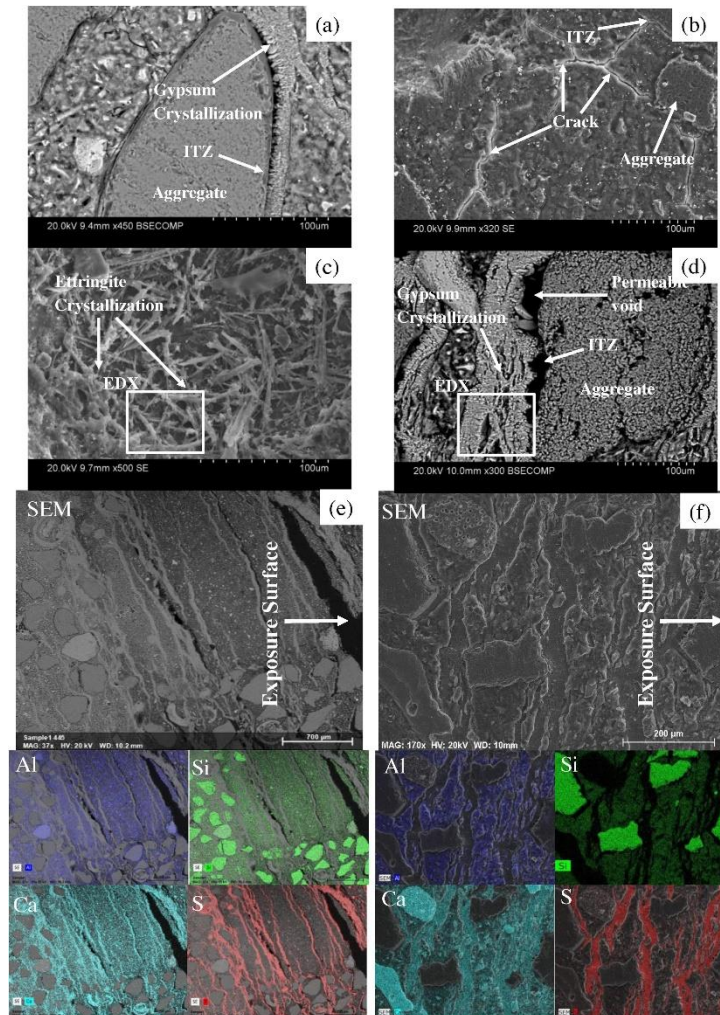


Figure 2-12. SEM images with EDX elemental mapping of sulphate resistant Portland cement mortar (SRPC) after exposure to aggressive sewer environment in chamber 1 (low H<sub>2</sub>S content) and 2 (low H<sub>2</sub>S content) for 24 months.(Khan et al., 2020).

#### 2.4.1.5 Others

Recent research greatly expanded the source and type of precursors for geopolymers (Provis et al., 2015), such as pulverized fuel ash, fluidized bed fly ash, palm oil fuel ash, municipal solid waste incineration fly ash, volcanic ash, red mud, calcinated mine waste, ceramic waste and waste glass powder, as listed in Table 2-5.

Fernando and Said (2011) tried immersion test of alkali-activated mine waste mud in 5% of sulphuric, hydrochloric and nitric acid solutions and found that the sample

showed better performance in appearance change and weight change than OPC. They attributed this phenomenon to the less calcium compounds and lower water absorption rate of the alkali-activated samples. Ariffin et al. (2013) tested the acid resistance of blends composed of pulverized fuel ash and palm oil fuel ash and found that the blends experienced less mass and compressive strength loss than OPC. They claimed that C-S-H gel in OPC was more susceptible to acid environment than N-A-S-H gel. Chindaprasirt et al. (2014) found that incorporation of around 3.75% of silica fume in alkali-activated fluidized bed fly ash blends could help to develop the compressive strength and durability performance. Duan et al. (2015) found a lower porosity of alkali-activated fluidized bed fly ash/metakaolin blends which contributed to the better performance. Jin et al. (2016) found smaller strength loss in metakaolin-based geopolymers than OPC when exposed to acid rain (pH = 2). Mellado et al. (2017) concluded that the low mechanical stability of alkali-activated ceramic waste. Vafaei et al. (2018) tested the blends of waste-glass powder and calcium aluminate cement in acidic solution which showed superior durability performance than OPC. They attributed to the higher stability of aluminosilicate structure and relatively low calcium content. Zhang et al. (2016a) also found comparable performance of alkali-activated red mud and class F fly ash blends to OPC in acidic environment which was consistent with Okoye et al. (2017).

Table 2-5 Summary of studies investigating durability of alkali-activated other precursors exposed to acid attack.

Sample		Curing (Temperature/Humidity, °C/%)	Acid solution		Ref.
Precursor	Activator (Na <sub>2</sub> O%/Ms)		Acid (pH)	Con.	
Fluidized bed FA + Silica fume		65 °C for 24 h, then 25 °C/80%	H <sub>2</sub> SO <sub>4</sub>	3 vol%	(Chindapasirt et al., 2014)
Pulverized fuel ash Palm oil fuel ash		room at 28°C for 28 d	H <sub>2</sub> SO <sub>4</sub> (1)	2%	(Ariffin et al., 2013)
Calcinated mine waste mud		Room curing	HCl H <sub>2</sub> SO <sub>4</sub> HNO <sub>3</sub>	5%	(Fernando and Said, 2011)
Bottom ash	NaOH + Na <sub>2</sub> S	75°C for 48 h, 23±2°C/50%	H <sub>2</sub> SO <sub>4</sub> (1)	3%	(Sata et al., 2012)
Volcanic ash		oven at 80°C for 24 h, ambient	H <sub>2</sub> SO <sub>4</sub> (1)	5 wt%	(Yankwa Djobo et al., 2016)
Ceramic waste		65°C for 48h, 23 ± 1°C/100%	HNO <sub>3</sub> (2)	1 M	(Mellado et al., 2017)
Waste-glass powder		Room at 23°C/95% for 24h, 90°C for 2h	H <sub>2</sub> SO <sub>4</sub> (3) HCl (3)		(Vafaei et al., 2018)
Quartz powder Glass waste		20 ± 2 °C or 80 ± 2 °C	H <sub>2</sub> SO <sub>4</sub> (1)	3%	(Zhang et al., 2018b)
Lithomarge precursor	Na <sub>2</sub> S	Multi-step curing	H <sub>2</sub> SO <sub>4</sub> HCl	0.10, 0.31 and 0.52 mol/l	(Kwasny et al., 2018)

#### 2.4.2 Type of activator

Generally, activators refer to caustic alkali (e.g., NaOH and KOH), alkali-containing silicates (commonly sodium silicate, i.e., waterglass), aluminates, phosphates, sulphates, carbonates (commonly Na<sub>2</sub>CO<sub>3</sub>), etc. A product of the suspension of silica fume in sodium hydroxide water solution was proved to be used as activators but should be cured under specific conditions (Živica and Krizma, 2013). The caustic content, Na<sub>2</sub>O/SiO<sub>2</sub> ratio and total amount of Na<sub>2</sub>O and SiO<sub>2</sub> could influence the development of compressive strength of AAMs. For example, the compressive strength of samples activated by NaOH solution increased with the content of Na<sub>2</sub>O in activators (Fernández-Jiménez and Palomo, 2005). The higher content of Na<sub>2</sub>O increased the pH of activators, which had a positive effect to the kinetics of reaction (Palomo et al., 1999b). Bakharev (2005) activated fly ash by the sodium hydroxide and sodium silicate solutions, respectively, and found that the former showed better sulphuric acid resistance. The former deteriorated through the formation of cracks, while the later deteriorated through crystallisation of zeolites and formation of fragile grainy structures. The reaction between samples and acid solution governed the

degradation process of FA-based geopolymers. Ourgessa et al. (2019) found that the higher molarity and higher liquid to solid ratio of sodium hydroxide solution could benefit the strength and porosity of alkali-activated fly ash, and then promote the acid resistance.

Lloyd et al. (2012b) found that the corroded depth of alkali-activated fly ash pastes decreased, and the acid resistance improved with the increase amount of soluble silicate and sodium content, respectively. A denser corroded layer (Si-rich) formed at the samples that hindered the degradation of acid attack. On the other hand, with the increase amount of sodium, the corroded depth decreased but the corroded layer became brittle and more likely to generated shrinkage cracks which caused by dissolution and precipitation of soluble compounds.

The effect of activators dosage on the acid resistance of AAMs was also investigated. Aiken et al. (2018) found that the application of high dosage activators was conducive to the formation of dense structures, reduce the porosity and alkalinity loss of geopolymers under acidic conditions. However, very little impact on sulphuric acid resistance of neat fly ash based geopolymer was found as the similar reaction product and corrosion mechanism. The author further stated that the acid resistance of FA-based geopolymers rely on the reaction productions rather than the porosity.

Another infusing factors of activators on the acid resistance of AAMs was the alkaline cations. Bouguermouh et al. (2017) investigated the role of alkaline cations on microstructure and composition of metakaolin-based geopolymers after acid attack. They found that sodium hydroxide was better for metakaolin with high kaolinite while potassium hydroxide was better for low kaolinite metakaolin in acidic environment. The former was due to the formation of more stable aluminosilicate cross-linked polymer structure, while the later was due to the filling effect of secondary minerals (quartz and muscovite) occupied in pores avoiding the release of alkali cations into the acidic solution, as shown in Figure 2-13.

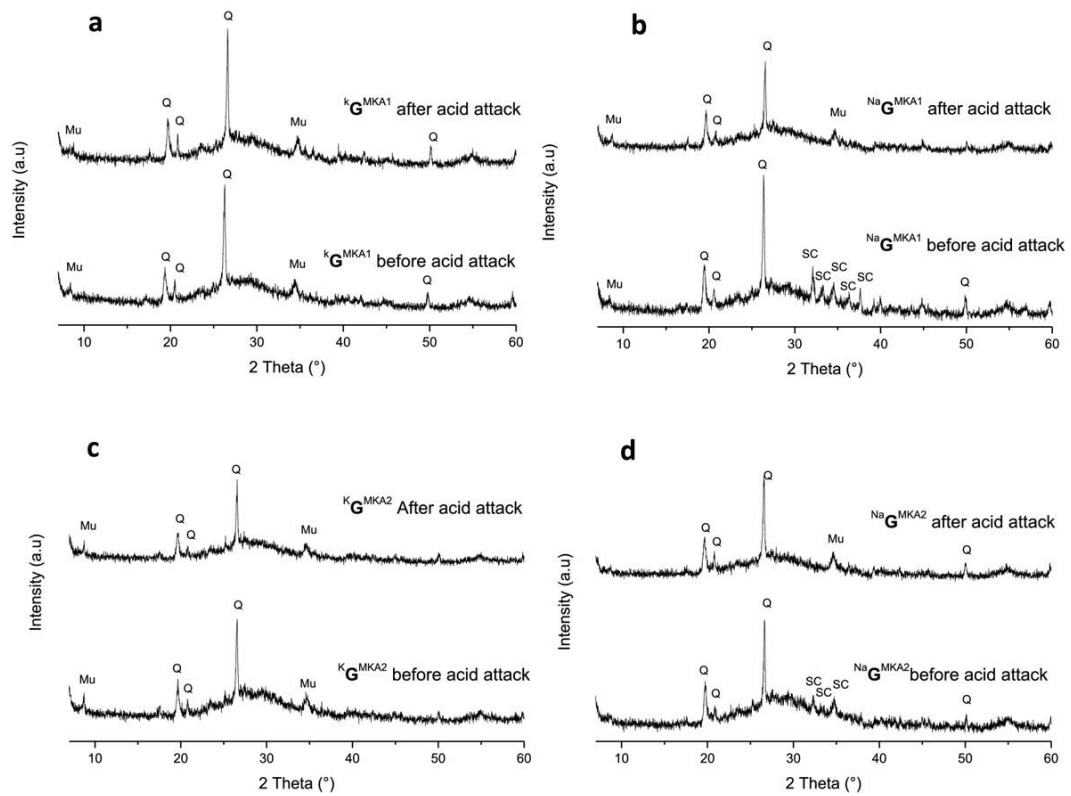


Figure 2-13. XRD patterns of low kaolinite MKA1 and MKA2 activated by sodium hydroxide, high kaolinite KR activated by potassium hydroxide, respectively Bouguermouh et al. (2017).

## 2.4.3 Curing program

### 2.4.3.1 Effect of curing program on alkali-activation reaction

The effect of curing program on the acid resistance of AAMs was related to the change of alkali-activation reaction under different curing regimes. The detailed alkali-activation process was summarized in the section 2.2. Thermal curing was proved to accelerate the dissolution, conformation and condensation processes (Graytee et al., 2018). As a result, the geopolymer cured at suitable higher temperature environment could improve the compressive strength of the geopolymer with the more polymers.

The infusing factors related to curing regimes included temperature, humidity and pressure of the curing environment. Bai et al. (2018) found that moist curing could ensure better mechanical properties of steel slag modified geopolymer, compared to exposed curing and sealed curing. Zribi et al. (2019) have confirmed that curing temperature could decrease the consolidating time from few days at room temperature to few hours at 60 °C. After consolidation, the compressive strength increased as a function of curing time for both samples. Ranjbar et al. (2018) tried hot-pressed curing

which offered an efficient method for production of high strength binders in an extremely short time which is remarkably applicable in low energy precast. The increase in both temperature and time provided a positive effect on the dissolution of reactive portion of the aluminosilicate precursors. Zhao et al. (2019) put 7-day ambient cured sample in the oven at 50°C and 80°C for 1 day, respectively, and found that samples cured at 50°C showed higher compressive strength. For samples cured at 80°C, as the formation of internal cracks and the faster moisture evaporation during the curing process sampled showed lower compressive strength. Nguyen et al. (2013) also found that the higher curing temperatures resulted in higher compressive strengths, although curing at temperature over 60°C could not increase the compressive strength significantly.

#### *2.4.3.2 Effect of curing program on the acid resistance*

For fly ash based geopolymers, Yankwa Djobo et al. (2016) did sulphuric acid (5% of H<sub>2</sub>SO<sub>4</sub> solution with pH = 1) corrosion test on volcanic ash based geopolymer mortars, which cured at room temperature (27 ± 3 °C) for 7 days and oven curing 80 °C for one day, respectively before demold. They found that samples cured at 27 °C had a 24% of compressive strength loss and 3.51% of weight loss at 180 days. For samples cured at 80 °C, 60% of strength loss and 3.1% of weight loss were found, which meaning rapid evaporation at 80°C resulted in poor pore structure with high connectivity then led to bad acid resistance. However, there were conflicting conclusions from researchers. Song et al. (2005) cured the class F fly ash based geopolymer concrete at either 23°C or 70°C for 24 hours, and found that specimens had similar degradation trends regardless of the curing conditions. Sreevidya et al. (2012) cured fly ash based geopolymers at 60°C for 24 hours and then cured ta ambient environment for 27 days. The samples remained structurally intact and did not show any recognizable change in color after immersed into 5% sulphuric solution and 5% nitric acid for 14 weeks.

The effect of microwave curing on acid resistance of fly ash based geopolymer was conducted by Chindaprasirt et al. (2012). The household microwave (2.45 GHz, 90 Walt) radiation could develop the acid resistance of high calcium fly ash based geopolymers, as indicated by the relatively low strength loss. Microwave radiation heightened the dissolution of fly ash at the early stage of geopolymerization and then a dense and strong sample was obtained that improved the acid resistance.

## **2.5 Mechanism of acid corrosion for PC and AAMs**

### **2.5.1 Sources of acidic environment**

Acidic environment for concrete mostly related to the industrial processes and urban activity (Zivica and Bajza, 2001a). The source of acid media for concrete included acid rain caused by gaseous carbon dioxide, sulphur dioxide and nitrogen oxide from burning a large amount of fossil fuels or biological substances, and sewerage corrosion happened in sewer system. Corrosion in sewer system related to the bacterial activity including the production of hydrogen sulphide which could be oxidised to sulphuric acid (Sand and Bock, 1984). So far, the literatures were mostly related to the sulphuric acid on geopolymers as it related to the practical environments, i.e., sewer swage, acidic rain, oil well etc.

### **2.5.2 Aggressivity of acid**

#### *2.5.2.1 Dissociation degree of the acid*

The aggressivity of acidic solutions was depended significantly on the real concentration rather than pH value. This was because that pH value depended on the dissociation degree of the acid. Strong acids (i.e. HCl, HNO<sub>3</sub> and H<sub>2</sub>SO<sub>4</sub>) had a high dissociation degree might possess lower pH value even in small quantities in solution comparing a weak acid, for example organic acid (Zivica and Bajza, 2001a). Shi and Stegemann (2000a) found that acetic acid appeared much more aggressivity than nitric acid, that was contradiction with Pavlík (1994). The reason for this phenomenon was related to the former took constant pH value while the later adapted constant concentration. With the same pH value, acetic acid showed much corrosive than nitric acid for alkali-activated slag paste (Shi, 2003), as much higher concentration of acetic acid than nitric acid due to the difference in dissociation degree. At the same concentration, mineral acids seem more corrosive to pastes than organic acids (Shi and Stegemann, 2000c, Pavlík, 1994). The aggressivity of same acid solution increased with both concentration and, verified by deepened corroded depth of samples exposed to lower pH acid solution (Lloyd et al., 2012a).

#### *2.5.2.2 Anions present in acid*

The chemical character of anions presenting in solution was another influencing factor on the aggressivity of acid (Zivica and Bajza, 2001a) as the anion related to the reaction products formed between acid solution and cement materials. The reaction product directly impacted the performance of building constructions in service. Regarding to Bakharev (2005), high-resistant AAMs deteriorated with the formation of fissures in amorphous polymer matrix, while low-resistant AAMs deteriorated through the crystallisation of zeolites and formation of fragile grainy structures. The severity of acid attack also depended on the solubility of reaction products. Zivica and Bajza (2002) expound that the soluble reactants were not conducive to acid resistance as porous surface contributing further deterioration, while the formation of insoluble reactants enhancing acid resistance vice versa. However, this statement depended significantly on the amount of formed reaction products. For example, sulphuric acid attack caused a higher degree of surface deterioration, mass loss and microstructure change. The reaction products, such as calcium sulphate, was deposited inside the sample matrix, which might hinder the further erosion by acid ions ( $H^+$ ,  $H_3O^+$ ). However, the expansion imposed internal disintegrating stresses and might cause cracks and further degradation of matrix (Allahverdi and Škvára, 2005). For HCl or  $HNO_3$  solutions, the reaction products (i.e.,  $CaCl_2$  or  $Ca(NO_3)_2$ ) were soluble, and diffused into acid solution which providing pathway for erosion (Allahverdi and Škvára, 2006).

### 2.5.3 Corrosion mechanism of AAM in acid media

Following illustrations summarized from Aiken et al. (2018) and Allahverdi and Škvára (2001) could describe the corrosion mechanism happened in AAMs with different gel structures (as shown in Figure 2-14. When alkali-activated materials contacted the acid solution, ion exchange happened immediately. The soluble components exited between framework diffused into solution (i.e.,  $Na^+$ ,  $Mg^{2+}$ ), the ionized ions from acid, such as  $H^+$ ,  $H_3O^+$ ,  $Cl^-$ ,  $SO_4^{2-}$ ,  $CH_3COO^-$ ,  $NO_3^-$  diffused into samples simultaneously.

- (1) The framework of solid blend suffered electrophilic attack by hydrogen protons. Along with the diffusion of  $Na^+$ ,  $Al^{3+}$  ejecting from the Si-O-Al bond under the

attack of hydrogen protons and diffused into solution. Smaller amounts of soluble  $\text{Ca}^{2+}$ ,  $\text{Mg}^{2+}$ ,  $\text{K}^+$  and  $\text{Fe}^{2+}$  cations diffused into acid solution at the same time.

- (2) For alkali-activated fly ash blends, the dealumination happened in the framework of N-A-S-H gel and left a silica-rich zeolites network (Lloyd et al., 2012b) showing a higher acid resistance (Breck, 1984).
- (3) For alkali-activated slag blends, three calcium-containing substances (calcium hydroxide, calcium silicate hydrate and calcium oxide layers in Tobermorite-like structure) were susceptible to acid attack (Allahverdi and Škvára, 2001, Shi, 2003, Aiken et al., 2018, Lee and Lee, 2016). When  $\text{Ca}^{2+}$  met the diffusing anions like  $\text{NO}_3^-$ ,  $\text{Cl}^-$  and  $\text{CH}_3\text{COO}^-$ , produced soluble salts which causing shrinkage cracks that accelerated the transport of ions through the corroded layer (Allahverdi and Škvára, 2001). When  $\text{Ca}^{2+}$  met the diffusing  $\text{SO}_4^{2-}$ , white calcium sulphate was precipitated causing expansion and peeling of the surface materials.

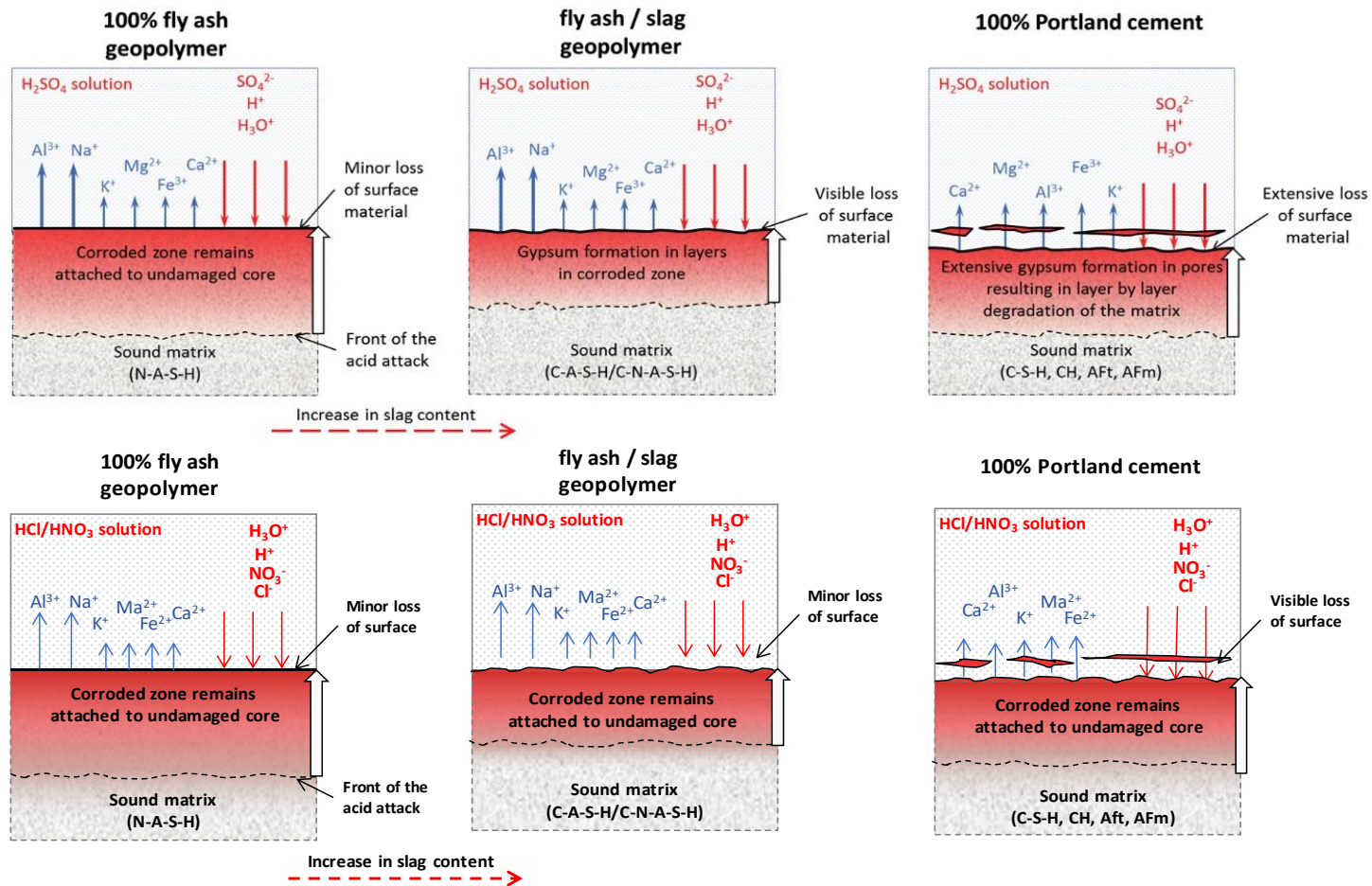


Figure 2-14. Schematic diagram of the mechanism of acid attack in 100% fly ash GPs, fly ash/slag GPs and 100% PC mixes. Modified based on Aiken et al. (2018).

## 2.6 Summary and outlook

Shi and Stegemann (2000b) proposed a hypothesis that the acid resistance of cement materials mainly depended on the nature of hydration products rather than the permeability porosity of hardened cement pastes. They found that hardened specimens formed a protective layer consisting mainly of  $\text{SiO}_2 \cdot n\text{H}_2\text{O}$  gel. Bakharev (2005) found that the median pore size was of more importance for the durability of materials exposed to acidic environment compared to porosity. The intrinsic influencing factors on the acid corrosion mechanism is still not clear.

Although the change of mass and compressive strength could not be effective evaluation indicator, a better acid resistance of alkali activated materials than OPC was widely recognized around academics. The excellent corrosion resistance of hardened low-calcium alkali-activated pastes could be attributed to the absence of  $\text{Ca}(\text{OH})_2$  (Bakharev et al., 2003). The residual aluminosilicate type gel in the affected area was less soluble and more mechanically sound than that formed in Portland cement. Figure 2-15 described the relationship between properties and CaO content in system, including compressive strength development, strength loss, mass loss, corrosion depth and appearance change when exposed to acidic environment. For low calcium system, it could keep better performance in appearance and mass change. The problem was the lower initial compressive strength and higher penetration depth. Conversely, with the increase of CaO content (slag content), the exfoliation corrosion of the samples started to become severe. The compressive strength loss of AAMs increased, but residual compressive strength kept higher than low calcium system. The complex performance was the main barrier for establishing a standard.

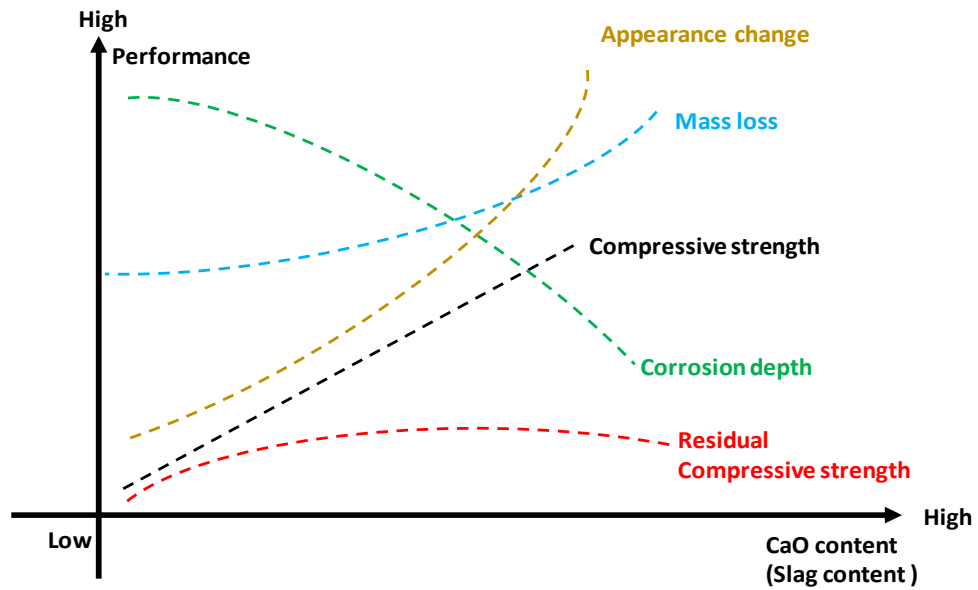


Figure 2-15. Description of relative relationship between properties with CaO content in alkali-activated blenders, no numerical signification (Rafeet et al., 2019). The distances and lines shown in the figure are indicative.

The journey for setting standards for mix design/formulation and early-age properties of alkali-activated material was still lengthy (Ko et al., 2014), as existing cement standards were most prescriptive including composition and performance criteria. Ko et al. (2014) suggested that the standards for AAMs should be derived from existing standards to minimum the challenging and time-consuming. Recommendations for future study included transformation from prescriptive standard to performance standard. Table 3 summarized the existing standards regarding to durability test which was possible to be used for AAMs.

The future research should consider making contribution to the establishment of standards based on the specific performance of blends. Due to most published research focusses on laboratory test, there was rarely result about real service test according to real performance of geopolymers in sewer environment and there was a need to conduct experiments on site and collect data to guide future laboratory research. Simultaneously, micron and nano-scale analysis of the structure and mechanism of corrosion should also be carried out.

Thus, the research gap of this thesis is summarized as follows:

1. The intrinsic influencing factors on the acid corrosion mechanism of alkali-activated materials is still not clear. Under the influence of single factor, the degradation mechanism of alkali-activated materials has not been studied yet as the influence of the impurity from raw materials is inevitable.
2. The effect of Si/Al and Ca/Si ratios on the degradation of the alkali-activated materials should be explored to further guide the material design in practical engineering applications.
3. The comparison on the degradation of the reaction products derived from laboratory synthesised precursors and industrial raw materials should be built to clearly classify the effects of the impurities.

## CHAPTER 3. RESEARCH PLAN AND METHODOLOGY

### 3.1 Introduction

The chapter gives an overview research plan and methodology used in this thesis.

### 3.2 Research flow chat

This study focuses on the following aims:

- A. Investigation of the structural depolymerization of N-A-S-H and C-(N)-A-S-H gel exposed to sulphuric acid
- B. Investigation of the phase evolution of the C-(N)-A-S-H/N-A-S-H gels to sulphuric acid attack
- C. Investigation of the effect of Si/Al and Ca/Si ratios on the sulphuric acid resistance of AAMs
- D. Investigation of the phase decomposition of AAMs exposed to real sewerage attack

The flow chart of this thesis is shown in Figure 3-1.

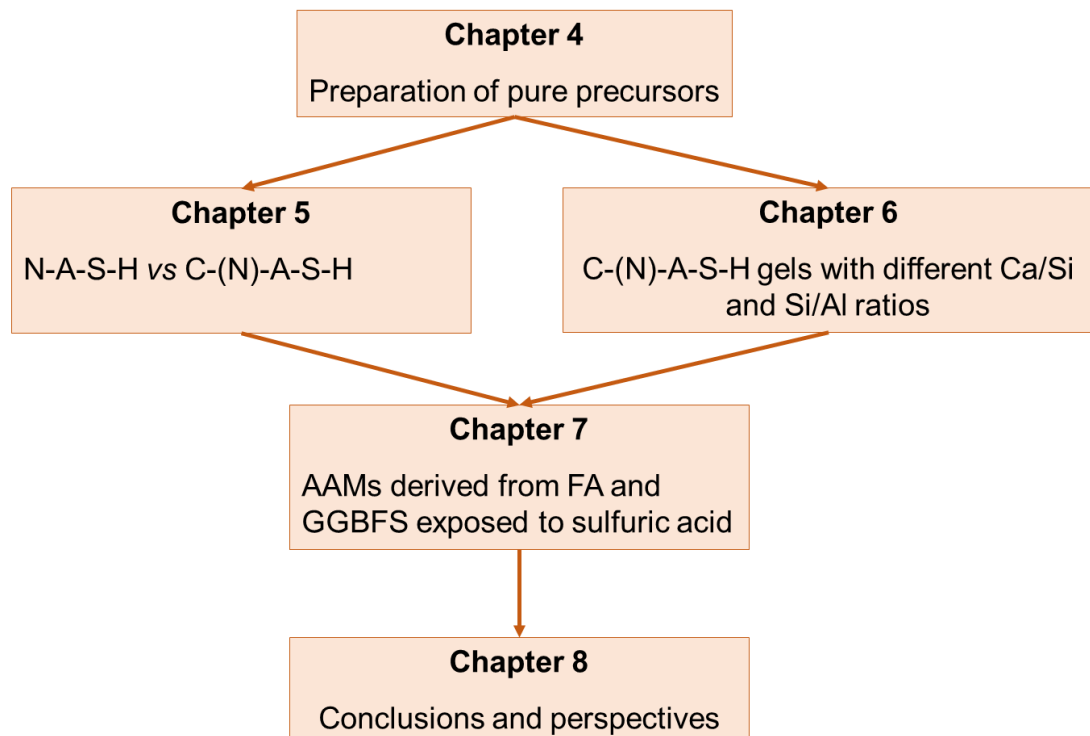


Figure 3-1. Research flow chart of this thesis

### 3.3 Raw materials

The raw materials used in this thesis are summarized in the Table 3-1. More details about the application of each material in separate experiment will be detailed in each chapter. It should be noted that distilled water is used during the formation of pure AAMs gels (Chapter 4, 5, and 6), while tap water is used in the preparation of AAMs used for sulphuric acid attack and sewerage attack (Chapter 7).

Table 3-1. Raw materials used in this thesis.

Materials	Description	Source
Polyethylene glycol (PEG)	Average MW = 20 kDa, Mr=200g/mol	SIGMA-ALDRICH, INC.
Polyvinyl alcohol (PVA)	Average MW = 31-56 kDa	SIGMA-ALDRICH, INC.
Colloidal silica suspension	40 wt.% suspension in water	SIGMA-ALDRICH, INC.
Aluminium nitrate nonahydrate (Al(NO <sub>3</sub> ) <sub>3</sub> ·9H <sub>2</sub> O)	98.0% purity	SIGMA-ALDRICH, INC.
Calcium nitrate tetrahydrate (Ca(NO <sub>3</sub> ) <sub>2</sub> ·4H <sub>2</sub> O)	>=99.0% purity	SIGMA-ALDRICH, INC.
NaOH pellet	>=99.0% purity	Chem-supply
Sodium Silicate/Waterglass	M <sub>s</sub> =2	Chem-supply
Fly ash	Industrial by-products	Nielsen Concrete pty ltd
GGBFS	Industrial by-products	Nielsen Concrete pty ltd
Sulphuric acid solution	98.0% purity	Chem-supply

### 3.4 Characterisation

Many analytical technologies have been used to characterize the chemical and nanostructure of materials. In this study, electron microscopy, solid state nuclear magnetic resonance (NMR) spectroscopy, Fourier transform infrared spectroscopy (FTIR), X-ray diffraction (XRD), X-ray fluorescence (XRF), combined thermogravimetric analysis/mass spectrometry (TGA) and Gas adsorption will be used to characterize geopolymers. Except for SEM-EDX, specimens used for other characterizing techniques both will be ground by hand using a mortar and pestle and immersed in acetone to remove loosely bound water and halt the alkali-activation reaction without any significant changes in geopolymers specimens (Ismail et al., 2013b).

#### 3.4.1 Scanning electron microscopy/Energy-dispersive X-ray spectroscopy (SEM-EDX)

SEM-EDX could scan the microstructure and micromorphology of specimens before and after acid corrosion. Specimens will be dried in oven at 60 °C for 24 hours and then be gold coated before test. 5 kV and 15 kV accelerated voltages with 10 mm working distance will both be tried to get high resolution figures. Transmission electron microscopy (TEM) which similar to SEM will also be used to get higher resolution results, and could give more information about sample as a whole (Walkley et al., 2016c).

### **3.4.2 X-ray diffraction (XRD)**

According to aforementioned literatures (Aiken et al., 2018, Shi, 2003), the crystalline phase is one of the key influence parameters on the acid performance of geopolymers. X-ray diffraction could be used to identify crystalline and semi-crystalline phase in geopolymers. Different crystal phase could diffract X-ray radiation at the surface of material.

According to Bragg's Law (Bragg and Bragg, 1913), the wavelength of the incident X-ray radiation ( $\lambda$ ) can be functioned with scattering angle ( $\theta$ ) and the interplanar atomic spacing ( $d$ ), as shown in Equation 3-1.

$$2d\sin\theta=n\lambda \qquad \text{Equation 3-1}$$

There are two method to analysis materials with XRD; one is to measure the scattering angle with known  $\lambda$  X-ray and calculate out  $d$  to get the structural analysis, the other one is to apply a crystal with known  $d$  to calculate out  $\lambda$  to get the elements contained in materials.

### **3.4.3 X-ray fluorescence (XRF)**

To check the designed chemical components of all samples and the change of component during acid corrosion, XRF can identify the elements present within material. The sample will be prepared by lithium tetraborate and metaborate in platinum crucibles at 1050°C for 15 minutes to produce a glass bead.

### **3.4.4 Combined thermogravimetric analysis (TGA)**

TGA could measure the mass change of materials with the increasing of temperature, while different component in materials loss at different temperature. It can

qualitatively analyse the content of component in material. In this study, all samples will be prepared with powder, and at a heating rate of 10°C/min from 30°C to 1000°C in ambient air (C-(N)-A-S-H system) and nitrogen purge (N-A-S-(H) system) at 200ml/min, respectively. All sample will be hold in the instrument for 20 minutes at 30°C to keep consistency.

Mercury intrusion porosimetry (MIP) was recommended the only available characterization procedure that can cover nearly the whole range of pore sizes of materials (Diamond, 2000). MIP will be used to measure the pore size distribution and porosity of materials. Samples (diameter < 2.5mm) before and after acid corrosion will be prepared and first immersed into acetone solution for 24 hours to halt hydration reaction in materials and then put them in 60°C oven for 48 hours to dry after evaporation of acetone.

#### **3.4.5 Inductively coupled plasma/ atomic emission spectroscopy (ICP-OES)**

ICP-OES will used to measure the leach concentration of calcium, silicon and alumina from geopolymers into acid solutions.

#### **3.4.6 Fourier transform infrared spectroscopy (FTIR)**

Chemical bond environment in materials could absorb particular frequency infrared light and change the intensity received by detector. Based on Fourier transform function, the intensity of light can be transformed to the function of wavelength (Smith, 2011). All samples in this study will be performed over the range 4000 - 400  $\text{cm}^{-1}$ , scanning 64 times at a resolution of 4  $\text{cm}^{-1}$ .

#### **3.4.7 Nuclear magnetic resonance spectroscopy (NMR)**

Active nuclei (e.g.,  $^{29}\text{Si}$  and  $^{27}\text{Al}$ ) will be used in solid state magic angle spinning nuclear magnetic resonance spectroscopy (SS MAR NMR) to obtain the information of coordination state of Al and the connectivity of Si in both N-A-S-(H) and C-(N)-A-S-H framework systems before and after acid corrosion. NMR could help to get the information about the change of atomic structure of geopolymers which is becoming an important technology for analysing of materials.

## CHAPTER 4. SYNTHESIS OF STOICHIOMETRICALLY CONTROLLED ALUMINOSILICATE PRECURSORS AND ALKALI-ACTIVATED GELS

### 4.1 Introduction

Alkali-activated materials (AAMs), also known as geopolymers, have been incredible pace in the last two decades, motivated by environmental protection and waste utilization, and are increasingly considered as potential green alternatives to Portland-based cement (Provis, 2018). Accordingly, geopolymers based on alkali-activation of fly ash and blast furnace slag. As the raw materials used to produce geopolymers, fly ash and slag are industrial by-products, with inconsistent properties and physical-chemical characteristics (Zhang et al., 2016b). Furthermore, this can be particularly challenging to promote the wide application of geopolymers in the industry like Portland cement. To understand the chemistry of geopolymers and alkali-activated binders, the production of precursor powders via chemical synthesis routes has gained significant attention as a method of control the consistency of raw materials (Walkley et al., 2016b, Cui et al., 2010). The premise for this approach to be acceptable is that the chemically synthesized powders could produce the same reaction product as AAMs under alkali-activated process.

Pechini firstly described a method of preparing powder formulations used in the manufacture of ceramic dielectrics require the calcination of a mechanically-ground mixture of metal oxides and carbonates in definite proportions (Pechini, 1967). Recent studies have adopted variations of this process to synthesise calcium, silicon or aluminium containing oxides powders (Pramanik and Pathak, 1994, Gülgün et al., 1999, Cui et al., 2008, Walkley et al., 2016b, Ye and Huang, 2020). Walkley et al. (2016b) developed a fast, reproducible method by employing an organic polymeric steric entrapment solution-polymerisation route to synthesise reactive aluminosilicate and calcium aluminosilicate powders. The stoichiometrically controlled alkali-aluminosilicate gels produced by synthesized powders were characterised by a series of technological methods (Walkley et al., 2016a, Walkley et al., 2016c).

In this chapter, three innovative aluminosilicate powders and four calcium aluminosilicate powders are prepared by the same approach developed by (Walkley et

al., 2016b). The alkali-activated gels derived from powders are compared with that derived from fly ash and slag. This chapter provide basic information on the raw materials.

## 4.2 Research method

### 4.2.1 Materials preparation for synthesis pure aluminosilicate

The GGBFS collected from Neilsens Concrete Pty Ltd (Australian) was an industry by-product of iron and steel making. The molten iron slag was quenched from the blast furnace in water to produce granular products, and then the granular products were grounded into powders with similar particle sizes like Portland cement. The GGBFS was classified as alkaline with the alkalinity coefficient [ $M_o = (CaO + MgO)/(SiO_2 + Al_2O_3)$ ] of 0.97 and hydraulicity modulus of 2.05 [ $b = (CaO + MgO + Al_2O_3)/SiO_2$ ] as per GB/T 18046-2017 and met the requirements in AS 3582.2:2016 (Standard). The commercial MK was collected from MetaMax - BASF, which was a manufactured product produced by heating the mineral kaolin at temperature of 600 - 800 °C. The mean particle size of MK is 4.56 μm. The FA was collected from Neilsens Concrete Pty Ltd (Australian), which was a by-product of the power station from coal combustion. The chemical composition of the FA and GGBFS is shown in Table 4-1. Polyethylene glycol (PEG) with average molecular weight 20 kDa and polyvinyl alcohol (PVA) with average molecular weight 31-56 kDa are used as organic solvents for calcium aluminosilicate powder and aluminosilicate powder, respectively. Colloidal silica (SiO<sub>2</sub>) with 40 wt.% suspension in water, aluminium nitrate nonahydrate (Al(NO<sub>3</sub>)<sub>3</sub>·9H<sub>2</sub>O) with 98.0% purity and calcium nitrate tetrahydrate (Ca(NO<sub>3</sub>)<sub>2</sub>·4H<sub>2</sub>O) with 99.0% purity are metal source. The chemical reagents used to synthesize particles are all from Sigma-Aldrich. Distilled water is used throughout this chapter. The stoichiometry was designed to achieve the elemental ratios outlined in Table 4-2.

Table 4-1. Chemical composition (oxide basis) of fly ash and GGBFS.

wt.%	SiO <sub>2</sub>	Al <sub>2</sub> O <sub>3</sub>	CaO	MgO	SO <sub>2</sub>	Fe <sub>2</sub> O <sub>3</sub>	Na <sub>2</sub> O	K <sub>2</sub> O	others
FA	56.36	33.85	2.71	0.66	0.14	2.88	0.42	0.76	2.72
GGBFS	28.98	12.87	34.68	6.06	2.17	0.43	0.24	0.25	14.32

Table 4-2. Designed molar ratios for precursor powders.

Sample	Empirical formula	Ca/(Al+Si)	Al/Si	Polymer
N1	0.5SiO <sub>2</sub> ·Al <sub>2</sub> O <sub>3</sub>	-	3.52	PVA
N2	1.0SiO <sub>2</sub> ·Al <sub>2</sub> O <sub>3</sub>	-	2.00	PVA
N3	1.5SiO <sub>2</sub> ·Al <sub>2</sub> O <sub>3</sub>	-	1.33	PVA
C1	1.0CaO·SiO <sub>2</sub> ·0.09Al <sub>2</sub> O <sub>3</sub>	0.85	0.18	PEG
C2	1.9CaO·SiO <sub>2</sub> ·0.09Al <sub>2</sub> O <sub>3</sub>	1.60	0.18	PEG
C3	1.0CaO·SiO <sub>2</sub> ·0.03Al <sub>2</sub> O <sub>3</sub>	0.94	0.06	PEG
C4	1.5CaO·SiO <sub>2</sub> ·0.03Al <sub>2</sub> O <sub>3</sub>	1.42	0.06	PEG

Precursor powders were prepared in the laboratory following the methods used by Gülgün et al. (1999) and Walkley et al. (2016b). Solutions will be stirred using a thermostatic stirrer, which can control the temperature and stirring speed.

- 1) Solutions preparation. Preparation of 5 wt.% PVA and PEG solution. Add hydrolysed PVA or PEG to distilled water, stirring for 1 hour at 60 °C. Add aluminium nitrate nonahydrate powder to distilled water to prepare 40 wt.% solutions. Add calcium nitrate tetrahydrate powder to distilled water to prepare 40 wt.% solutions, stirring for 1 hour at 60°C.
- 2) Synthesis of aluminosilicate powders. Add aluminium nitrate nonahydrate solution into above PVA solution, stirring for 1 hour at 60°C before adding colloidal silica, and then stirring for 1 hour at 80°C to evaporate water in solution to form a dry viscous aerated gel. This gel will then be calcined at a muffle furnace at the laboratory, with 3°C/min to 550°C and held for 1 hour.
- 3) Synthesis of calcium-aluminosilicate powders. Add aluminium nitrate nonahydrate solution and calcium nitrate tetrahydrate solution into PEG solution, stirring for 1 hour at 60°C before adding colloidal silica, and then stirring for 1 hour at 80°C to form a viscous aerated gel. Before calcination, this gel will be put in a 100°C oven overnight to remove any remaining water. Then this gel will then be calcined at a muffle furnace at the laboratory, with 3°C/min to 900°C and held for 1 hour.

#### 4.2.2 Characterisation

The particle size distribution of the precursors were tested by a laser diffraction particle size analyser (Microtrac S3500), in a measuring time of 10 seconds.

X-ray diffraction (XRD) using a Bruker D2 Phaser instrument with Cu K $\alpha$  radiation, a nickel filter, a step size of 0.02° and 0.5 s/step. Data were obtained in the range from 5 to 70° 2 $\theta$ . Phase analysis was performed using Jade 6 with PDF patterns.

Fourier Transformed Infrared Spectroscopy (FTIR) was collected with a Perkin Elmer FTIR-ATR spectrometer from 4000 to 400  $\text{cm}^{-1}$  with 64 scans at a resolution of 4  $\text{cm}^{-1}$ . The spectra were fitted using a baseline correction and deconvoluted in the range of 600 - 1300  $\text{cm}^{-1}$  using Gaussian curves. Deconvolution processes were carried out using Origin software (Origin 6.0, OriginLab Corp., Northampton, MA, USA) and the Lorentzian multi-peaks fit module.

The X-Ray fluorescence was identified to analyse the chemical elements presented within the material. The sample was prepared by lithium tetraborate and metaborate in platinum crucibles at 1050°C for 15 minutes to produce a glass bead.

Thermogravimetric analysis (TGA) measured the mass change of materials with the increase of temperature, while different components in materials lose at different temperatures. Differential thermogravimetric (DTG) analysis was performed to analyse the mass change rate to temperatures. All samples were prepared with powder and at a heating rate of 10°C/min from 30°C to 1000°C in ambient air (C-(N)-A-S-H system) and nitrogen purge (N-A-S-H system) at 200ml/min, respectively.

### **4.3 Results and discussion**

Figure 4-1 shows the particle size distribution and passing percentage of synthesized precursors, metakaolin and GGBFS. The particle size of GGBFS is less than 100 microns, while metakaolin shows two peaks at 1-100 and 100-600 microns. The synthesized precursors show similar particle size distribution as metakaolin with two peaks.

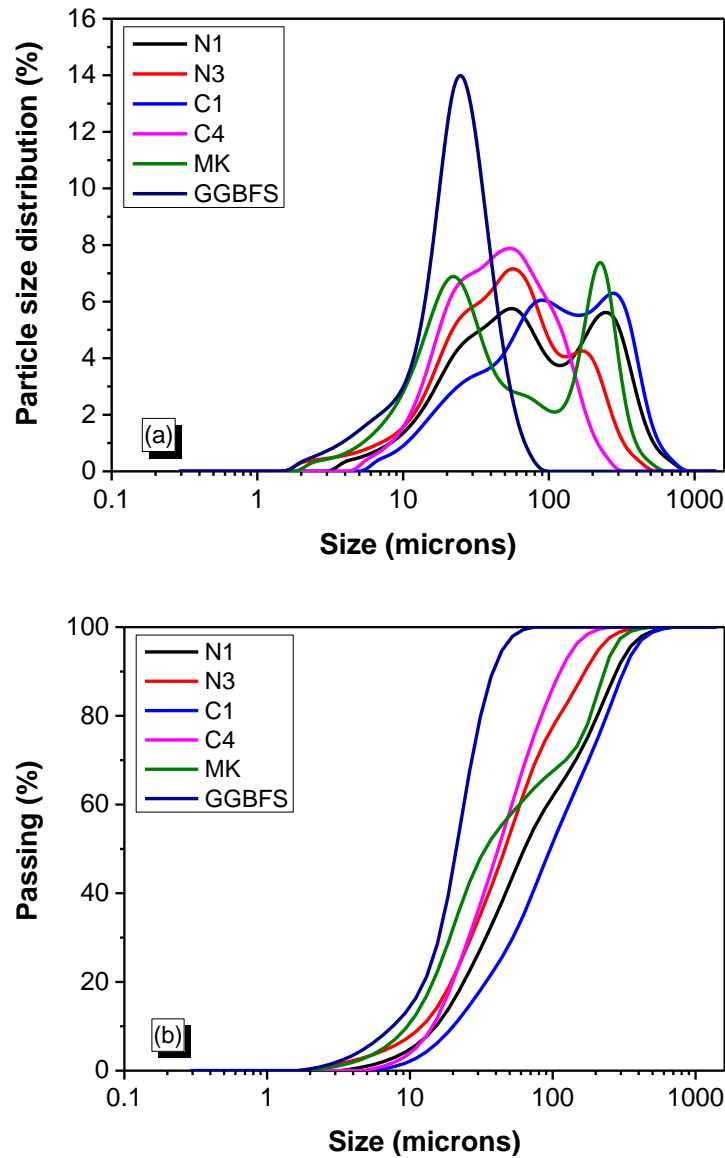


Figure 4-1. Particle size distribution and passing summary of synthesized precursors, metakaolin and GGBFS.

#### 4.3.1 Chemical compositions

Figure 4-2 shows the bulk oxide composition of metakaolin and slag, which are within the general scope in the published studies (Lothenbach et al., 2011). The chemical compositions of precursor powders synthesized in the lab are also shown in Table 4-3. It should be noted that the bulk oxide composition of the metakaolin and slag could not present the active compounds of the raw materials. The table shows the designed and measured physical compositions of the synthesized precursor powders. The difference is less than 4%. The data indicated that the synthesized precursor powders kept good consistency and could be used for the following research.

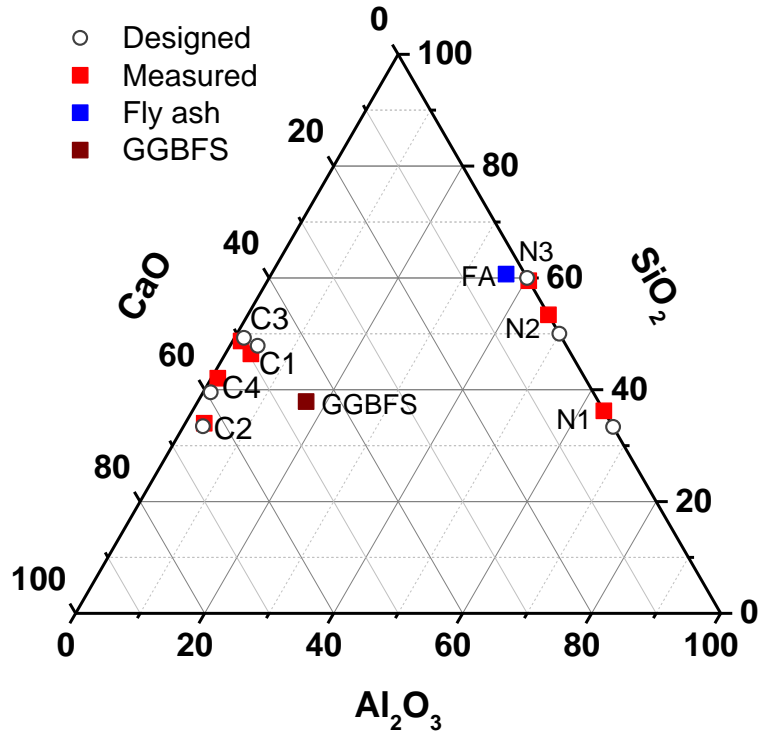


Figure 4-2. Ternary diagram of the chemical composition ( $\text{CaO-Al}_2\text{O}_3\text{-SiO}_2$ ) of solid raw materials, as determined by X-ray fluorescence analysis.

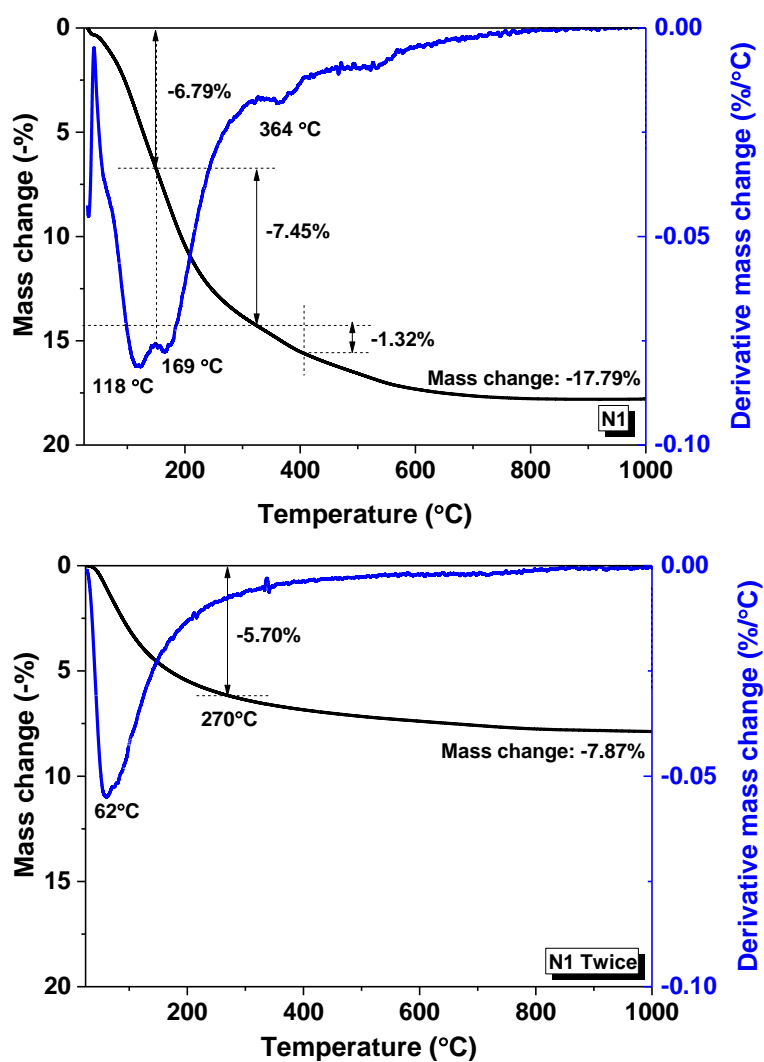
Table 4-3. The designed and measured physical compositions of synthesized precursor powders.

Sample		N1	N2	N3	C1	C2	C3	C4
Designed	$\text{Al}_2\text{O}_3$	0.66	0.50	0.40	0.04	0.03	0.01	0.01
	$\text{SiO}_2$	0.33	0.50	0.60	0.48	0.33	0.49	0.40
	$\text{CaO}$	-	-	-	0.48	0.64	0.49	0.59
Measured	$\text{Al}_2\text{O}_3$	0.64	0.47	0.41	0.04	0.03	0.01	0.01
	$\text{SiO}_2$	0.36	0.53	0.59	0.46	0.34	0.49	0.42
	$\text{CaO}$	-	-	-	0.50	0.63	0.50	0.57

### 4.3.2 Thermogravimetric-differential thermogravimetric (TGA-DTG) of precursors

Figure 4-3 shows the TGA-DTG data of each precursor powder. The sodium-free samples N1 and N3 show 17.79% and 13.71% of mass loss after being heated to 1000 °C. The mass loss mainly happens at around 30 - 400 °C with a dominant peak at around 118 °C, which is mainly contributed to the evaporation of absorbed water and decomposition of residual polymers. Minor mass loss happens after 500 °C which indicates that the polymer in the raw precursor gels is fully calcined. However, the DTG data of samples N1 and N3 both show an overlapped peak at the range of 60 -

400 °C. Thus, the samples N1 and N3 were treated with the second calcination process at 550 °C for 1 hour, and the TGA-DTG curves of the recalcined samples are shown in Figure 4-3. The mass losses of samples N1 and N3 reduce to 7.87% and 6.64%, respectively. And the mass loss mainly centres at around 60 °C, which is contributed to the water loss. Calcium-free samples show a high absorption rate of water from air. Thus, the non-sodium precursors used for following chapters are treated by heated at 550 °C for 2 hours. This might be due to its higher specific surface area after calcination.



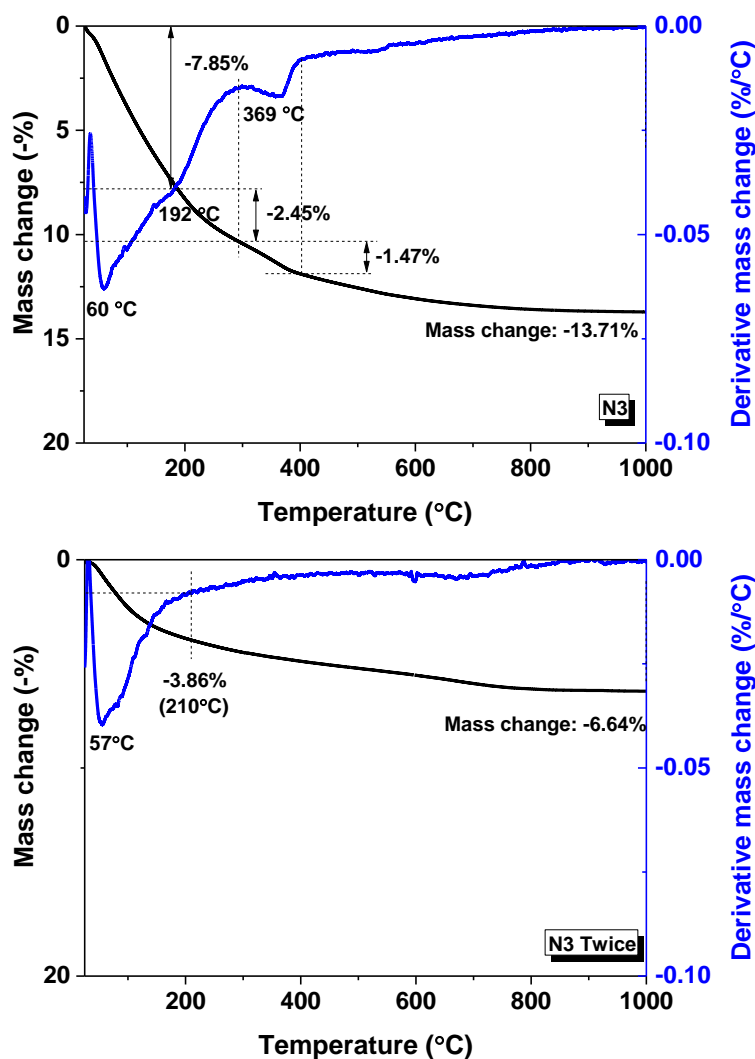
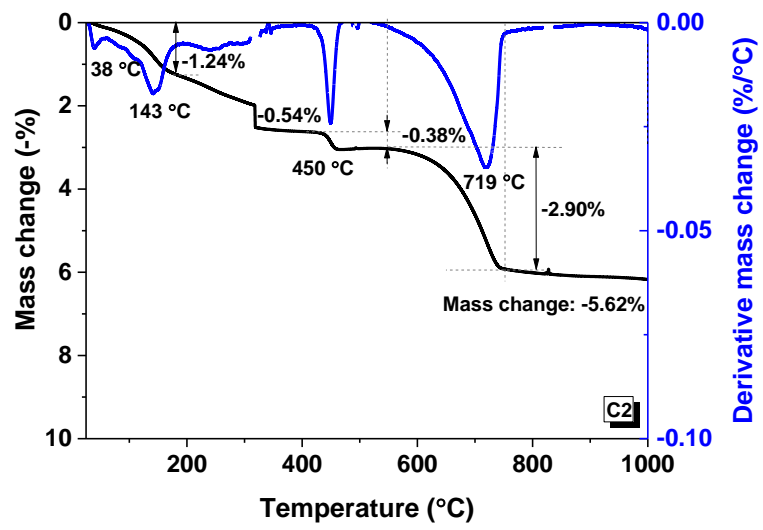
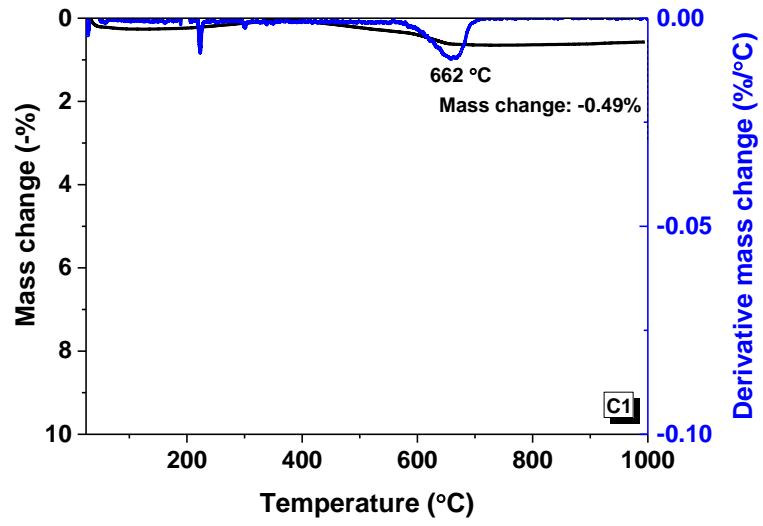


Figure 4-3. TGA-DTG data of the precursors N1, N2 and N3 as marked.

Figure 4-4 shows the TGA-DTG data of the calcium-containing precursors, which displayed minor mass loss when the temperature increased to 1000 °C. The mass losses of samples C1, C3 and C4 are only 0.49%, 1.64% and 0.57%, respectively, which could be ignored. The small loss peak at around 662 °C of the DTG data might be due to the decomposition of calcite which formed between the calcium oxide in sample and carbon oxide from the decomposition of PEG. It should be noted that sample C2 showing significant mass loss of 5.62%. The mass loss of sample C2 consists of three parts at 143 °C, 450 °C and 719 °C, which attribute to the evaporation of free water, decomposition of calcium oxide and decomposition of calcite. High content of calcium in sample C2 is the reason for its higher amount of formed calcite during calcination.



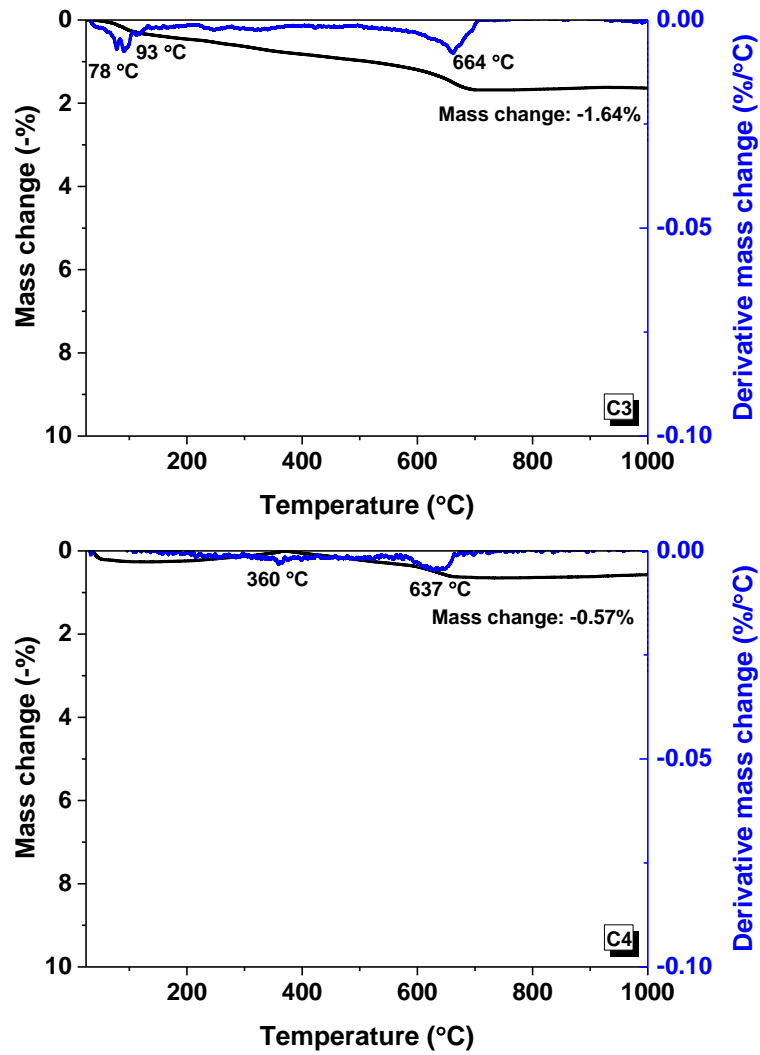


Figure 4-4. TGA-DTG data of the calcium-containing precursors C1, C2, C3 and C4 as marked.

Figure 4-5 shows the TGA-DTG data of the FA, MK and GGBFS. The mass losses of sample FA, MK and GGBFS are 1.96%, 1.94% and 1.96%, respectively. The mass loss peak of MK is at around 67 °C, which is contributed to the evaporation of absorbed water. The mass loss peaks of FA and GGBFS at 132 °C and 125 °C, respectively, are contributed to loss of absorbed or bounded water in sample. The mass loss peak at around 680 °C, which are contributed to the loss of absorbed water and the decomposition of calcite.

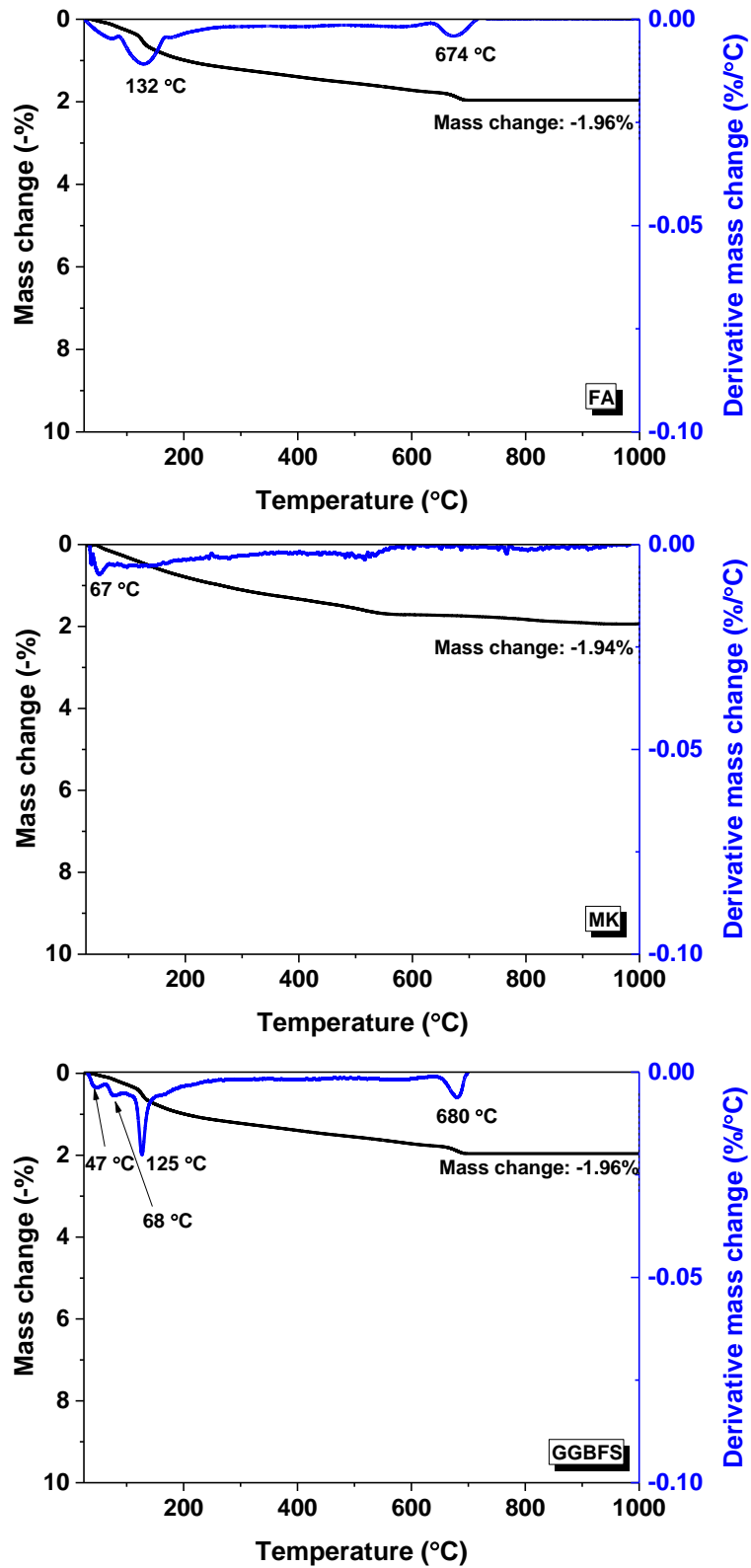


Figure 4-5. TGA-DTG data of the industrial precursors of FA, MK and GGBFS as marked.

### 4.3.3 X-ray diffraction (XRD) analysis

Figure 4-6 shows the XRD patterns of the calcium-free precursors N1, N2 and N3, which displaying a domain featureless hump at about  $22^\circ 2\theta$ . This broad peak is designated as a characteristic peak of aluminosilicates (Walkley et al., 2016b). There are no crystalline phases detected in the calcium-free precursors. The precursors treated at  $550^\circ\text{C}$  for 2 hours is enough to remove polymers used for synthesized process and prevent the formation of crystals.

The XRD patterns of the calcium-containing precursors are shown in Figure 4-7. All samples show a hump which centred at around  $29^\circ 2\theta$ , indicating the presence of amorphous phases. Sample C1 shows crystalline phases of calcium silicate (CS, PDF#27-0088), dicalcium silicate ( $\text{C}_2\text{S}$ , PDF#33-0302) and yoshiokaite ( $\text{Ca}_{5.3}\text{Al}_{10.7}\text{Si}_{5.3}\text{O}_{32}$ , PDF#80-1547). Three crystalline phases of calcium silicate (CS, PDF#47-0159), dicalcium silicate ( $\text{C}_2\text{S}$ , PDF#86-0399 and 24-0034) and tricalcium aluminate ( $\text{C}_3\text{A}$ , PDF#31-0148). As shown, higher content of Ca and Al in sample C2 promotes the formation of tricalcium aluminate and provides two polymorphs of dicalcium silicate. The sample C3 shows five crystalline phases which are calcium silicate (CS, PDF#76-0925), tricalcium aluminate ( $\text{C}_3\text{A}$ , PDF#32-0148), yoshiokaite, pseudowollastonite (PDF#74-0874) and quartz (PDF#79-1912). The formation of quartz in sample C3 is due to the relatively higher content of silicon. The sample C4 shows four crystalline phases which are dicalcium silicate ( $\text{C}_2\text{S}$ , PDF# 33-0322), tricalcium silicate ( $\text{C}_3\text{S}$ , PDF# 49-0422, 31-0301), and yoshiokaite. Lower content of aluminium in sample C4 promotes the formation of tricalcium silicate. The calcium and aluminium content in precursors could influence the polymorph of crystalline. With the increase content of aluminium, sample C2 shows the formation of tricalcium aluminate. The lower content of aluminium in samples C3 and C4 promote the formation of tricalcium silicate.

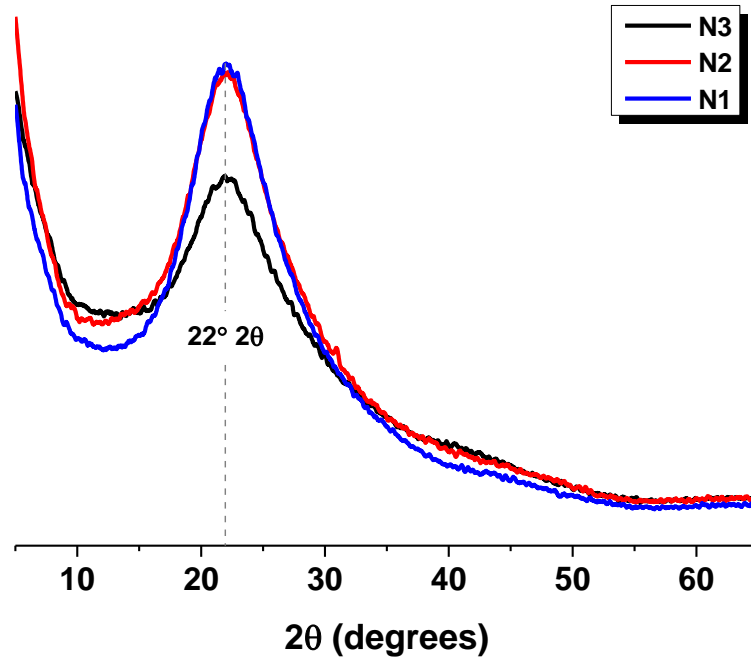


Figure 4-6. XRD patterns of each synthesized calcium-free precursors as marked.

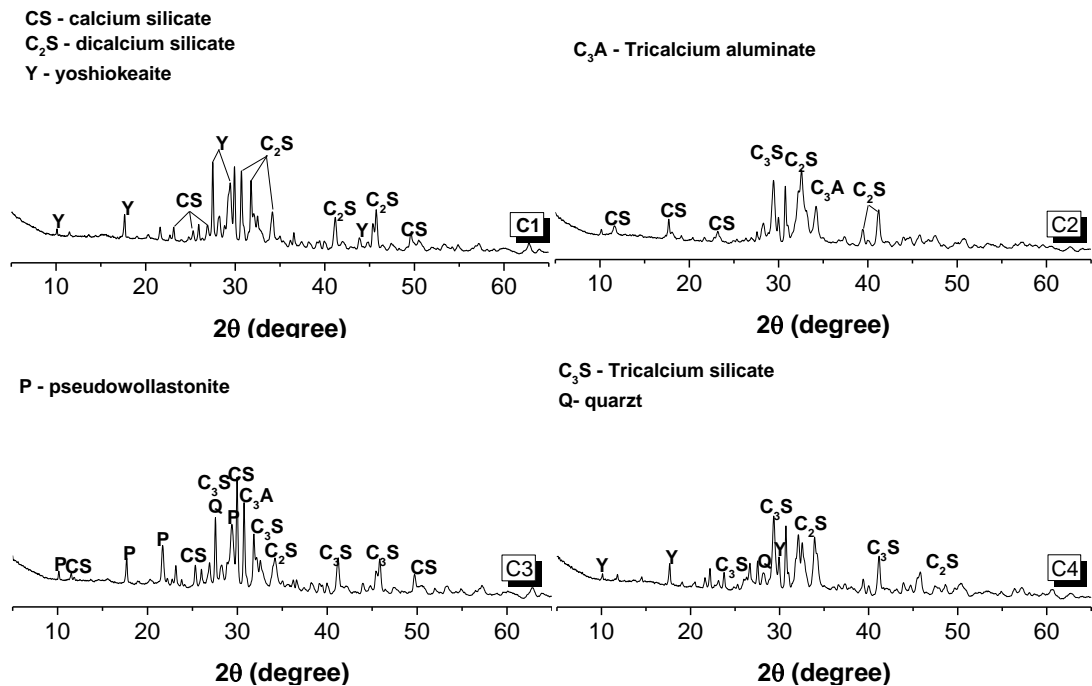


Figure 4-7. XRD patterns of each synthesized calcium-containing precursors as marked.

Figure 4-8 shows the XRD patterns of FA and GGBFS. Sample FA shows a broad hump at around  $22^\circ 2\theta$ , indicating the formation of amorphous phase of aluminosilicate, which is consistent with the dominant hump formed in the calcium-free precursors showed in Figure 4-6. Crystalline phases, including calcite (PDF#05-0586), quartz (PDF#46-1045), mullite (PDF#20-0425) and tricalcium silicate

(PDF#24-0034), are solon identified. Sample GGBFS shows a broad hump at around  $29^\circ 2\theta$ , due to diffuse scattering between  $25\text{-}35^\circ 2\theta$ , which is consistent with the XRD patterns of calcium-containing precursors. Longhi et al. (2020) founded the MK showed the formation of broad hump in the range of  $15\text{-}35^\circ 2\theta$  with the presence of crystalline phases of anatase and halloysite. The synthesized precursors exhibit similar amorphous characteristics to industrial raw materials, and different crystalline phases. As known, the reactivity of precursors derived from amorphous phases (Zhang et al., 2016b).

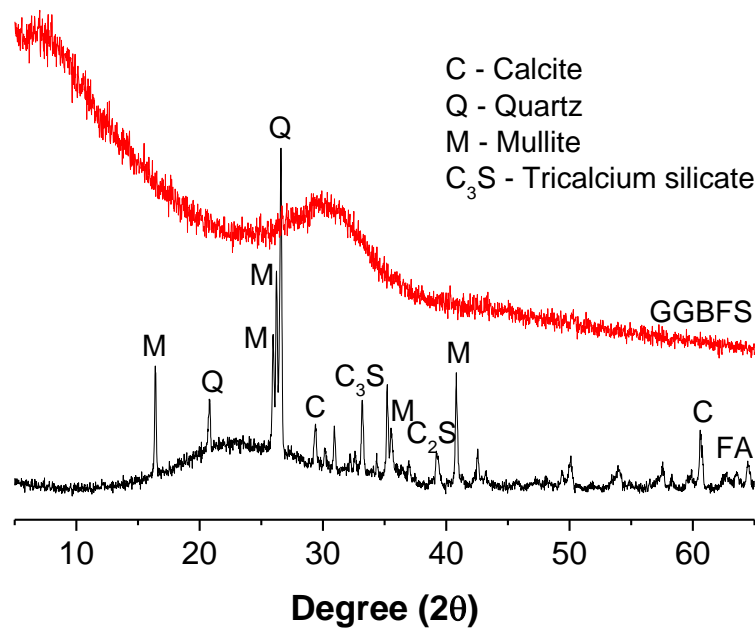


Figure 4-8. XRD patterns of fly ash and GGBFS.

#### 4.3.4 Fourier transform infrared spectroscopy (FTIR) analysis

Figure 4-9 shows the FTIR patterns of each precursor. The calcium-free precursors N1, N2, N3 and MK display a main peak at around  $1062\text{ cm}^{-1}$ , contributed to the asymmetric stretching vibration of Si-O-T bonds, where T could be Si or Al (Catherine A. Rees, 2007). The bending vibration of Al-O bond at  $\text{AlO}_6$  octahedral sites is contributed another peak at around  $808\text{ cm}^{-1}$  (Zhang et al., 2013). The small peaks at around  $636$  and  $430\text{ cm}^{-1}$  are contributed to symmetrical stretching and bending of Si-O-T bonds, respectively (Walkley, 2016). The significant shoulder at around  $1198\text{ cm}^{-1}$  might be due to the symmetric stretching vibration of Si-O-Si bonds (Criado et al., 2007). For calcium-containing precursors, an overlapped peak formed at around  $877\text{ cm}^{-1}$  which is contributed to the asymmetric stretching vibration of Si-O-T bonds. The

lower wavenumbers compared to the calcium-free precursors might be due to the addition presence of aluminium in the vibration associated to Si-O-T bonds (Zhang et al., 2013). The symmetric stretching vibration of C-O-C bonds of calcite is found in the synthesized precursors at around 1475 to 1419  $\text{cm}^{-1}$ . And the high calcium content in sample C2 and C4 promotes the formation of calcite.

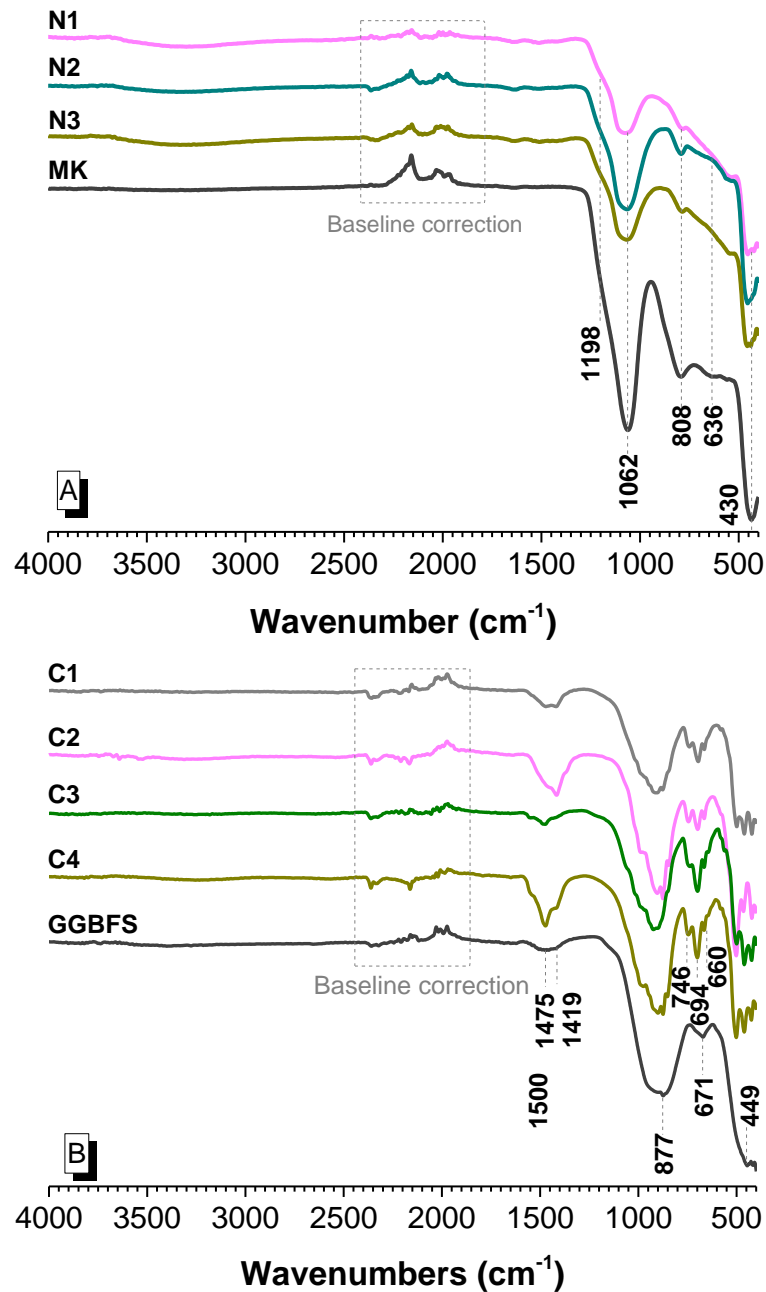


Figure 4-9. FTIR patterns of each precursor.

#### 4.4 Concluding remarks

The synthesized precursors used stoichiometrically controlled routine at the laboratory are analysed and compared with the industrial precursors in this chapter. It was found that the synthesized precursors show similar chemical properties as the industrial precursors from the TGA, XRD and FTIR results. Different chemical compositions of the synthesized precursors have minor effect on the characterization results. The non-calcium precursors are mainly amorphous with a higher surface area and higher amount of absorbed water during sample preparation. The calcium in the calcium aluminosilicate powders promotes the formation of crystalline phases. This chapter proved that the synthesized routines could be an effective method for the intrinsic investigation of alkali-activated materials in the following chapters.

## CHAPTER 5. STRUCTURAL DEPOLYMERIZATION OF N-A-S-H AND C-(N)-A-S-H GELS BY SULPHURIC ACID ATTACK

### 5.1 Introduction

Durability of cementitious materials is an important property due to the growing demand for long-service-life of structures but with low maintenance cost. Concrete is an alkaline material with an initial pH of pore solution around 13, which helps to protect the steel bar in concrete from corrosion (Dyer, 2017, Cao et al., 2021a). The corrosion of reinforced concrete is dominated by acid-base reactions, causing pH reduction inside concrete, which will further accelerate the acid corrosion of steel bars and hydration products of concrete (Grenng et al., 2018). Acidic environment also occurs in geothermal wells and groundwater, causing degradation to the underground concrete structures (Khan et al., 2019). Among various acidic conditions, sulphuric acid corrosion is considered to be the major cause for acidic degradation of concrete structures (Aiken et al., 2018). Alkali-activated materials (AAMs), also widely called geopolymers, have emerged as promising environmentally friendly cementitious materials due to the low carbon dioxide emissions and waste utilization in manufacturing (Ma et al., 2019). In comparison to ordinary Portland cement (OPC), AAMs usually contain much higher alkali concentration, and perform better in terms of mass change and compressive strength change when subjected to acid attack (Bakharev et al., 2003). However, the detailed corrosion mechanism of AAMs is not clear due to the complexity of raw materials and activators and the product variation.

The acid resistance of cementitious materials is strongly dependent on the interaction between hydration products and acidic media (Bernal et al., 2012b). Hardened OPC-based materials are composed of hydration products calcium hydroxide (CH) and calcium silicate hydrate (C-S-H) gel (Cao et al., 2021b), whereas AAMs are composed of N-A-S-H, C-(N)-A-S-H and their blends, depending on the aluminosilicate materials (Longhi et al., 2020). While the N-A-S-H gel is known as a three-dimensional alkali aluminosilicate hydrate gel network, consisting of crosslinked  $[AlO_4]$  and  $[SiO_4]$  tetrahedra linked via shared oxygen atoms, with terminal hydroxyl groups on the gel surface (Provis and Van Deventer, 2014). It is generally described as an amorphous, nanocrystalline zeolite phase (Provis et al., 2005b). The N-A-S-H

gel usually presents ratios of  $0.1 \leq \text{Na/Si} \leq 0.3$  and  $1 \leq \text{Si/Al} \leq 4$  (Winnefeld et al., 2010, Fernández-Jiménez and Palomo, 2005). The C-(N)-A-S-H gel is described as an imperfect crosslinked/non-crosslinked Tobermorite-like structure, assembled by two one-dimensional Si tetrahedron chains (randomly Al substitution into paired tetrahedron) and a calcium octahedron chain (Schilling et al., 1994, Fernández - Jiménez et al., 2003). The C-(N)-A-S-H type gel formed in alkali-activated slag possesses a relatively low calcium content [ $\text{Ca}/(\text{Si} + \text{Al}) < 1.5$ ] compared to the C-S-H gels formed in OPC ( $1.5 \leq \text{Ca/Si} \leq 2$ ) (Taylor, 1997, Myers et al., 2013), and the Al/Si is usually less than or equal to 0.2 (Pardal et al., 2009). Alkali cations, such as  $\text{Na}^+$ , are incorporated into C-(N)-A-S-H/N-A-S-H gel via a charge balancing mechanism, where they exist in the interlayer charge-balancing  $[\text{AlO}_4]^{5-}$  tetrahedra as well as adsorbed to the surface of gel (Longhi et al., 2019). Understanding the stability of the molecular composition and microstructure evolution of C-(N)-A-S-H/N-A-S-H phases exposed to aggressive environment is critical for the application of AAMs, especially their durability.

Previous research has attempted to reveal the effects of many factors (i.e. precursors, activators, sample size, acid type, etc.) on acid resistance of AAMs (Davidovits, 1991, Zhang et al., 2018c, Ourgessa et al., 2019, Ren et al., 2020, Aiken et al., 2018). It was reported that sulphuric acid attack caused weight increment and volume expansion of alkali-activated slag (C-(N)-A-S-H is the dominant binding gel), while minor weight and appearance change for alkali-activated fly ash (N-A-S-H is the dominant binding gel) (Aliques-Granero et al., 2017). This is due to the formation of gypsum for high calcium alkali-activated binders. Higher residual compressive strength of alkali-activated slag after acid corrosion was found comparing to alkali-activated fly ash (Shi, 2003, Bakharev et al., 2003). During the acid attack, the alkali-activated fly ash binder showed leaching of aluminium, sodium, and calcium except for silicon (Temuujin et al., 2011). It is hypothesized that a silicon-rich porous structure was left after acid corrosion in samples. However, elements leaching in acid solution caused a minor change of compressive strength, which proved that this silicon-rich structure contributed most source of the compressive strength in low calcium system (Temuujin et al., 2011, Allahverdi and Škvára, 2001). This phenomenon differs from acid attack on OPC.

Decalcification of the binding gels (i.e., C-S-H or C-(N)-A-S-H) has been identified in the both OPC and alkali-activated slag after exposed to acid. The exposed layer of OPC is highly porous silica-rich gel while an aluminosilicate type gel is formed in the affected area of the activated slag sample, and the latter was less soluble and more mechanically sound (Bernal et al., 2012a). Acid attack on fly ash based geopolymer resulted in the substitution of  $\text{Na}^+$  and  $\text{K}^+$  ions by  $\text{H}^+$  or  $\text{H}_3\text{O}^+$ , breaking Si-O-Al and Si-O-Si bonds in N-A-S-H gel, releasing silicic acid (Okoye et al., 2017). N-A-S-H gel was found to have good stability though (Longhi et al., 2019). The free sodium existing in the pore solution of the sample can easily diffuse into the external environment. However, acidic corrosion is a complex process. The impacts of contaminants such as iron, carbon, sulphur, etc. are inevitable but none has been illustrated and fully understood (Fernández-Jiménez and Palomo, 2003).

The overall aim of this work is to distinguish the acid corrosion mechanisms of N-A-S-H and C-(N)-A-S-H gels. To avoid those possible effects of contaminants from industrial wastes and keep the same alkali activation procedure for AAM manufacturing, pure precursors were designed and synthesized in the laboratory. After activation by alkali solution, stoichiometric controlled AAM gels, i.e., N-A-S-H and C-(N)-A-S-H, were obtained. The experiment illustrated the evolution of the molecular structure of the gels, particularly the bond change after exposure to  $\text{H}_2\text{SO}_4$  solution. This work is expected to provide knowledge on improving the acid resistance and application for AAMs as new construction materials.

## **5.2 Experimental methods**

### **5.2.1 Geopolymer binder synthesis**

The aluminosilicate powder and calcium-aluminosilicate powder used in this study were synthesized via an organic steric entrapment solution-polymerization route (Walkley, 2016). The precursor compositions (empirical formula  $1.5\text{SiO}_2 \cdot \text{Al}_2\text{O}_3$ ) was chosen to represent the range of bulk silicon and aluminium content typically found in fly ashes (Provis and Van Deventer, 2014). Another precursor (empirical formula  $1.07\text{CaO} \cdot \text{SiO}_2 \cdot 0.086\text{Al}_2\text{O}_3$ ) was chosen to enable synthesis of binders exhibiting chemistry range in regions of the calcium aluminium-substituted silicate hydrated gels in alkali-activated slag (Provis and Van Deventer, 2014). The activating solution was prepared by the dissolution of sodium hydroxide powders (Sigma-Aldrich, 98 wt.%

purity) in sodium silicate solution ( $\text{Na}_2\text{O} = 14.7\%$  (mass),  $\text{SiO}_2 = 29.4\%$ , D-Grade™, PQ Australia) and distilled water with desired modulus ( $M_s = \text{SiO}_2/\text{Na}_2\text{O}$ ) of 1. The stoichiometry was designed to obtain a cation ratio of the reaction mixture like the  $\text{Na}_2\text{O}-\text{Al}_2\text{O}_3-\text{SiO}_2-\text{H}_2\text{O}$  (N-A-S-H) gel and  $\text{CaO}-(\text{Na}_2\text{O})-\text{Al}_2\text{O}_3-\text{SiO}_2-\text{H}_2\text{O}$  [C-(N)-A-S-H] gel, the reaction products of alkali-activated fly ash and alkali-activated slag, respectively (Provis and Van Deventer, 2014) (see Table 5-1). The activating solutions were mixed with the aluminosilicate powder and calcium aluminosilicate powder in casting containers to form the homogeneous pastes, which are denoted as NASH sample and C(N)ASH sample, respectively. The pastes were stayed in containers (cylinders with diameter of 10 mm and height of 20 mm) with sealed lid and cured at ambient temperature for 120 days. The water/solid ratios (w/s) used for NASH sample and C(N)ASH sample were 1.0 and 0.75, respectively, to obtain a workable and homogeneous paste.

Table 5-1. Molar ratios in the precursor powder and the reaction mixture for NASH sample and C(N)ASH sample.

Sample ID	Empirical formula	Precursor powder			Reaction mixture		
		Si/Al	Ca/Al	w/s	Si/Al	Na/Al	Ca/(Al + Si)
NASH	$1.5\text{SiO}_2 \cdot \text{Al}_2\text{O}_3$	0.75	0.00	1.00	1.13	0.75	0.00
C(N)ASH	$1.070\text{CaO} \cdot \text{SiO}_2 \cdot 0.086\text{Al}_2\text{O}_3$	5.81	4.65	0.75	7.18	1.59	0.57

### 5.2.2 Acid corrosion testing procedures

Acid corrosion test was conducted based on the general guidelines in ASTM C267. Following 120 days of sealed curing at 25 °C, five specimens from each mix were submerged in 5 containers with 5% sulphuric acid solution ( $\text{H}_2\text{SO}_4$ ) at a liquid to sample mass ratio of 6, respectively. Another five samples were submerged into distilled water as references. The specimens were taken out from the leachates after 1 d, 3 d, 7 d, 28 d and 56 d, respectively. Visual inspection was carried out on each sample. The leaching behavior of each sample had been monitored by recording the pH and elemental concentrations of the distilled water and the 5% sulphuric acid solutions during 56-day immersion of samples. Then the samples were dried overnight in a vacuum oven at 40 °C. The mass loss of samples was calculated by Equation 5-1.

$$\Delta m = \frac{m_o - m_c}{m_o} \times 100\% \quad \text{Equation 5-1}$$

where:  $\Delta m$  (%) is the mass change of the specimen during corrosion;  $m_o$  is the mass of the dried specimen before corrosion;  $m_c$  is the mass of the dried specimen after corrosion.

Inductively coupled plasma mass spectrometry (Thermo X-series II ICP-MS with a CETAC - 500 auto-sampler) was used to analyse the immersion solutions of each sample to determine elements leached from the paste into the acid solution and water.

Part of the 28-d sample was reserved for scanning electron microscopy energy-dispersive X-ray spectroscopy (SEM-EDS) test. The SEM samples were kept in the original appearance of the fracture surface to see natural microstructure (it affected the quality of picture though). All the rest of the exposed samples were ground with acetone using a pestle and mortar by hand to stop reaction. Figure 5-1 shows the experimental procedure.

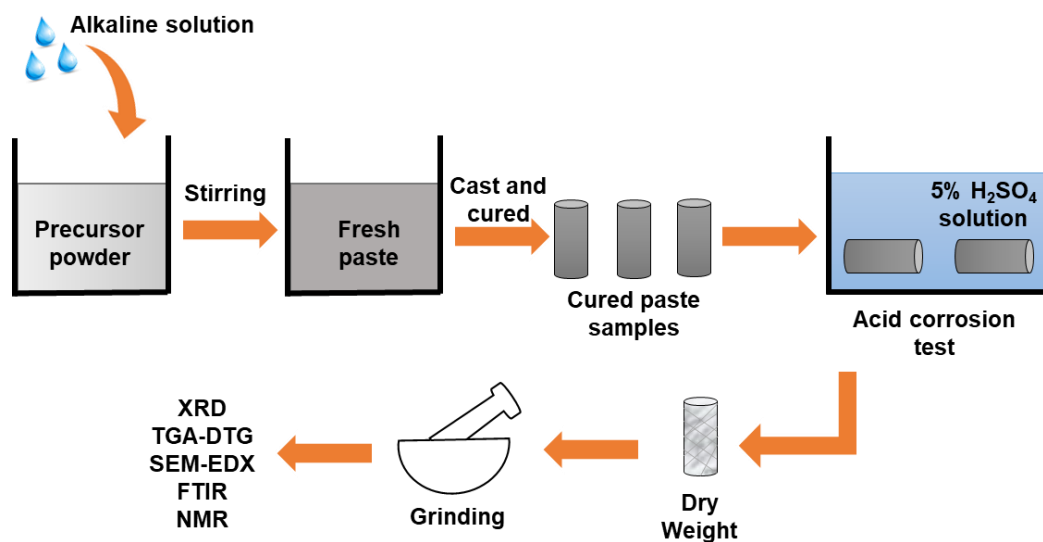


Figure 5-1. The experimental procedure.

### 5.2.3 Characterisation

The following characterization techniques were used:

- X-ray diffraction (Bruker D8 Advance powder XRD) patterns were collected between 5 and 60° 2 $\theta$  with a step size of 0.02° 2 $\theta$ , using Cu K $\alpha$  radiation with wavelength 1.54 Å, at voltage 40 kV and current 40 mA. Jade 6 software with the powder diffraction file (PDF) database was used to analyse the diffraction patterns.

- Combined thermogravimetric analysis - differential thermogravimetric (TG-DTG) was conducted on TA Instruments Discovery SDT 650. The temperature was increased from room temperature up to 1000 °C at a rate of 10 °C/min in a nitrogen environment. The weight loss information obtained from the TG curve and first derivative (DTG) was used to confirm the type of hydrates and reaction products.
- Fourier transform infrared spectroscopy (FTIR) using Perkin Elmer FTIR-ATR spectrometer in absorbance mode from 4000 to 400 cm<sup>-1</sup>. Using absorbance values, the spectra were fitted using a baseline correction and deconvoluted in the range of 600 -1300 cm<sup>-1</sup> by Origin 9.1 (OriginLab Corporation, USA) with a Gaussian multi-peak fit module.
- Solid-state single pulse <sup>27</sup>Al and <sup>29</sup>Si magic angle spinning (MAS) NMR spectra were collected on a Bruker 300 MHz Advance III 400WB spectrometer with double air bearing 4 mm MAS probe. Samples were spined at 8 kHz with 1 μs pulse (pi/12) and 1 s relaxation period between scans. The position of peaks was also verified with the CPMAS spectrum. Repetition delay was 100 s, determined to be sufficient for complete relaxation. Up to 1000 scans were collected. Deconvolution of the <sup>29</sup>Si MAS NMR spectra was performed by OriginLab. The minimum possible number of peaks was used to enable an accurate but meaningful interpretation of the spectra.
- SEM-EDS was performed using a Hitachi SU3500 instrument equipped with a 50 mm<sup>2</sup> Oxford Instruments silicon drift detector. Analyses were made at 1000 - 10000 magnification at 5 - 15 kV with lower accelerator energies for imaging with secondary electron returns only and higher accelerator energies for imaging in backscatter mode and the EDS point analyses.

## 5.3 Results and discussion

### 5.3.1 Visual inspection and mass change

Figure 5-2 displays the appearance of the dried NASH sample and C(N)ASH sample before and after 28 days of exposure to sulphuric acid. The surface appearance of unexposed NASH sample was more porous than the C(N)ASH sample. This is partly due to the high reactivity of the aluminosilicate powder for the NASH sample. The rapid coagulation during sample preparation resulted in less compacted paste. On the

other hand, it is related to the nature of binding gel formed in each system. It was found that the N-A-S-H gel formed in the fly ash system showed less dense and more porous than the C-(N)-A-S-H gel and C-(A)-S-H gel formed in the slag dominant systems (Wang et al., 2021a). It agrees with previous findings that C-(N)-A-S-H gel is a space-filling C-(A)-S-H gel which could significantly reduce porosity (Provis et al., 2012). After exposure to sulphuric acid solution for 28 days, the NASH sample partially dissolved and had visible cracks around the residual edge of the sample. The exposed C(N)ASH sample suffered severe damage with a completely split which due to the formation of expansive reaction product(s) during acid attack. There was trace amount of calcite formed (as determined by TG-DTG and XRD in the following), which was due to the carbonation on the surface of sample. After exposure to sulphuric acid, the calcite was decomposed completely. Together with the released  $\text{Ca}^{2+}$  from the dicalcium of C-(N)-A-S-H gels, reactive  $\text{Ca}^{2+}$  reacts with diffusing  $\text{SO}_4^{2-}$  ions and forms expansive gypsum, accelerated the damaged of the C(N)ASH sample. This was consistent with the previous results that calcium-containing sample showed visible damage (Aiken et al., 2018). The destruction form of the C(N)ASH sample confirmed the initial failure at the concrete surface, which is the formation of cracks caused surface peeling (Aiken et al., 2018, Zhang et al., 2018c).

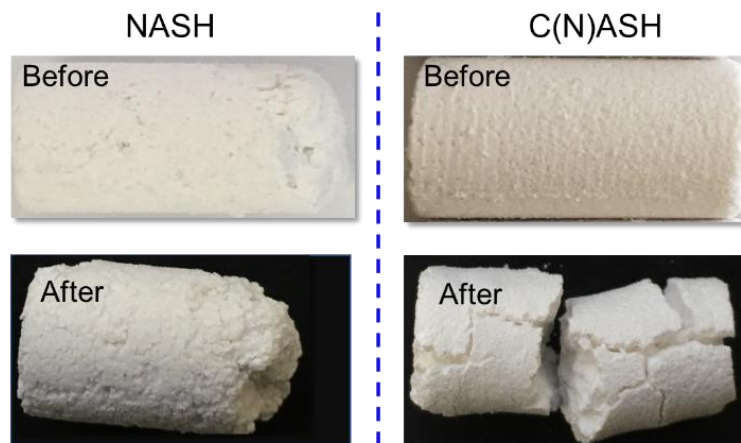


Figure 5-2. The appearance of NASH sample and C(N)ASH sample before and after 28 days exposure to sulphuric acid.

Figure 5-3 shows the mass changes of the two synthesised NASH sample and C(N)ASH sample after exposure to distilled water and the 5% sulphuric acid solution. Positive value represents a mass gain, and negative value represents a mass loss. In distilled water, a minor mass loss occurred in both the NASH sample and C(N)ASH

sample, which was likely due to the leaching of alkali. When exposure to sulphuric acid, it could be observed that the C(N)ASH sample had an evident mass gain over the exposure time, while the NASH sample displayed a mass loss. After 56 days of exposure to sulphuric acid, the C(N)ASH sample had a mass gain of 0.8%, and the NASH sample had a small mass loss of 0.15%. The increased weight of the C(N)ASH sample is related to the formation of reaction products (confirmed in the following sections) and the decreased weight of the NASH sample was due to the dissolution of reaction product. The results are consistent with the above appearance change of the samples. From the results, the distilled water had minor effect on the mass change of samples while the sulphuric acid attack had significant influence on the mass change of samples. This suggests that the synthetic C-(N)-A-S-H and N-A-S-H gels are stable in distilled water while sensitive to sulphuric acid solution. In the following section, the leaching performance of N-A-S-H gel and C-(N)-A-S-H gel in distilled water and sulphuric acid solution could explain this phenomenon.

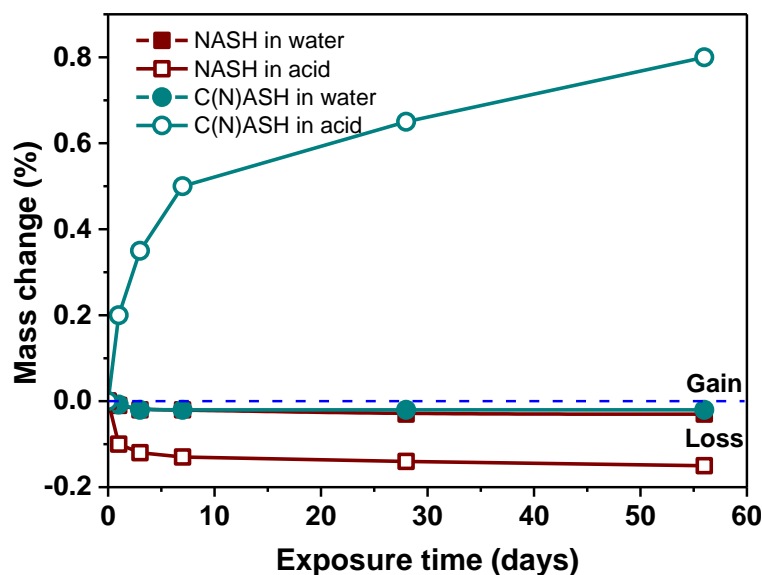


Figure 5-3. The mass change (%) of the NASH sample and C(N)ASH sample after exposure to water and 5% sulphuric acid solution.

### 5.3.2 Leaching behaviour

Figure 5-4 displays the evolution of the pH values of the immersion solutions (i.e., distilled water and the 5% sulphuric acid solutions) with exposure time. As shown in Figure 5-4 (a), the initial pH of the distilled water was 6.6, and it increased rapidly to 9 for the NASH sample after 1 day of immersion and remained high thereafter. Similar behavior was observed for the C(N)ASH sample with the pH increased to 12. The

increased pH was due to the leaching of hydroxyl ions from samples into the leachates. This took place because of the differential pH between distilled water and samples which were alkaline in nature. The higher pH value of the leachate for the C(N)ASH sample compared to the NASH sample suggests its higher leaching amount of hydroxyl ions ( $\text{OH}^-$ ) from samples.

For the samples immersed in 5% sulphuric acid solution, the pH of the resulted solution for the NASH sample has minor increment from 0.11 to 0.4, while it increased to approximately 2.7 for the C(N)ASH sample. Ions leaching (such as hydroxyl ions) were facilitated by the transfer of acidic ions, i.e.,  $\text{H}^+$ ,  $\text{H}_3\text{O}^+$ , and  $\text{SO}_4^{2-}$ , into the samples, while metal cations (i.e.,  $\text{Ca}^{2+}$ ,  $\text{Al}^{3+}$ , and  $\text{Na}^+$ ) into the acid solution. The consumption of  $\text{H}_3\text{O}^+$  ions in the sulphuric acid solution of the NASH sample and C(N)ASH sample were 53.2% and 99.75%, respectively, according to acid-base neutralization reaction. The results are consistent with previous findings that the alkali-activated fly ash sample showed lower pH value than the alkali-activated slag after exposure to sulphuric acid solution (Aiken et al., 2018). As well known the  $\text{OH}^-$  ions acted as catalyst during alkali-activation process (Palomo et al., 2015). The greater impact of the C(N)ASH sample on the pH evolution of both distilled water and sulphuric acid solution was related to its lower consumption of  $\text{OH}^-$  ions during the formation of reaction products.

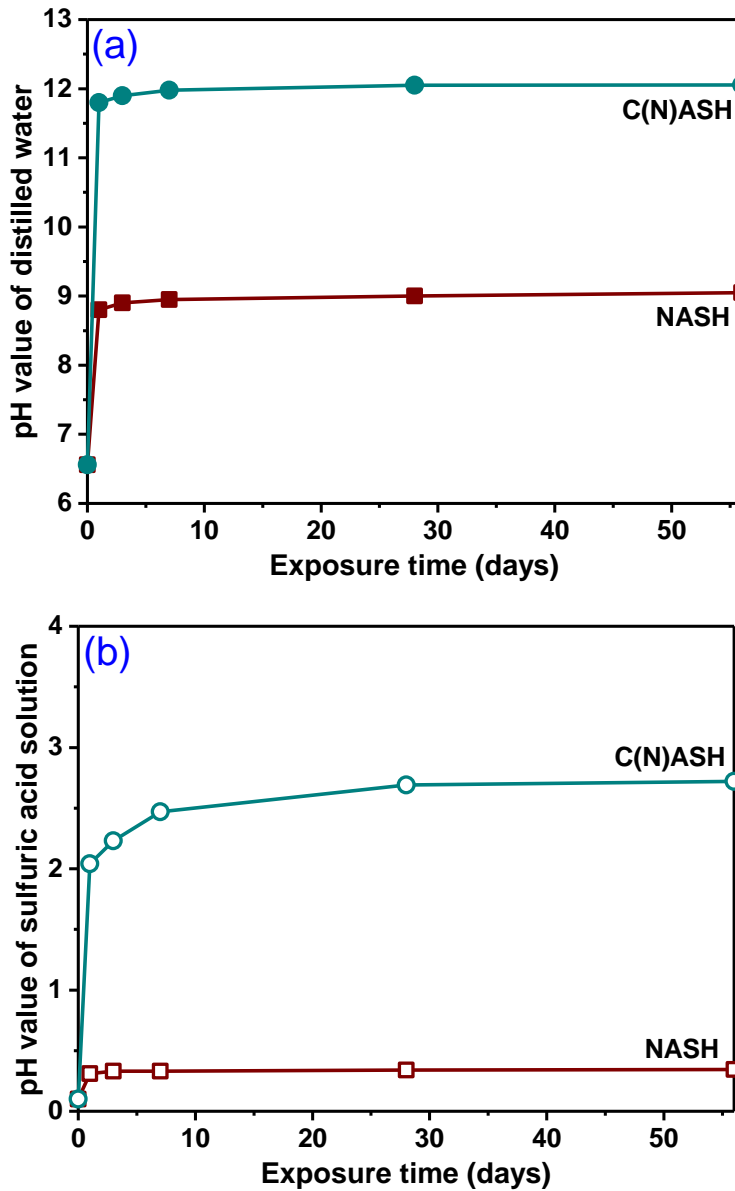
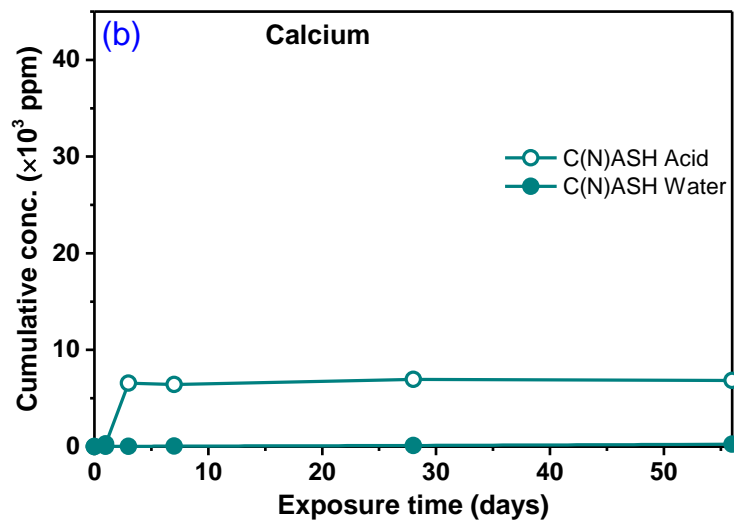
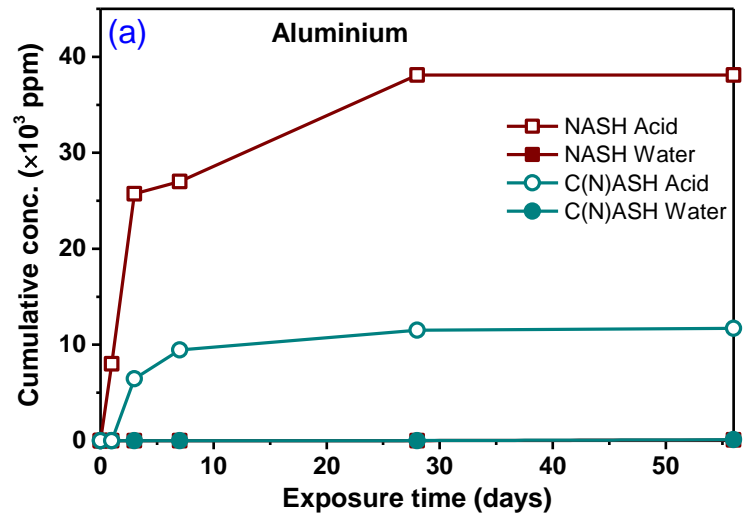


Figure 5-4. pH values of the (a) distilled water and (b) 5% sulphuric acid solution after 56 days of immersion of the NASH sample and C(N)ASH sample.

Figure 5-5 displays the cumulative concentration of aluminium (Al), calcium (Ca), sodium (Na), and silicon (Si) presented in the distilled water and 5% sulphuric acid solutions during 56-day immersion of NASH sample and C(N)ASH sample. There were no significant quantities of aluminium, calcium, or silicon (< 116, 249, and 145 ppm, respectively) present in the water solutions leached out from any of the NASH sample and C(N)ASH sample. The main element identified in water was sodium, which increased concentration with the exposure time. The cumulative concentration of Na leached out from the NASH sample and C(N)ASH sample was 4886 ppm and 15248 ppm after 56 days exposure to water, respectively. This was not surprising due

to the sodium silicate and sodium hydroxide solutions which were used as activators in the mixes. As known, the existing Na in alkali-activated materials included three types, i.e. free Na (the majority), union Na, and compound Na (Huang et al., 2018). The free Na existed in the pore solution of the sample and easily diffused into the external environment. Union Na was converted from free Na, existing in an unstable form. The compound Na existed in a stable form in the reaction hydrate, i.e., N-A-S-H gel. The results suggested that more free Na leaching out from the C(N)ASH sample than the NASH sample to distilled water. This result also suggests a possible high efflorescence potential of geopolymer when a small dose of calcium is introduced, and indeed, it has been found by Longhi et al. (2021).

For sulphuric acid leachates, a significant amount of aluminium, sodium, and silicon leached out from both the NASH sample and C(N)ASH sample. As shown in Figure 5-5 (a), the concentration of aluminium from the C(N)ASH sample and NASH sample resulted in the highest concentration of 11719 ppm and 38100 ppm, respectively. Higher concentration of Al in the leachate of the NASH sample suggested that the dealumination in the N-A-S-H gel was easier. The calcium content leaching out from the C(N)ASH sample reached the highest value (6830 ppm) on the first day and kept constant thereafter. It is a result of the decalcification of C-(N)-A-S-H gel and the dissolution of other reaction products in the C(N)ASH sample. The concentration of sodium leached from the C(N)ASH sample (41200 ppm) was significantly higher than that of the NASH sample (6734 ppm). The bound  $\text{Na}^+$  and compound  $\text{Na}^+$  are converted back to free  $\text{Na}^+$  under acid attack (Longhi et al., 2019), therefore, the Na concentrations were significantly higher in the acid solution leachate than in the water leachate. The difference of sodium concentration in the distilled water and acid solution was regarded to be the amount of bound  $\text{Na}^+$  and compound  $\text{Na}^+$ . The cumulative concentration of silicon leached from the NASH sample and C(N)ASH sample reached 18350 and 8918 ppm, respectively, after 56 days of acid exposure. In view of the above results, the NASH sample showed higher leaching concentrations of Al and Si than the C(N)ASH sample, except for Na.



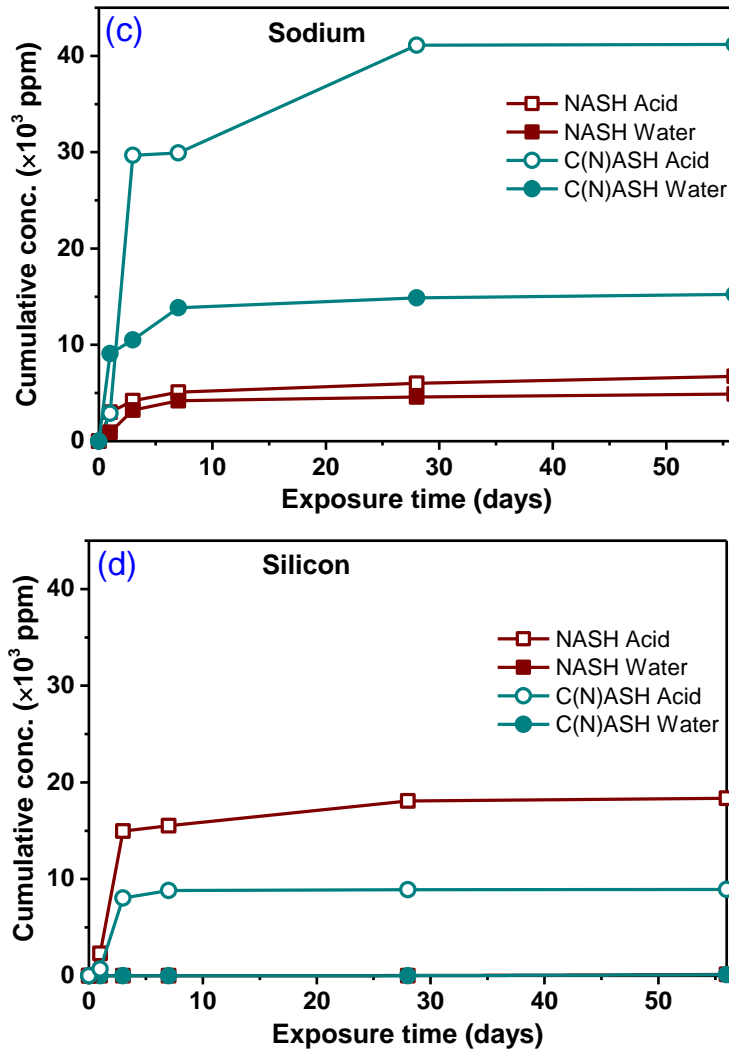


Figure 5-5. Cumulative concentrations of aluminium, calcium, sodium, and silicon leached from the NASH sample and C(N)ASH sample exposed to distilled water and 5% sulphuric acid solution for 56 days.

Figure 5-6 shows the Si/Al and Na/Al ratios in unexposed NASH sample and C(N)ASH sample and their acid leachates. For the NASH sample, Al was the most easily precipitated element, followed by Na and, lastly Si. The most readily precipitated element in C(N)ASH sample was Na, followed by Al, and finally Si. In view of leaching behaviour, lower concentration of Na was leached out from the NASH sample under sulphuric acid attack. Instead, more Al was leached out from the NASH sample when exposure to acid solution. Hence, Al-O from the framework of N-A-S-H gel was susceptible to hydrogen ions attack. It means the destroy of N-A-S-H gel under acid conditions is due to dealumination from the gel framework, while the destroy of C-(N)-A-S-H gel under acid conditions is due to the continuous leaching of Na, together with the continuous loss of Al (dealumination). This is different from the

previous mechanism that for the C-S-H gels that formed in OPC system, which the sulphuric acid leads to the decalcification and finally destroy of matrix.

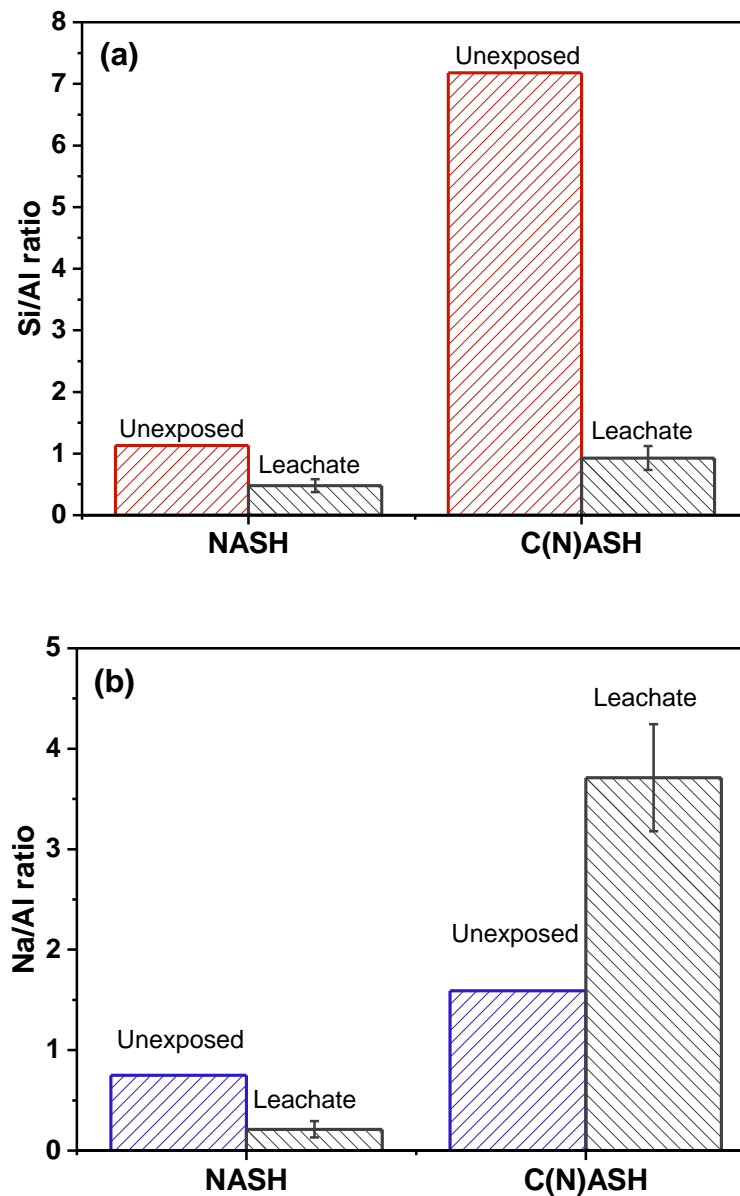


Figure 5-6. The ratios of (a) Si/Al and (b) Na/Al in the unexposed NASH sample and C(N)ASH sample and their acid leachates.

### 5.3.3 X-ray diffraction (XRD) analysis

Figure 5-7 shows the XRD results for the NASH sample and C(N)ASH sample before and after 28 days of sulphuric acid exposure. As shown in Figure 5-7 (a), a broad featureless hump was visible between  $20^\circ$  and  $35^\circ 2\theta$  for the NASH sample, confirmed the formation of amorphous reaction products (i.e. N-A-S-H gel) as discussed above (Wang et al., 2021a). The minor crystalline peaks observed in the NASH sample were

attributed to the phases like paragonite ( $\text{NaAl}_2(\text{AlSi}_3)\text{O}_{10}(\text{OH})_2$ , PDF # 24-1047) and albite ( $\text{NaAlSi}_3\text{O}_8$ , PDF # 80-1094). After sulphuric acid exposure, the broad peak at the NASH sample shifted to around  $22^\circ 2\theta$ , suggesting the breakage of the N-A-S-H gel (Longhi et al., 2019). This result suggested that the N-A-S-H gel was vulnerable to sulphuric acid attack. Paragonite and albite were no longer present in the exposed NASH sample. This was different to the crystalline phases found in alkali-activated fly ash which was invulnerable to sulphuric acid attack (Aiken et al., 2018). The peaks attributed to tamarugite ( $\text{NaAl}(\text{SO}_4)_2 \cdot 6\text{H}_2\text{O}$ , PDF # 71-2385) was identified in the exposed NASH sample. This suggests that the decomposition of N-A-S-H gel leads to the precipitation of Na and Al in the leachates.

As shown in Figure 5-7 (b), the XRD pattern of the C(N)ASH sample exhibits a broad feature centered at approximately  $29^\circ 2\theta$ , characteristic of a disordered reaction product consistent with that formed in AAMs derived from slag (Walkley, 2016). This phase was assigned to a poorly crystalline C-(A)-S-H phase displaying some structural similarity with calcium aluminium silicate (CAS, PDF # 23-0105). Calcite ( $\text{CaCO}_3$ , PDF # 72-1937 and PDF # 41-1475) was formed at the similar reflection angle with CAS which was formed during preparation process. Pectolite ( $\text{NaCa}_2\text{HSi}_3\text{O}_9$ , PDF # 33-1223), wollastonite ( $\text{CaSiO}_3$ , PDF # 84-0654) and calcium aluminate silicate ( $\text{Ca}_3\text{Al}_6\text{Si}_3\text{O}_{16}$ , PDF # 47-0162) were also identified in the unexposed C(N)ASH sample. After exposure to sulphuric acid for 28 days, the exposed C(N)ASH sample demonstrated the presence of gypsum ( $\text{CaSO}_4 \cdot 2\text{H}_2\text{O}$ , PDF#33-0311). The trace of amorphous hump shifted to around  $22^\circ 2\theta$  and decreased in the intensity, which was considered as the distinguishing feature of residual C-(A)-S-H gel. The crystalline phases identified in unexposed C(N)ASH sample was no longer present. There was no ettringite identified in the XRD pattern of the exposed C(N)ASH sample. This is due to the formation of gypsum is favored than ettringite when calcium availability was enough (Ye and Huang, 2020). The findings explain the different appearance changes of the NASH sample and C(N)ASH sample when exposed to acid, as discussed above.

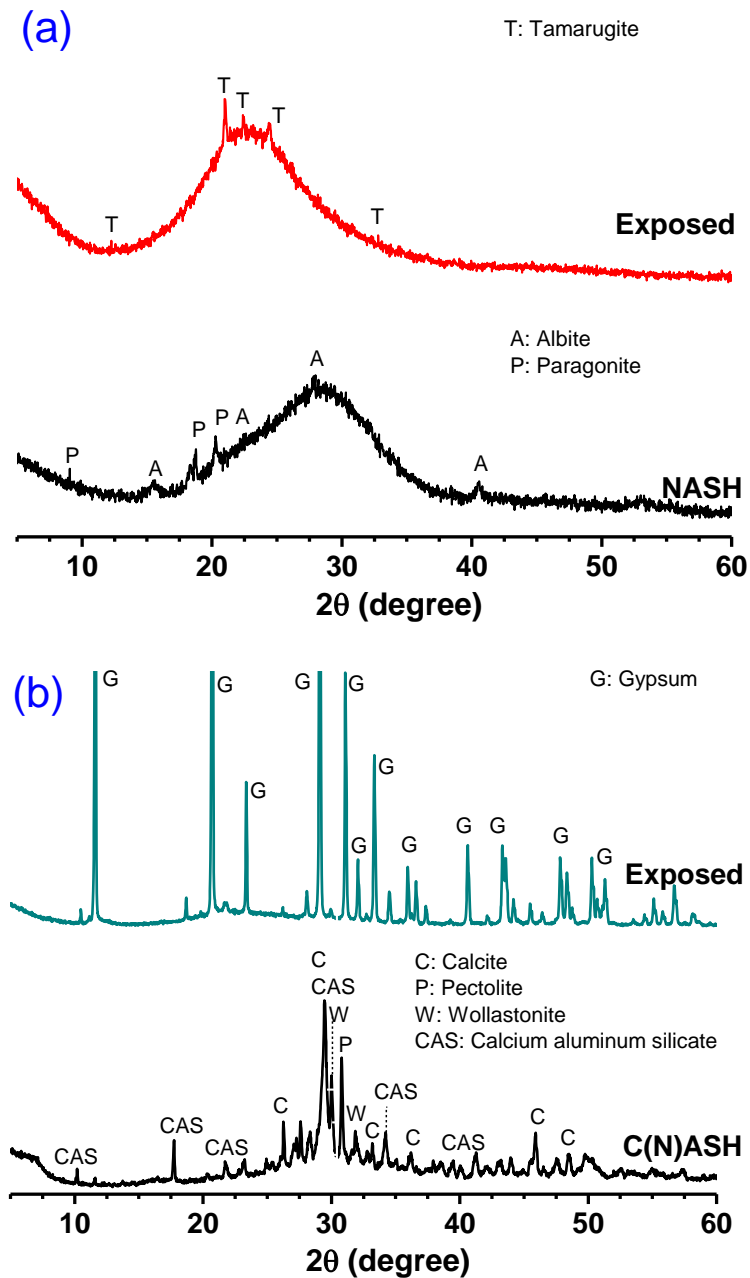


Figure 5-7. X-ray diffractions of the (a) NASH sample and (b) C(N)ASH sample before and after 28 days sulphuric acid attack.

### 5.3.4 Thermogravimetric-differential thermogravimetric (TG-DTG) analysis

Figure 5-8 displays the mass change at high temperatures of the NASH sample and C(N)ASH sample before and after exposure to sulphuric acid attack. The unexposed and exposed NASH samples showed final mass loss of 27.8% and 29.7%, respectively. For the unexposed NASH sample, the mass loss peak in the DTG curves centred at 71 °C, which was due to the removal of free water (Walkley, 2016). The larger shoulder at around 105 °C for the unexposed NASH sample was attributed to the dehydration

of gel product (i.e. N-A-S-H gel), which continued to around 300 °C (Bernal et al., 2011c). A small mass loss peak was observed at 255 °C which was associated with the loss of tightly physically bound water in albite and paragonite, identified in the XRD patterns (Feng et al., 2012, Walkley, 2016). After exposed to acid attack, the mass loss peak due to the removal of free water shifted to a higher temperature at around 78 °C. The reduced intensity of dehydration peak at around 105 °C suggested that reduced amount of bound water of N-A-S-H gel when exposed to sulphuric acid. Another mass loss happened in the range of 416-617 °C, which was due to the dehydration of reaction product (tamarugite) (Ariffin et al., 2013, Yang et al., 2016, Lothenbach et al., 2016).

The C(N)ASH sample before and after exposure to sulphuric acid attack showed the final mass loss of 12.5% and 17.9%, respectively. The mass loss of the unexposed C(N)ASH sample continued to around 650 °C, while the mass loss of the exposed C(N)ASH sample happened predominately before 300 °C. The mass loss happened in the range of 30 °C to 680 °C in the DTG curve of the unexposed C(N)ASH sample which was related to the removal of free water and the dehydration of C-(N)-A-S-H gel (Lothenbach et al., 2016). The small peak at 676 and 680 °C suggested the decomposition of calcite (Felicetti, 2004, Hager, 2014). The mass loss peak of the exposed C(N)ASH sample before 100 °C was the removal of free water and/or loosely bound moisture which was not removed during preparation of the powdered sample (Aiken et al., 2018). The mass loss peak at the range of approximately 90 and 150 °C were believed to be due to the dehydration of gypsum, as shown in Figure 5-8 (Singh and Garg, 2000, Strydom et al., 1995, Alarcon-Ruiz et al., 2005, Svinning et al., 2008).

The weight loss due to the decomposition of gypsum can be used to calculate the amount of gypsum present in the exposed samples, using the molecular mass of gypsum and water as shown in Figure 5-8 (Lothenbach et al., 2016). Considering the contribution of water loss from the C-(N)-A-S-H gel (it can be obtained from the deconvoluted peaks of the DTG curves of the exposed C(N)ASH sample), the amount of calculated  $\text{CaSO}_4 \cdot 2\text{H}_2\text{O}$  accounted for around 60 wt.% of the exposed sample according to the Equation 5-2 and Equation 5-3.

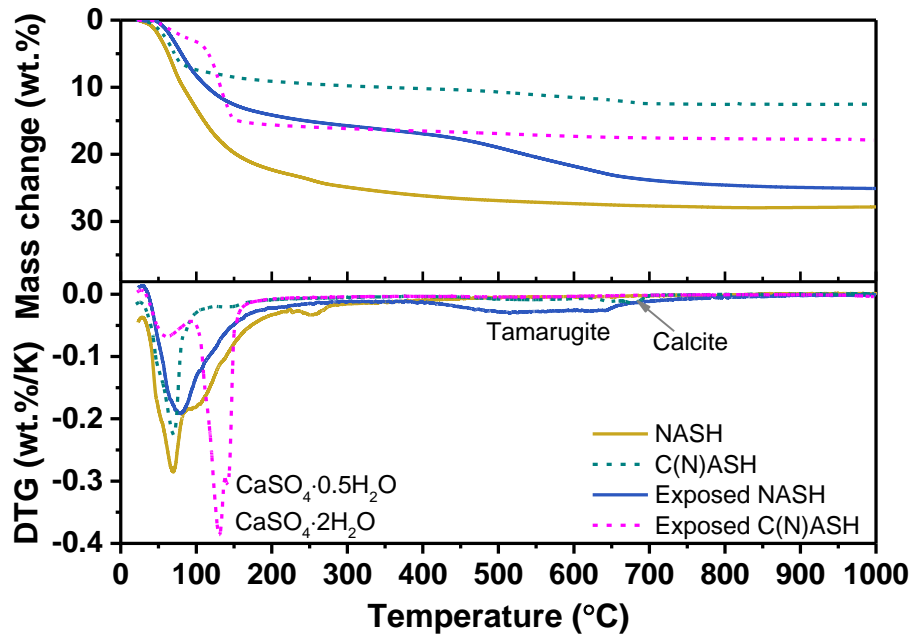
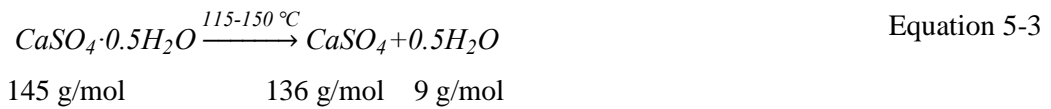
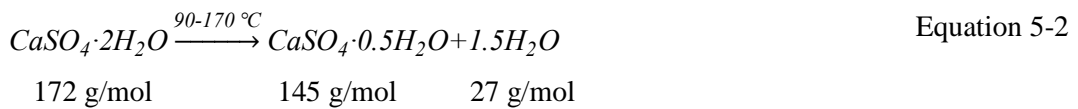


Figure 5-8. Mass change and differential mass change (DTG) of the NASH sample and C(N)ASH sample before and after 28 days of sulphuric acid attack.



### 5.3.5 Fourier transform infrared spectroscopy (FTIR) analysis

Figure 5-9 presents the FTIR spectra for the precursors and the NASH sample and C(N)ASH sample before and after exposure to sulphuric acid attack. In the spectrum of the precursor for the NASH sample, an intense peak was observed at approximately  $1072 \text{ cm}^{-1}$ , which was assigned to asymmetric stretching vibrations of Si-O-T bonds, where T = Si or Al in tetrahedral coordination (Rees et al., 2007). The band at approximately  $781 \text{ cm}^{-1}$  that was assigned to bending vibrations of Al-O bonds in  $\text{AlO}_6$  octahedra (Zhang et al., 2012). In the spectrum of the precursor for the C(N)ASH sample, a broad band was observed at  $910 \text{ cm}^{-1}$ , and a shoulder could also be observed at  $993 \text{ cm}^{-1}$ . These bands were attributed to the stretching vibrations of Si-O-T bonds due to a highly depolymerized silica network and consistent with that observed in slag (Bernal et al., 2011a, Walkley, 2016). A sharp shoulder at  $841 \text{ cm}^{-1}$  was likely due to the presence of  $\text{HCO}_3^-$  formed during sample preparation (Walkley, 2016). The small

featural bands centered at 696 and 460  $\text{cm}^{-1}$  were attributed to symmetrical stretching and bending of Si-O-T bonds, respectively (Walkley, 2016).

The alkali activation process in the NASH sample is observed by the shifting of the main peak from 1072  $\text{cm}^{-1}$  to 972  $\text{cm}^{-1}$ . This change was due to the decrease of tetrahedral Si sites, replaced by the tetrahedral Al during the formation of N-A-S-H gel (Longhi et al., 2019). The small band observed at approximately 1647  $\text{cm}^{-1}$  for each sample was assigned to H-O-H bending mode (Aiken et al., 2018). The broad band at the range of about 3700-2700  $\text{cm}^{-1}$  was attributed to the presence of free and chemically bound water due to the activation process. For C(N)ASH sample, alkali-activation produced a broad intense band at approximately 955  $\text{cm}^{-1}$ , attributed to asymmetric stretching vibrations of Si-O-T bonds in the chain structure of C-(N)-A-S-H gel (Walkley et al., 2016c). The broad band at 1417  $\text{cm}^{-1}$  was attributed to the asymmetric stretching of O-C-O bonds in  $\text{CO}_3^{2-}$ .

FTIR data for the NASH sample after exposure to acid attack exhibited a movement of the main peak to a higher wavenumber from 972  $\text{cm}^{-1}$  to 1060  $\text{cm}^{-1}$ . This change was related to the decomposition of N-A-S-H gel under acid attack. Two more intensive peaks at 945  $\text{cm}^{-1}$  and 797  $\text{cm}^{-1}$  in the corroded NASH sample were recognized as the residual N-A-S-H gel. Sulphuric acid attack caused a significant change on the FTIR spectrum of the exposed C(N)ASH sample. The main band was centered at approximately 1100  $\text{cm}^{-1}$ , and two intensive peaks formed at 667  $\text{cm}^{-1}$  and 600  $\text{cm}^{-1}$ . These changes indicated the decomposition of C-(N)-A-S-H gel and the formation of corrosion products, mainly gypsum.

The overlapping bands are identified in the FTIR spectra by deconvolution of the main band, which are summarized in Table 5-2. For NASH sample, the bands at 1050  $\text{cm}^{-1}$  and 987  $\text{cm}^{-1}$  were assigned to the asymmetric stretching vibration ( $\sigma_{as}$ ) of Si-O-T bond, and 947  $\text{cm}^{-1}$  to asymmetric stretching vibration of non-bridging oxygen sites (i.e., Si-O-Na). The bands at 853  $\text{cm}^{-1}$  and 712  $\text{cm}^{-1}$  were assigned to the bending vibration ( $\delta$ ) of Si-OH bond and Si-O-Al<sup>IV</sup> bond, respectively. After exposed to sulphuric acid attack, new bands appeared at 1214  $\text{cm}^{-1}$  and 1118  $\text{cm}^{-1}$  were assigned to the asymmetric stretching vibration of S-O bond in  $\text{SO}_4^{2-}$ , accounting for around 36 % (Lane, 2007). High polymerized Si-O bonds at 1071  $\text{cm}^{-1}$  and 1034  $\text{cm}^{-1}$  were accounted for 51% since the dealumination of the N-A-S-H gel leaving a silica-rich

gel. There was no Si-O-Al<sup>IV</sup> identified in the exposed NASH sample. The results confirmed that acid attack resulted in the dealumination of N-A-S-H gel and breakdown of Si-O-Na bond. Al was easier leaching out from N-A-S-H gel than Na and the delamination resulted the destroy of N-A-S-H gel under acid attack.

Compared to the NASH sample, the Al-substitution in the C-(N)-A-S-H gel of the C(N)ASH sample could be deconvoluted out as Si-O-Al bond at 1023 cm<sup>-1</sup>. The Si-O-Na bond in the C-(N)-A-S-H gel accounted for around 2%, much less than 19% in the N-A-S-H gel. This was likely related to the different action mechanism of alkali in the N-A-S-H gel and C-(N)-A-S-H gel, while Na incorporated into silicate chains in the N-A-S-H gel but acted as charge balance in the C-(N)-A-S-H gel at Al-substitution site. After exposed to sulphuric acid attack, the Si-O-Na bond in the exposed C-(N)-A-S-H gel could still be identified. The results suggested that acid attack caused the dealumination of the C-(N)-A-S-H gel along with leaching of alkali but had minor effect on the Si-O-Na bond in the C-(N)-A-S-H gel.

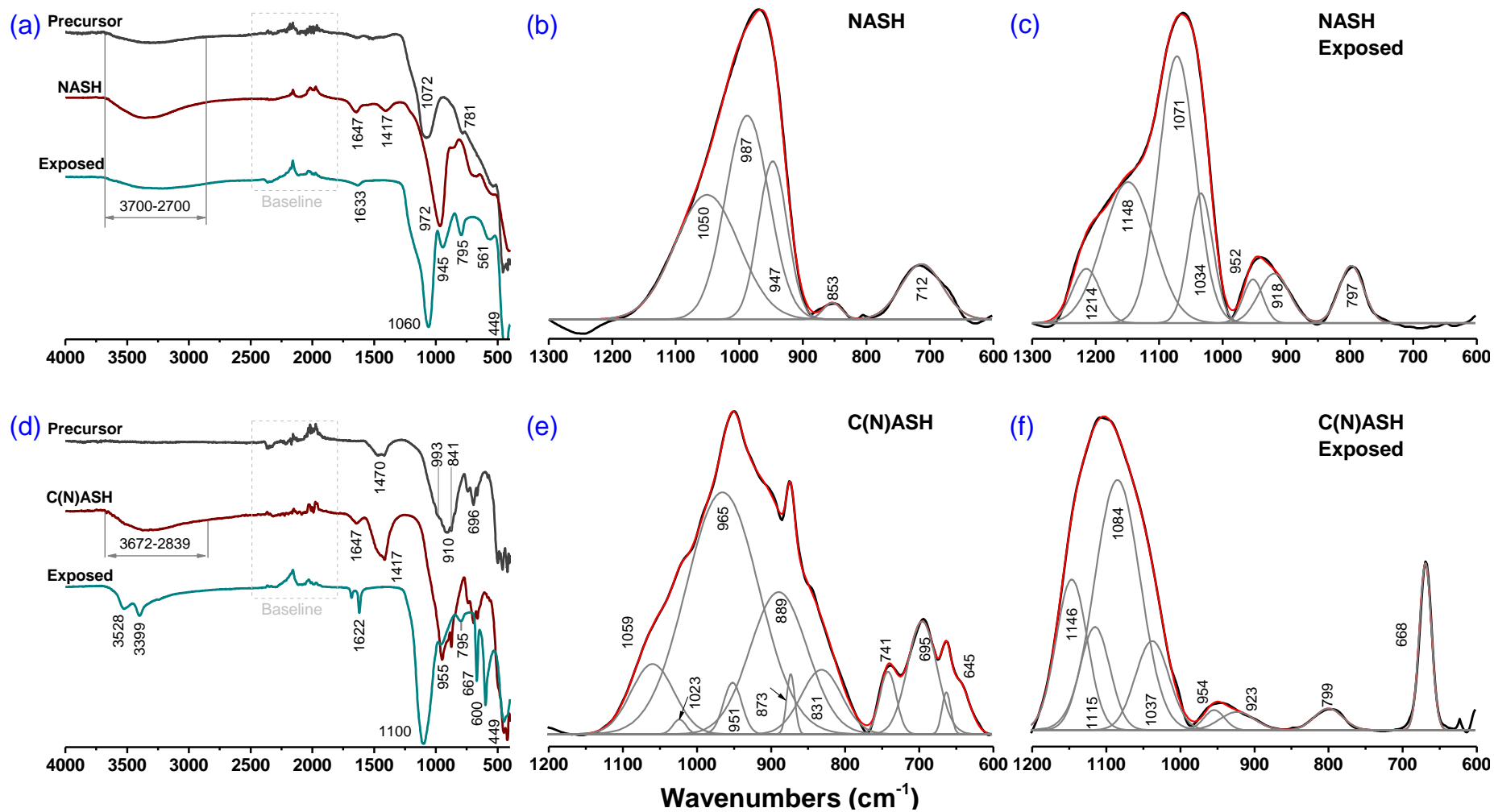


Figure 5-9. FTIR spectra (absorbance) and deconvoluted spectra of the NASH and C(N)ASH samples before and after exposure to sulphuric acid.

Table 5-2 Summary of bands in the deconvoluted FTIR spectrum of Si-O-T bands for the NASH and C(N)ASH samples before and after exposed to acid attack in the range of 1300 cm<sup>-1</sup> ~ 600 cm<sup>-1</sup>.

Asymmetric stretching vibration ( $\sigma_{as}$ ), symmetric stretching vibration ( $\sigma_s$ ) and bending vibration ( $\delta$ ). \* means bands with trace occupation.

	Position (cm <sup>-1</sup> )	Assignment	Account (Relative area %)	Ref.
NASH	1050	$\sigma_{as}$ Si-O, Q <sup>3</sup> + Q <sup>4</sup>	33	(García-Lodeiro et al., 2008, Rees et al., 2007)
	987	$\sigma_{as}$ Si-O, Q <sup>2</sup>	37	(García-Lodeiro et al., 2008)
	947	$\sigma_{as}$ Si-O-Na	19	(Zhang et al., 2012)
	853	$\delta$ Si-O	1	(Zhang et al., 2012)
	712	$\delta$ Si-O-Al <sup>IV</sup>	10	(Zhang et al., 2012)
Exposed NASH	1214	$\sigma_{as}$ SO <sub>4</sub> <sup>2-</sup>	8	(Lane, 2007)
	1118	$\sigma_{as}$ SO <sub>4</sub> <sup>2-</sup>	28	(Lane, 2007)
	1071	$\sigma_{as}$ Si-O, Q <sup>4</sup> , silica gel	39	(Lane, 2007)
	1034	$\sigma_{as}$ Si-O, Q <sup>3</sup> , silica gel	12	(García-Lodeiro et al., 2008)
	952	$\sigma_{as}$ Si-O-Na	3	(García-Lodeiro et al., 2008)
	918	$\sigma_{as}$ Si-O	6	(Zhang et al., 2012)
	797	$\delta$ Si-O	6	(Zhang et al., 2012)
C(N)ASH	1059	$\sigma_{as}$ Si-O, Q <sup>3</sup> + Q <sup>4</sup>	8	(García-Lodeiro et al., 2008)
	1023*	$\sigma_{as}$ Si-O-Al	0.5	(García-Lodeiro et al., 2008)
	965	$\sigma_{as}$ Si-O, Q <sup>2</sup>	46	(García-Lodeiro et al., 2008)
	951*	$\sigma_{as}$ Si-O-Na	2	(García-Lodeiro et al., 2008)
	889	$\delta$ Si-O	21	(Zhang et al., 2012)
	873*	$\sigma_{as}$ C-O	1	(Zhang et al., 2012)
	831	$\sigma_s$ Si-O, C-S-H	7	(Król et al., 2018)
	741	$\delta$ Si-O-T, precursor	3	(Zhang et al., 2012)
	695	$\delta$ Si-O-T, precursor	9	(Zhang et al., 2012)
	645	$\delta$ Si-O-T, precursor	3	(Zhang et al., 2012)
Exposed C(N)ASH	1146	$\sigma_{as}$ SO <sub>4</sub> <sup>2-</sup> , gypsum	18	(Lane, 2007)
	1115	$\sigma_{as}$ SO <sub>4</sub> <sup>2-</sup> , gypsum	12	(Lane, 2007)
	1084	$\sigma_{as}$ Si-O, Q <sup>4</sup> , silica gel	44	(García-Lodeiro et al., 2008)
	1037	$\sigma_{as}$ Si-O, Q <sup>3</sup> , silica gel	12	(García-Lodeiro et al., 2008)
	954	$\sigma_{as}$ Si-O-Na	2	(García-Lodeiro et al., 2008)
	923	$\sigma_{as}$ Si-O	2	(García-Lodeiro et al., 2008)
	799	$\delta$ Si-O	2	(Zhang et al., 2012)
668	$\sigma_{as}$ SO <sub>4</sub> <sup>2-</sup> , gypsum	8	(Lane, 2007)	

### 5.3.6 Scanning electron microscopy (SEM) and energy dispersive X-ray (EDX) analysis

Figure 5-10 shows the SEM images of NASH sample and C(N)ASH sample before and after exposure to sulphuric acid attack. The fracture section of the unexposed NASH sample showed a homogeneous but granular surface. After acid attack, the microcracks generated inside the paste matrix. This was due to the leaching of aluminium and sodium from the paste of NASH sample. The unexposed C(N)ASH sample showed a denser microstructure than the NASH sample. After exposed to acid attack, it was clear to see the formation of column-like gypsum grains in the exposed C(N)ASH sample. The coarse gypsum grains forming in a dense matrix can result in high stress and lead to loosening of the C(N)ASH matrix, and further cracking of the samples (as shown in Figure 5-2).

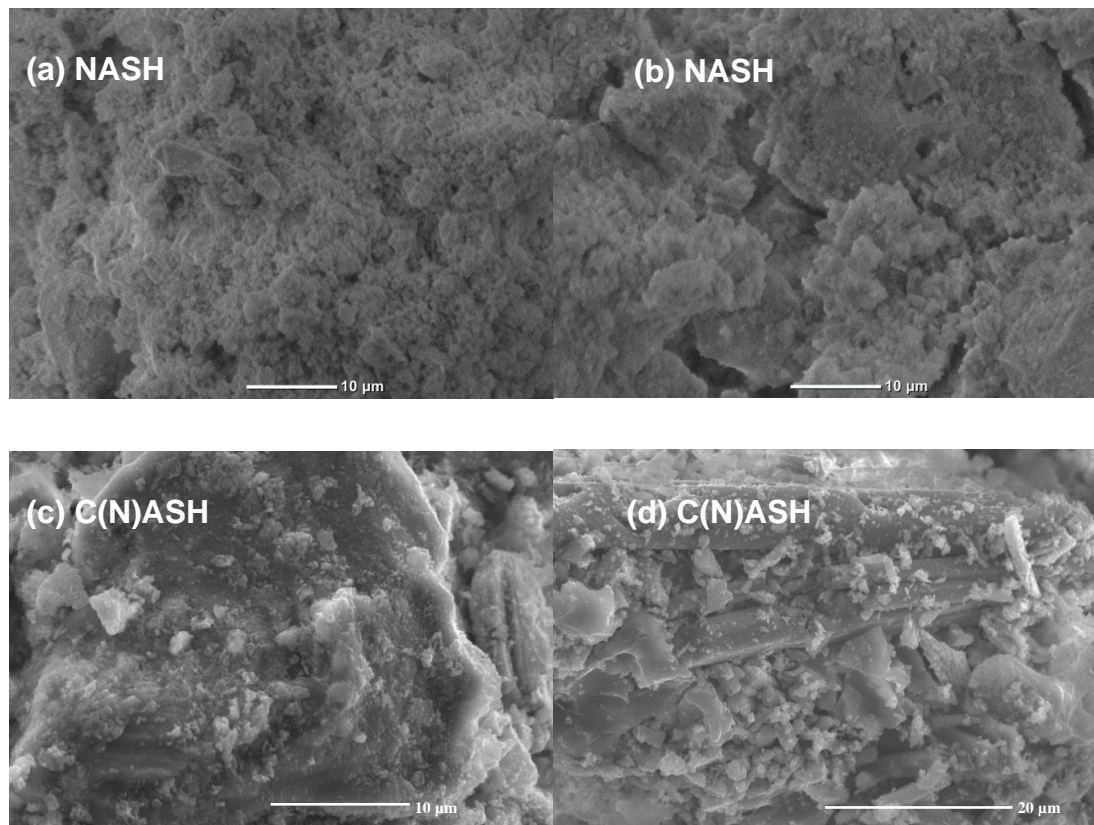


Figure 5-10. SEM images of the NASH and C(N)ASH samples before and after exposure to sulphuric acid.

Figure 5-11 shows the summary of atomic ratios of Na/Al versus Si/Al for the NASH sample before and after unexposed to acid attack. The elemental composition of unexposed NASH sample displayed a broad range of values within the region  $1.0 \leq \text{Si/Al} \leq 4.5$  and  $0.5 \leq \text{Na/Al} \leq 2.0$ , which was comparable with that of alkali-activated fly ash (Fernández-Jiménez and Palomo, 2005). After exposed to acid for 28 days, the

exposed NASH sample exhibited a range of values clustered around two distinct regions: one with the cation ratios of  $3.5 \leq \text{Si}/\text{Al} \leq 5.2$  and  $3.5 \leq \text{Na}/\text{Al} \leq 6$ , and another with the cation ratios of  $4 \leq \text{Si}/\text{Al} \leq 5.2$  with free Na. This suggested that sulphuric acid attack resulted in the residual N-A-S-H gel exhibiting a high Si/Al ratio due to the dealumination. Meanwhile, sodium leaching out from the N-A-S-H gel resulting in Na/Al ratio near 0.

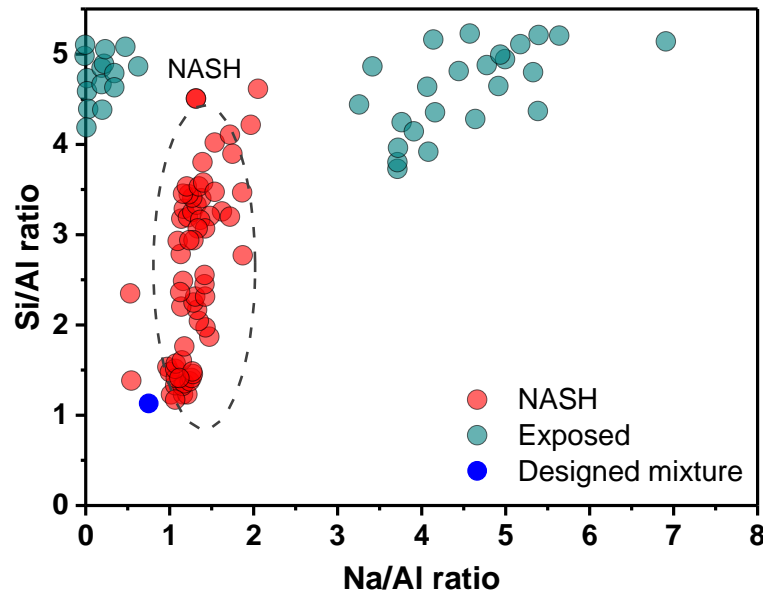


Figure 5-11. Atomic ratios Na/Al versus Si/Al for the unexposed and exposed regions of the NASH sample as marked, determined by EDX analysis. A random selection of points evenly distributed across a representative  $1000 \mu\text{m} \times 1000 \mu\text{m}$  section of the sample were used for analysis. The approximate region defined for N-A-S-H refers to (Walkley, 2016).

Figure 5-12 shows the summary of atomic ratios Ca/Si versus Al/Si for projection of material chemistry of the unexposed and exposed C(N)ASH samples. The chemistry of the unexposed C(N)ASH sample lied within the region commonly associated with a C-(N)-A-S-H gel of  $0.79 \leq \text{Ca}/\text{Si} \leq 1.86$  and  $0.11 \leq \text{Al}/\text{Si} \leq 0.28$ . After exposed to sulphuric acid attack for 28 days, the chemistry of the exposed C(N)ASH sample showed two regions: one with the cation ratios of  $0 \leq \text{Al}/\text{Si} \leq 0.1$  and  $0 \leq \text{Ca}/\text{Si} \leq 2$ , and another which exhibited cation ratios of  $\text{Al}/\text{Si} = 0$  and  $0 \leq \text{Ca}/\text{Si} \leq 15$ . The very high Ca/Si is due to the formation of gypsum as EDS analysis may bring in a region of elements into counting. It means the destroy of C-(N)-A-S-H gel under acid conditions related to both dealumination and decalcification.

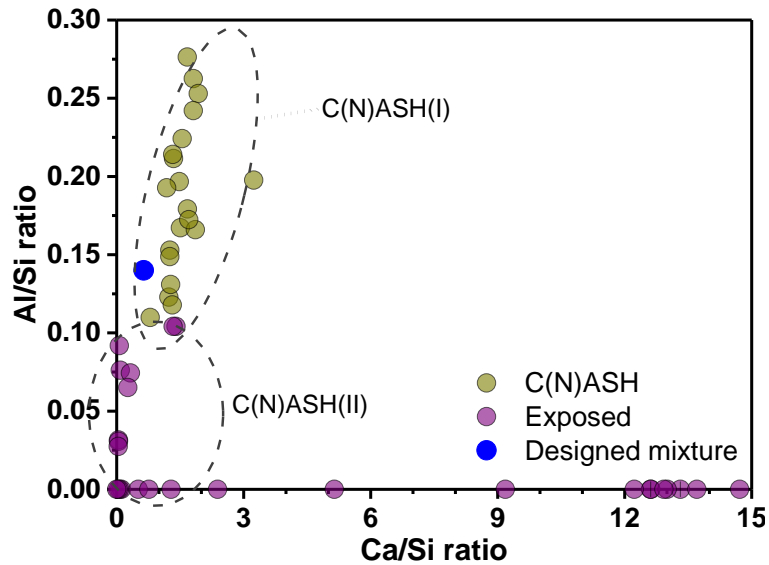


Figure 5-12. Atomic ratios Ca/Si versus Al/Si for the unexposed and exposed regions of the C(N)ASH sample as marked, determined by EDX analysis. A random selection of points evenly distributed across a representative  $1000\ \mu\text{m} \times 1000\ \mu\text{m}$  section of the sample were used for analysis. Approximate regions of C-(N)-A-S-H are determined from (Walkley, 2016).

### 5.3.7 Solid-state MAS NMR spectroscopy analysis

#### $^{27}\text{Al}$ MAS NMR spectroscopy

Figure 5-13 shows the  $^{27}\text{Al}$  MAS NMR spectra of the NASH sample and C(N)ASH sample before and after exposure to acid attack. From Figure 5-13 (a), the unexposed NASH sample consisted of one main resonance centered at 55 ppm, which was assigned to aluminium in tetrahedral ( $\text{Al}^{\text{IV}}$ ) coordination (Walkley, 2016). The  $\text{Al}^{\text{IV}}$  was assigned in a  $q^4$  (i.e.,  $q^4 = \text{Si}$  is in tetrahedral coordination and bonded to 4 other tetrahedral atoms) environment within a highly polymerized N-A-S-H gel framework (Duxson et al., 2005a, Longhi et al., 2019). A low-intensity resonance at  $\delta_{\text{obs}} = 4$  ppm was attributed to octahedral ( $\text{Al}^{\text{VI}}$ ) coordination in the unreacted precursor (Walkley, 2016). The spectra of precursor powder was typical of those commonly observed for aluminosilicate glasses, displaying three broad peaks which are assigned to tetrahedral ( $\text{Al}^{\text{IV}}$ ), pentahedral ( $\text{Al}^{\text{V}}$ ), and octahedral ( $\text{Al}^{\text{VI}}$ ) aluminium (Walkley, 2016). During the alkali-activation process,  $\text{Al}^{\text{V}}$  and  $\text{Al}^{\text{VI}}$  within precursor powder dissolved and reacted to form  $\text{Al}^{\text{IV}}$  species (Duxson et al., 2005a). After exposure to acid attack for 28 days, the exposed NASH sample showed two narrow resonances centered at -1 ppm and -4.6 ppm, respectively, which were both assigned to  $\text{Al}^{\text{VI}}$  in a well-defined octahedral coordination (Walkley, 2016). This was consistent with greater stability of

$\text{Al}^{\text{VI}}$  species under acidic conditions when compared to  $\text{Al}^{\text{IV}}$  and  $\text{Al}^{\text{V}}$  species (Longhi et al., 2019). In view of the above results, the dealumination and sodium removal from the N-A-S-H gel resulted in the decomposition of the solid phase in the NASH sample.

The spectra of the unexposed C(N)ASH sample displayed a broad resonance spanning from 20 ppm to 80 ppm and centered at approximately 58 ppm, which was assigned to tetrahedral ( $\text{Al}^{\text{IV}}$ ) coordination in geopolymer binder (Walkley, 2016). The broad contribution of  $q^4(4\text{Si})$  species indicated a significant crosslinking of C-(N)-A-S-H gel (Walkley, 2016). The spectra of the exposed C(N)ASH sample showed a narrow resonance at approximately 0 ppm which was assigned to  $\text{Al}^{\text{VI}}$  in well-defined octahedral coordination, as well remained a low-intensity broad resonance spanning from 40 ppm to 60 ppm as shown in Figure 5-13 (b). The formation of aluminium sulphate was contributed to the resonance at around 0 ppm. The resonance at 50 ppm was assigned to the tetrahedral ( $\text{Al}^{\text{IV}}$ ) coordination in the residual C-(N)-A-S-H gel.

The broad resonance of  $^{27}\text{Al}$  MAS NMR spectra of the NASH sample and C(N)ASH sample before exposure to acid attack suggested that Al predominantly existed in a distorted tetrahedral environment  $q^4(4\text{Si})$  in both N-A-S-H gel and C-(N)-A-S-H gel. However, the resonance of Al in the C-(N)-A-S-H gel showed slightly wider than that in the N-A-S-H gel. It means more complicated Al environment in the C-(N)-A-S-H gel. After exposure to sulphuric acid, the Al environment in the N-A-S-H gel was easily attacked and combined Al was converted into movable ions. There was no remaining undamaged Al environment and the Al in the residual sample was in an active state. It could be seen that a part of original Al environment in the C-(N)-A-S-H gel was undamaged by acid attack, and less active Al was identified than N-A-S-H gel. When combined with the appearance change, it was found that, whereas the appearance of the NASH sample had not altered significantly, the N-A-S-H gel had been completely destroyed. Even though the C(N)ASH sample had cracks, a portion of the C-(N)-A-S-H gel persisted.

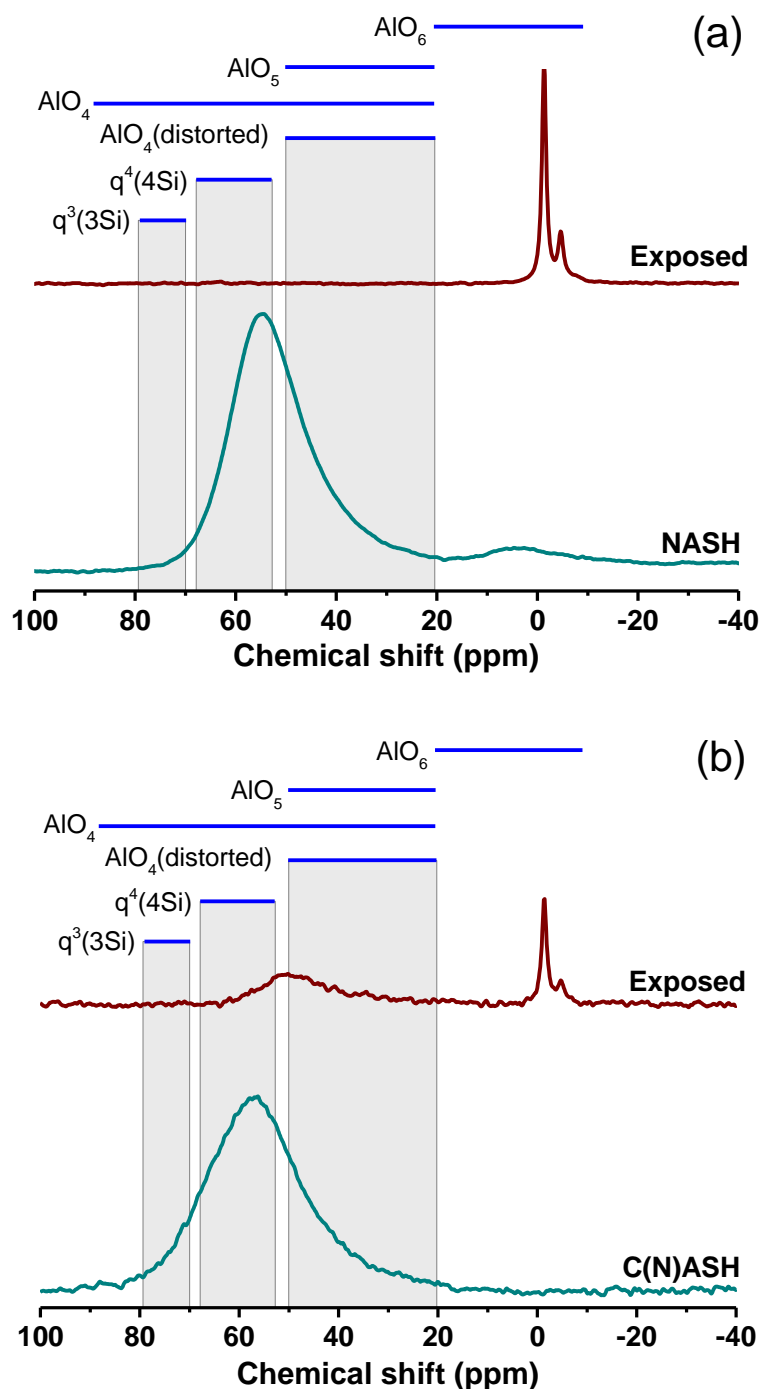


Figure 5-13.  $^{27}\text{Al}$  MAS NMR data of the NASH sample and C(N)ASH sample before and after exposure to sulphuric acid attack.

### $^{29}\text{Si}$ MAS NMR spectroscopy

The  $^{29}\text{Si}$  MAS NMR spectra and deconvoluted peaks for the NASH sample and C(N)ASH sample before and after exposed to sulphuric acid are presented in Figure 5-14 and Figure 5-15. According to (Walkley and Provis, 2019), Si sites were generally identified using the notation of the type  $Q^n(m\text{Al})$  with  $0 \leq m \leq n \leq 4$ , where

Si in tetrahedral coordination (represented by Q) was bonded to  $n$  other tetrahedral units ( $m$  is the number of Al) via oxygen bridges. The summary of the deconvolution peaks is shown in Table 5-3.

As shown in Figure 5-14 (a), the  $^{29}\text{Si}$  MAS NMR spectra of the unexposed NASH sample was deconvoluted into eight peaks which indicating Si environments attributed to  $\text{Q}^4(0\text{Al})$ ,  $\text{Q}^4(1\text{Al})$ ,  $\text{Q}^4(2\text{Al})$ ,  $\text{Q}^4(3\text{Al})$ ,  $\text{Q}^3$ ,  $\text{Q}^2$ ,  $\text{Q}^2(1\text{Al})$  and  $\text{Q}^0$ , in agreement with other studies (Walkley, 2016, Myers et al., 2013, Cao et al., 2021a). The  $\text{Q}^0$  resonance might be attributed to dissolved precursors or monomer silicate structures from remnant soluble silicate that has not react (Longhi et al., 2019). The  $\text{Q}^3$  and  $\text{Q}^2$  sites resonate exists in this study. This is contradictory with the results of N-A-S-H gel derived from metakaolin (Longhi et al., 2019). There is no  $\text{Q}^1$  site in the spectra of the unexposed NASH sample. The results indicate that the framework of N-A-S-H is highly polymerised (Myers et al., 2013). After exposure to acid attack, the deconvoluted peaks of the exposed NASH sample are contributed to  $\text{Q}^3(1\text{Al})$ ,  $\text{Q}^4(3\text{Al})$ ,  $\text{Q}^4(2\text{Al})$ ,  $\text{Q}^4(1\text{Al})$  and  $\text{Q}^4(0\text{Al})$  sites. There is no  $\text{Q}^2$ ,  $\text{Q}^1$ , and  $\text{Q}^0$  sites remained in the residual gel. It should be noted that there is no Al in tetrahedral coordination from  $^{27}\text{Al}$  MAS NMR data (presented above) in the exposed NASH sample. This is because that part of the  $[\text{AlO}_4]$  tetrahedrons detach from Si-O-Al bond under acid attack and leach out from the framework of N-A-S-H gel. And part of the  $[\text{AlO}_4]$  tetrahedrons transfer to octahedrons that Al in six coordination and incorporate into the Si-O-Al bond in the residual gels. This increases the polymerization of residual gels.

Engelhardt's formula (Equation 5-4) was used to calculate the molar Si/Al ratio of the N-A-S-H gel before and after exposure to sulphuric acid in the NASH sample (Longhi et al., 2019). The Si/Al ratio of the unexposed NASH sample is 1.9 while increased to 2.3 after exposure to sulphuric acid. The results show that the dealumination of N-A-S-H gel is along with a higher Si/Al ratio in residual gel and higher polymerization.

$$\frac{\text{Si}}{\text{Al}} = \frac{\sum_{m=1}^4 I_{A_{\text{Q}^4(m\text{Al})}}}{\sum_{m=1}^4 0.25 \times m \times I_{A_{\text{Q}^4(m\text{Al})}}} \quad \text{Equation 5-4}$$

Where,  $I_{A_{\text{Q}^4(m\text{Al})}}$  is the normalized relative integral areas of each deconvoluted  $\text{Q}^4(m\text{Al})$  peaks as shown in Table 5-3.

The  $^{29}\text{Si}$  MAS NMR spectra and deconvoluted peaks of the unexposed C(N)ASH sample and exposed C(N)ASH sample are presented in Figure 5-15. The  $^{29}\text{Si}$  MAS NMR spectra of the unexposed C(N)ASH sample displays a relative narrowing resonance spanning from -70 to -100 ppm, which were deconvoluted into peaks at -98, -95, -92, -87, -84, -80, and -76 ppm, attributed to  $\text{Q}^4(3\text{Al})$ ,  $\text{Q}^4(4\text{Al})$ ,  $\text{Q}^3$ ,  $\text{Q}^3(1\text{Al})$ ,  $\text{Q}^2$ ,  $\text{Q}^2(1\text{Al})$ ,  $\text{Q}^1$ , and  $\text{Q}^0$ , respectively. The reduced width of resonance and the increased intensity of  $\text{Q}^2$ ,  $\text{Q}^1$ , and  $\text{Q}^0$  sites suggested that the C-(N)-A-S-H gel showed higher order than the N-A-S-H gel (in agreement with XRD analysis). The chemical shifting to lower field indicates the change of Si environments due to  $\text{Q}^4(\text{mAl})$  loss in the exposed C(N)ASH sample. This also confirms the dealumination mechanism of C-(N)-A-S-H gel as discussed above.

According to (Myers et al., 2013), the MCL and molar Si/Al ratio of the non-crosslinked and crosslinked C-(N)-A-S-H gel can be determined based on the following equations (Equation 5-5 to Equation 5-8):

$$\text{MCL}_{[\text{NC}]} = \frac{2I_A[\text{Q}^1 + \text{Q}^2 + \frac{3}{2}\text{Q}^2(1\text{Al})]}{I_A(\text{Q}^1)} \quad \text{Equation 5-5}$$

$$\frac{\text{Si}}{\text{Al}_{[\text{NC}]}} = \frac{2I_A[\text{Q}^1 + \text{Q}^2 + \text{Q}^2(1\text{Al})]}{I_A[\text{Q}^2(1\text{Al})]} \quad \text{Equation 5-6}$$

$$\text{MCL}_{[\text{C}]} = \frac{4I_A[\text{Q}^1 + \text{Q}^2 + \text{Q}^2(1\text{Al}) + \text{Q}^3 + 2\text{Q}^3(1\text{Al})]}{I_A(\text{Q}^1)} \quad \text{Equation 5-7}$$

$$\frac{\text{Si}}{\text{Al}_{[\text{C}]}} = \frac{I_A[\text{Q}^3(1\text{Al})]}{I_A[\text{Q}^1 + \text{Q}^2 + \text{Q}^2(1\text{Al}) + \text{Q}^3 + \text{Q}^3(1\text{Al})]} \quad \text{Equation 5-8}$$

where [C] denotes crosslinked C-(N)-A-S-H structures and [NC] denotes non-crosslinked C-(N)-A-S-H structures.

In the unexposed C(N)ASH sample, the MCL and Si/Al ratio of non-crosslinked C-(N)-A-S-H gel are 9.0 and 5.7, respectively. The synthetic C-(N)-A-S-H gel displays a similar MCL and Si/Al ratios as the alkali-activated fly ash/slag pastes, which showed a range of 6.43-9.76 for MCL and corresponding Si/Al ratio of 6.35-4.74 (Gao et al., 2017). After exposed to sulphuric acid, the MCL reduces to 6.7 and the Si/Al reduces to 3.3. The reduced MCL indicates the shorten of the framework in the non-crosslinked C-(N)-A-S-H gel after acid attack which is due to dealumination. The declined Si/Al ratio is due to the change of the coordination of Al from four to six,

which is consistent with the  $^{27}\text{Al}$  MAS NMR results. The MCL and Si/Al ratio of the crosslinked C-(N)-A-S-H gel increase from 22 to 26 and from 0.13 to 0.45, respectively, after exposed to sulphuric acid solution. The acid attack caused increment of crosslinked C-(N)-A-S-H gel with minor changes in the chain length. However, the exposed C-(N)-A-S-H gel shows a similar framework like N-A-S-H gel, which could be seen from the high intensity of  $Q^4(\text{mAl})$  resonance, as shown in Figure 5-15 (b). Thus, the Si/Al ratio calculated based on Engelhardt's formula (Equation 5-4) is 3.8, which is higher than that of the exposed N-A-S-H gel. The results confirm that the decalcification in C-(N)-A-S-H gel leads to a destruction of the orderly layered structure. Further exploration on the acid corrosion mechanism of the C-(N)-A-S-H gel could focus on the effect of Ca/Si ratio in this type of gel.

The N-A-S-H gel shows higher polymerization (higher MCL) and lower Si/Al than the C-(N)-A-S-H gel. After exposure to sulphuric acid, the exposed N-A-S-H gel showed increased polymerization and increased Si/Al ratio due to the dealumination, while the C-(N)-A-S-H gel increased crosslinking with reduced Si/Al ratio due to decalcification. The change of Si/Al ratio of the C-(N)-A-S-H gel is inconsistent with that from SEM-EDX results. This suggests that an elemental mapping characterization analysis on the bulk area of alkali-activated materials is hard to explain the intrinsic change of their reaction products. Overall, it is confirmed that the silicon chains in N-A-S-H gel and C-(N)-A-S-H gel tend to form highly crosslinked silica framework after sulphuric acid.

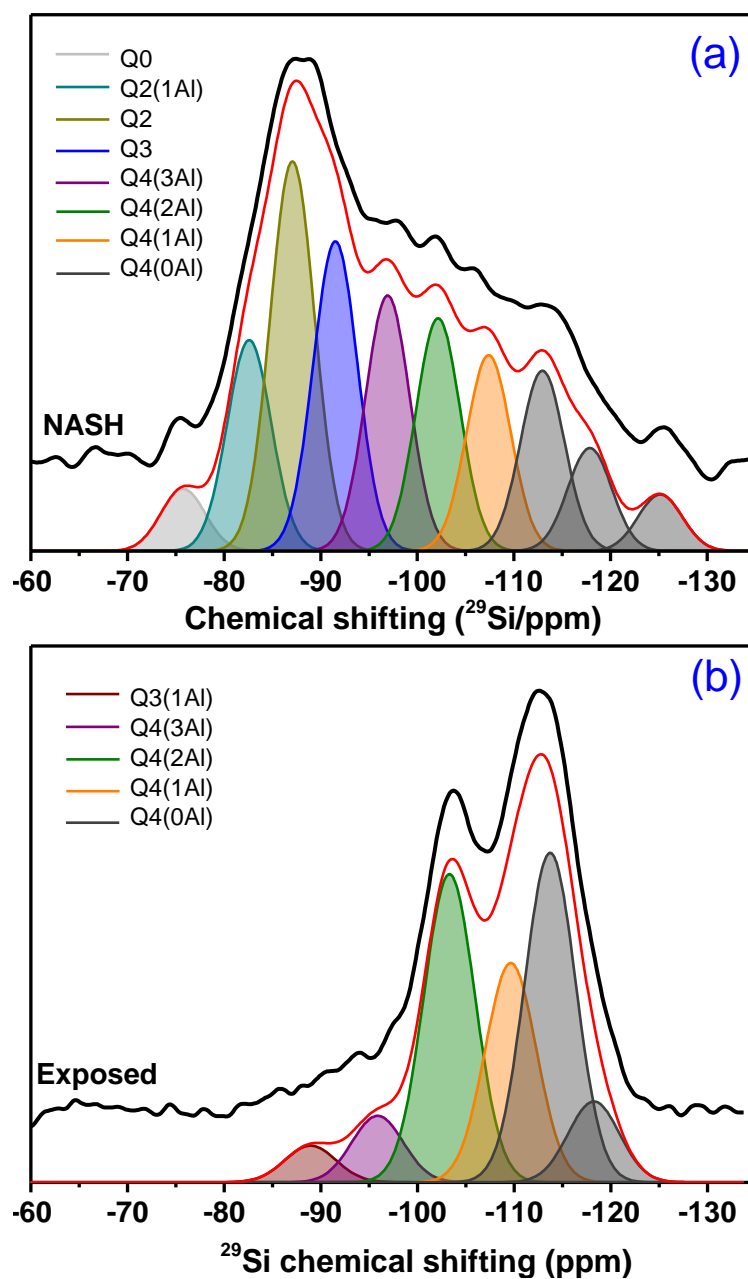


Figure 5-14.  $^{29}\text{Si}$  MAS NMR data (black lines) of (a) the unexposed NASH sample and (b) the exposed NASH sample after 28 days of sulphuric acid attack. The fitting line (red) of the spectra for the samples and associated spectral deconvolutions are also shown.

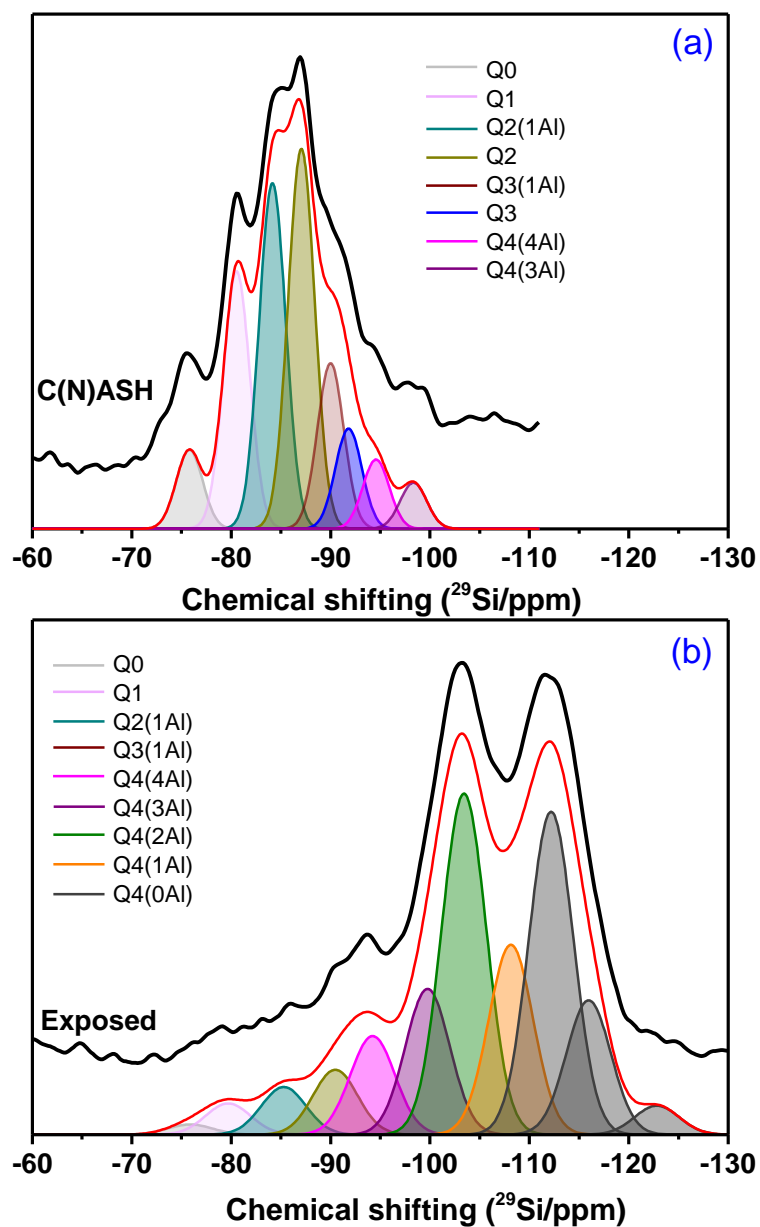


Figure 5-15.  $^{29}\text{Si}$  MAS NMR data (black lines) of (a) the unexposed C(N)ASH sample and (b) the exposed C(N)ASH sample after 28 days of sulphuric acid attack. The fitting line (red) of the spectra for the samples and associated spectral deconvolutions are also shown.

Table 5-3 Deconvolution results of <sup>29</sup>Si NMR spectra for the NASH sample and C(N)ASH sample before and after exposed to sulphuric acid. The IA (%) is the normalized relative integral area of each deconvoluted resonance in the spectra.

Sample	Coordination	Q <sup>0</sup>	Q <sup>1</sup>	Q <sup>2</sup> (1Al)	Q <sup>2</sup>	Q <sup>3</sup> (1Al)	Q <sup>3</sup>	Q <sup>4</sup> (4Al)	Q <sup>4</sup> (3Al)	Q <sup>4</sup> (2Al)	Q <sup>4</sup> (1Al)	Q <sup>4</sup> (0Al)
NASH	Pos. (ppm)	-75	-	-83	-87	-	-92	-	-97	-102	-107	-113 - -125
	I <sub>A</sub> (%)	3.1	-	10.6	19.5	-	15.5	-	12.8	11.7	9.8	17
Exposed NASH	Pos. (ppm)	-	-	-	-	-89	-	-	-96	-103	-107	-110 - -118
	I <sub>A</sub> (%)	-	-	-	-	3.5	-	-	6.4	29.6	21.1	39.5
C(N)ASH	Pos. (ppm)	-76	-80	-84	-87	-90	-92	-95	-98	-	-	-
	I <sub>A</sub> (%)	5.5	17.8	24.0	26.3	11.5	6.9	4.8	3.2	-	-	-
Exposed C(N)ASH	Pos. (ppm)	-76	-80	-85	-	-90	-	-94	-100	-103	-108	-112 - -123
	I <sub>A</sub> (%)	0.7	2.2	3.4	-	4.6	-	7.0	10.3	24.1	13.4	34.3

## 5.4 Concluding remarks

In this study, stoichiometrically controlled N-A-S-H and C-(N)-A-S-H gels were used to investigate the durability properties of two typical types of AAMs under sulphuric acid attack, i.e., calcium free/low calcium AAMs (alkali-activated fly ash) and calcium bearing AAMs (alkali-activated slag). It was discovered that dealumination dominated the microstructural change of N-A-S-H gel under the sulphuric acid attack. This dealumination had minor effect on the bulk structure integrity (but not sure about the impact on micromechanical properties). The C-(N)-A-S-H gel showed both dealumination and decalcification, together with significant and rapid loss of sodium and slow loss of silicon. In addition to the normal mechanism that gypsum forms and leads to cracking at sulphuric and sulphate conditions, an important finding is that dealumination and the loss of sodium continues after decalcification and the loss of a small amount of silicon. The non-crosslinked C-(N)-A-S-H gel reduced with decrease of Si/Al ratio after exposure to sulphuric acid, while the Si/Al ratio of N-A-S-H gel increased. One common feature for the two types of AAM gels is that after acid attack, silicate polymerization degree ( $Q^4$  concentration) increases, especially for C-(N)-A-S-H gel. Further exploration on the acid corrosion mechanism of the C-(N)-A-S-H gel could focus on the effect of Ca/Si ratio. However, the formation of coarse crystalline gypsum grains is still the controlling factor to structural destroy and needs to be controlled.

## CHAPTER 6. PHASE EVOLUTION OF C-(N)-A-S-H/N-A-S-H GELS BY SULPHURIC ACID ATTACK

### 6.1 Introduction

The degradation mechanism of conventional Portland cement (PC) in the aggressive environment is the main aspect of durability research driven by the expanding market need for constructions with long service life and minimal maintenance (Beushausen et al., 2019). The deterioration of PC concrete sewer pipes in acidic environments is one of the primary factors of poor durability (Taheri et al., 2020). For example, the microbially induced sulphuric acid corrosion of concrete pipes in the sewer systems can cause the degradation of microstructure and performance failure, reducing the service life (Sterling et al., 2010). Acid corrosion also occurs in other scenarios where concretes contact with aggressive acidic media, such as in fertiliser production and metal finishing process (Lloyd et al., 2010).

Sulphuric acid corrosion of PC concrete has been illustrated by the reaction between  $H^+$  and  $SO_4^{2-}$  from acid solution and calcium hydroxide (CH) in concrete, resulting in a decline of pH value of concrete at the beginning, then decomposition of calcium silicate hydrate (C-S-H) gel (Ahmad Muhd Izzat, 2013). The gypsum and ettringite are deposited at the surface and inside the pores of concrete due to the reaction between diffusing  $SO_4^{2-}$  anions from sulphuric acid and  $Ca^{2+}$  cations. The formation of expansive products is the direct inducement of peeling off and strength reduction of concrete.

In addition to the permeability of concrete, the CH of hydrated cement paste could be the main factor that determines the degradation in the acid environment (Cao et al., 2021a). Reducing CH content in PC concrete is thus considered to be an effective way to improve acid resistance (Yuan et al., 2013, Cao et al., 2021a). There are two approaches to reduce the calcium hydroxide content in concrete, including (1) partial replacement of PC by supplementary cementitious materials, like fly ash and blast furnace slag, and (2) entire replacement by alternative binders, such as alkali-activated materials (AAMs) (Aiken et al., 2017, Aydın and Baradan, 2014, Cao et al., 2020, Li et al., 2019). The partial replacement of PC by SCMs results in the consumption of CH and the incorporation of additional Al in C-S-H, forming C-A-S-H gel (Skibsted

and Andersen, 2013). There is no CH forming for AAMs derived from low calcium or free calcium precursors. When high calcium bearing precursors are used, sodium-containing C-(N)-A-S-H is formed in AAMs (Cao et al., 2020).

AAMs with relatively less calcium content ( $\text{Ca/Si} \approx 1.0$ ) than PC ( $1.5 < \text{Ca/Si} < 2$ ) attract more and more interest because of their lower environmental footprint and comparable or even better acid resistance (Zhang et al., 2017, Provis et al., 2015, Davidovits, 2008, Ahmad Muhd Izzat, 2013). The alkalinity of AAMs is higher than PC which could help to mitigate the pH drop of the pore solution (Bernal and Provis, 2014). However, many different raw materials which contain varying concentrations of  $\text{SiO}_2$ ,  $\text{CaO}$  and  $\text{Al}_2\text{O}_3$  are used as precursors. The reaction products in AAMs are well known for their large variation. It is an advantage because various industrial materials locally available can be used, but it is also a problem as the challenges sit in standardization and performance prediction. Hence, understanding the mechanism of sulphuric acid attack on AAMs with different cations ratios (e.g.  $\text{Ca/Si}$  and  $\text{Si/Al}$  ratios) is important to optimize mix design, thereby promoting its wide application and achieving the environmental benefit by reducing the  $\text{CO}_2$  emissions (Shi et al., 2019).

Many variables including precursors, activators, acid type, and acid severity have been involved to investigate the acid resistance of AAMs (Provis and Van Deventer, 2014). The performance (i.e., residual compressive strength and structural integrity) of AAMs derived from fly ashes were superior to OPC when exposed to 2% sulphuric acid. The more stable cross-linked N-A-S-H gel had higher resistance to acid attack than C-S-H gel. The increased slag content in alkali-activated fly ash and slag binders was found to result in high losses of weight and compressive strength under a sulphuric acid environment (Aiken et al., 2018). This means that increasing C-(N)-A-S-H gel content with the increased incorporation ratio of slag has a detrimental effect on the sulphuric acid resistance of AAMs (Aiken et al., 2018). However, the increased calcium content as slag content increases leads to an increased porosity when samples are exposed to sulphuric acid (Provis et al., 2012). The increased porosity of samples is harmful to the strength (Ourgessa et al., 2019). Whether N-A-S-H gel or C-(N)-A-S-H gel is more resistant to dissolution in acidic conditions, it is still ambiguous. The influence of interaction between N-A-S-H and C-(N)-A-S-H gels in AAMs on acid resistance is barely reported before.

The attack of sulphuric acid on AAMs was demonstrated in (Aiken et al., 2018): a) ions from acid solution penetrate into the sample, while moveable sodium cations leach from the sample into the solution; b) the Si-O-Al bonds are attacked by hydrogen protons ( $H^+$ ,  $H_3O^+$ ), causing Al to break away from the bonds, leaving a siliceous framework; c) gypsum are formed in the penetrated layer due to the reaction between diffusing  $SO_4^{2-}$  anions and  $Ca^{2+}$ . However, there is very limited direct evidence regarding the decomposition and acid resistance of C-(N)-A-S-H and N-A-S-H gels in acidic environments. The literature reviews are frequently contradictory, and the majority of the experimental study contains many unknown factors.

To promote the application of AAMs in harsh acidic environments, it is critical to study the molecular structure evolution of these controlled alkali-activated gels during exposure to the acid solution, particularly on the coordination involving network and modifying cations. The objective of this study is therefore to investigate the decomposition mechanism of C-(N)-A-S-H/N-A-S-H gels in AAMs. To achieve this goal, the method of synthesising AAMs gels that allows strict stoichiometric control and retains actually alkali activation process is accepted (Walkley, 2016). This method has been shown feasible which needs to synthesise high-purity precursors first and then synthesise binder phases in the laboratory (Walkley et al., 2016a). The designed AAMs with strict Ca/Si and Si/Al ratios can be further used to investigate the decomposition mechanism of C-(N)-A-S-H/N-A-S-H gels (Walkley et al., 2016b).

## **6.2 Materials and methods**

### **6.2.1 Raw materials and alkali-activated gels manufacture**

‘Pure’ precursor powder used in this study was synthesised via a verified sol-gel process (Walkley et al., 2016b). As shown in Table 6-1, the designed Al/Si ratios and Ca/(Al + Si) ratios in the low calcium samples aims to span the range of bulk ratios observed in many sodium silicate solutions activated slag systems ( $Al/Si \leq 0.25$  and  $0.67 \leq Ca/(Al + Si) \leq 1.2$ ) (Bernal et al., 2011a). High calcium samples were designed with a higher Ca/(Al + Si) ratio which was close to the ratio observed in conventional PC (Taylor, 1997).

The sodium silicate solution collected from PQ Australian with 14.7% of  $Na_2O$  (in mass) and 29.4% of  $SiO_2$  was first mixed with distilled water, and then the sodium

hydroxide pellets (99 wt.%, Sigma-Aldrich) was dissolved in the above solution. The modulus ( $\text{SiO}_2/\text{Na}_2\text{O}$ ) of the activator was fixed at 1.0, and the alkali content ( $\text{Na}_2\text{O}$ ) was 4 wt.% of the precursor powders. Table 6-1 presents the mixture proportions of the investigated binders. The activating solution was prepared 24 hours before mixing with precursors to avoid the influence of dissolution heat. The activating solution was added into and mixed with the precursor powder for 3 minutes and then the homogeneous paste was cast into cylinders ( $r \times h = 10 \text{ mm} \times 20\text{mm}$ ). All samples were cured in the sealed cylinders until further testing.

According to the Ca/Si and Al/Si ratios as shown in Table 6-1, the four synthesised pastes were categorized as low-Ca high-Al (LCHA), high-Ca high-Al (HCHA), low-Ca low-Al (LCLA), and high-Ca-low Al (HCLA). The LCHA and LCLA are expected to form N-A-S-H gels in addition to non-crosslinked C-(N)-A-S-H gel, while sample HCHA is expected to form crosslinked C-(N)-A-S-H gel and sample HCLA is expected to form C-A-S-H gel in addition to C-(N)-A-S-H/N-A-S-H gels (Myers et al., 2015a, Walkley et al., 2016c). At nanoscale or below, the sodium-containing C-(N)-A-S-H gel shows a similar structure like C-S-H and C-A-S-H gel in PC, which are usually described as Tobermorite structure that contains Ca-O octahedron chain and. There are more Al tetrahedrons that are substituted into the paired sites of Si-O tetrahedron chains (Schilling et al., 1994). N-A-S-H gel generated from Ca-free or low-Ca calcium systems shows a similar structure to nanocrystalline zeolite, in which Si or Al tetrahedrons are connected to form a frame structure by sharing one oxygen atom (Provis et al., 2005b). Both C-(N)-A-S-H and N-A-S-H are X-ray diffraction amorphous and their exact contents in AAMs depend on the calcium and aluminium contents of precursors (Duxson et al., 2007a). N-A-S-H gel displays high crosslinking in the Al-rich Ca-less systems, while the crosslinking of C-(N)-A-S-H gel reduces as increasing the Al content (Walkley et al., 2016c). These four pastes in this study are representative of the products in alkali-activated slag blending with various amounts of metakaolin or fly ash that are common practices in the industry.

Table 6-1 Measured formula (*mol %*) by XRF of the precursor powders and each binder.

Sample ID	Precursor powders	Composition ratio of binders				
		w/s	Ca/(Al + Si)	Na/Al	Al/Si	Ca/Si
LCHA	0.998CaO·SiO <sub>2</sub> ·0.147Al <sub>2</sub> O <sub>3</sub>	0.75	0.85	0.51	0.16	0.99
HCHA	1.731CaO·SiO <sub>2</sub> ·0.148Al <sub>2</sub> O <sub>3</sub>	0.75	1.44	0.69	0.16	1.67
LCLA	0.958CaO·SiO <sub>2</sub> ·0.046Al <sub>2</sub> O <sub>3</sub>	0.75	0.91	1.53	0.05	0.95
HCLA	1.264CaO·SiO <sub>2</sub> ·0.041Al <sub>2</sub> O <sub>3</sub>	0.75	1.19	1.96	0.04	1.24

### 6.2.2 Acid corrosion test

Immersion test in sulphuric acid solution is adapted as acid corrosion method that following the basic guidelines in ASTM C267 (Aiken et al., 2018). Samples were cured for 120 days to be fully hydrated and then were submerged in 3% sulphuric acid solutions individually with an acid solution to sample mass ratio of 20. Samples submerged in distilled water were references. The pH value and cumulative leaching cations (i.e., Na, Si, Al, and Ca) of each solution were tested and recorded at predetermined intervals of 1, 3, 7, 28, and 56 days. The corroded sample from the acid solution was dried at 60 °C vacuum oven for around 6 hours. The weight of the dried samples before and after being immersed into sulphuric acid solution was recorded. The dried samples were hand-grinded with a pestle and mortar for characterisation analysis.

### 6.2.3 Characterisation analysis

The details about characterisation techniques such as X-ray diffraction, thermogravimetric analysis, Fourier transform infrared spectroscopy, and magic angle spinning (MAS) NMR spectra used in this study refer to the previous publication in (Wang et al., 2021b). The peak deconvolution of the MAS NMR spectrum was carried by Origin software in Gaussian mode and the assignments of deconvoluted peaks are based on (Gao et al., 2017).

## 6.3 Results

### 6.3.1 Leaching behavior

The pH values evolution of the distilled water with immersing samples is shown in Figure 6-1. The start pH value of the distilled water before immersing samples is 6.0 and the pH values of all samples increase immediately over 11 after the first 24-hour immersion and show minor change thereafter. It is clear that the ions (Na<sup>+</sup> and OH<sup>-</sup>) transfer from samples into the distilled water causing the increment of pH values as

alkaline activating solutions are used. The pH values of distilled water for soaking high calcium samples (HCHA and HCLA) are slightly higher than that of low calcium samples (LCHA and LCLA). This trend is hard to identify for AAMs derived from raw materials like fly ash or slag due to the influence of impurities. The higher pH values for high calcium samples suggest the higher availability and mobility of alkalis in the samples.

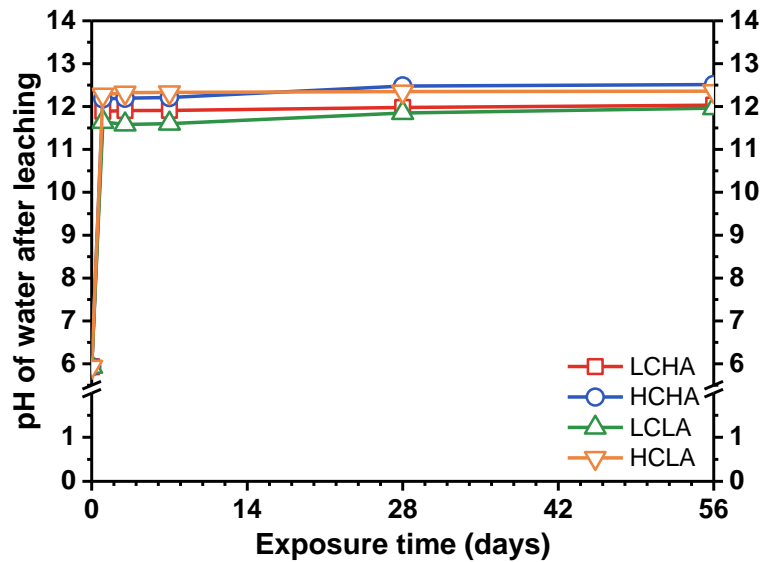


Figure 6-1. The pH value of distilled water with immersed samples during 56 days exposure.

The evolution of pH value of the 3% sulphuric acid solutions with immersing samples is shown in Figure 6-2, while the initial pH is 0.6. The pH values for each mix increase slowly to approximately 1.5 after 7 days of exposure. After 56 days of exposure, the pH value of the acid solution which soaking sample LCHA increases to around 2, while that of the other three samples reaches around 3. The lowest pH value of the acid solutions for immersing sample LCHA suggests that it has the lowest neutralizing capacity in sulphuric acid solution. This is due to that the sample LCHA consumes a large amount of alkali to participate in the hydration reaction, which is consistent with the previous finding (Provis and Van Deventer, 2007).

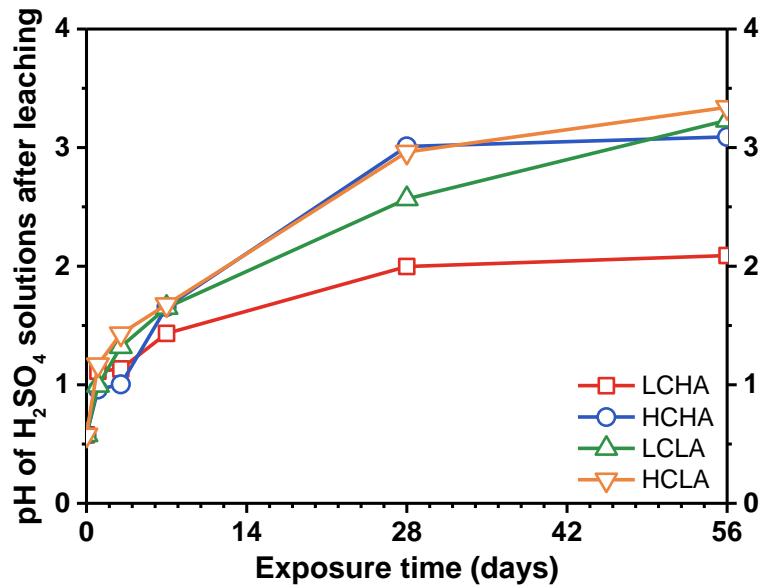


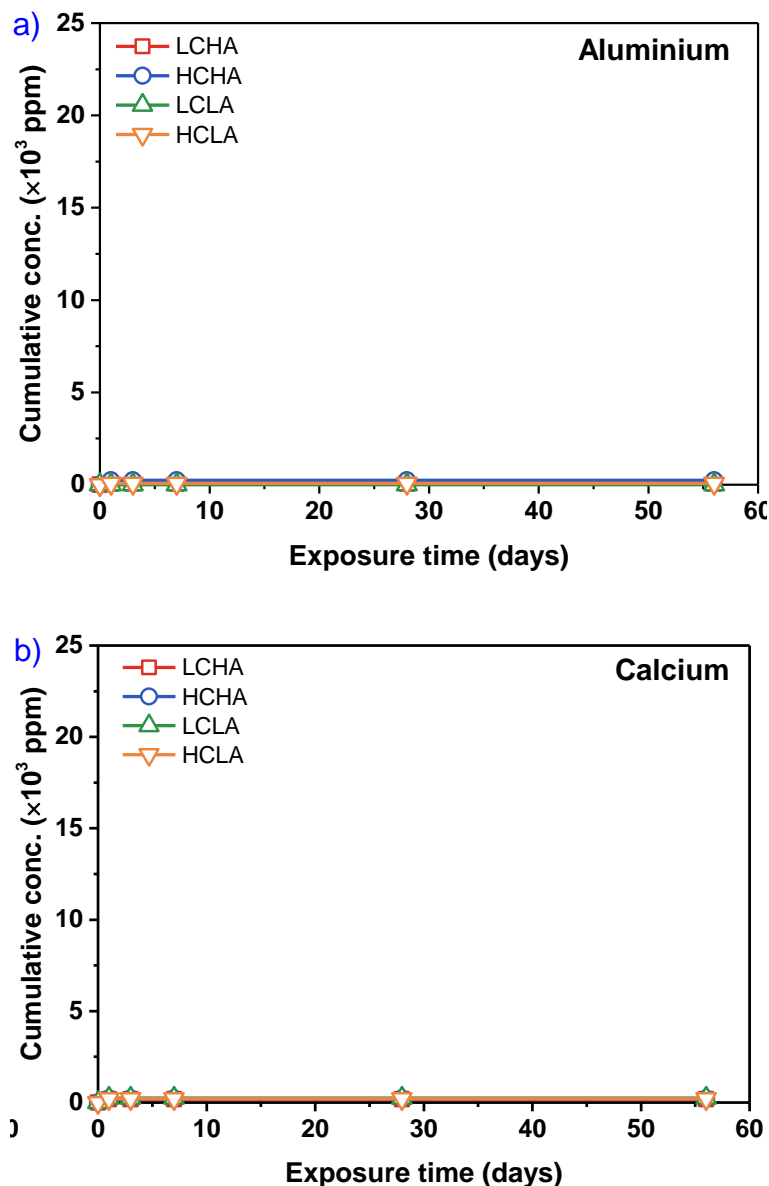
Figure 6-2. The pH value of 3% sulphuric acid solutions with immersed samples during 56 days exposure.

The cumulative concentration of each cation (aluminium, calcium, sodium, and silicon) in distilled water with immersing samples is shown in Figure 6-3. The cumulative concentration of aluminium and calcium cations in the distilled water is less than 75 and 236 ppm, respectively, which are negligible compared to sodium and silicon. This suggests that the aluminium and calcium are hard to dissolve from samples when exposed to water. On the other hand, sodium and silicon are the main leached elements in the water leachates. This is due to the high availability of sodium and silicon from activating solutions which are prepared by sodium silicate solution and sodium hydroxide and sodium have higher mobility compared to the other cations.

In Figure 6-3 c, Al-rich samples LCHA and HCHA exhibit lower concentrations of sodium than samples LCLA and HCLA. As known, free Na cations present in the macroscopic pores or gel pores are easily diffused out from samples when immersed into solutions (Huang et al., 2018). The substitution of  $[\text{SiO}_4]^{4-}$  tetrahedrons by  $[\text{AlO}_4]^{5-}$  tetrahedrons combined the Na cations in the gel framework to balance the negative (Walkley, 2016). The combined Na cations which are incorporated into the C-(N)-A-S-H/N-A-S-H gels in the AAMs are relatively difficult to diffuse. The decreased sodium concentrations for the Al-rich samples indicate that less leachable  $\text{Na}^+$  cations are available in the pastes. It is confirmed that the higher aluminium contents in the samples LCHA and HCHA could help to impede  $\text{Na}^+$  leaching, which

is due to the formation of a great quantity of Al-substituted C-(N)-A-S-H/N-A-S-H gels in the samples.

Figure 6-3 d displays the detected silicon in the water leachates. Silicon acts as the main ‘former’ element of the three-dimensional aluminosilicate framework of the C-(N)-A-S-H/N-A-S-H gels (Walkley, 2016). The sample LCLA displays the highest leaching concentration of silicon (i.e., 3973 ppm), while insignificant silicon leaching was identified in the other three samples (< 182, 680, and 133 ppm, respectively). It seems that inadequate calcium and aluminium in sample LCLA formed fewer reaction products (or they may have higher solubility, which is unlikely if silicon polymerized) along with deficient consumption of activators.



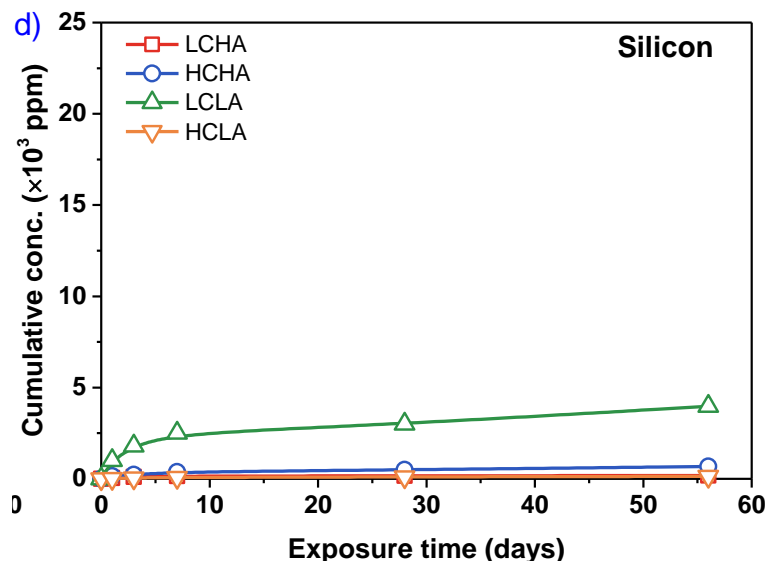
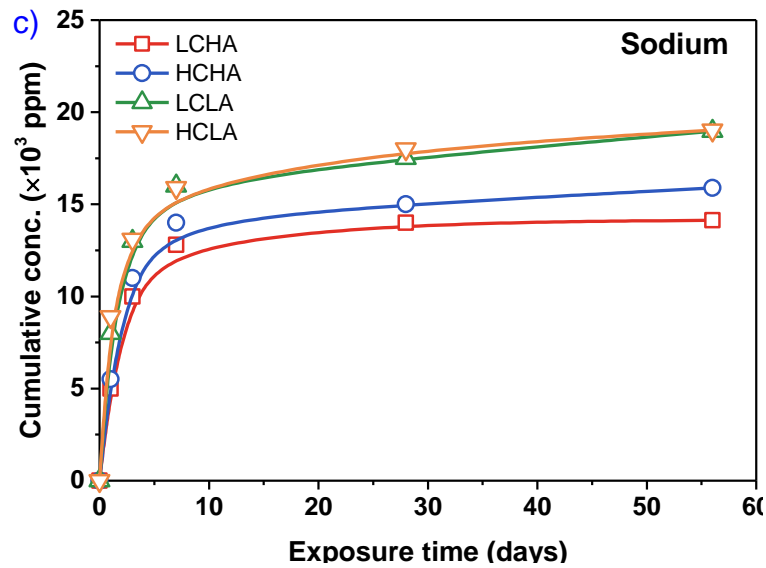


Figure 6-3. Cumulative concentrations of cations (aluminium, calcium, sodium, and silicon) in the distilled water with immersing samples.

Figure 6-4 displays the leaching amounts of aluminium, calcium, sodium, and silicon in the acid solutions. Significant higher concentrations of each cation are observed for samples exposed to the sulphuric acid compared to the distilled water. This is due to the acid attack that caused the reaction products to decompose and the sample to be damaged.

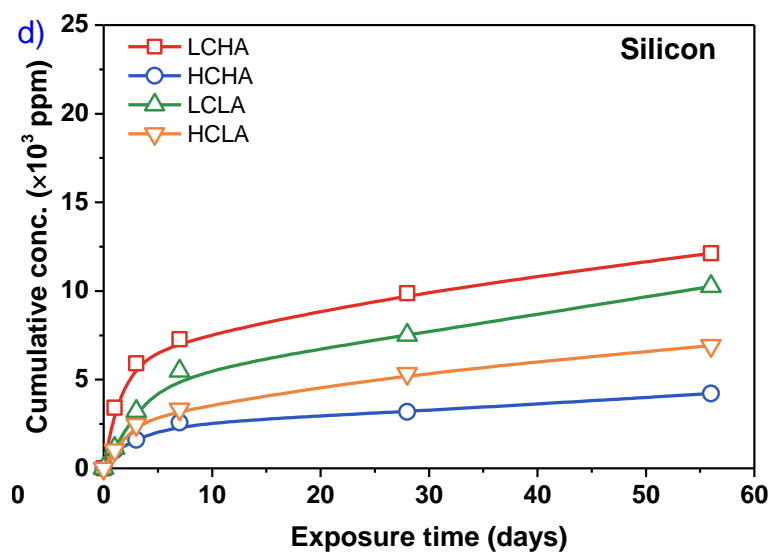
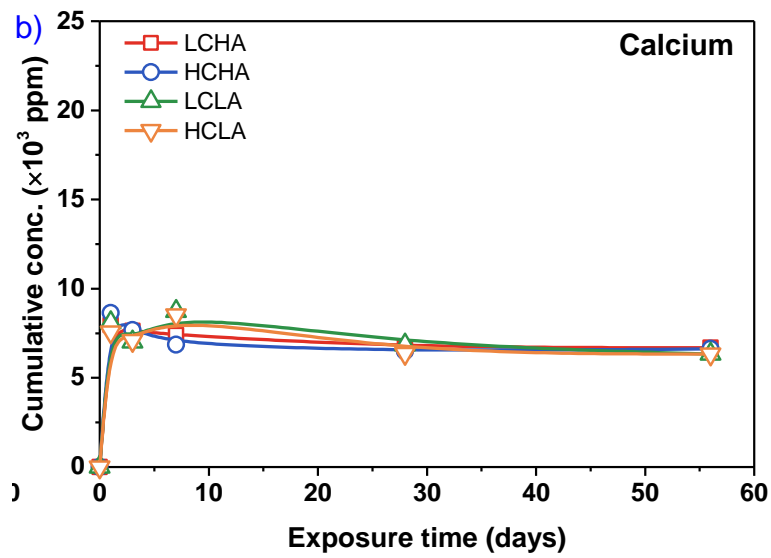
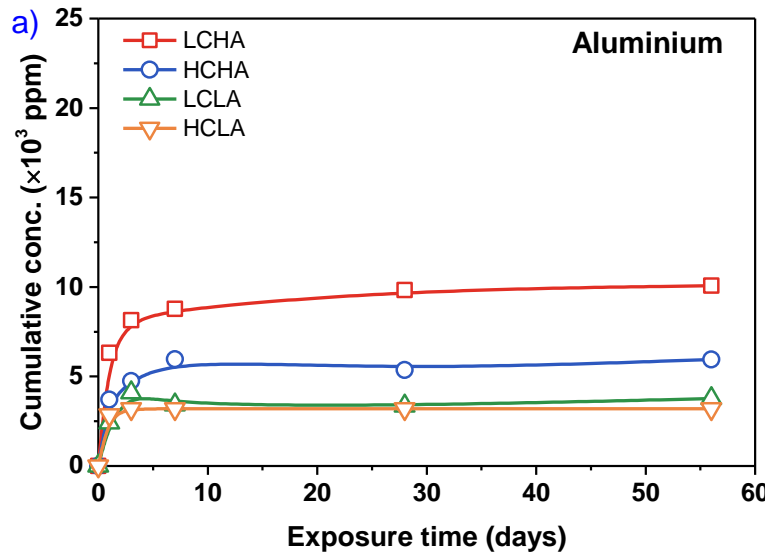
For aluminium, the sample LCHA exhibits the highest final concentration of 10078 ppm, followed by samples HCHA, LCLA, and HCLA of 6955, 4769, and 3665 ppm, respectively. The different concentrations of aluminium leaching out from the four samples during exposure to acid solutions is caused by the diversity of original

aluminium content in binders and the formed reaction products. Samples derived from Al-rich precursors leach a higher amount of Al. The samples with greater calcium content but the same aluminium content have less aluminium leaching (HCHA vs. LCHA, and HCLA vs. LCLA). A similar phenomenon is found by (Aiken et al., 2018) that the aluminium concentrations decrease as the slag contents increase. The reason has not been clearly stated in previous studies as the influence of the raw materials is unknown. The results in this study indicate that the reaction products in the high-calcium binders had better resistance to dealumination than that in low-calcium binders. Calcium has a positive effect against dealumination when alkali-activated materials are exposed to sulphuric acid.

For silicon, it increases at a relatively moderate rate in the exposure period in comparison to other elements. In other words, the silicon is constantly leaching from the sample during exposure to sulphuric acid. Sample LCHA reaches the highest cumulative concentration of silicon of 12417 ppm after 56 days of acid attack, followed by samples LCLA, HCLA, and HCHA of 10128, 6040, and 4997 ppm, respectively. In conclusion, samples derived from lower calcium precursors leach higher amount of silicon. This suggests that silicon in low calcium AAMs is more susceptible to acid attack.

For calcium, the concentrations reach approximately 7500 ppm for all the samples after the first day of exposure, regardless of their initial content and it maintains at this value thereafter. This is due to that the saturation point of calcium in sulphuric acid solution reached, which is consistent with (Aiken et al., 2018).

For sodium, sample HCLA reaches the highest concentration of 22328 ppm after 56 days of acid attack. The final sodium concentrations of the samples LCLA, HCHA, and LCHA are similar to that of distilled water (as shown in Figure 6-4 c). The leaching of sodium from the samples is driven by the concentration diffusion effect, whether in acid solution or water. The ions transfer of  $H^+$  or  $H_3O^+$  from sulphuric acid accelerates the diffusion process of sodium, but it has minor effect on the equilibrium concentration. Further research is necessary to confirm what the concentration of sample HCLA when exposed to sulphuric acid is higher than that exposed to water.



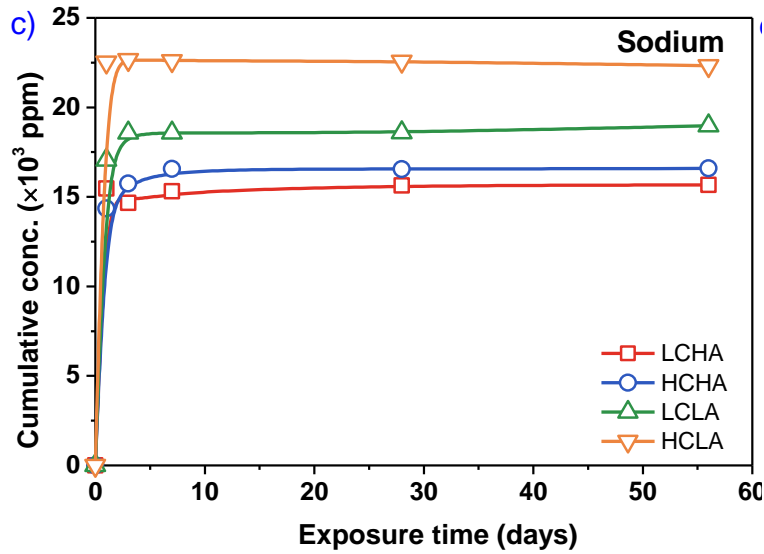


Figure 6-4. Cumulative concentrations of cations (aluminium, calcium, sodium, and silicon) in the 3% sulphuric acid with immersing samples.

The cation ratios of each mix exposed to the sulphuric acid solutions and the distilled water are summarized in Figure 6-5 and Figure 6-6. The Ca/Al cation ratios of each sample leached into water leachates are shown a magnitude higher than that in acid solution (see Figure 6-5). This is due to that the Al from each sample is relatively lower than Ca, although the contents of Ca and Al in water are both negligible. When exposed to sulphuric acid, the leaching amount of Al from each sample increases significantly. It can be observed that the Ca/Al ratios decrease as the exposure time increases. The Ca/Al ratios of samples HCHA and HCLA are higher than that of samples LCHA and LCLA, which confirms the positive effect of Ca against dealumination.

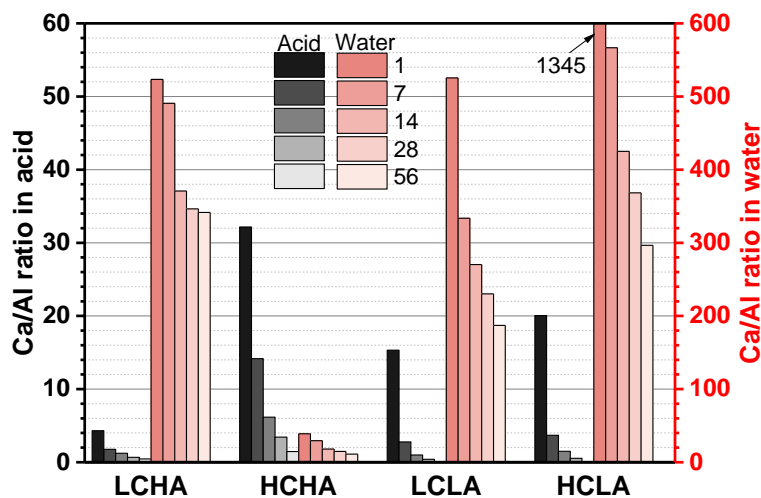


Figure 6-5. Ca/Al ratios of each sample leaching into the acid and water leachates.

Figure 6-6 shows the Ca/Si ratios of each sample leaching into the acid and water leachates. When the samples are exposed to distilled water, there is minor detected Ca and Si. When the samples are exposed to sulphuric acid, sample LCHA shows the lowest Ca/Si ratios while sample HCHA shows the highest ratios. The Ca/Si ratios are higher than the designed ratios for both samples, suggesting that the Ca is easier leaching out from samples than Si.

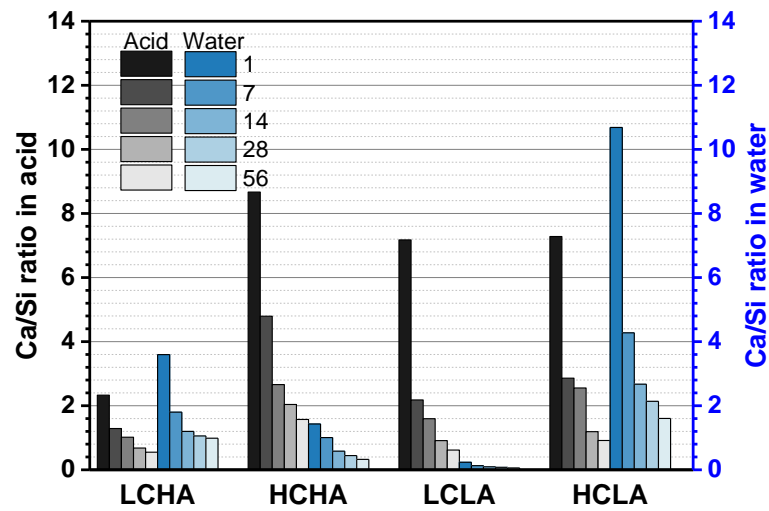


Figure 6-6. Ca/Si ratios of each sample leaching into the acid and water leachates.

### 6.3.2 X-ray diffraction (XRD)

Figure 6-7 shows the XRD patterns of the samples before and after exposure to sulphuric acid, while the unexposed samples displaying a broad featured diffraction hump centered at approximately  $29^\circ 2\theta$  (Figure 6-7 a), suggesting the presence of amorphous aluminosilicate phases (i.e. C-(N)-A-S-H/N-A-S-H gels) in the reaction products (Walkley et al., 2016b, Walkley et al., 2016c). In addition to the major amorphous phase, other crystalline phases were found. Calcite ( $\text{CaCO}_3$ , PDF # 81-2027), wollastonite phase ( $\text{CaSiO}_3$ , PDF # 84-0655), and pectolite phase ( $\text{NaCa}_2\text{HSi}_3\text{O}_9$ , PDF # 33-1223) were identified in all the samples. For high calcium binders HCHA and HCLA, the broad humps centered at approximately  $7^\circ 2\theta$  indicated the presence of vertumnite-like phase [ $\text{Ca}_4\text{Al}_2(\text{Si}_{2.89}\text{Al}_{2.23}\text{O}_{5.18}(\text{OH})_{21.88}(\text{H}_2\text{O})_{4.38}$ , PDF # 83-1522] and calcium alumina carbonate hydrate phase ( $\text{Ca}_4\text{Al}_2\text{O}_6\text{CO}_3 \cdot 11\text{H}_2\text{O}$ , PDF # 41-0219). The high Ca/Al ratio of the sample HCLA promoted the formation of vertumnite. The intensive peak at  $18^\circ 2\theta$  in sample HCHA was recognized as

portlandite ( $\text{Ca}(\text{OH})_2$ , PDF # 78-0315). The high intensity of the peak at  $11.8^\circ 2\theta$  in sample HCHA suggested the high crystallization degree of the calcium silicate phase. For low calcium samples LCHA and LCLA, the peak at around  $18^\circ 2\theta$  was identified as a zeolite-like phase ( $\text{Na}_{12}\text{Al}_{12}\text{Si}_{12}\text{O}_{48}\cdot 27\text{H}_2\text{O}$ , PDF # 47-0716). Especially for sample LCLA, pseudowollastonite [ $\text{Ca}_3(\text{Si}_3\text{O}_9)$ , PDF # 74-0874] was detectable. There was a minor difference in the main reaction product (i.e., C-(N)-A-S-H/N-A-S-H gels) among the four samples. The formed crystalline phases mainly belonged to the aluminosilicate-like structure. The calcium content promoted the formation of the calcium-containing aluminosilicate phase, otherwise, the sodium-containing zeolite phase formed.

Figure 6-7 b displays the XRD patterns of the samples after exposure to sulphuric acid attack, demonstrating the presence of gypsum ( $\text{CaSO}_4$ , PDF# 33-0311) at  $11.7, 20.7, 23.4, 29.1, 31.1, 33.4, 40.7, 43.3,$  and  $56.8^\circ 2\theta$ . The broad amorphous hump still presented but shifted central position from  $29^\circ 2\theta$  to approximately  $22^\circ 2\theta$  (Walkley et al., 2016b). The decomposition of the amorphous C-(N)-A-S-H/N-A-S-H gels in reaction products caused the shifting when exposed to sulphuric acid. For high calcium HCLA and HCHA, the amorphous hump was almost invisible, indicating less amorphous gels left in the high calcium system. The decalcification is the main reason for the decomposition of the C-(N)-A-S-H gel in AAMs. The peaks that attributed to calcium aluminate hydrate and CH in samples HCHA and HCLA no longer existed after exposure to sulphuric acid.

The crystalline phases formed in the samples were vulnerable to the sulphuric acid attack in addition to the dissolution of C-(N)-A-S-H/N-A-S-H gels. Due to the strong diffraction patterns of gypsum, it is difficult to distinguish very specific changes of other minor crystalline products and the difference in acid resistance of each mix.

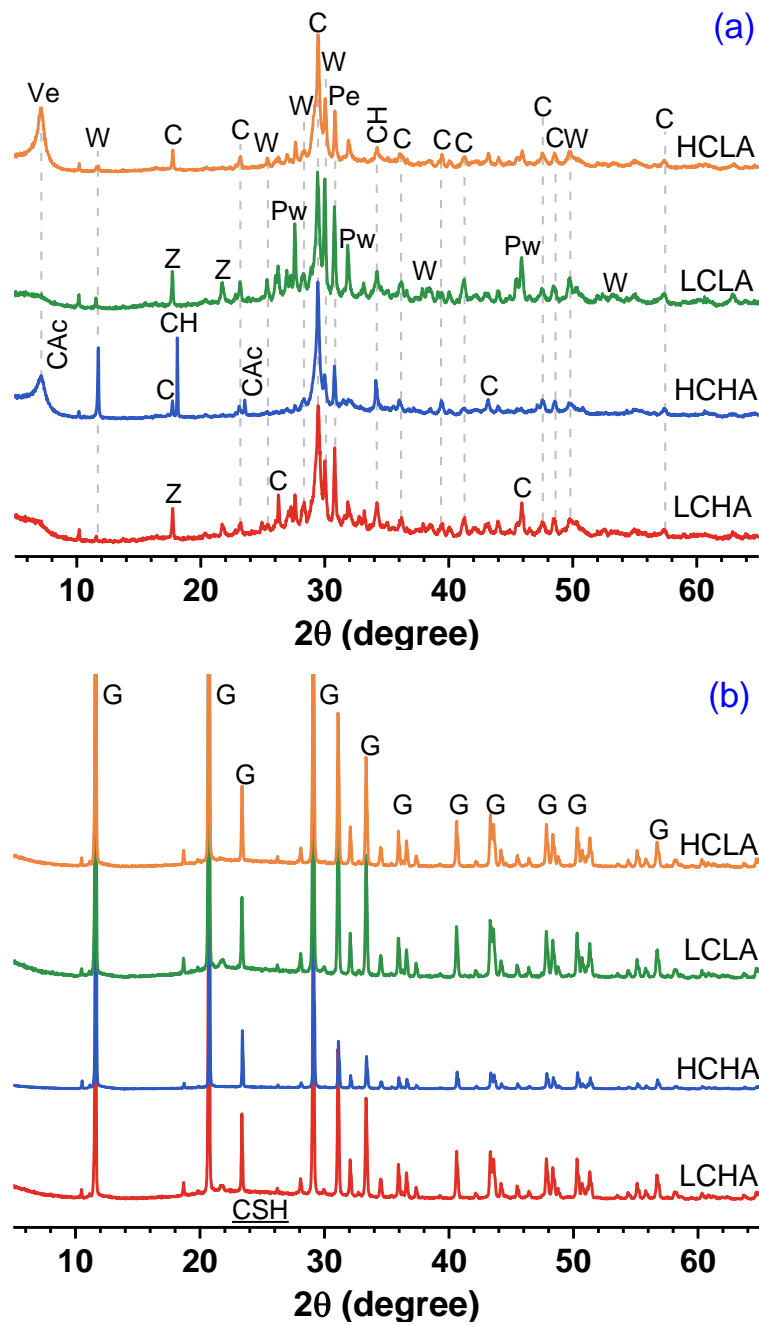
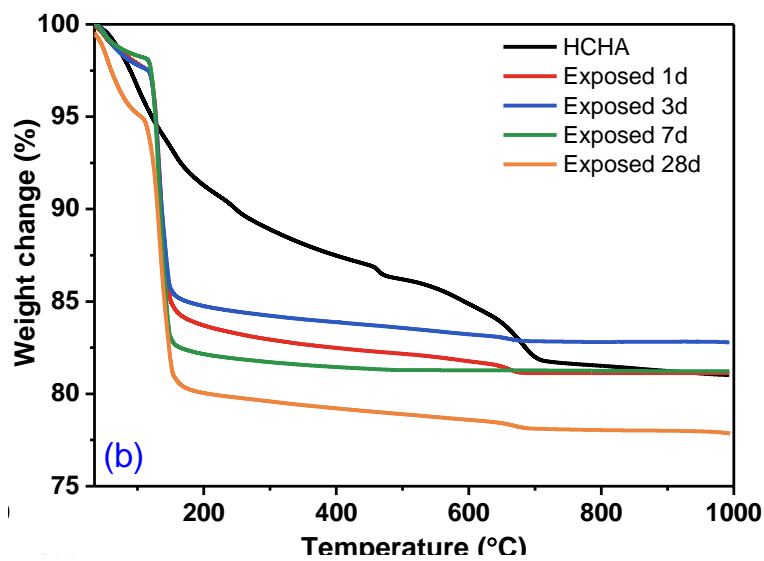
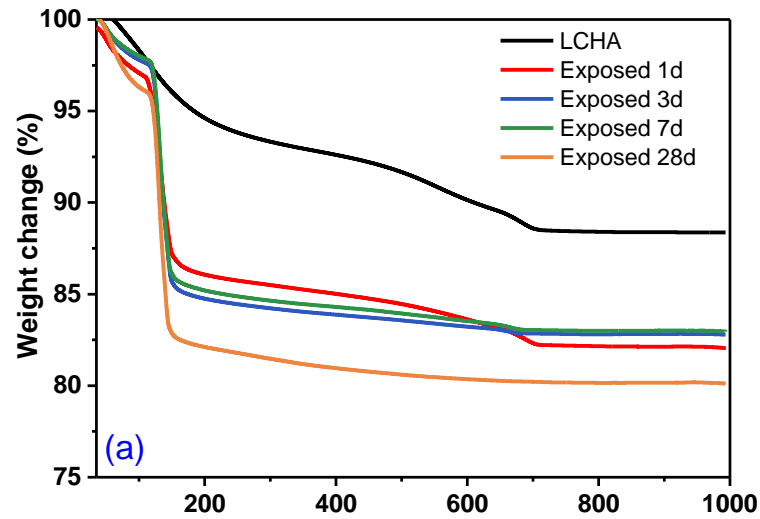


Figure 6-7. XRD patterns of the samples (a) before and (b) after exposure to 3% sulphuric acid for 28 days of acid corrosion (C-calcite, Z-zeolite, W-wollastonite, Pe-pectolite, Ve-vertumnite, Pw-pseudowollastonite, CAc-calcium aluminium carbonate hydrate, G-gypsum, CSH - amorphous calcium silicate hydrate).

### 6.3.3 Thermogravimetric analysis (TGA)

Figure 6-8 displays the mass change from TGA analysis of each binder before and after exposure to sulphuric acid. The mass loss of unexposed binders occurred from ambient temperature to approximately 700 °C, showing the total mass losses between 12% and 19%. The evaporation of free water from samples contributes to the mass

loss below 100 °C, and the mass loss with the N-A-S-H gel occurs at around 100 °C. The decomposition of C-(N)-A-S-H gels and crystalline phases are contributed to the mass loss that happened after 200 °C. The mass losses of exposed samples are higher than unexposed samples and mainly happen at around 150 °C.



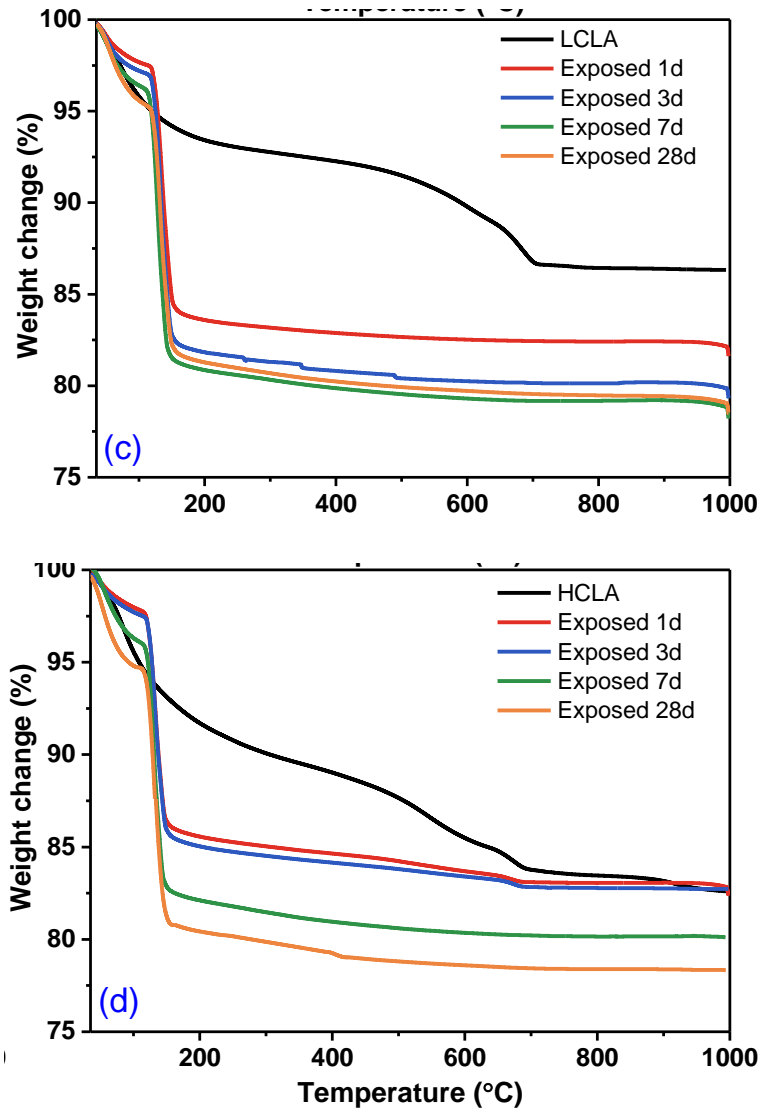


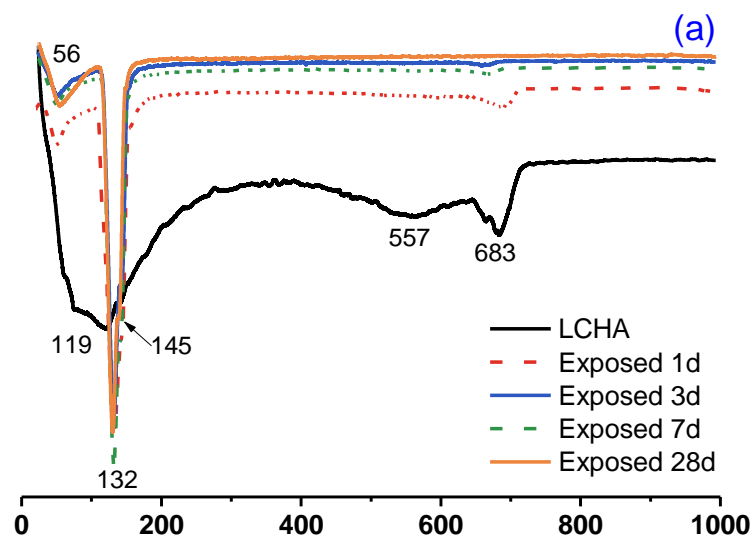
Figure 6-8. Thermogravimetric data of the samples before and after exposure to 3% sulphuric acid for 1 d, 3 d, 7 d, and 28 d as marked.

Figure 6-9 shows the differential thermogravimetric (DTG) curves of each sample before and after exposure to sulphuric acid. There is a broader mass loss area between 30 °C and 400 °C for high-Al samples LCHA and HCHA, while the range locates at around 30 °C and 300 °C for samples LCLA and HCLA. This might be due to the highly crosslinking in the C-(N)-A-S-H/N-A-S-H gel derived from high-Al precursors. And the first mass loss peak is located at 100-110 °C for samples LCHA and HCHA and 63-85 °C for samples LCLA and HCLA suggested that the evaporation of free water from N-A-S-H gel dominant samples is hard than that dominated by C-(N)-A-S-H gels. The DTG curves of each sample show the occurrence of three dominant mass loss peaks at 63-119, 548-575, and 670-686 °C, respectively. The mass loss peaks located below 200 °C are mainly due to the evaporation of free water and

dehydration of interlayer water from C-(N)-A-S-H/N-A-S-H gels (Walkley et al., 2016a, Bernal et al., 2011c). The mass loss peaks that appeared at 548-575 °C and 670-686 °C are due to the decomposition of calcium carbonates (Collier, 2016). The mass loss peak identified at around 464 °C for sample HCHA is due to the dehydroxylation of CH (Vedalakshmi et al., 2003, Phung et al., 2019). The small mass loss peak at around 248 °C is likely due to the release of bond water from the calcium aluminium carbonate hydrate phase (Walkley et al., 2016a). This suggested that the C-(N)-A-S-H gel starts to have a certain degree of carbonation in sample HCHA.

The main mass loss for all exposed samples occurs between 50 and 200 °C and increases with exposure time. The final mass loss of samples LCHA, HCHA, LCLA, and HCLA which were exposed to sulphuric acid for 28 days is 19.88%, 22.14%, 21.11%, and 21.61%, respectively. The high calcium samples show higher mass loss than the low calcium samples. The DTG curves of exposed samples have peaked at approximately 55 °C which was likely due to the removal of absorbed or loosely bound water (Aiken et al., 2018).

The TGA results confirm the formation of gypsum in each exposed binder, suggesting that C-(N)-A-S-H/N-A-S-H gels of all binders are vulnerable to sulphuric acid attack. The synthesised AAMs decompose quickly once exposed to 3% of sulphuric acid with the formation of gypsum, which is consistent with the leaching behaviour and XRD analysis. It suggests that the pure C-(N)-A-S-H/N-A-S-H gels in AAMs have very low acid resistance to acidic attack.



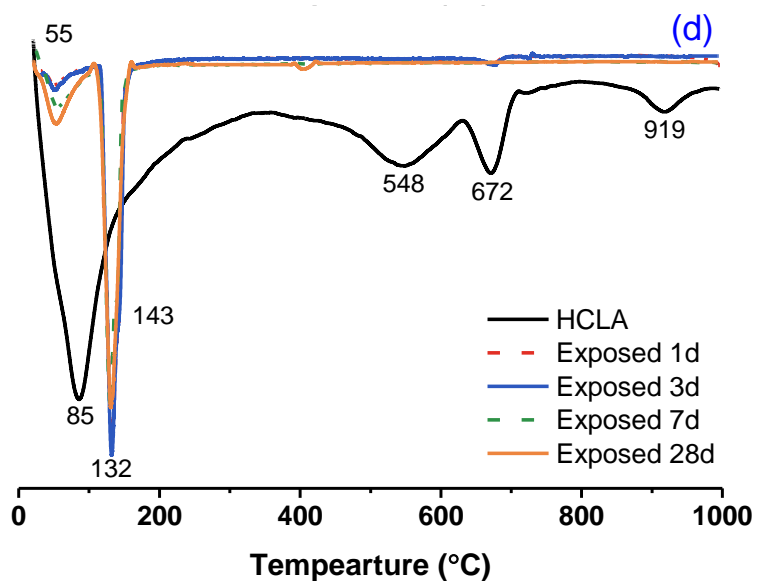
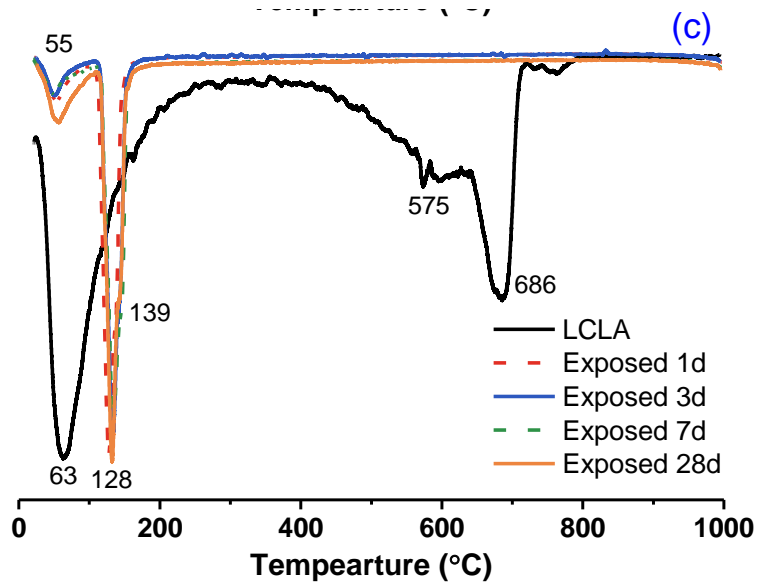
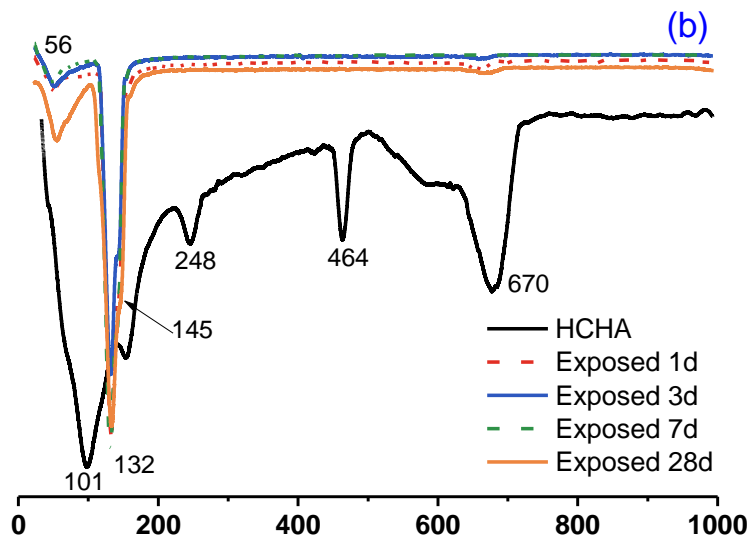
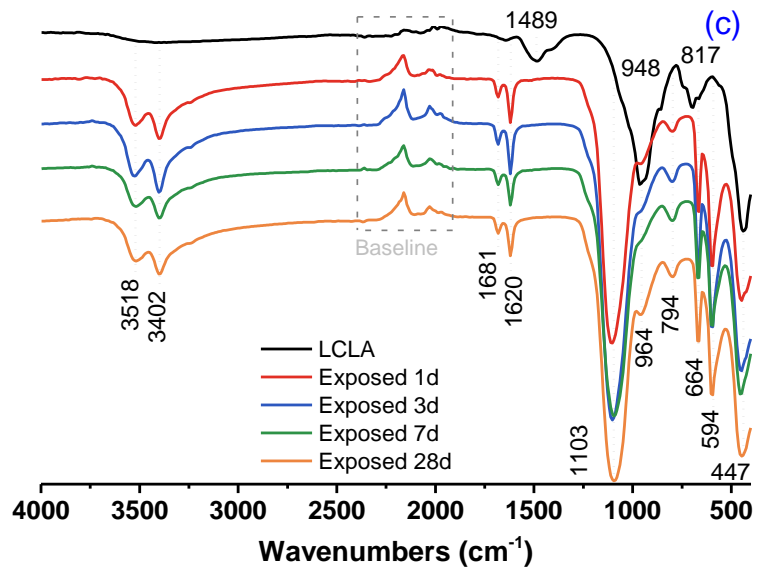
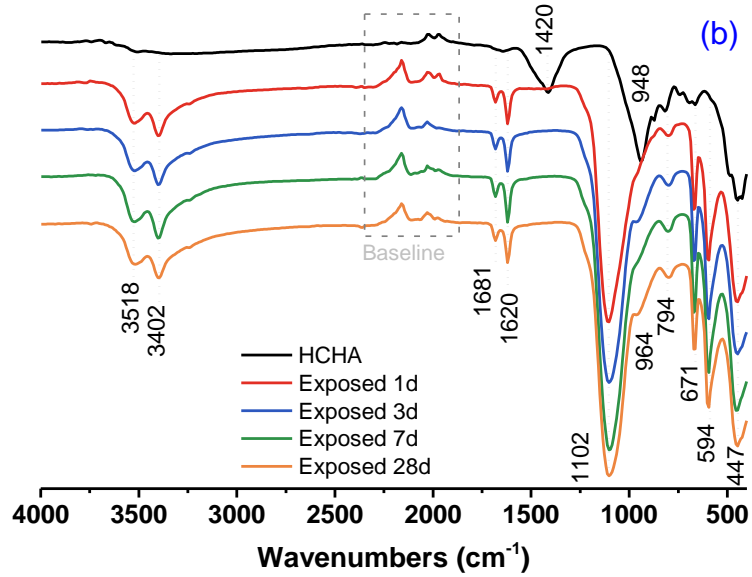
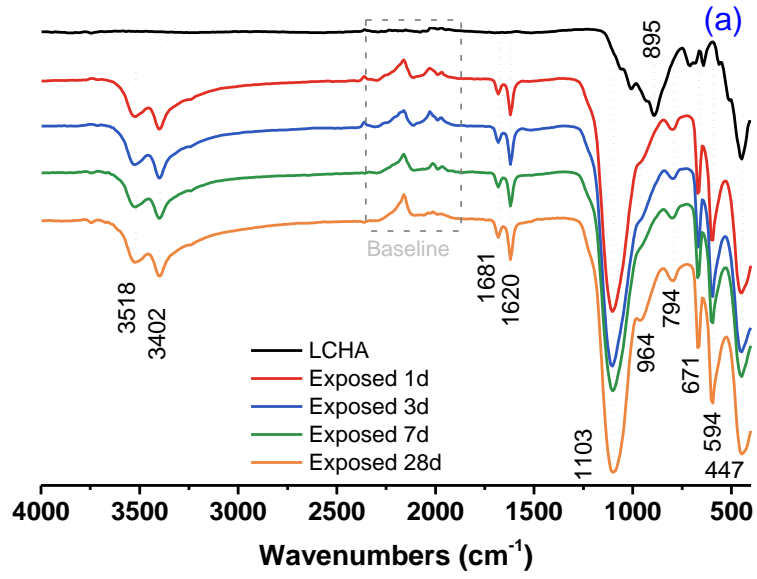


Figure 6-9. Differential thermogravimetric curves for the samples before and after exposure to 3% sulphuric acid for 1 d, 3 d, 7 d, and 28 d as marked.

### 6.3.4 Fourier transform infrared spectroscopy (FTIR)

Figure 6-10 shows the FTIR spectra of the unexposed and exposed binders. FTIR band assignments of unexposed and exposed samples are summarized in Table 6-2 and Table 6-3, respectively. For all samples, the asymmetric and symmetric stretching vibrations of Si-O-T (T=Si or Al) bonds in the chain structure of C-(N)-A-S-H/N-A-S-H gels contribute to the bands in the range of 900 - 1100  $\text{cm}^{-1}$  (Bernal et al., 2011b). The C-(N)-A-S-H gel is likely to be present at low wavenumbers (around 970  $\text{cm}^{-1}$ ) and N-A-S-H gel presents at approximately 1100  $\text{cm}^{-1}$ , which is due to the different Si/Al ratios and crosslinking of gels (García-Lodeiro et al., 2008). The bands of C-(N)-A-S-H gels are sharpened by increasing the structure order of the gel (Walkley et al., 2016c). The deformation of  $\text{SiO}_4$  tetrahedra contributes to the bands in the range of 400 - 500  $\text{cm}^{-1}$  (Yu et al., 1999). The symmetrical stretching vibration of the C-O-C bond in carbonates bands is assigned to the bands in the range of 1400 - 1500  $\text{cm}^{-1}$  of samples HCHA, LCLA, and HCLA (Huang and Kerr, 1960). The different hydrogen bond strengths in  $\text{H}_2\text{O}$  or hydrates account for the broadband at 3000-3800  $\text{cm}^{-1}$  which is assigned as stretching vibrations of O-H groups (Yu et al., 1999).

The main bands of samples LCHA, HCHA, LCLA and HCLA shift to higher wavenumber at 1103, 1102, 1095, and 1142  $\text{cm}^{-1}$ , respectively, after being exposed to sulphuric acid. The shifting of this band indicates the increase of Si/Al ratios of Si-O-T bonds which is due to higher amount of aluminium leach out from the samples than silicon (Aiken et al., 2018, Bašćarević et al., 2013). The frequency of this band increases along exposure days. The double peaks bands at 1620 - 1681  $\text{cm}^{-1}$  and 3402 - 3518  $\text{cm}^{-1}$  are assigned to the bending of H-OH bands of gypsum crystal appearing after acid corrosion (Borhan et al., 2010). The band at 447  $\text{cm}^{-1}$  due to the deformation of  $[\text{SiO}_4]$  tetrahedra is not altered by acid exposure (Yu et al., 1999). The gypsum contributes to the presence of the peaks at 594 and 671  $\text{cm}^{-1}$  (Borhan et al., 2010).



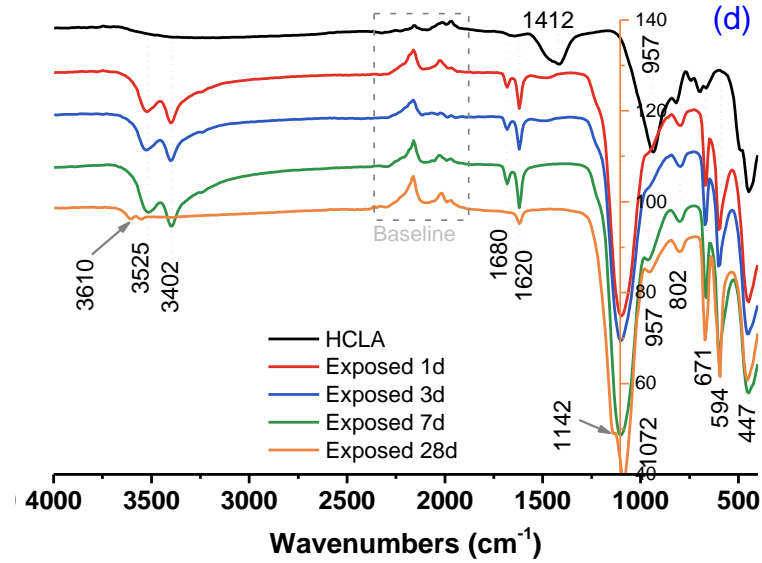


Figure 6-10. FTIR spectra of alkali-activated binders before and after exposure to 3% sulphuric acid. The baseline is enclosed in the dashed square.

Table 6-2 FTIR band assignments of unexposed samples (García Lodeiro et al., 2009).

Band	LCHA (cm <sup>-1</sup> )	HCHA (cm <sup>-1</sup> )	LCLA (cm <sup>-1</sup> )	HCLA (cm <sup>-1</sup> )	Assigned to
1	-	1650	1650	1650	v -OH (Ca(OH) <sub>2</sub> )
2	-	1420	1489	1412	v C-O (carbonates)
3	1065	-	1057	-	v Si-O
4	1010	-	1018	-	v Si-O
5	-	-	957	-	v Si-O (SiO <sub>4</sub> , Q <sup>2</sup> )
6	934	948	926	948	v Si-O (SiO <sub>4</sub> , Q <sup>2</sup> )
7	895	872	856	872	v C-O (carbonates)
8	-	818	-	818	v Si-O (SiO <sub>4</sub> , Q <sup>1</sup> )
9	710	741	741	741	v S-O-S (deformation)
10	679	694	694	694	δ Si-O-S (deformation)

Table 6-3 FTIR band assignments of exposed samples (Lee and Lee, 2016, Aiken et al., 2018).

Band	LCHA (cm <sup>-1</sup> )	HCHA (cm <sup>-1</sup> )	LCLA (cm <sup>-1</sup> )	HCLA (cm <sup>-1</sup> )	Assigned to
1	-	-	-	3610	v -OH
2	3518	3518	3518	3525	v -OH (gypsum)
3	3402	3402	3402	3402	v -OH (gypsum)
4	1681	1680	1681	1680	δ -OH (gypsum)
5	1620	1620	1620	1620	δ -OH (gypsum)
6	-	-	-	1142	v Si-O (silica gel)
7	1103	1102	1103	1072	v Si-O (silica gel)
8	964	964	964	957	v Si-O (SiO <sub>4</sub> , Q <sup>2</sup> )
9	794	794	794	794	v Si-O (SiO <sub>4</sub> , Q <sup>1</sup> )
10	671	671	664	671	δ Si-O-S (SiO <sub>4</sub> deformation)
11	594	594	594	594	δ Si-O-S (SiO <sub>4</sub> deformation)
12	447	447	447	447	δ Si-O-S (SiO <sub>4</sub> deformation)

To analyse the dominant group of bands, the magnified FTIR spectra in the range of 600-1150 cm<sup>-1</sup> and 550-1300 cm<sup>-1</sup> of unattacked and attacked samples are displayed in Figure 6-11. As shown in Figure 6-11 a, the group of bands at 934, 948, 957, 1010,

1018, 1057, and 1065  $\text{cm}^{-1}$  can attribute to Si-O stretching vibrations. The bands at 1010, 1018, 1057, and 1065  $\text{cm}^{-1}$  in samples LCHA and LCLA can attribute to Si-O-T bonds distinguished in the N-A-S-H gel, while those at 934, 948, and 957  $\text{cm}^{-1}$  could be assigned to the bonds in the C-(N)-A-S-H gel. This confirms that low-Ca precursors promote the formation of N-A-S-H gel while high calcium precursor promotes the formation of C-(N)-A-S-H gel. C-(N)-A-S-H gel with a certain degree of crystallinity contributes the well-shaped band at approximately 948  $\text{cm}^{-1}$  in the samples HCHA and HCLA.

The band at approximately 664  $\text{cm}^{-1}$  and the group between 694 and 741  $\text{cm}^{-1}$  are due to the bending vibrations of the Si-O-Si bonds, which are features of silicate chains identified in Jennite (Walkley et al., 2016b). The main bands and shoulders at 895  $\text{cm}^{-1}$ , 871  $\text{cm}^{-1}$  and 856  $\text{cm}^{-1}$  in the spectra of samples (as shown in Fig. 11 a) are associated with the asymmetric stretching of Si-O-Al bonds in the C-(N)-A-S-H/N-A-S-H gels with the presence of  $\text{AlO}_4^{5-}$  groups (Bernal et al., 2011b). The frequency and intensity of the main band are influenced by the Si-O-Al angle and occupancy of neighboring sites. For sample LCHA, greater Al and insufficient Ca in precursor promoted the Al inclusion within the N-A-S-H/C-A-S-H gels, i.e., the substitution of aluminium in silicon chains. The effect of aluminium content on this band was minor in high calcium samples HCHA and HCLA.

As shown in Figure 6-11 b, a sharp peak is identified at approximately 1100  $\text{cm}^{-1}$  for four attacked samples. This band could be attributed to the characteristic of the Si-O stretching bond in silica gels, which are the remnant of C-(N)-A-S-H/N-A-S-H gels after dealumination during acid attack (García-Lodeiro et al., 2008). The small shoulders at around 956 and 794  $\text{cm}^{-1}$  could be assigned to the Si-O bond in the unbroken gels. The sharp peaks at approximately 671 and 594  $\text{cm}^{-1}$  are the typical characteristic bands of gypsum (Aleksandra et al., 2005). Given the above results, the FTIR spectra of four samples highly show similarity after the acid attack. This suggests a similar Si-O-T environment in the residues of each sample after the acid attack.

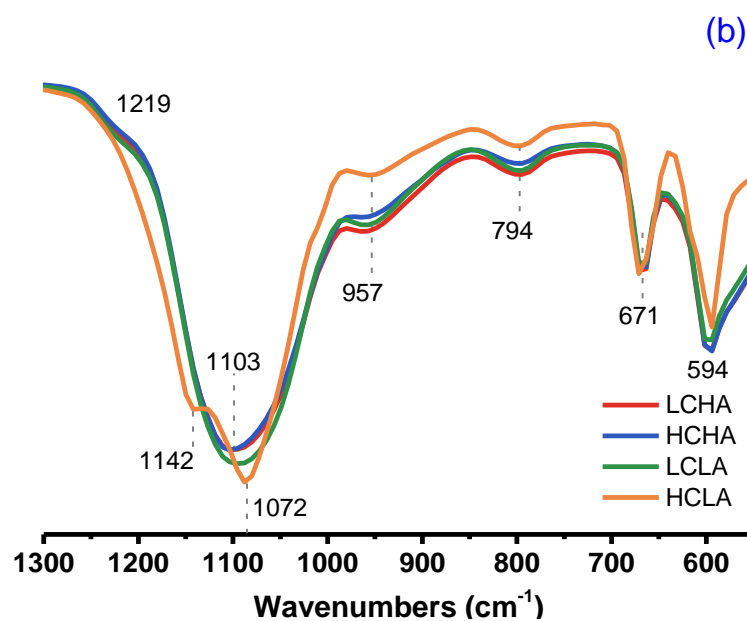
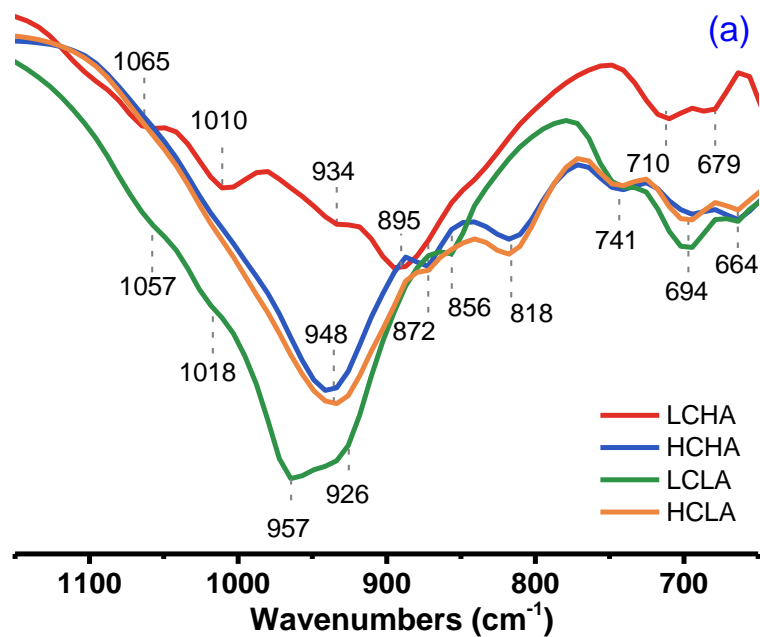


Figure 6-11. Magnified FTIR spectra of (a) unexposed samples between 650-1150  $\text{cm}^{-1}$  and (b) attacked gels between 550-1300  $\text{cm}^{-1}$ .

### 6.3.5 Solid-state nuclear magnetic resonance spectroscopy

#### 6.3.5.1 $^{27}\text{Al}$ NMR

Figure 6-12 displays the  $^{27}\text{Al}$  MAS NMR spectrum of the unexposed and exposed binders. The spectra of four samples in Figure 6-12 a shows signals that could be assigned to  $\text{Al}^{\text{IV}}$ ,  $\text{Al}^{\text{V}}$ , and  $\text{Al}^{\text{IV}}$ , with peak maxima near, respectively, 55 to 75 ppm, 35 to 40 ppm, and 5 to -5 ppm (Walkley et al., 2016c, Bernal et al., 2013b, Walkley

and Provis, 2019, Sun et al., 2006, Duxson et al., 2005a). The distribution of  $Al^{IV}$  coordination at crystalline C-(N)-A-S-H gel shows higher chemical shifting than that at amorphous N-A-S-H gel and poorly crystalline C-(N)-A-S-H gel (Walkley et al., 2016c). For sample LCHA, the main resonance locates at approximately 56.9 ppm which is assigned to  $[AlO_4]^{5-}$  tetrahedra which presences at bridge sites in Si-O chains in amorphous N-A-S-H and or poorly crystalline C-(N)-A-S-H gel. Similarly, the resonance located at 53.5 ppm for sample LCLA is assigned to  $Al^{IV}$  coordination at amorphous N-A-S-H gel. The resonances for samples HCHA and HCLA are located at approximately 70 ppm, which is higher than sample LCLA and LCHA. This proves that N-A-S-H gel is the dominant reaction gels in the low-Ca system, regardless of the aluminium content. It should be noted that  $Al^V$  is detected higher significance for sample LCLA.  $Al^V$  is highly reactive in nature which concerts to  $Al^{IV}$  during the alkali-activation process (Duxson et al., 2005a). A high amount of  $Al^V$  in sample LCLA indicates its low degree of reaction.

The resonance identified as  $Al^{IV}$  environments in samples HCHA and HCLA is located at 62.5 ppm and 62.8 ppm, respectively. The C-(N)-A-S-H gel formed in HCLA may cause higher chemical shifting due to the lower Al-substitution in the bridge sites (Sun et al., 2006). Another wideband ranging from -5 ppm to 5 ppm is assigned to partly overlapping the spinning sideband of the octahedral  $Al^{VI}$  peak, identified as additional reaction products (i.e., AFm phase and  $C_xAH_y$  phase) for high calcium samples HCHA and HCLA. These aluminate phases precipitate at the surface of C-(N)-A-S-H/N-A-S-H gels or precipitate as a separate phase located in the interlayer region of the gel (Schilling et al., 1994, Andersen et al., 2006). The  $Al^{VI}$  peak in AFm phases locates at higher chemical shifting than that in  $C_xAH_y$  phases (Walkley and Provis, 2019). The low intensity of  $Al^{IV}$  resonance for sample HCHA indicates less formation of Al-substituted C-(N)-A-S-H gel. Excess Al incorporates in the formation of Al-containing AFm phases and  $C_xAH_y$  phases.

Figure 6-12 b displays the spectrum of each alkali-activated gel after exposed to the acid attack. The main resonance which detected as  $Al^{IV}$  coordination in the samples LCHA and LCLA shifts slightly to lower chemical shifting (relocating at approximately 50 ppm) with decreased intensity, indicating the increased amorphous property (Brus et al., 2016). The dealumination of C-(N)-A-S-H/N-A-S-H gels under

acid attack results in the increase of active  $\text{Al}^{\text{V}}$ . An accumulation of octahedral aluminium  $\text{Al}^{\text{VI}}$  happens in the intraframework space, resulting in the appearance of the sharp octahedral Al resonance at around -1 ppm which could be assigned to aluminium sulphate ( $\text{Al}_2(\text{SO}_4)_3$ ) (Berger et al., 2018).

Especially for sample HCHA, the main resonance shifts slightly to 50.5 ppm but remains a relatively high intensity, which could be due to the overlapping of the tetrahedral  $\text{Al}^{\text{IV}}$  and  $\text{Al}^{\text{V}}$ . The intensity of the resonance attributed to the accumulation of octahedral  $\text{Al}^{\text{VI}}$  in other Al-containing phases decreases. This suggests that the high Al leaching of sample HCHA exposure to acid attack is due to the decomposition of Al-containing AFm phases and  $\text{C}_x\text{AH}_y$  phases. For sample HCLA, only octahedral aluminium can be detected in the corroded sample. This indicates the total dissolution of the high calcium low Al-substitution C-(N)-A-S-H gel and additional aluminate phases. This indicates that the Al-O bonds in C-(N)-A-S-H/N-A-S-H gels for high calcium samples are higher vulnerable to acid attack compared to amorphous N-A-S-H gel in low calcium samples. But the additional aluminate phases in sample HCHA protect the dealumination of C-(N)-A-S-H gel from acid corrosion to a certain extent.

The changes in the coordination of aluminium detected by the experiment have a great relationship with the initial calcium and aluminium content of the samples. High calcium and aluminium content in sample HCHA promote the formation of another aluminate phase which contains octahedral six-coordination Al in addition to C-(N)-A-S-H/N-A-S-H gels. Once the sample is contacted with an acid environment, this second aluminate phase is corroded by sulphuric acid prior to C-(N)-A-S-H/N-A-S-H gels. According to the dealumination from reaction products, C-(N)-A-S-H/N-A-S-H gels in sample HCHA show the highest resistance to acid attack, followed by amorphous N-A-S-H gel, while the C-(N)-A-S-H gel with low Al-substitution shows the lowest acid-resistance.

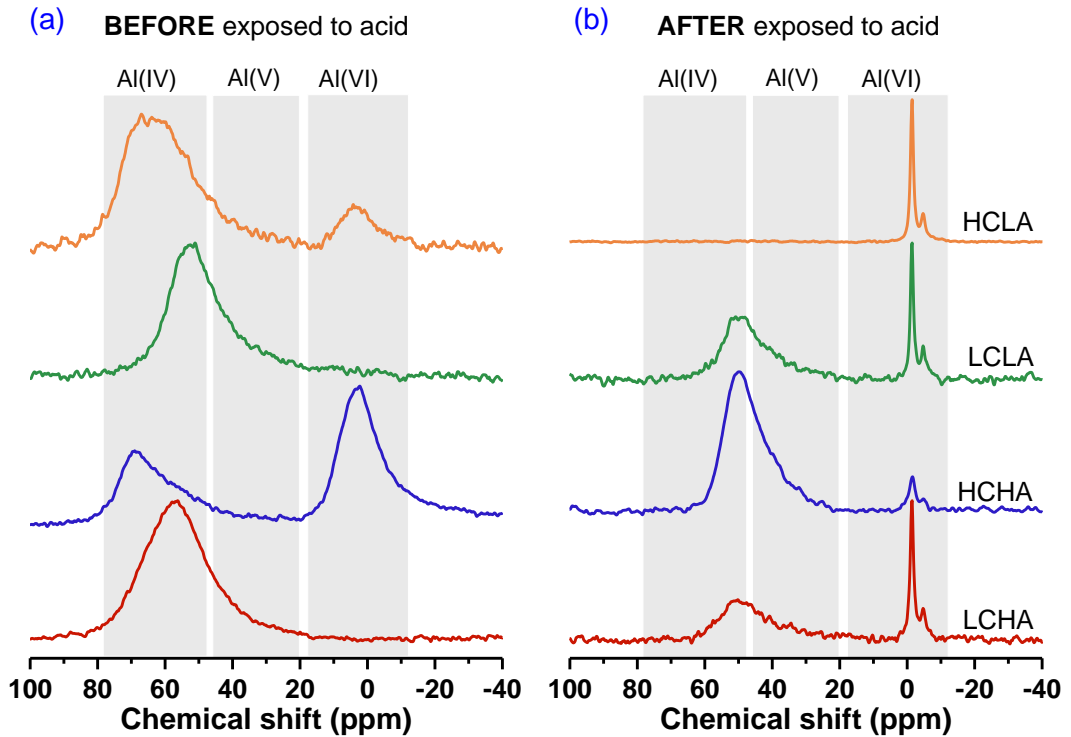


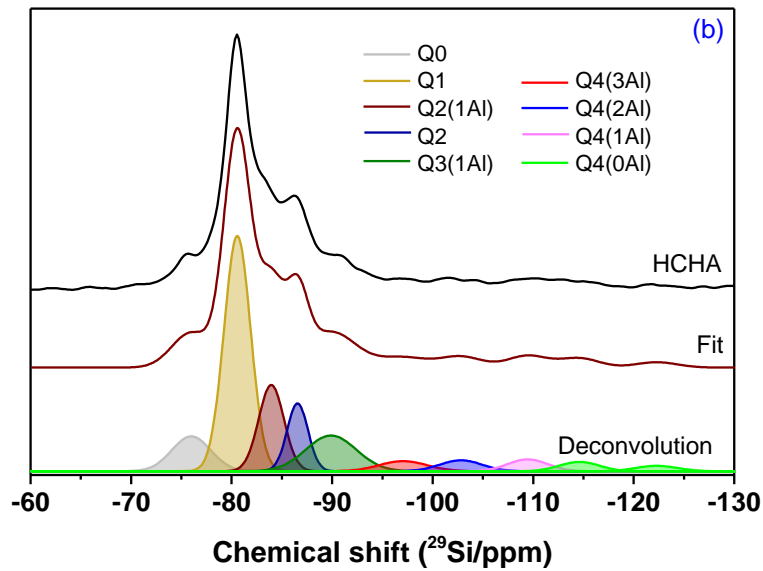
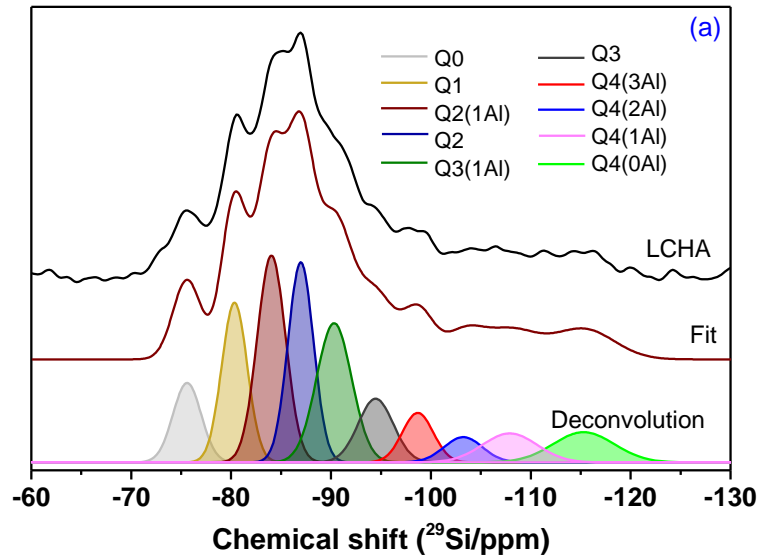
Figure 6-12.  $^{27}\text{Al}$  MAS NMR spectrum of samples before and after acid exposure.

#### 6.3.5.2 $^{29}\text{Si}$ NMR

Figure 6-13 displays the  $^{29}\text{Si}$  MAS NMR spectrum and the summary of Si coordination environments based on the deconvolution peaks of the unexposed binders. The resonance of C-(N)-A-S-H gel at  $^{29}\text{Si}$  MAS NMR spectrum of AAMs is reported that centered at around -85 ppm, and the resonance of N-A-S-H gel is centered at around -110 ppm (Bernal et al., 2013b). The spanning of the Si resonance confirms the coexistence of C-(N)-A-S-H gel and N-A-S-H gel in the binders, showing that N-A-S-H gel is the dominant gel for the samples LCHA and LCLA while C-(N)-A-S-H gel dominates the resonances for samples HCHA and HCLA (Walkley and Provis, 2019, Bernal et al., 2013b).

The increased content of  $\text{Q}^3$ ,  $\text{Q}^4(3\text{Al})$ ,  $\text{Q}^4(2\text{Al})$ , and  $\text{Q}^4(1\text{Al})$  in the reaction products of LCHA indicates the high Al-substitution rate in the amorphous N-A-S-H gel (Walkley et al., 2016c, Wang and Scrivener, 2003). The development of  $\text{Q}^2$  and  $\text{Q}^3(1\text{Al})$  resonances in sample HCHA is promoted by the high Ca content, indicating the presence of a crosslinked C-(N)-A-S-H gel (Myers, 2015). The presence of a non-crosslinked C-(N)-A-S-H gel in sample LCLA is suggested by the larger amounts of  $\text{Q}^0$  and  $\text{Q}^1$ . The presence of significant  $\text{Q}^1$  and  $\text{Q}^2$  sites in a depolymerised Al-

insufficient aluminosilicate phase in sample HCLA indicates that C-A-S-H is structurally comparable to a distorted tobermorite structure (Walkley et al., 2015). The silicon environment of the reaction products has a high similarity in samples HCHA and HCLA.



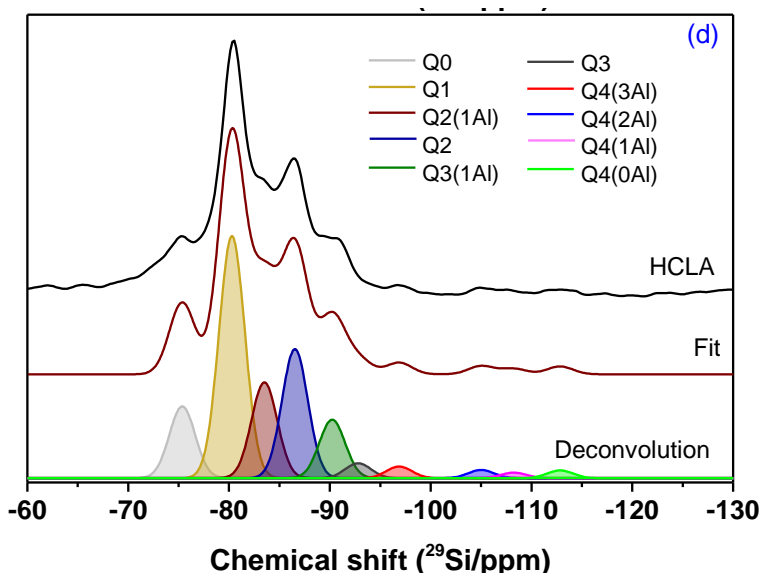
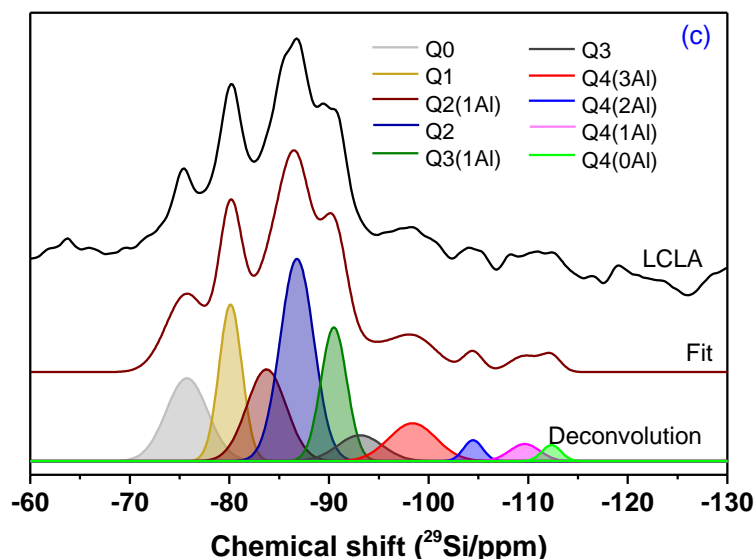
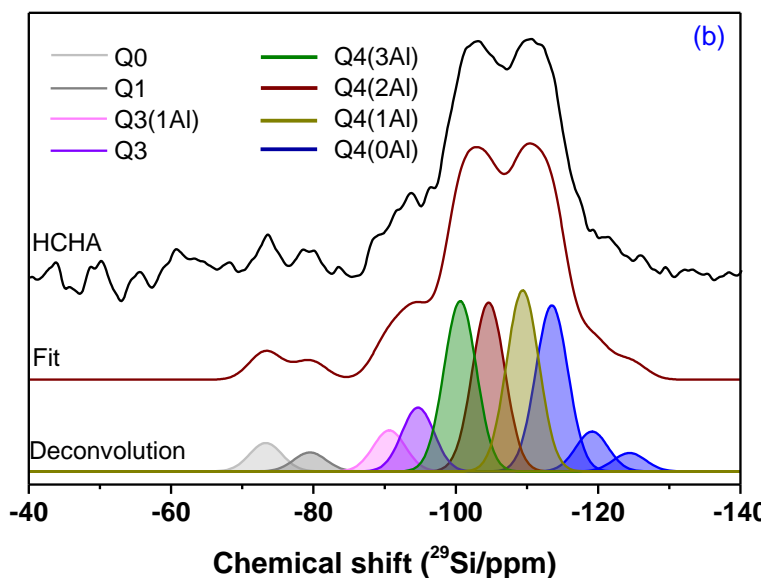
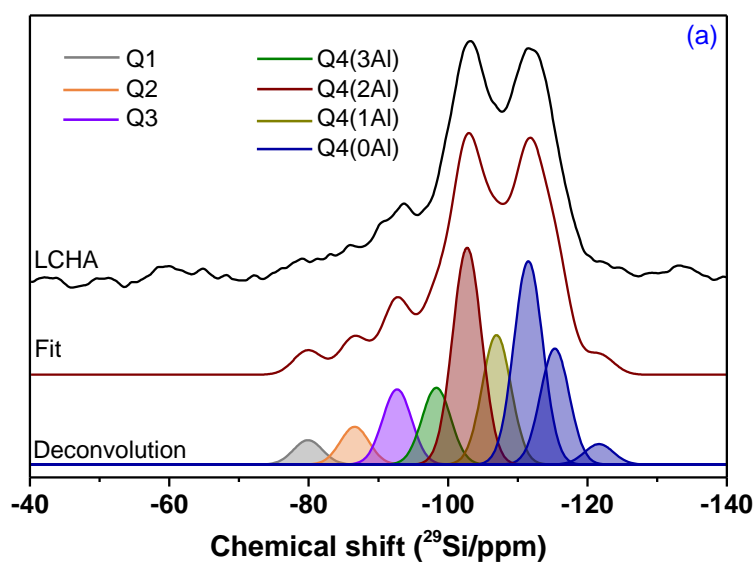


Figure 6-13.  $^{29}\text{Si}$  MAS NMR spectrum and deconvolution spectrum of samples after exposure to distilled water. The tetrahedral coordination of Si is presented by Q.  $\text{Q}^n(\text{mAl})$  represents that the calculated Si site is connected by n another Si site via oxygen bond and m of them are Al.

Figure 6-14 displays the  $^{29}\text{Si}$  MAS NMR spectrum and the summary of Si coordination environments based on the deconvolution of the overlapped peaks of binders after being exposed to the acid attack. A comparison of the  $^{29}\text{Si}$  MAS NMR spectra of the exposed and unexposed samples clearly shows that the process of acidic decomposition of C-(N)-A-S-H/N-A-S-H gels is an aluminium removal and siliceous gel formation process with the presenting of increased amounts of  $\text{Q}^4(2\text{Al})$ ,  $\text{Q}^4(1\text{Al})$ , and  $\text{Q}^4(0\text{Al})$  structural units.

As seen in low calcium samples LCHA and LCLA, still a small amount of residual  $Q^3(1Al)$  could be detected. The deconvoluted resonance peaks at -121.9 and -124.9 ppm for samples HCHA and HCLA are attributed to  $Q^4(0Al)$ , which is different from  $Q^4(0Al)$  which typically resonates in the region higher than -120 ppm (Walkley and Provis, 2019). This is due to the strong shielding effect for the central silicon atom, which might be caused by reducing the Si-O-Si bond angle or replacing the coordination environment with calcium (Walkley and Provis, 2019).



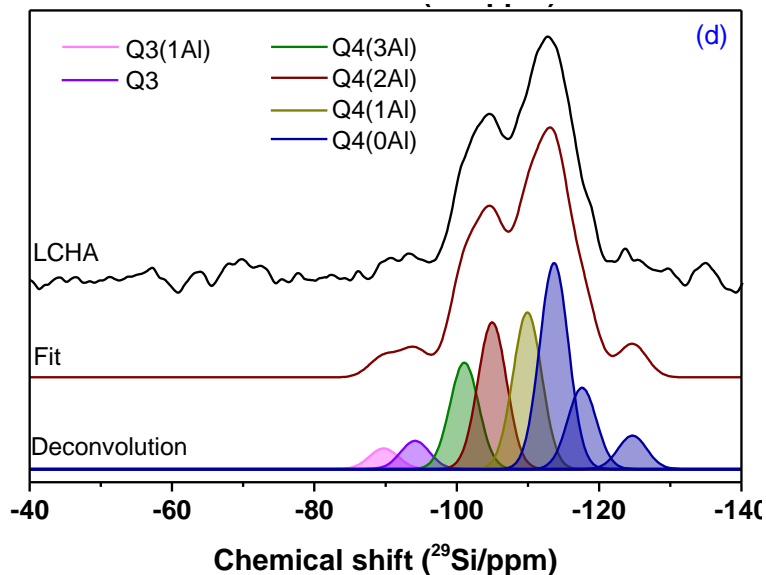
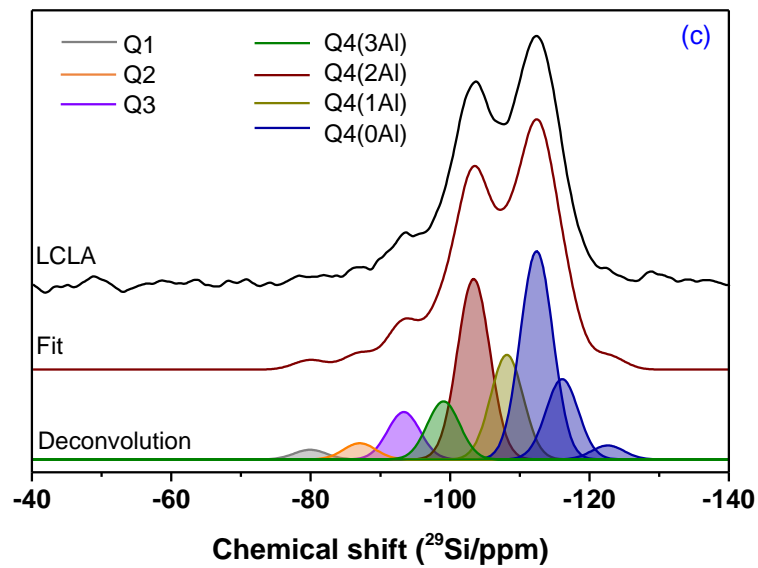


Figure 6-14.  $^{29}\text{Si}$  MAS NMR spectrum and deconvolution spectrum of samples after being exposed to 3% sulphuric acid. The tetrahedral coordination of Si is presented by Q.  $Q^n(m\text{Al})$  represents that the calculated Si site is connected by n another Si site via oxygen bond and m of them are Al.

Figure 6-15 shows the change of Si coordination characterized in  $^{29}\text{Si}$  MAS NMR spectra of the unexposed and exposed binders.  $Q^1$ ,  $Q^2$  and  $Q^3$  are the main resonances for the four unexposed samples. Especially for sample HCHA, the presence of a significant quantity of  $Q^1$  sites demonstrates the presence of more short chains in the produced C-(N)-A-S-H/N-A-S-H gel (Myers et al., 2015b).

The  $Q^0$  and  $Q^1$  sites in the residual binders almost disappear after being exposed to sulphuric acid attack. There are two possible explanations for the greater intensity of  $Q^4(3\text{Al})$ ,  $Q^4(2\text{Al})$ ,  $Q^4(1\text{Al})$ , and  $Q^4(0\text{Al})$  sites: the dissolution of C-(N)-A-S-H is prior

to N-A-S-H gels, and reaggregation of monomers to form a siliceous gel in samples, consistent with FTIR observations.

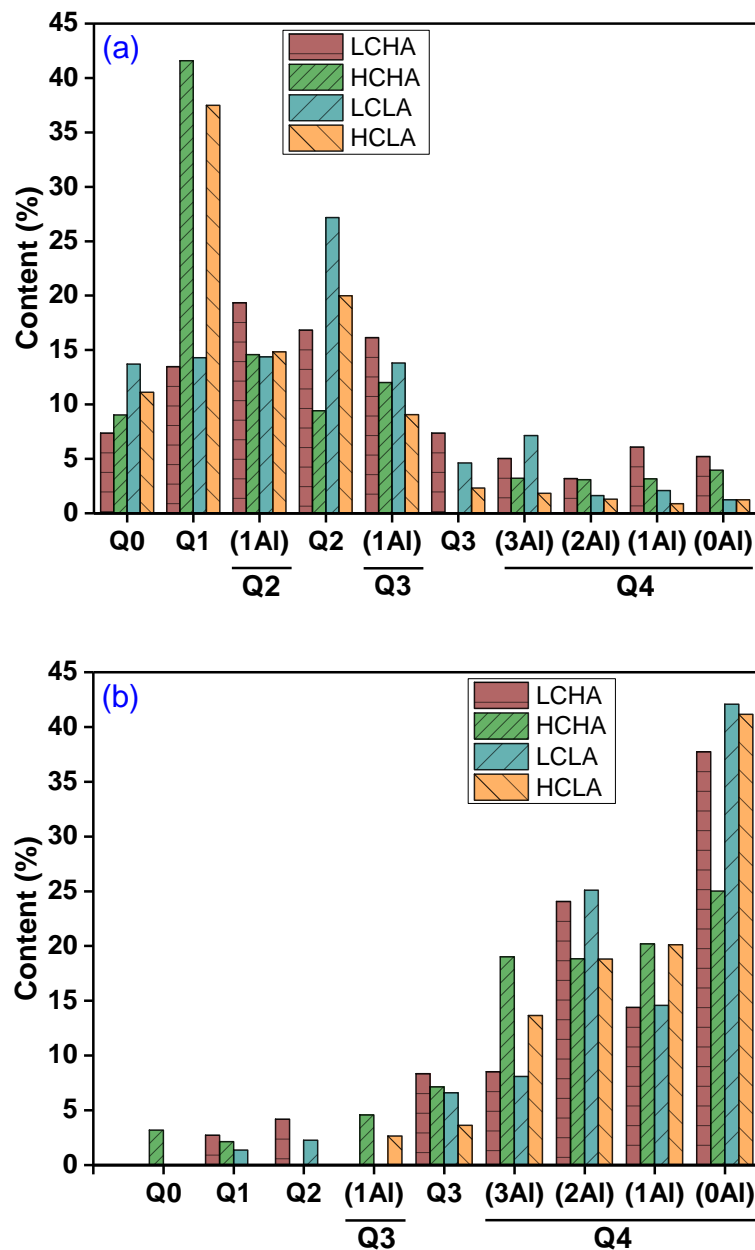


Figure 6-15. The Si coordination characterized in  $^{29}\text{Si}$  MAS NMR spectra of the samples (a) before and (b) after being exposed to sulphuric acid. There is around  $\pm 1\%$  of uncertainty for each calculated percentage.

The mean chain length (MCL) and the Si/Al ratios of the C-(N)-A-S-H and N-A-S-H gels in the unexposed and exposed binders are summarized in Table 6-4. For low-Al systems, such as the alkali-activated slag system, the non-crosslinked (NC) C-(N)-A-S-H gel are the dominant gels, while the crosslinked (C) C-(N)-A-S-H gel and N-A-S-H gel present at high-Al systems like alkali-activated fly ash. MCL and Si/Al ratio

of the non-crosslinked C-(N)-A-S-H and N-A-S-H gels are based on Equation 6-1, Equation 6-2, and Equation 6-3, while MCL and Si/Al ratio of the crosslinked C-(N)-A-S-H/N-A-S-H gels are based on Equation 6-4 and Equation 6-5.

$$MCL_{NC} = \frac{2[Q1+3Q2(1Al)+Q2]}{Q1} \quad \text{Equation 6-1} \quad (\text{Gao et al., 2017})$$

$$Si/Al_{CASH} = \frac{2[Q1+Q2+Q2(1Al)]}{Q2(1Al)} \quad \text{Equation 6-2}$$

$$Si/Al_{NASH} = \frac{\sum_{n=0}^4 Q4(nAl)}{\sum_{n=0}^4 \frac{n}{4} Q4(nAl)} \quad \text{Equation 6-3}$$

$$MCL_C = \frac{4[Q1+Q2(1Al)+Q2+Q3+2Q3(1Al)]}{Q1} \quad \text{Equation 6-4} \quad (\text{Myers et al., 2013})$$

$$Si/Al_{C(N)ASH} = \frac{Q1+Q2+Q2(1Al)+Q3+Q3(1Al)}{Q3(1Al)} \quad \text{Equation 6-5}$$

In comparison to the sample LCLA and LCHA, the C-A-S-H gels, both crosslinked and non-crosslinked, display shorter MCL and greater Si/Al ratio in the unexposed samples HCLA and HCHA the results demonstrate that high calcium content in samples, which is consistent with (Myers et al., 2015b). The shorter MCL is due to the higher content of Q<sup>1</sup> sites in the gel framework derived from high-Ca precursors. Increased Al content also promotes a shorter MCL and higher Si/Al ratio in the C-A-S-H gel. This is due to the incorporation of Al from high-Al precursors contributing to the formation of Q<sup>2</sup> and Q<sup>3</sup> type sites.

There is no Q<sup>2</sup>(1Al) presenting in the exposed samples. The MCL of non-crosslinked C-A-S-H gel decreases and the Si/Al ratio of the four samples could not be calculated. The reduced chain length and Si/Al ratio of C-A-S-H gel are inseparable from the decalcification and dealumination of the samples under acid attack. The Si/Al ratios in the N-A-S-H gels slightly increased. The MCL of crosslinking C-(N)-A-S-H gels increases, especially for sample HCHA from 8.6 to 34.7, with reduced Si/Al ratio. The increased MCL means the formation of a reunited silica gel, while the reduced Si/Al ratio means the higher amount of Al in the formed silica gel. The [SiO<sub>4</sub>] monomers from the decomposed gels could reaggregate together to form a siliceous gel, which could increase the Al involvement throughout enveloping effect.

Table 6-4 Summary of the deconvolution results of <sup>29</sup>Si MAS NMR spectra for the unexposed and exposed samples. The mean chain length (MCL) and Si/Al ratios are calculated for non-crosslinked C-A-S-H gel, N-A-S-H gel, and crosslinked C-(N)-A-S-H gels, respectively.

Unexposed samples		Q <sup>0</sup>	Q <sup>1</sup>	Q <sup>2</sup>	Q <sup>2</sup>	Q <sup>3</sup>	Q <sup>3</sup>	Q <sup>4</sup>	Q <sup>4</sup>	Q <sup>4</sup>	Q <sup>4</sup>	MCL	Si/Al	Si/Al	MCL	Si/Al	
				(1Al)		(1Al)		(3Al)	(2Al)	(1Al)	(0Al)	NC	CASH	NASH	C	C(N)ASH	
LCHA	Pos. (ppm)	-75.6	-80.3	-84.0	-87	-90.3	-94.5	-98.7	-103.2	-107.9	-115.3						
	Content (%)	7.4	13.5	19.3	16.8	16.1	7.4	5.0	3.2	6.1	5.2	8.8	5.1	2.8	26.5	4.5	
HCHA	Pos. (ppm)	-76.0	-80.6	-84.0	-86.6	-89.9	-	-97.1	-102.8	-109.4	-114.6						
	Content (%)	9.0	41.6	14.6	9.4	12.0	-	3.2	3.1	3.2	4.0	3.5	9.0	2.8	8.6	6.5	
LCLA	Pos. (ppm)	-75.7	-80.1	-83.7	-86.8	-90.5	-93.1	-98.4	-104.5	-109.7	-112.3						
	Content (%)	13.7	14.3	14.4	27.2	13.8	4.6	7.1	1.6	2.1	1.2	8.8	7.8	1.8	24.7	5.1	
HCLA	Pos. (ppm)	-75.4	-80.3	-83.5	-86.5	-90.2	-92.8	-96.9	-105.0	-108.2	-112.8						
	Content (%)	11.1	37.5	14.8	20.0	9.1	2.3	1.8	1.3	0.9	1.2	4.3	9.8	2.3	9.9	9.0	
Exposed samples																	
LCHA	Pos. (ppm)	-	-79.9	-	-86.6	-	-92.7	-98.3	-102.7	-107.0	-111.5						
	Content (%)	-	2.7	-	4.2	-	8.4	8.5	24.1	14.4	37.8	5.1	-	3.9	22.5	-	
HCHA	Pos. (ppm)	-73.3	-79.5	-	-	-90.7	-94.7	-100.6	-104.6	-109.4	-113.5						
	Content (%)	3.2	2.1	-	-	4.6	7.1	19.0	18.8	20.2	25.0	2.0	-	2.9	34.7	3.0	
LCLA	Pos. (ppm)	-	-79.9	-	-87.0	-	-93.4	-99.1	-103.4	-108.2	-112.4						
	Content (%)	-	1.35	-	2.25	-	6.6	8.1	25.1	14.6	42.1	5.3	-	4.0	30.2	-	
HCLA	Pos. (ppm)	-	-	-	-	-89.74	-94.2	-101.1	-105.0	-109.9	-113.7						
	Content (%)	-	-	-	-	2.65	3.6	13.7	18.8	20.1	41.2	-	-	3.8	-	2.4	

## 6.4 Discussions

### 6.4.1 The effect of chemical composition on leaching performance

There is a higher leaching amount of free  $\text{Na}^+$  from samples HCLA and HCHA in water leachates compared to samples LCLA and LCHA. This confirmed the negative effect of incorporation of calcium on the movement of free sodium ions, further anti-efflorescence performance, which is consistent with (Longhi et al., 2021). The leaching of free  $\text{SiO}_4^{4-}$  ions from sample LCLA to water is due to the insufficient consumption of activators due to relatively less amount of reactive  $\text{Ca}^{2+}$  and  $\text{Al}^{3+}$ . The high amount of leaching sodium is due to fewer  $\text{Na}^+$  are present in the interlayer of the gels by charge-balancing mechanism as deficient Al was incorporated in the formed gels of low aluminium sample HCLA in comparison with sample HCHA. This suggests that the formation of additional C-S-H gel in sample HCLA. The higher calcium content in the mixture can reduce the leaching amount of free  $\text{Al}^{3+}$  ions in comparison of samples LCHA to HCHA, and LCLA to HCLA when they are exposed to the acid solution. This suggests that the Si-O-Al bonds in C-(N)-A-S-H gel are more resistant to acid attack than those in N-A-S-H gel. There is a higher amount of leaching  $\text{SiO}_4^{4-}$  ions for the low calcium samples LCHA and LCLA compared to the samples HCLA and HCHA when they are exposed to acid attack. This suggests that higher  $\text{SiO}_4^{4-}$  leaching out from N-A-S-H gel than C-(N)-A-S-H gel. The dealumination from the Si-O-Al bond resulted in silicon monomers and dimers from polymerized silicate chains. The surrounded calcium sheets might reduce the transfer of silicon monomers and dimers to free  $\text{SiO}_4^{4-}$  ions further reducing their leaching.

In view of the leaching phenomenon, the concentration of aluminium and silicon leached out from sample LCHA are the highest among four samples, indicating that its reaction product (i.e., mainly N-A-S-H gel) is more sensitive to acid attack. Compared with the incompletely reacted samples LCLA, HCLA with additional C-S-H gel show better acid resistance in regarding the leaching amount of free Si ions. This is because that the additional C-S-H gel has a buffering capability which improves the leaching behavior in the sample HCHA (Liu et al., 2020).

### 6.4.2 Corrosion mechanisms of C-(N)-A-S-H and N-A-S-H gels

The schematic presentation of acid attack on C-(N)-A-S-H and N-A-S-H gels are shown in Figure 6-16. The C-(N)-A-S-H gel shows a layered sandwich structure with two Ca-O octahedrons and crosslinked silicate chains and the N-A-S-H gel shows a highly crosslinked network, while Al-O tetrahedron could only present in the bridge sites. Once exposed to sulphuric acid attack, the  $H^+$  attack causes the breakdown of the Ca-O sheets with the leaching of  $Ca^{2+}$ , along with the leaching of  $Na^+$  and  $Al^{3+}$ . The increased MCL of crosslinking chains indicated that the fractured silicate chains reunited together due to the vacancies precipitated by Al-O being occupied by Si-O. After being exposed to acid, the MCL of N-A-S-H gel shows a slight increase, along with the leaching of  $Na^+$ ,  $Al^{3+}$  and  $Si^{4+}$ . The acid attack has minor effect on the silicon network in the N-A-S-H gel. It means the three-dimensional N-A-S-H gel shows high resistance to depolymerization under  $H^+$  attack.

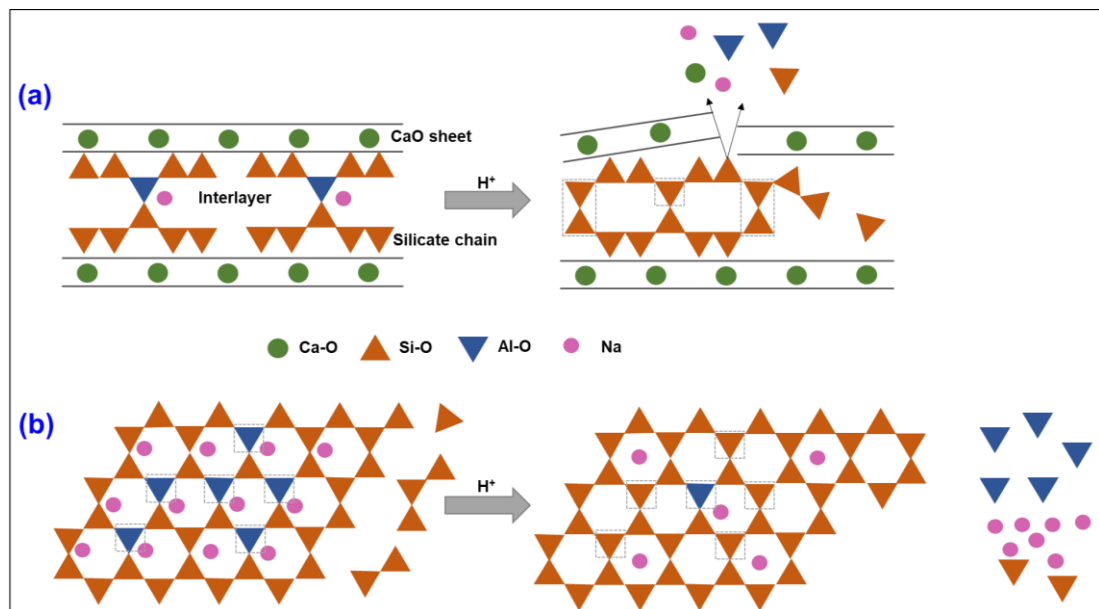


Figure 6-16. Schematic presentation (two-dimensional) of acid attack on (a) C-(N)-A-S-H and (b) N-A-S-H gels: Ca-O octahedron indicated in green circle, Si-O tetrahedron and Al-O tetrahedron indicated in orange and dark blue triangles, Na cation indicated in pink circle, water indicated in light blue circle.

## 6.5 Concluding remarks

Four AAMs derived from pure precursor powders with different molecular composition ratios are exposed to the sulphuric acid solution. The following conclusions can be drawn:

- Low calcium samples LCHA and LCLA show a higher leaching amount of Al than high calcium samples HCHA and HCLA. This indicates that the calcium content in the mixture promotes the resistance of samples to dealumination when exposed to sulphuric acid.
- The formation of additional reaction products (i.e.,  $C_xAH_y$  and CH) in sample HCHA is likely decomposed prior to C-(N)-A-S-H/N-A-S-H gels which suggest that it could help to retard the attack of sulphuric acid on the C-(N)-A-S-H/N-A-S-H gels. The negative effect of CH with the formation of expansive products is not negligible, while an optimal calcium content in the AAMs should be considered.
- More silicon leaches out from sample LCHA, suggesting that the strength of the Si-O bond in N-A-S-H gel appears weaker than the C-(N)-A-S-H gel, which the calcium prevents the leaching of silicon from samples.
- When exposed to sulphuric acid, the silicon chains length of the C-(N)-A-S-H gel increases with increased Si/Al ratio. However, the chain length of the N-A-S-H gel increases with reduced Si/Al ratio.

The AAMs derived from pure precursors with designed mixture composition show comparable macroscopic destruction to that derived from industrial materials under sulphuric acid attack. From the gel destruction mechanism, the findings presented in this study show that the re-polymerisation of silicon chains happening in both C-(N)-A-S-H gel and N-A-S-H gel due to the dealumination under acid attack. This work highlights the need to design an optimal Ca/Al ratio in the AAMs for required behavior in the acid environment.

## **CHAPTER 7. EFFECT OF RAW MATERIALS ON THE ACID RESISTANCE OF ALKALI-ACTIVATED SLAG/FLY ASH BINDERS BY SULPHURIC ACID ATTACK**

### **7.1 Introduction**

Cementitious materials are absolutely central to buildings and infrastructures in recent decades around the world. Researchers have shown a continuous interest in the durability of cementitious materials as growing demand for structures to have a long service life with minimal maintenance (Glasser et al., 2008). Especially, the wastewater infrastructure elements are expected to have service lives of 50 to 100 years, or even longer. It is found that the service life of wastewater infrastructure reduces to around 30 years due to biogenic sulphuric acid corrosion occurring in sewer environment with high hydrogen sulfide concentration (Song et al., 2019). Investigation of the degradation mechanisms of different cementitious materials to sulphuric acid is thus an increasingly important area in the durability research (Grengg et al., 2020). To date there has been little agreement on which influencing factors dominate the acid resistance of cementitious binders.

Except to the ordinary Portland cement (OPC), alkali-activated materials (AAMs) have been one of the most intense research hotspots due to its friendly environment impact and comparable durability performance (Provis, 2018). The reason for the popularity of the AAMs is the application of high level of industrial wastes like fly ash and ground furnace-blast slag, further reducing the emission of green gas generated from the production process of Portland cement. Thus, a considerable amount of literature has been published on the comparison of the acid corrosion resistance of OPC and AAMs. The acid corrosion resistance of OPC is evaluated by the change of surface, mass and strength, and the evaluation indexes has also been extended to evaluate the acid corrosion resistance of AAMs. Previous research has concluded a convergence that alkali-activated fly ash (AAFA) shows the highest residual strength ratio and the least mass change after sulphuric acid corrosion, following by alkali-activated slag (AAS) and OPC, but AAFA had the lowest initial strength which is unfavorable for practical applications (Zhang et al., 2018c, Aiken et al., 2018).

Shi and Stegemann (2000a) investigated the acid corrosion mechanism of AAS paste and highlighted that the protective layer or the hydration products were more important than the permeability porosity of hardened cement pastes. This view is supported by Sata et al. (2012) who illustrated the better acid resistance of AAMs due to the more stable cross-linked aluminosilicate polymer structure than the OPC hydration structure. Zhang et al. (2018c) demonstrated that the denser matrix of AAS is advantage to impede the aluminium loss from sample. As known the leaching of free aluminium from raw materials related to the pore structure of the sample and the ejection of aluminium from gel structure was due to the protons attack on the Si-O-Al bonds. The lost aluminium whether from unreacted raw materials or reaction products need to be explored in the following study.

The reaction product of AAFA is mainly sodium alumina silicate hydrate (N-A-S-H) which is generally described as a nanocrystalline zeolite-phase, which Si or Al tetrahedron connected to form a net structure by sharing one oxygen atom (Palomo et al., 2015). N-A-S-H gel had a high leaching of aluminium and sodium expect for silicon when immersed into hydrochloric acid solution (Temuujin et al., 2011). It is assumed that a silicon-rich porous structure was left after acid corrosion in N-A-S-H gel. However, elements leaching in acid solution caused minor change of compressive strength, which proved that the silicon-chain framework contributed most source of the compressive strength in N-A-S-H system (Temuujin et al., 2011, Fernández-Jiménez et al., 2007, Allahverdi and Škvára, 2001). Higher residual compressive strength of AAS after acid corrosion was found by previous research (Shi, 2003, Bakharev et al., 2003). The reaction product of AAS is a coexistence of different gel products including calcium silicate hydrate (C-S-H), aluminium-substituted calcium silicate hydrate (C-A-S-H) and N-A-S-H (Palomo et al., 2015). Decalcification of the C-S-H and C-A-S-H gels under acid attack provides diffusing  $\text{Ca}^{2+}$  cations which could form expansive ettringite and gypsum when countering the diffusing  $\text{SO}_4^{2-}$ .

So far, the influencing of decalcification and dealumination on the microstructure and microhardness of the exposed samples is still not clear. This paper attempts to examine the degradation resistance of OPC and alkali-activated materials (AAMs) exposed to sulphuric acid corrosion. The common assessment methods like the change of sample appearance, mass, and compressive strength are used to provide supplementary

information. The effect of decalcification and dealumination on the microstructure of the samples after exposed to sulphuric acid is investigated to explore the sulphuric acid corrosion mechanism on cementitious matrix. At last, combined with previous results in Chapter 5 and Chapter 6, a mathematical model is built in this chapter.

## 7.2 Materials and methods

### 7.2.1 Materials

The fly ash from Cement Australian and the ground granulated blast furnace slag (GGBFS) from Neilsen's Concrete Pty Ltd, Australian were used as precursors for AAMs. The fly ash conformed to the requirement as a cementitious material in concrete and mortar according to Australian Standard AS3582.2 and was classified as a class F fly ash according to ASTM C618 with a calcium amount of about 2.7% and LOI of 1.1%. The general-purpose Portland cement (clinker over 92%) was supplied by Bunnings Warehouse, Australian. The chemical composition of raw materials was analysed by X-ray fluorescence (XRF) as shown in Table 7-1.

Table 7-1. Chemical compositions and physical properties of raw materials.

Chemical compositions, %	OPC	Fly ash	GGBFS
SiO <sub>2</sub>	20.24	56.36	28.98
Al <sub>2</sub> O <sub>3</sub>	5.15	33.85	12.87
CaO	65.13	2.71	34.68
Fe <sub>2</sub> O <sub>3</sub>	3.17	2.88	0.43
MgO	1.33	0.66	6.06
SO <sub>3</sub>	3.41	0.14	2.17
Na <sub>2</sub> O	0.44	0.42	0.24
K <sub>2</sub> O	0.52	0.76	0.25
TiO <sub>2</sub>	0.28	1.91	-
Others	0.33	0.31	14.32

The X-ray diffraction patterns of fly ash, GGBFS and OPC were shown in Figure 7-1. Fly ash showed a broad hump in the range between 16 to 35° 2θ with the crystalline phases of mullite and quartz. The GGBFS showed a dominant hump between 25 and 32° 2θ indicating its amorphous character. The crystalline phases in OPC were mainly alite (3CaO·SiO<sub>2</sub>) and belite (2CaO·SiO<sub>2</sub>) with a trace of quartz and gypsum.

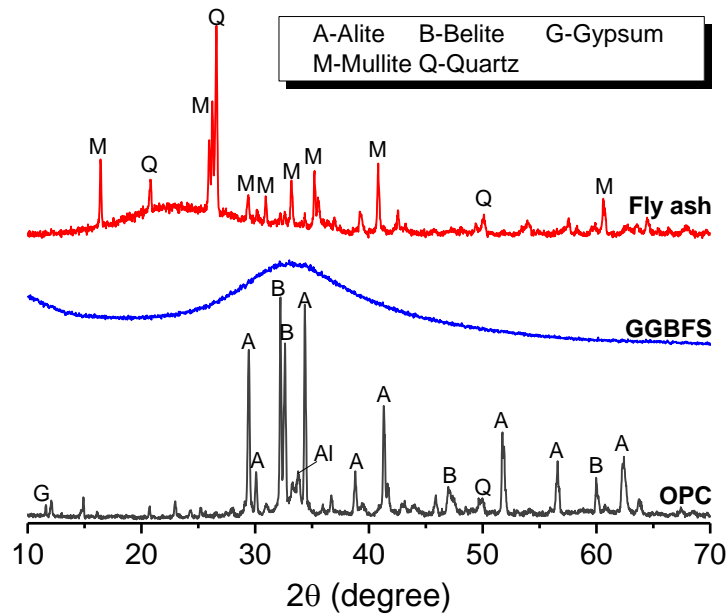


Figure 7-1. XRD patterns of fly ash, GGBFS and OPC.

The alkaline activating solution for AAMs was formulated by dissolution sodium hydroxide pellets (Sigma-Aldrich, 98 wt.% purity) into commercial sodium silicate solution ( $\text{Na}_2\text{O} = 14.7\%$  (mass),  $\text{SiO}_2 = 29.4\%$ , D-Grade™, PQ Australia) with water. The modulus ( $\text{SiO}_2/\text{Na}_2\text{O}$ ) of activator was fixed at 1.0. The alkali content ( $\text{Na}_2\text{O}$ ) in the activators were 4 wt.% and 6 wt.% of the precursor powders, respectively. The activators are prepared at least 24 hours before sample casting. The fine aggregate used was siliceous sand sourced in Australia and was dried in 80 °C oven for 48 hours.

### 7.2.2 Sample preparation

The mix proportions of this study including one OPC sample and four AAMs samples were shown in Table 7-2 based on the mix design optimisation carried out by Wang et al. (2021a) and Li et al. (2018). The AAM\_1 and AAM-2 were synthesised by fly ash with different Ca/Si and Si/Al ratios representing low-calcium AAMs, while AAM\_3 and AAM\_4 was derived from GGBFS representing high-calcium AAMs. The mortar mix proportions used were designed with cement to sand ratio of 2.5 for all mortars to reach a fair comparison. The OPC mortar adopted a water to cement ratio of 0.45. For AAMs, the water to solid ratio is designed as 0.45 which was calculated from the ratio of water to binder content including the solid and water proportions of the activating solutions.

The dry binder components were mixed with sand using a 10 L capacity planetary mixer for 3 minutes. For paste samples, this step was not necessary. The activator was then added to the mixing bowl and mixed with the dry components for another 4 minutes. The fresh mortar was casted into 40 mm triplex plastic molds in two layers. The fresh pastes were casted into cylinders of 15 mm diameter and 30 mm high. All samples were sealed before curing. The AAM\_1 and AAM\_2 samples were cured at 50 °C for 24 hours before demolding. The demolded and sealed samples were continually cured at 50 °C oven for another 6 days. Then the samples were taking out from oven and further cured at ambient environment for another 21 days. The AAM\_3, AAM\_4 and OPC samples were cured at room temperature and demold after 24 hours curing. Then the demolded samples were sealed and cured at ambient until test. The designed curing condition was depended on the setting properties of different samples as AAMs derived from fly ash showing a slow setting at room temperature.

Table 7-2. Mix proportions of the binder mixes (kg/m<sup>3</sup>). The mix proportions of the paste samples were identical to the mortars except they contained no sand.

Sample	OPC	Fly ash	GGBFS	Sand	Activator		Bulk Ca/Si	Bulk Si/Al
					Na <sub>2</sub> O%	Ms		
OPC	100	-	-	250	-	-	3.451	6.687
AAM_1	-	100	-	250	4.0	1.0	0.048	6.039
AAM_2	-	100	-	250	6.0	1.0	0.047	6.233
AAM_3	-	-	100	250	4.0	1.0	1.131	8.664
AAM_4	-	-	100	250	6.0	1.0	1.068	9.175

### 7.2.3 Testing procedure

#### 7.2.3.1 Water absorption test

The modified water absorption test was based on the ASTM C642. After cured for 28 days, three mortar samples (40-cm cube) from each mix were dried with a laboratory oven at 40°C. The modified temperature was considering the influence of thermal treatment on alkali-activated binders (Ismail et al., 2013a). The dried samples were immersed into water until the samples are fully saturated. The boiling process is not conducted in this study considering the influence of temperature on AAMs. The water absorption rate and volume of open pores (VOP) are calculated based on the following Equation 7-1 and Equation 7-2.

$$\text{Water absorption rate (\%)} = [(m_s - m_o)/m_o] \times 100 \quad \text{Equation 7-1}$$

$$\text{VOP} = [(m_s - m_o)/(V \times \rho)] \quad \text{Equation 7-2}$$

where,  $m_s$  (g) is the mass of surface-dry sample in air after water immersion;  $m_o$  (g) is the mass of oven-dried sample in air;  $V$  ( $\text{cm}^3$ ) is the total volume of specimen;  $\rho$  ( $1 \text{ g/cm}^3$ ) is the density of water.

#### 7.2.3.2 Sulphuric acid immersion

Acid attack procedure was designed based on the general principles provided in ASTM C267 and the previous work (Aiken et al., 2018, Zhang et al., 2018c, Živica, 2004). After cured for 28 days, the initial compressive strength of each mix is tested using an MTS universal mechanical testing machine with a loading speed of 1 mm/min. The mortar samples were immersed into water for 4 days to allow the samples to be fully saturated. This step could help to reduce the impact of initial penetration on the test results. The initial mass and volume of the saturated mortars were recorded before transfer samples from water to acid solutions. Then the mortars were transferred into 3% and 5% sulphuric acid solutions, respectively, with an acid solution to sample volume ratio of 1.0. But a group of samples that continued to immerse in water was set as the control group. The mass, volume and compressive strength of each mix exposed to water, 3% and 5% of sulphuric acid solutions were recorded after 7-, 14-, and 28-days of exposure, respectively. The water and acid solutions were replenished every week.

#### 7.2.4 Characterization

The paste samples were used for mineralogical degradation and microstructural analysis of each cementitious materials when exposed to sulphuric acid. After 28 days curing the dried paste samples were submerged in 3% sulphuric acid solution. Another batch of samples were submerged into water as control group. The samples were taken out from solutions after 28 days and dried at 60 °C oven overnight. The dried sample was cut in two from the middle. Part of samples was reserved for optical microscope observation. The inner part and outer part (as shown in Figure 7-2) of the sample were collected separately and ground into powder for characterization test.

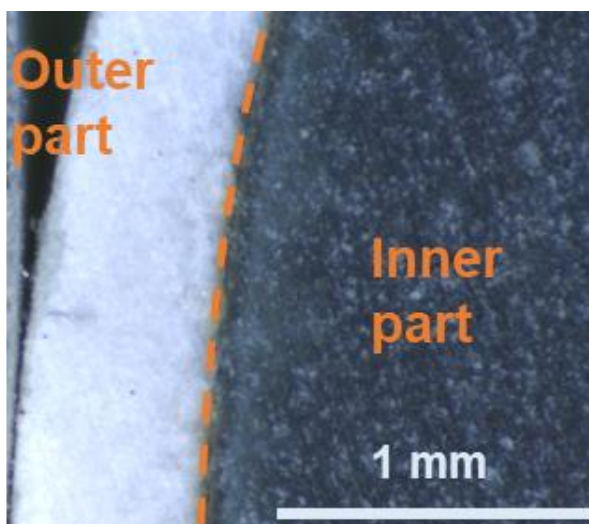


Figure 7-2. The cross-section photographs of the paste exposed to 3% sulphuric acid solution with clearly outer and inner parts.

The obtained powders were dried at 35 °C oven for 24 h before following characterisation test. X-ray diffraction (Bruker D8 Advance powder XRD) patterns were collected between 5 and 60° 2 $\theta$  with a step size of 0.02° 2 $\theta$ , using Cu K $\alpha$  radiation with wavelength 1.54 Å, at voltage 40 kV and current 40 mA. Jade 6 software with the powder diffraction file (PDF) database was used to analyse the diffraction patterns. Combined thermogravimetric analysis - differential thermogravimetric (TG-DTG) was conducted on TA Instruments Discovery SDT 650. The temperature was increased from room temperature up to 1000 °C at a rate of 10 °C/min in a nitrogen environment. The weight loss information obtained from the TG curve and first derivative (DTG) was used to confirm the type of hydrates and reaction products. Fourier transform infrared spectroscopy (FTIR) using Perkin Elmer FTIR-ATR spectrometer in absorbance mode from 4000 to 400 cm<sup>-1</sup>. Using absorbance values, the spectra were fitted using a baseline correction and deconvoluted in the range of 600 -1300 cm<sup>-1</sup> by Origin 9.1 (OriginLab Corporation, USA) with a Gaussian multi-peak fit module. Scanning electron microscopy with energy dispersive X-ray (SEM-EDX) was performed using a Hitachi SU3500 instrument equipped with a 50 mm<sup>2</sup> Oxford Instruments silicon drift detector. Analyses were made at 1000 - 10000 magnification at 5 - 15 kV with lower accelerator energies for imaging with secondary electron returns only and higher accelerator energies for imaging in backscatter mode and the EDX map analyses.

## 7.3 Results and discussion

### 7.3.1 Physical degradation

#### 7.3.1.1 Porosity

Figure 7-3 shows the volume of open pores at OPC and AAMs mortars. Three samples are used for each mix. OPC sample shows the lowest volume of open pores with VOP of 7.88%, while AAM\_1 sample shows the highest volume of open pores with VOP of 12.78%, following by AAM\_2, AAM\_3, and AAM\_4. The highest porosity of fly ash based AAM\_1 and AAM\_2 is likely related to the porous nature of the structure of the formed hydration products, i.e., N-A-S-H gel (Aiken et al., 2018).

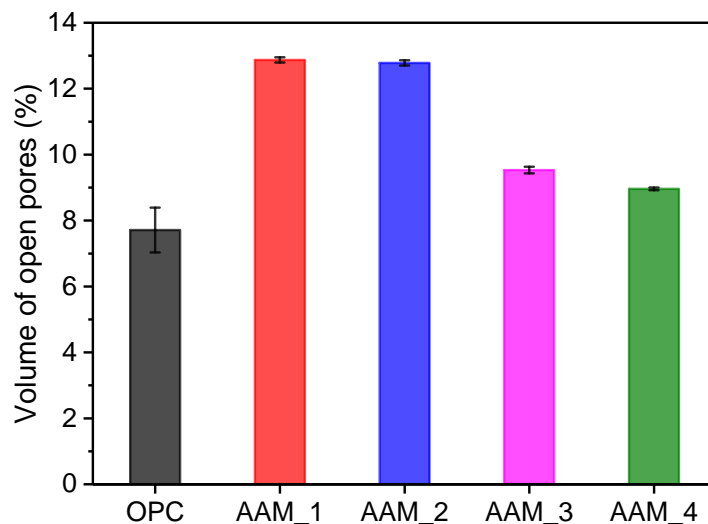


Figure 7-3. The volume of open pores of each sample.

#### 7.3.1.2 Visual appearance

Figure 7-4 displays the appearance of the OPC and AAMs mortars after exposed to water and sulphuric acid solutions for 28 days. The edges of AAM\_1 mortar slightly peeled off after 49 days of exposure to water. The other mortars exposed to water have no significant surface deterioration. The OPC mortars suffer visible damage after exposure to 3% sulphuric acid solution with peeling off the surface (sand particles have been exposed). As the acid concentration increased to 5%, the deterioration on the surface increases with the formation of white products. The AAM\_2 mortars have no damage after exposed to 3% sulphuric acid solution but have observed visible damage on the edges of the sample when exposed to 5% sulphuric acid. The AAM\_3

and AAM\_4 mortars form white products on the surface when exposed to 3% sulphuric acid. The damage on the edges of AAM\_3 and AAM\_4 mortars become visible when exposed to 5% sulphuric acid.

	Water	3% H <sub>2</sub> SO <sub>4</sub>	5% H <sub>2</sub> SO <sub>4</sub>
OPC			
AAM_1			
AAM_2			
AAM_3			



Figure 7-4. Photographs of cementing mortars after 28 days exposure to water, 3 and 5% solutions of sulphuric acid.

Figure 7-5 shows the truncated cross-section of the paste exposed to water and 3% sulphuric acid solution. For OPC and AAMs pastes exposed to water, there is limited change observed on the cross-section, while the slag-based AAM\_3 and AAM\_4 pastes generate slightly whitish products on the surface. After exposed to 3% sulphuric acid solution, the OPC and slag-based AAMs pastes could be clearly distinguished between the inner and outer parts. The outer part of exposed OPC sample shows yellow-white layer (131  $\mu\text{m}$ ) and brown layer (44  $\mu\text{m}$ ). The fly ash based AAM\_1 and AAM\_2 pastes exposed to sulphuric acid are divided into two parts with one yellow layer. There is one whitish layer formed for slag-based AAM\_3 and AAM\_4 pastes. The analysis on the different parts of each sample is shown in the following section.

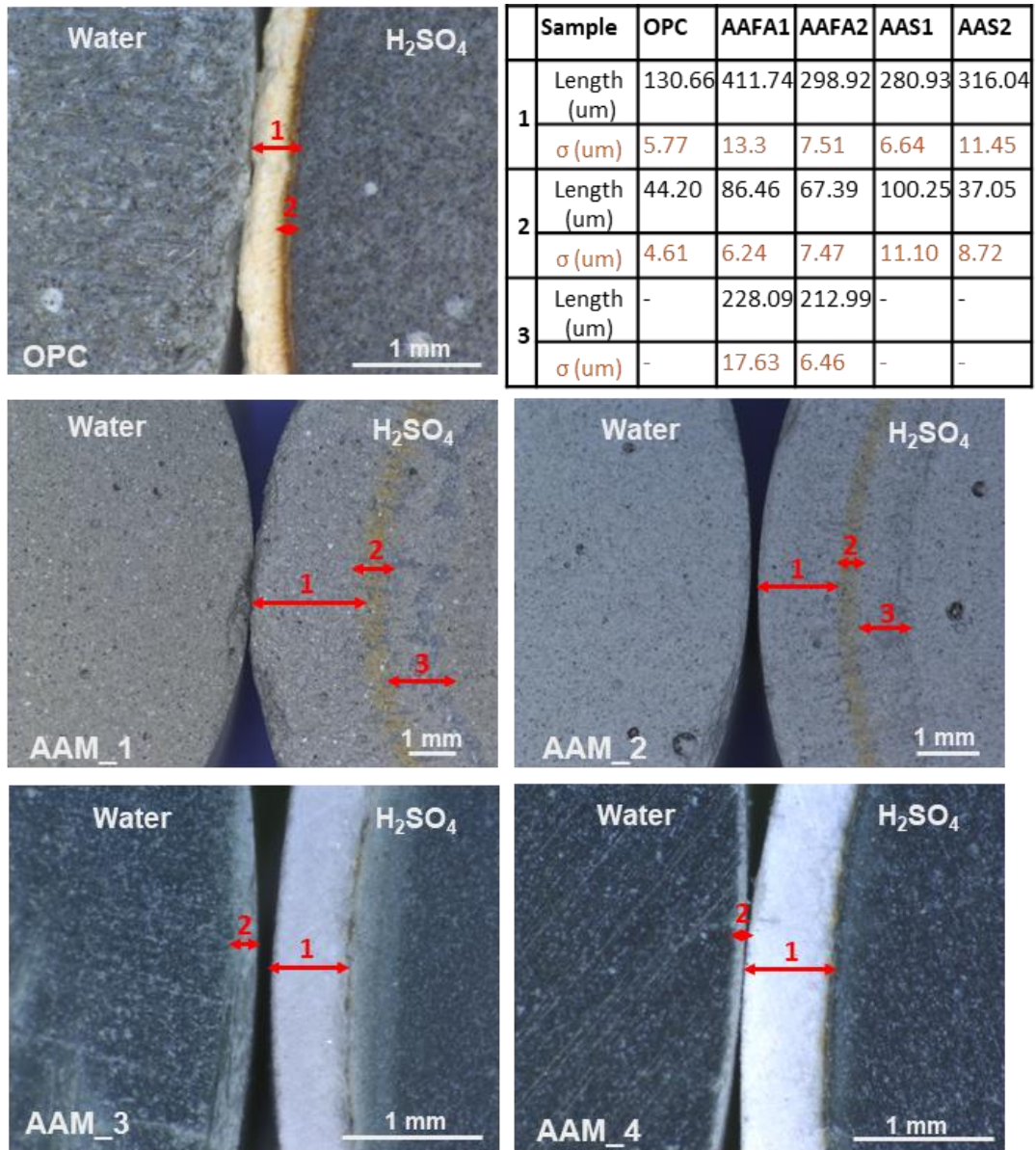


Figure 7-5. The truncated cross-section of the OPC and AAMs pastes exposed to water and 3% sulphuric acid solution.

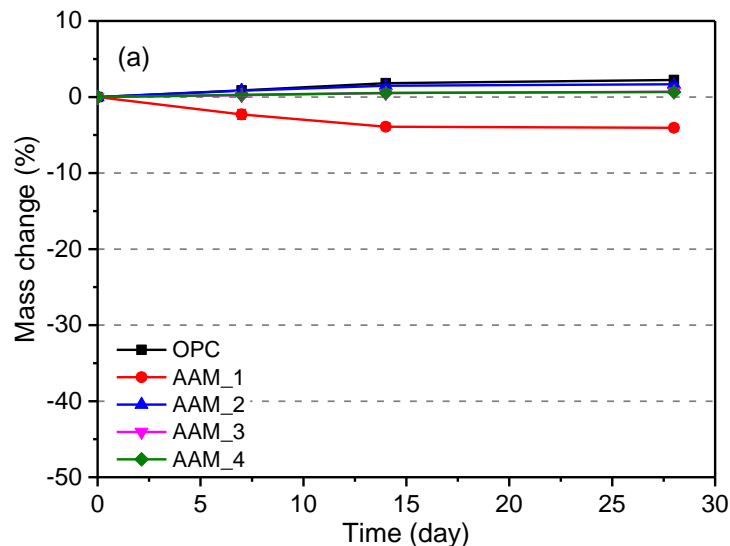
### 7.3.1.3 Mass change

Figure 7-6 displays the mass change of OPC and AAMs mortars during 28 days of exposure to water, 3% and 5% of sulphuric acid solutions. The positive values represent a mass gain, and the negative values represent a mass loss. As shown in Figure 7-6 (a), except for AAM\_1 which show continuous mass loss, the mass of other samples increased slightly. This is consistent with the observation of appearance of the samples. The mass of OPC mortars exposed to water increases slightly by 2.5%, followed by AAM\_2 by 1.6%, AAM\_3 and AAM\_4 by 0.6%. The increased mass for

each mortar exposed to water is due to the continued hydration of raw materials as the samples was pre-saturated with water before test.

After exposed to 3% sulphuric acid as shown in Figure 7-6 (b), the mass loss of OPC and AAM\_1 mortars is pronounced as the increases of exposure time. There is a mass gain for AAM\_2, AAM\_3 and AAM\_4 mortars whether exposed to water or sulphuric acid. The mass losses of OPC and AAM\_1 reach 20% and 30% respectively at 28 days. Compared to that exposed to water, the mass increment of AAM\_2 is unchanged while the mass of slag-based AAM\_3 and AAM\_4 increases by 2.8%. The significant mass increment of later is due to the formation of white products on the surface of the sample.

After exposed to 5% sulphuric acid as shown in Figure 7-6 (c), the mass loss of OPC mortars reaches 42%, while the mass loss of AAM\_1 is 26%. The mass of the other three mortars continually increases with the exposure time and the acid concentration. The AAM\_2 shows a finally mass increase of 3%. The increasing mass of AAMs is related to the formation of reaction products between samples and sulphuric acid. The final mass of the AAM\_3 and AAM\_4 samples also show an increasing trend despite the peeling of the surface layer as shown in the Figure 7-4.



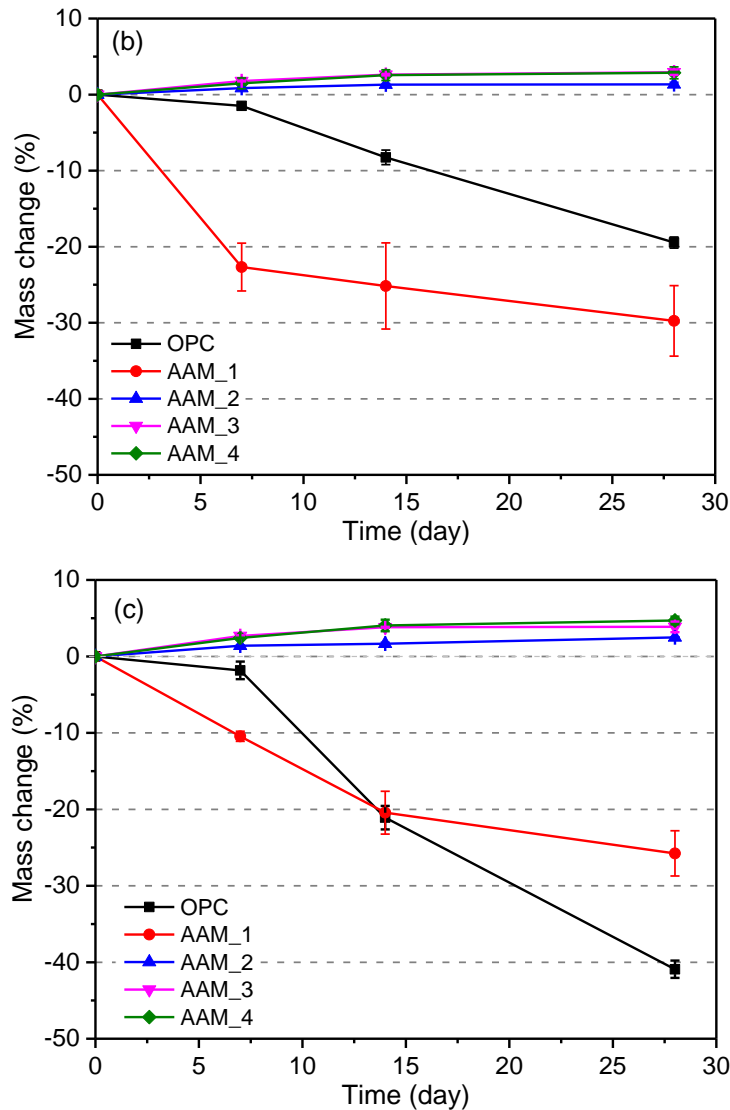


Figure 7-6. Mass change of different cementing mortars for 28 days of exposure to (a) water, (b) 3% sulphuric acid and (c) 5% sulphuric acid.

#### 7.3.1.4 Volume change

Figure 7-7 displays the volume change of each mix for 28 days exposure to water, 3% and 5% of sulphuric acid solutions. The positive values represent a volume gain, and the negative values represent a volume loss. The samples exposed to water has minor change on volume. Except for AAM\_2, the other mixes exposed to 3% sulphuric acid solution show an increased volume with the exposure time. The increased volume is consistent with the formation of expansive products on the surface of samples. The decreased volume of AAM\_2 is due to the surface exfoliation. After exposed to 5% of sulphuric acid solution, the volume of exposed AAM\_3 and AAM\_4 mortars are larger than that exposed to water and 3% of sulphuric solution, which means continued

increasing volume with the damage on the edges of the sample. The flaking of OPC and fly ash-based AAM mortars causes decreased volume.

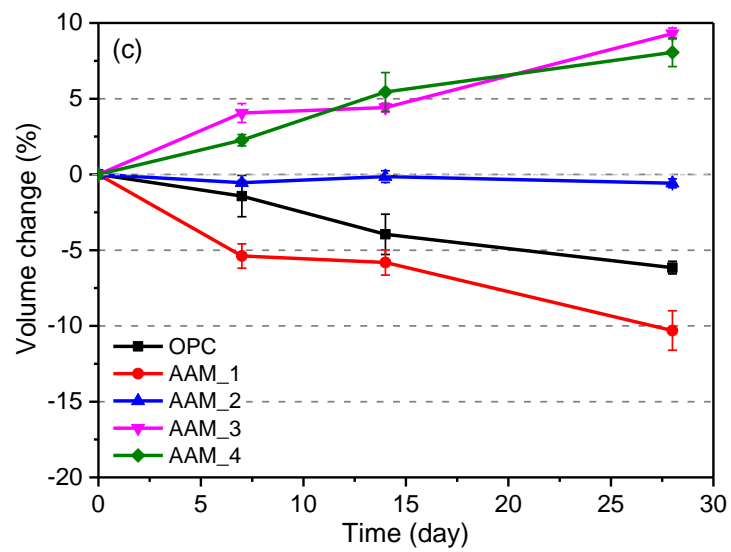
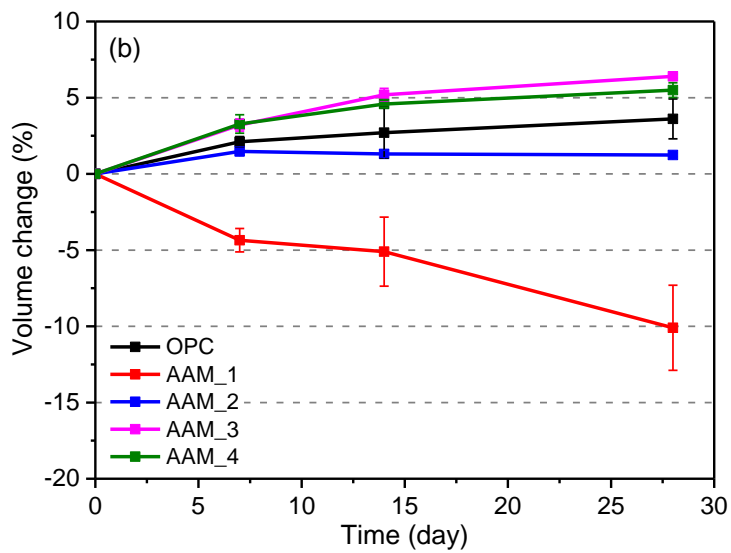
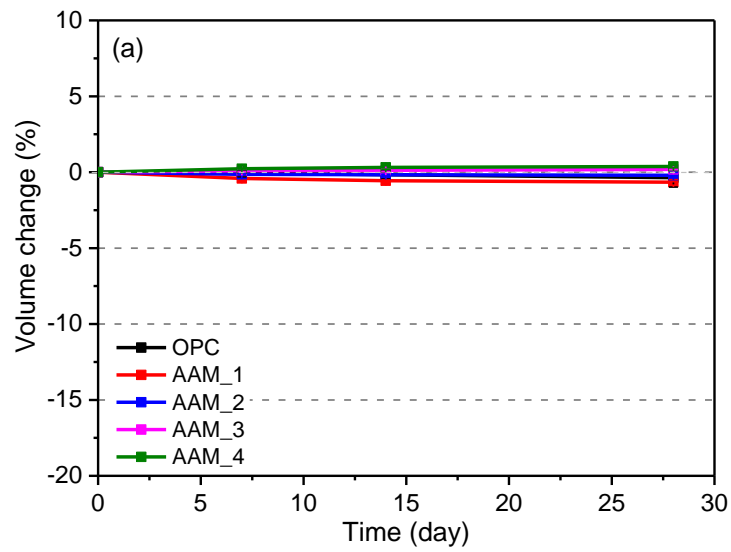


Figure 7-7. Volume change of different cementing mortars for 28 days of exposure to (a) water, (b) 3% sulphuric acid and (c) 5% sulphuric acid.

### 7.3.1.5 Compressive strength

Figure 7-8 shows the compressive strength change of each mortar during 28 days of exposure to water, 3% and 5% sulphuric acid solutions. The unexposed AAM\_4 mortar shows the highest initial compressive strength (65 MPa), following by AAM\_3 and OPC mortars (38 MPa and 28 MPa, respectively), and the fly ash based AAM\_1 mortar shows the lowest compressive strength (2 MPa). The compressive strength of the OPC mortars increased to 32 MPa after exposed to water for 7 days, while reduced to around 20 MPa later as extension of exposure time. The compressive strength of OPC mortars reduces to 18 MPa after 7 days exposure to 3% sulphuric acid. The strength loss is similar when acid concentration increases to 5%. There is a minor change among compressive strength of fly-ash based mortars exposed to either water or acid solution. For slag based AAM\_3 and AAM\_4 mortars, there is a big drop to around 23 MPa after exposed to water for 7 days. The strength latterly (14-day and 28-day) increases slightly to 25 MPa with the extension of exposure time to water. The compressive strength of the slag-based mortars exposed to sulphuric acid shows a tinny decrease trend with the increase of acid concentration.

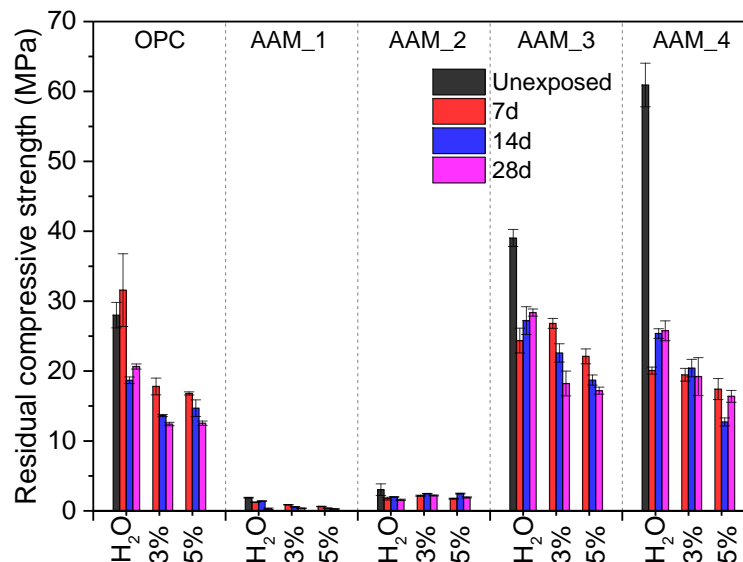


Figure 7-8. Compressive strength of PC, AAFA and AAS mortars during 28 days of exposure to (a) water, (b) 3% sulphuric acid and (c) 5% sulphuric acid.

### 7.3.2 Mineralogical degradation

#### 7.3.2.1 Fourier transform infrared spectroscopy (FTIR)

Figure 7-9 exhibits the FTIR spectra for the OPC and AAMs pastes after exposure to water and sulphuric acid. As shown in Figure 7-4, the exposed sample was divided into the inner and outer parts. Each part was collected and analysed separately.

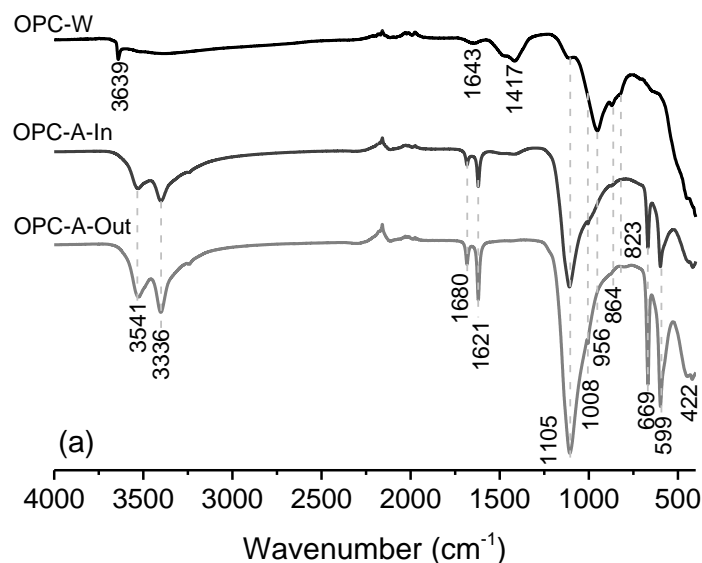
For OPC paste exposed to water, a main broad resonance locates at around  $954\text{ cm}^{-1}$  is attributed to the asymmetric stretching vibration of Si-O-T bonds, where T = Si or Al. The band at around  $1400\text{ cm}^{-1}$  is attributed to the vibration of C-O-C bonds from calcite generated in the sample. The bands at around  $1621\text{ cm}^{-1}$  and  $1680\text{ cm}^{-1}$  are attributed to the vibrations of -OH groups while the broad band at around  $3400\text{ cm}^{-1}$  is attributed to the vibrations of H-O-H group. The former indicates the presences of water molecules due to the crystallisation of reaction products and the later indicates the presence of free water absorbed by reaction products. The should at around  $1100\text{ cm}^{-1}$  which is attributed to the formation of gypsum becomes the strongest vibration of OPC paste after exposed to sulphuric acid solution. The peaks at 422, 599 and  $669\text{ cm}^{-1}$  are due to the formation of gypsum. The H-O-H vibration become intensive at around 3396 and  $3541\text{ cm}^{-1}$  which is due to the crystallization of water molecules in gypsum.

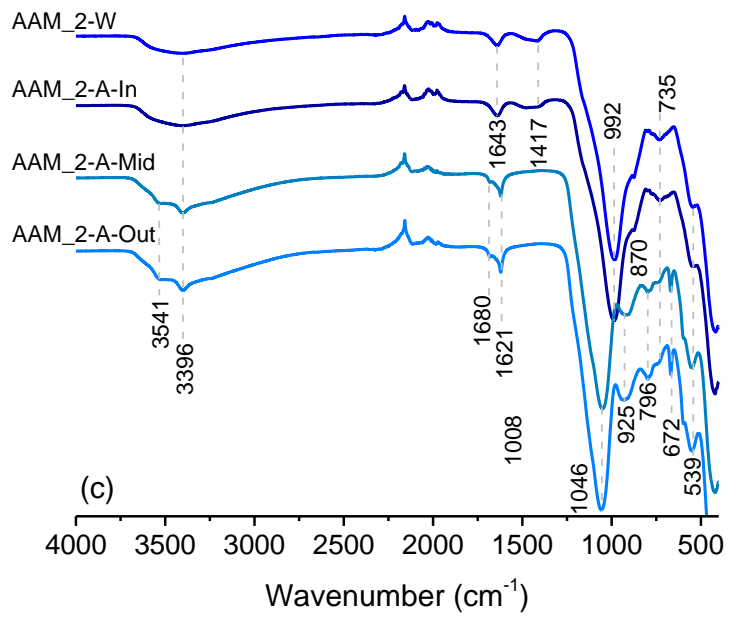
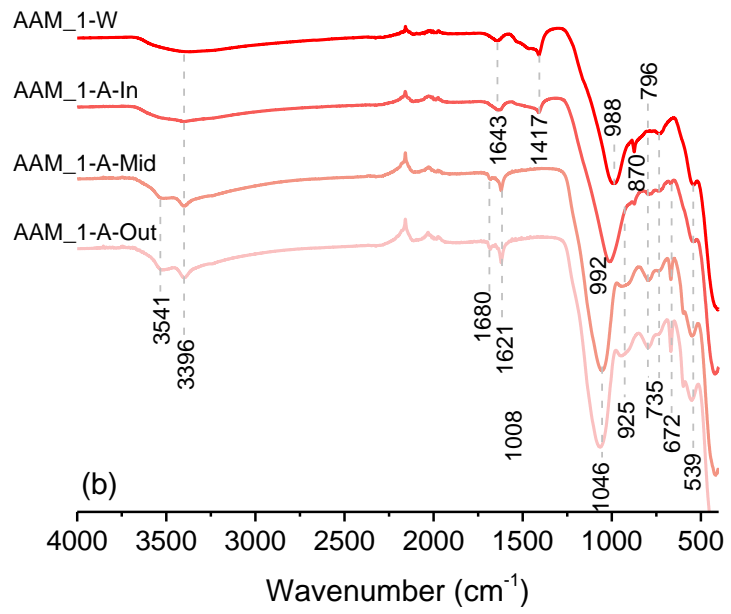
For AAM\_1 paste exposed to water, the main resonance is centred at around  $988\text{ cm}^{-1}$  and is assigned to the asymmetrical T-O stretch vibrations. Compared to OPC pastes, the main peak is located at a higher wavenumber indicating a lower Si/Al ratio in the reaction products. This is consistent with the T-O bonds centring at around  $1000\text{ cm}^{-1}$  on N-A-S-H gel, and possibly around  $970\text{ cm}^{-1}$  when presented at C-S-H gel. The reason for this phenomenon is likely the corporation of Al in the gel network. The inner part of AAM\_1 paste exposed to 3% sulphuric acid shows a similar spectrum to the sample exposed to water, indicating limited damage to the reaction products. However, the main peak of AAM\_1 paste exposed to 3% sulphuric acid shifts to a higher wavenumber at  $992\text{ cm}^{-1}$ . Then, the main peak of the outer part continually shifts to higher wavenumber at around  $1046\text{ cm}^{-1}$ . The shift of this peak from lower to higher wavenumber indicates an increase in the Si/Al ratio. This is due to the acid corrosion of the reaction products resulting in aluminium ejection from the N-A-S-H gel. The small peaks located at around 3541, 3336, 1680, 1621, 956, 864, 669, and

599  $\text{cm}^{-1}$  could be assigned to the characteristic peaks of gypsum. The AAM\_2 paste presents similar FTIR results as AAM\_1 except that the main peak of former is located at a slightly higher wavenumber.

There are two parts for slag based AAM\_3 and AAM\_4 pastes when they are exposed to water. For the inner parts exposed to water, the main peak is located at around 945 or 939  $\text{cm}^{-1}$  which indicates the formation of T-O bonds. Two small peaks between 1416 and 1409  $\text{cm}^{-1}$  are typical of stretching vibration of C-O bonds. The bands at around 3400 and 1658  $\text{cm}^{-1}$  are assigned to the water modular presenting at reaction products. The outer parts exposed to water shows an intensive peak at around 877  $\text{cm}^{-1}$  and a broad brand at around 1500  $\text{cm}^{-1}$  which are contributed to the vibration of C-O bonds in carbonates. Exposure to water results in the diffusion of cations (like  $\text{Ca}^{2+}$  and  $\text{Na}^+$ ) and the formation of carbonates. There is minor difference between the inner parts exposed to sulphuric acid and water. This indicates that the acid corrosion on the inner part of AAM\_3 and AAM\_4 pastes is minor. The outer parts of slag based AAMs paste which exposed to sulphuric acid solution show a similar spectrum to the outer part of OPC, indicating the formation of gypsum.

The outer parts of OPC and slag based AAMs exposed to sulphuric solution are similar. But it should be noted that no surface exfoliation on the pastes despite the formation of expansive gypsum. The fly ash based AAMs pastes exhibit decomposition of the reaction products from outside to inside under acid etching. This is different from the behaviour of mortars when exposed to sulphuric acid.





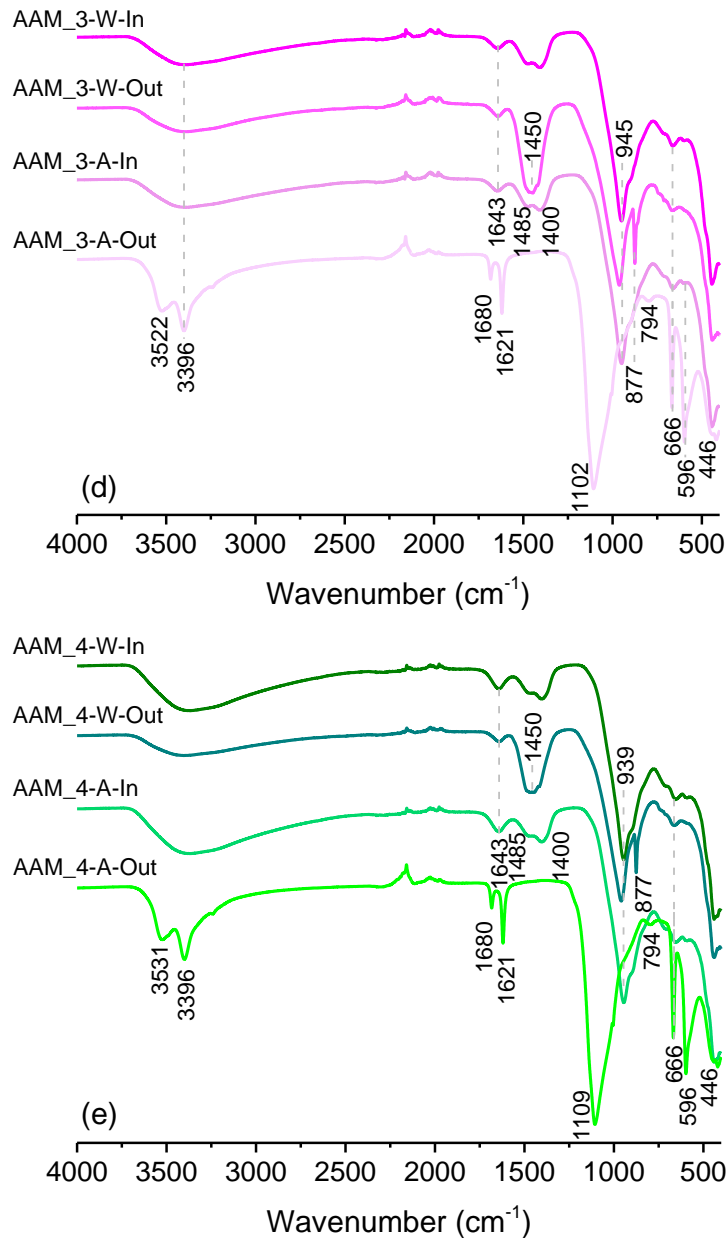


Figure 7-9. FTIR spectra of (a) OPC, (b) AAM\_1, (c) AAM\_2, (d) AAM\_3 and (e) AAM\_4 pastes exposure to water and sulphuric acid. The inner and outer part are tested separately.

### 7.3.2.2 Thermogravimetric analysis (TGA)

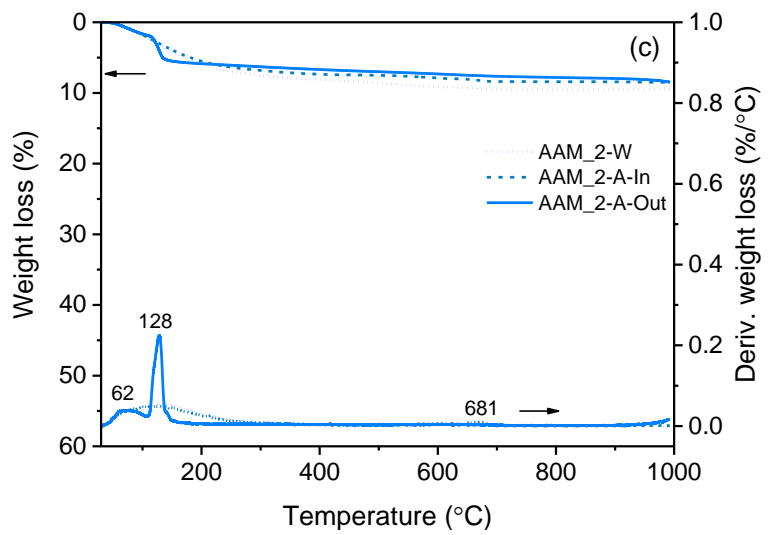
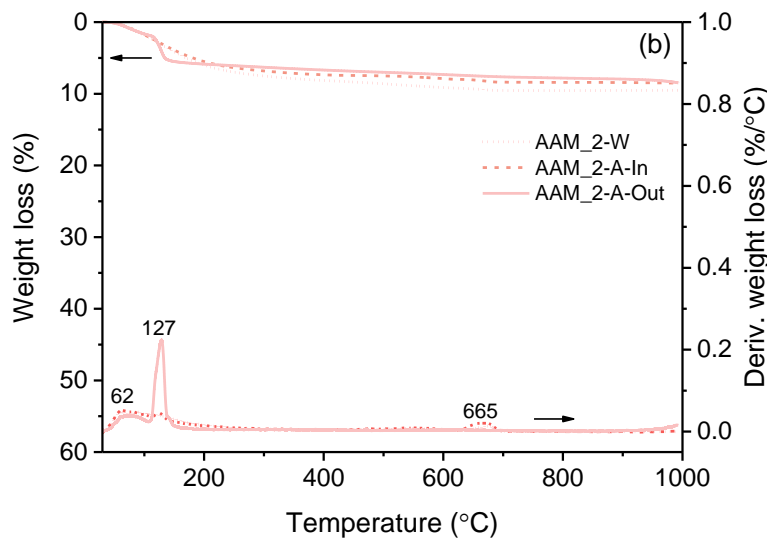
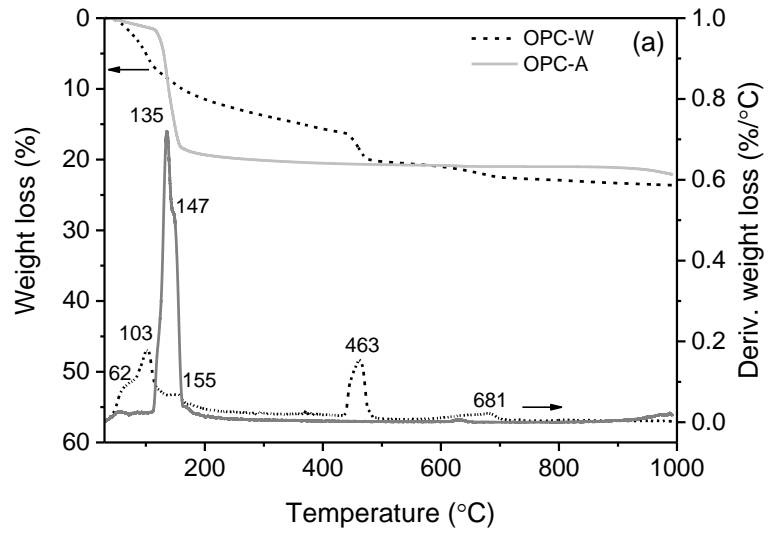
Figure 7-10 displays the TGA-DTG data for each mix when exposed to water and 3% sulphuric acid solution. As known the inner parts of OPC and slag based AAM pastes exposed to sulphuric acid have minor change compared to that exposed to water, so just the inner part of sample exposed to water is tested. The OPC and slag based AAM pastes show eventual mass losses between 20% and 25% in the testing period, while the fly ash based AAM pastes shows a mass loss of 10%. From the DTG data, the

lower mass loss for AAM\_1 and AAM\_2 pastes might be due to the lower water loss at around 127 °C.

The mass loss of OPC paste exposed to water continues up to around 700 °C, while showing main peaks centred at 105 °C, 463 °C and 677 °C, respectively. The small shoulder at 61 °C is contributed to the loss of free water while another small shoulder at 155 °C is contributed to decomposition of AFm phases such as semi-carbonate. The main peak at 105 °C is contributed to the decomposition of the reaction products (C-S-H gel). The peak at 463°C is contributed to the decomposition of calcium hydroxide, while the small peak at 677 °C is contributed to the decomposition of carbonates. For the outer part of OPC paste exposed to sulphuric acid, the mass loss mainly happens between 100 and 170 °C and the mass loss peak centers at around 134 °C. This is consistent with the decomposition character of gypsum exposed high temperature.

For AAM\_1 and AAM\_2 pastes exposed to water, there is a broad mass loss peak happened in the range between 50 and 300 °C which is contributed to the dehydration of reaction production (N-A-S-H). The small shoulder at around 61 °C is due to the loss of free water. The inner parts of AAM\_1 and AAM\_2 pastes show similar thermogravimetric data no matter exposed to water or sulphuric acid. The outer part of AAM\_1 and AAM\_2 pastes exposed to sulphuric acid shows a dominant mass loss peak centered at around 128 °C which is assigned to the decomposition of sulphates.

The AAM\_3 and AAM\_4 pastes exposed to water shows a continued mass loss to around 600 °C with the main loss peak is centered at around 94 °C. The mass loss before 100 °C is due to the removal of free water from the sample, while the dehydration of C-A-S-H gels contributes to the later mass loss. The outer parts of AAM\_3 and AAM\_4 pastes exposed to sulphuric acid show similar thermogravimetric data like the outer part of OPC paste, which is consistent with that similar gypsum formed in the OPC and slag based AAM pastes.



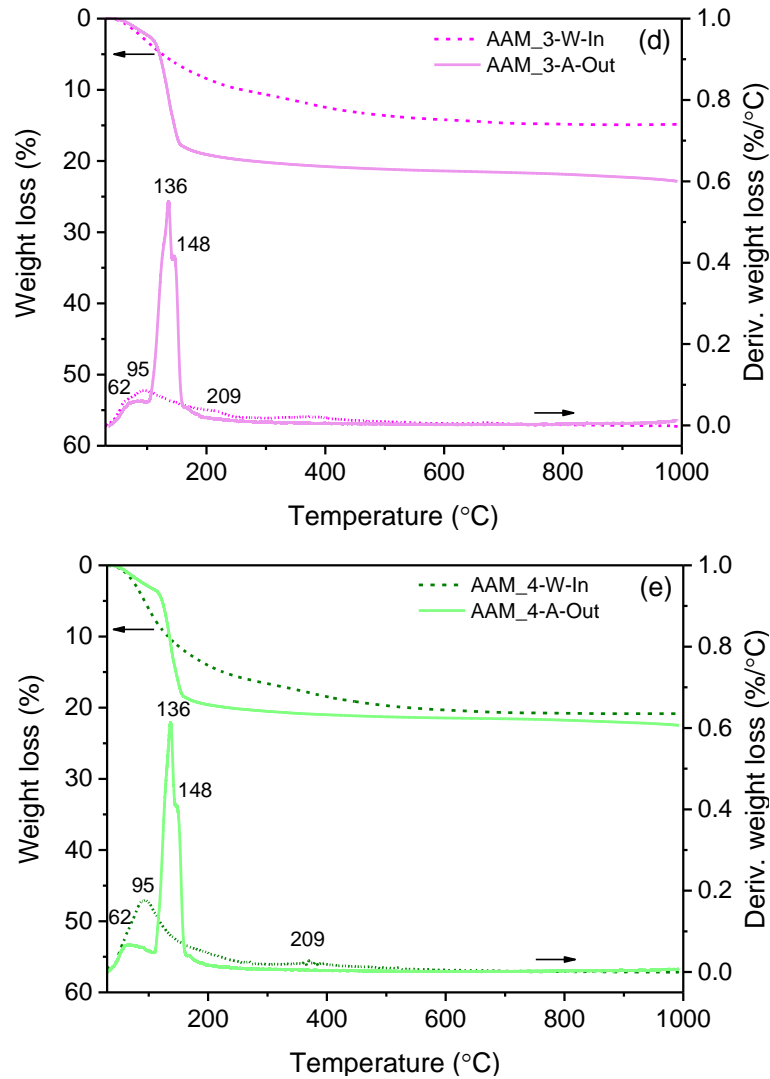


Figure 7-10. The TGA-DTG data of (a) OPC, (b) AAM\_1, (c) AAM\_2, (d) AAM\_3 and (e) AAM\_4 pastes exposure to water and sulphuric acid solution.

### 7.3.3 Microstructural change

#### 7.3.3.1 Scanning electron microscopy (SEM) and energy dispersive X-ray (EDX) analysis

Figure 7-11 shows the SEM images of each paste exposed to sulphuric acid for 28 days. The unreacted fly ash and slag particles could be clearly distinguished from the SEM images of sample AAM\_1 and AAM\_3. The increased SiO<sub>2</sub> content in the activator promotes the reaction of the raw materials (as shown in AAM\_2) and further increases the compressive strength.

Figure 7-12 shows the BSE images and elemental maps of the outer parts of OPC, AAM\_2 and AAM\_4 after exposure to 3% sulphuric acid for 28 days. The calcium

(Ca), silicon (Si), aluminium (Al) and sulphur (S) show almost indistinguishable distribution in samples OPC. It means the corrosive ionic sulphur has entered the interior of the sample. However, for sample AAM\_2, it is interesting to find that the immigration of sulphur is less and exists in the interior of the sample. At the edge of the AAM\_2 sample, the calcium is partially precipitated from the sample, while there is little change in the sodium and aluminium. For sample AAM\_3, the sulphur mainly accumulates on the surface of the sample and the content gradually decreases with erosion depth. It is interesting to find that the sodium also accumulates on the surface of the samples. However, the reason of aggregation for sodium and sulphur is different. Sodium diffuses gradually from the inside of the sample to the surface, while sulphur is the opposite. Figure 7-13 shows the chemical analysis of different elements relative content measured by EDX line scan after 28 days of immersion in the sulphuric acid. We could find there is a cross between Si and Al at around 400  $\mu\text{m}$ , which might be due to the presence of crystalline at this position. Minor chemical change was found among Na, Al, Si and Ca.

Figure 7-14 shows the BSE and elemental maps of the high magnification AAM\_2 and AAM\_3 pastes after exposed to sulphuric acid for 28 days. sulphur is hardly collected from the sample AAM\_2. For AAM\_3, the sulphur is found to accumulate around the partially reacted slag particles. The reason for this phenomenon might be that the existence of the weak interfacial zone leads to more pore retention of sulphur, on the other hand, the calcium content is higher around the slag particles, where the sulphur element accumulates.

From the results, we could find that the low calcium content in fly ash based AAMs is insufficient to form observable swelling calcium sulphate. And the calcium in fly ash based AAMs easily diffuse out of the sample. When the calcium content is not enough to form calcium sulphate, there is not enough ionic force inside the sample to maintain a high sulphur content. For OPC and slag-based AAMs, the high calcium content inside samples promotes the adsorption of sulphide ions once exposed to sulphuric acid. And the formation of calcium sulphate slowly invades from the outside of the sample to the inside

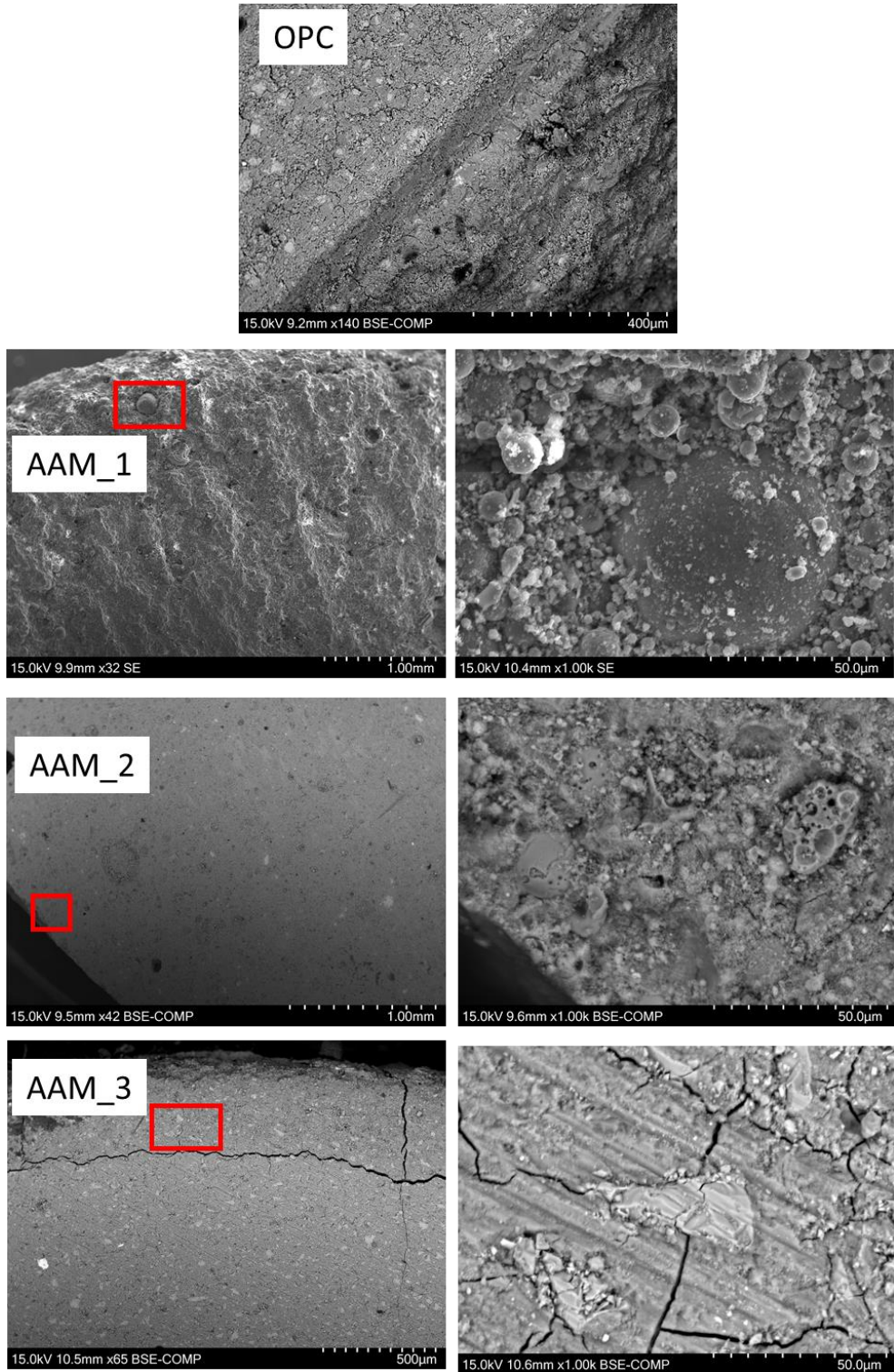


Figure 7-11. SEM images of the OPC, AAM\_1, AAM\_2, and AAM\_3 pastes after exposed to sulphuric acid for 28 days.

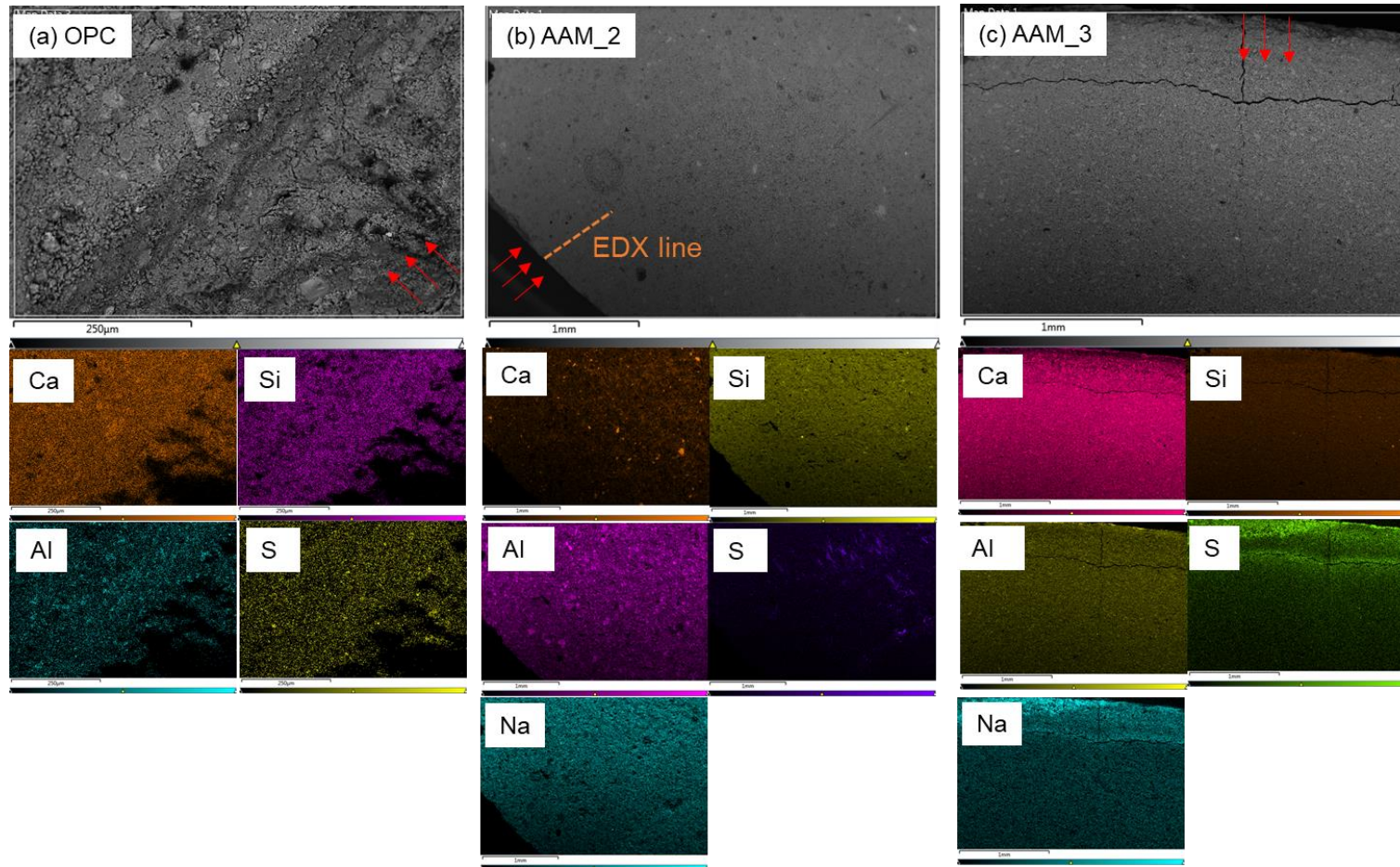


Figure 7-12. BSE images and elemental maps of the (a) OPC, (b) AAM\_2 and (c) AAM\_3 after exposed to sulphuric acid for 28 days. The elemental analysis shows the distribution of calcium (Ca), sulphur (S), silicon (Si), aluminium (Al) and sodium (Na). The red arrow represents the direction of sulphuric acid attack.

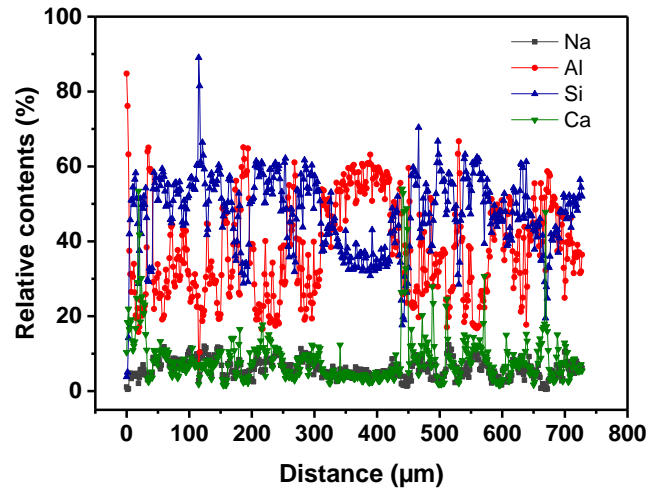


Figure 7-13. Chemical analysis of different elements relative content measured by EDX line scan after 28 days of immersion in the sulphuric acid.

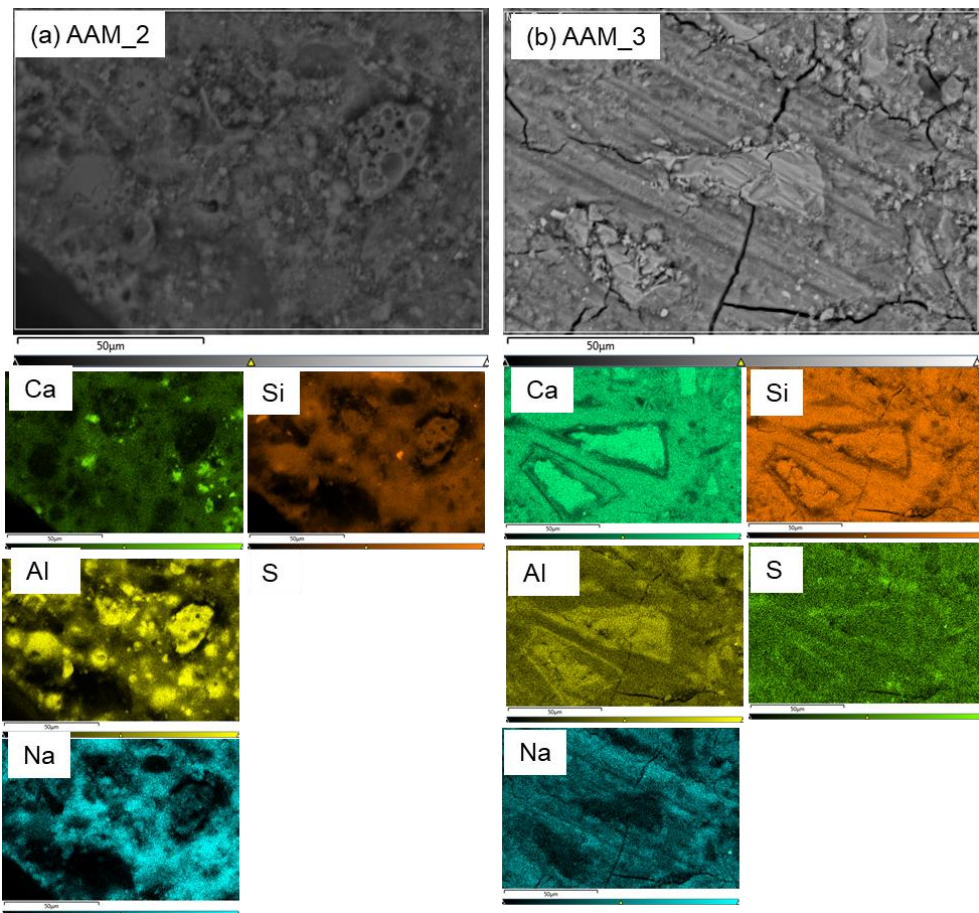


Figure 7-14. BSE images and elemental maps of the high magnification (a) AAM\_2 and (b) AAM\_3 after exposed to sulphuric acid for 28 days. The elemental analysis shows the distribution of calcium (Ca), sulphur (S), silicon (Si), aluminium (Al) and sodium (Na). The red arrow represents the direction of sulphuric acid attack.

## 7.4 Concluding remarks

In this chapter, the degradation process of the AAMs derived from different precursors was analysed. It was found that not only the raw materials have a greater impact on the acid corrosion mechanism of different AAMs, but also the failure principles of mortar and paste are different.

- The AAMs derived from fly ash shows more obvious mass loss and volume loss than that derived from slag under sulphuric acid attack, and the lower initial compressive strength is difficult to meet the practical engineering needs. For slag-based AAMs, the increased SiO<sub>2</sub> content could greatly improve the initial compressive strength but have less effect on the residual strength under sulphuric acid attack.
- From the results, it could be found that the failure of OPC and AAMs mortars exposed to sulphuric acid is mainly due to the peeling of the surface. The hydration products from the paste reacts with sulphuric acid to form expansive calcium sulphates. The calcium sulphates mainly exist in the weak area between the slurry and the fine aggregate, and the expansion stress causes the peeling. For pastes, the paste gradually reacts with sulphuric acid to form calcium sulphate, but the expansion stress will not cause spalling.
- For low-Ca AAMs derived from fly ash, minor sulphur intrudes into the sample, while the high-Ca AAMs derived from slag attracts more sulphur. The higher calcium content in AAMs attracts more sulphur into the sample due to the high ionic force between Ca<sup>2+</sup> and SO<sub>4</sub><sup>2-</sup>.

## CHAPTER 8. CONCLUSIONS AND RECOMMENDATIONS

### 8.1 Conclusions

The aim of this thesis was to explore the intrinsic degradation mechanism of alkali-activated materials (AAMs) exposed to sulphuric acid environment and provide fundamental knowledge for the application of the AAMs as high acid-resistance materials in practise. The research work included the synthesis of pure AAMs (i.e., N-A-S-H gel and C-(N)-A-S-H gel), the investigation on the degradation of the pure AAMs, the effect of the chemical composition of C-(N)-A-S-H/N-A-S-H gels on the acid resistance and the relationship between the industrial AAMs and synthesized AAMs when exposed to sulphuric acid.

The literature review in Chapter 2 declared the vacation of a clear degradation mechanism of AAMs when exposed to acid, understanding of the role of the Ca-Al-Si ratios in degradation and decomposition of the C-(N)-A-S-H/N-A-S-H gels, and the suggestion on the practice application of AAMs in acidic environment as the existence of contradictory conclusions. The criteria for judging acid resistance of AAMs are indicant as the complexity of the AAMs which is due to its wide sources of precursors and alkali-activation conditions. Understanding the decomposition of pure AAMs under acidic conditions without any contamination is a straightforward method. Building the relationship between pure materials and industrial materials, and to provide valuable references for the practical application of AAM are important and urgent.

To ensure the consistency of the physical and chemical properties of the synthesized precursors and industrial materials, except for the impurities, Chapter 4 compared the pure and industrial materials by application of characteristic methods, i.e., X-ray diffraction, Fourier transform infrared spectroscopy, and X-ray fluorescence etc. The synthesized calcium-free precursors are compared to the low-calcium fly ash and metakaolin. The calcium-free precursors are mainly amorphous with a higher surface area and higher amount of absorbed water during sample preparation. The synthesized precursors used stoichiometrically controlled routine at the laboratory showed indistinguishable characteristics with fly ash and metakaolin. Different chemical compositions of the synthesized precursors have minor effect on the characterization

results. The calcium content in the calcium aluminosilicate powders promotes the formation of crystalline phases, but with minor effect on the reactivity (Chapter 5 and 6). This chapter proved that the synthesized routines could be an effective method for the intrinsic investigation of alkali-activated materials in acidic environment.

To compare the different degradation of N-A-S-H and C-(N)-A-S-H gels exposed to sulphuric acid, Chapter 5 discovered that dealumination dominated the microstructural change of N-A-S-H gel under the sulphuric acid attack. This dealumination had minor effect on the bulk structure integrity (but not sure about the impact on micromechanical properties). The C-(N)-A-S-H gel showed both dealumination and decalcification, together with significant and rapid loss of sodium and slow loss of silicon. In addition to the normal mechanism that gypsum forms and leads to cracking at sulphuric and sulphate conditions, an important finding is that dealumination and the loss of sodium continues after decalcification and the loss of a small amount of silicon. The non-crosslinked C-(N)-A-S-H gel reduced with decrease of Si/Al ratio after exposure to sulphuric acid, while the Si/Al ratio of N-A-S-H gel increased. One common feature for the two types of AAM gels is that after acid attack, silicate polymerization degree ( $Q^4$  concentration) increases, especially for C-(N)-A-S-H gel. Further exploration on the acid corrosion mechanism of the C-(N)-A-S-H gel could focus on the effect of Ca/Si ratio. However, the formation of coarse crystalline gypsum grains is still the controlling factor to structural destroy and needs to be controlled.

The effect of Ca/Si ratio and Al/Si ratio on the degradation of the C-(N)-A-S-H/N-A-S-H gel was investigated in Chapter 6. The calcium content in C-(N)-A-S-H/N-A-S-H gel had influence on the leaching of aluminium, while higher concentration of aluminium was leached out from low-calcium samples. This indicates that the calcium content in the mixture promoted the resistance of samples to dealumination when exposed to sulphuric acid. This chapter confirmed the reactivity of the calcium-containing precursors. And the formation of additional reaction products (i.e., calcium aluminosilicate hydrate and calcium hydroxide) in high aluminium high calcium samples is likely decomposed prior to C-(N)-A-S-H/N-A-S-H gels which suggest that it could help to retard the attack of sulphuric acid on the C-(N)-A-S-H/N-A-S-H gels. The negative effect of calcium hydroxide with the formation of expansive products is not negligible, while an optimal calcium content in the AAMs should be considered.

The calcium prevented the leaching of silicon from high-calcium samples, suggesting that the strength of the Si-O bond in N-A-S-H gel appeared weaker than the C-(N)-A-S-H gel. When exposed to sulphuric acid, the silicon chains length of the C-(N)-A-S-H gel increases with increased Si/Al ratio. However, the chain length of the N-A-S-H gel increases with reduced Si/Al ratio. The AAMs derived from pure precursors with designed mixture composition show comparable macroscopic destruction to that derived from industrial materials under sulphuric acid attack. From the gel destruction mechanism, the findings presented in this chapter show that the re-polymerisation of silicon chains happening in both C-(N)-A-S-H gel and N-A-S-H gel due to the dealumination under acid attack. This work highlighted the need to design an optimal Ca/Al ratio in the AAMs for required behavior in the acid environment.

Chapter 7 investigated the acid degradation of alkali-activated fly ash and alkali-activated slag. This chapter found that the AAMs derived from fly ash showing more serious physical degradation compared to that derived from slag and Portland cement samples. The main reason for the less sulphur content inside samples was due to the less calcium content. It was found that not only the raw materials have a greater impact on the acid corrosion mechanism of different AAMs, but also the failure principles of mortar and paste are different. Compared to Portland cement samples, samples derived from slag showed higher initial compressive strength but more significant deduction after exposed to sulphuric acid.

## **8.2 Recommendations**

This work provides fundamental knowledge regarding to the acid degradation of the alkali-activated materials (AAMs), i.e., C-(N)-A-S-H and N-A-S-H gels. Based on the conclusions from the work, the following recommendations are need further investigated, before AAMs could be fully controlled and applied in the real acidic environment.

- The effect of acid anions on the synthesized C-(N)-A-S-H and N-A-S-H gels should be explored in the following research. The  $\text{SO}_4^{2-}$  has a significant influence on the reaction products of synthesized calcium-containing gels in sulphuric acid solution. Efforts are still needed in order to understand the

degradation mechanism of synthesized gels without the influence of reaction products.

- The simpler and stronger relationship between synthesized and industry precursors should be built to guide practical applications using synthesized precursors. This requires the synthesis of more proportioned raw materials to obtain clear relationships between elemental compositions and acid degradation.
- The influence elements in raw materials such as magnesium and iron need to be explored. As known, the magnesium is an important ingredient in the formation of alkali-activated materials. There are few studies investigating the role of magnesium in the acid degradation of alkali-activated materials.

## REFERENCES

- GB/T 18046-2017 Ground granulated blast furnace slag used for cement, mortar and concrete. 2017 (in Chinese).
2012. Standard Test Methods for Chemical Resistance of Mortars, Grouts, and Monolithic Surfacing and Polymer Concretes. *ASTM C267-01(2012)*. West Conshohocken, PA: ASTM International.
- AHMAD MUHD IZZAT, A. M. M. A. B., HUSSIN KAMARUDIN, ANDREI VICTOR SANDU, GHAZALI CHE MOHD RUZAIDI, MOHD TAHIR MUHAMMAD FAHEEM, LIGIA MIHAELA MOGA 2013. Sulfuric Acid Attack on Ordinary Portland Cement and Geopolymer Material. *REV. CHIM. (Bucharest)*, 64, 4.
- AIKEN, T. A., KWASNY, J., SHA, W. & SOUTSOS, M. N. 2018. Effect of slag content and activator dosage on the resistance of fly ash geopolymer binders to sulfuric acid attack. *Cement and Concrete Research*, 111, 23-40.
- AIKEN, T. A., SHA, W., KWASNY, J. & SOUTSOS, M. N. 2017. Resistance of geopolymer and Portland cement based systems to silage effluent attack. *Cement and Concrete Research*, 92, 56-65.
- ALARCON-RUIZ, L., PLATRET, G., MASSIEU, E. & EHRLACHER, A. 2005. The use of thermal analysis in assessing the effect of temperature on a cement paste. *Cement and Concrete Research*, 35, 609-613.
- ALEKSANDRA, K.-P., SLOBODANKA, M., SVETLANA, P., MIRJANA, D. & JASNA, D. 2005. The treatment of gypsum as a product of the flue gas desulphurization process. *Ceramics-Silikáty*, 49, 115-119.
- ALEXANDER, M. & BEUSHAUSEN, H. 2019. Durability, service life prediction, and modelling for reinforced concrete structures – review and critique. *Cement and Concrete Research*, 122, 17-29.
- ALEXANDER, M. & FOURIE, C. 2011. Performance of sewer pipe concrete mixtures with portland and calcium aluminate cements subject to mineral and biogenic acid attack. *Materials and Structures*, 44, 313-330.
- ALIQUES-GRANERO, J., TOGNONVI, T. & TAGNIT-HAMOU, A. 2017. Durability test methods and their application to AAMs: case of sulfuric-acid resistance. *Materials and Structures*, 50, 1-14.
- ALLAHVERDI, A. & ŠKVÁRA, F. 2001. NITRIC ACID ATTACK ON HARDENED PASTE OF GEOPOLYMERIC CEMENTS - PART 1. *Ceramics-Silikáty*, 45, 8.
- ALLAHVERDI, A. & ŠKVÁRA, F. 2005. SULFURIC ACID ATTACK ON HARDENED PASTE OF GEOPOLYMER CEMENTS: PART 1. MECHANISM OF CORROSION AT RELATIVELY HIGH CONCENTRATIONS. *Ceramics-Silikáty*, 49, 5.
- ALLAHVERDI, A. & ŠKVÁRA, F. 2006. SULFURIC ACID ATTACK ON HARDENED PASTE OF GEOPOLYMER CEMENTS: PART 2. CORROSION MECHANISM AT MILD AND RELATIVELY LOW CONCENTRATIONS. *Ceramics-Silikáty*, 50, 4.
- ANDERSEN, M. D., JAKOBSEN, H. J. & SKIBSTED, J. 2006. A new aluminium-hydrate species in hydrated Portland cements characterized by <sup>27</sup>Al and <sup>29</sup>Si MAS NMR spectroscopy. *Cement and Concrete Research*, 36, 3-17.
- ARIFFIN, M. A. M., BHUTTA, M. A. R., HUSSIN, M. W., MOHD TAHIR, M. & AZIAH, N. 2013. Sulfuric acid resistance of blended ash geopolymer concrete. *Construction and Building Materials*, 43, 80-86.

- ASTM 2019. Standard Specification for Coal Fly Ash and Raw or Calcined Natural Pozzolan for Use in Concrete. *ASTM C618-19*. West Conshohocken, PA: ASTM International.
- AYDİN, S. & BARADAN, B. 2014. Effect of activator type and content on properties of alkali-activated slag mortars. *Composites Part B: Engineering*, 57, 166-172.
- BACHU, S. & GUNTER, W. D. 2005. Overview of acid-gas injection operations in western Canada. *Greenhouse Gas Control Technologies 7*. Elsevier.
- BAI, T., SONG, Z.-G., WU, Y.-G., HU, X.-D. & BAI, H. 2018. Influence of steel slag on the mechanical properties and curing time of metakaolin geopolymer. *Ceramics International*, 44, 15706-15713.
- BAKHAREV, T. 2005. Resistance of geopolymer materials to acid attack. *Cement and Concrete Research*, 35, 658-670.
- BAKHAREV, T., SANJAYAN, J. G. & CHENG, Y. B. 2003. Resistance of alkali-activated slag concrete to acid attack. *Cement and Concrete Research*, 33, 1607-1611.
- BAŠČAREVIĆ, Z., KOMLJENOVIĆ, M., MILADINOVIĆ, Z., NIKOLIĆ, V., MARJANOVIĆ, N., ŽUJOVIĆ, Z. & PETROVIĆ, R. 2013. Effects of the concentrated  $\text{NH}_4\text{NO}_3$  solution on mechanical properties and structure of the fly ash based geopolymers. *Construction and Building Materials*, 41, 570-579.
- BECKWITH, R. 2011. Carbon capture and storage: a mixed review. *Journal of Petroleum Technology*, 63, 42-45.
- BELKOWITZ, J. S., BELKOWITZ, W. L. B., NAWROCKI, K. & FISHER, F. T. 2015. Impact of nanosilica size and surface area on concrete properties. *ACI Materials Journal*, 112, 419-427.
- BERGER, S., NOLDE, J., YÜKSEL, T., TREMEL, W. & MONDESHKI, M. 2018.  $^{27}\text{Al}$  NMR Study of the pH Dependent Hydrolysis Products of  $\text{Al}_2(\text{SO}_4)_3$  in Different Physiological Media. *Molecules*, 23, 808.
- BERNAL, S., RODRÍGUEZ, E., MEJÍA DE GUTIÉRREZ, R. & PROVIS, J. 2012a. Performance of alkali-activated slag mortars exposed to acids. *Journal of Sustainable Cement-Based Materials*, 1, 138-151.
- BERNAL, S. A., MEJÍA DE GUTIÉRREZ, R., PEDRAZA, A. L., PROVIS, J. L., RODRIGUEZ, E. D. & DELVASTO, S. 2011a. Effect of binder content on the performance of alkali-activated slag concretes. *Cement and Concrete Research*, 41, 1-8.
- BERNAL, S. A. & PROVIS, J. L. 2014. Durability of alkali - activated materials: progress and perspectives. *Journal of the American Ceramic Society*, 97, 997-1008.
- BERNAL, S. A., PROVIS, J. L., ROSE, V., GUTIÉRREZ, R. M. & BIERNACKI, J. 2013a. High - Resolution X - ray Diffraction and Fluorescence Microscopy Characterization of Alkali - Activated Slag - Metakaolin Binders. *Journal of the American Ceramic Society*, 96, 1951-1957.
- BERNAL, S. A., PROVIS, J. L., ROSE, V. & MEJÍA DE GUTIERREZ, R. 2011b. Evolution of binder structure in sodium silicate-activated slag-metakaolin blends. *Cement and Concrete Composites*, 33, 46-54.
- BERNAL, S. A., PROVIS, J. L., WALKLEY, B., SAN NICOLAS, R., GEHMAN, J. D., BRICE, D. G., KILCULLEN, A. R., DUXSON, P. & VAN DEVENTER, J. S. J. 2013b. Gel nanostructure in alkali-activated binders based on slag and fly ash, and effects of accelerated carbonation. *Cement and Concrete Research*, 53, 127-144.

- BERNAL, S. A., RODRÍGUEZ, E. D., MEJÍA DE GUTIÉRREZ, R., GORDILLO, M. & PROVIS, J. L. 2011c. Mechanical and thermal characterisation of geopolymers based on silicate-activated metakaolin/slag blends. *Journal of Materials Science*, 46, 5477-5486.
- BERNAL, S. A., RODRÍGUEZ, E. D., MEJÍA DE GUTIÉRREZ, R. & PROVIS, J. L. 2012b. Performance of alkali-activated slag mortars exposed to acids. *Journal of Sustainable Cement-Based Materials*, 1, 138-151.
- BEUSHAUSEN, H., TORRENT, R. & ALEXANDER, M. G. 2019. Performance-based approaches for concrete durability: State of the art and future research needs. *Cement and Concrete Research*, 119, 11-20.
- BORHAN, S., HESARAKI, S. & AHMADZADEH-ASL, S. 2010. Evaluation of colloidal silica suspension as efficient additive for improving physicochemical and in vitro biological properties of calcium sulfate-based nanocomposite bone cement. *J Mater Sci Mater Med*, 21, 3171-81.
- BOUGUERMOUH, K., BOUZIDI, N., MAHTOUT, L., PÉREZ-VILLAREJO, L. & MARTÍNEZ-CARTAS, M. L. 2017. Effect of acid attack on microstructure and composition of metakaolin-based geopolymers: The role of alkaline activator. *Journal of Non-Crystalline Solids*, 463, 128-137.
- BRAGG, W. H. & BRAGG, W. L. 1913. The reflection of X-rays by crystals. *Proceedings of the Royal Society of London A: Mathematical, Physical and Engineering Sciences*, 88, 428-438.
- BRECK, D. W. 1984. *Zeolite molecular sieves: structure, chemistry and use*, Krieger.
- BRUS, J., ABBRENT, S., KOBERA, L., URBANOVA, M. & CUBA, P. 2016. Chapter Two - Advances in <sup>27</sup>Al MAS NMR Studies of Geopolymers. In: WEBB, G. A. (ed.) *Annual Reports on NMR Spectroscopy*. Academic Press.
- BULLARD, J. W., JENNINGS, H. M., LIVINGSTON, R. A., NONAT, A., SCHERER, G. W., SCHWEITZER, J. S., SCRIVENER, K. L. & THOMAS, J. J. 2011. Mechanisms of cement hydration. *Cement and Concrete Research*, 41, 1208-1223.
- CAO, R., ZHANG, S., BANTHIA, N., ZHANG, Y. & ZHANG, Z. 2020. Interpreting the early-age reaction process of alkali-activated slag by using combined embedded ultrasonic measurement, thermal analysis, XRD, FTIR and SEM. *Composites Part B: Engineering*, 186, 107840.
- CAO, Y., WANG, Y., ZHANG, Z., MA, Y. & WANG, H. 2021a. Recent progress of utilization of activated kaolinitic clay in cementitious construction materials. *Composites Part B: Engineering*, 211, 108636.
- CAO, Y., WANG, Y., ZHANG, Z., MA, Y. & WANG, H. 2021b. Turning sandstone clay into supplementary cementitious material: activation and pozzolanic reactivity evaluation. *Composites Part B: Engineering*, 223, 109137.
- CATHERINE A. REES, J. L. P., GRANT C. LUKEY, AND JANNIE S. J. VAN DEVENTER 2007. Attenuated Total Reflectance Fourier Transform Infrared Analysis of Fly Ash Geopolymer Gel Aging. *Langmuir*, 23, 10.
- CHATTERJI, A. K. & RAWAT, R. S. 1965. Hydration of Portland Cement. *Nature*, 207, 713-715.
- CHAUDHARY, D. & LIU, H. 2009. Influence of high temperature and high acidic conditions on geopolymeric composite material for steel pickling tanks. *Journal of Materials Science*, 44, 4472-4481.
- CHEN, G.-H., LEUNG, D. H. W. & HUNG, J.-C. 2003. Biofilm in the sediment phase of a sanitary gravity sewer. *Water Research*, 37, 2784-2788.

- CHINDAPRASIRT, P., PAISITSRISAWAT, P. & RATTANASAK, U. 2014. Strength and resistance to sulfate and sulfuric acid of ground fluidized bed combustion fly ash–silica fume alkali-activated composite. *Advanced Powder Technology*, 25, 1087-1093.
- CHINDAPRASIRT, P., RATTANASAK, U. & TAEBUANHUAD, S. 2012. Resistance to acid and sulfate solutions of microwave-assisted high calcium fly ash geopolymer. *Materials and Structures*, 46, 375-381.
- COLLIER, N. C. 2016. Transition and decomposition temperatures of cement phases—a collection of thermal analysis data. *Ceramics-Silikaty*, 60.
- CRIADO, M., FERNÁNDEZ-JIMÉNEZ, A. & PALOMO, A. 2007. Alkali activation of fly ash: Effect of the SiO<sub>2</sub>/Na<sub>2</sub>O ratio: Part I: FTIR study. *Microporous and Mesoporous Materials*, 106, 180-191.
- CUI, X.-M., LIU, L.-P., ZHENG, G.-J., WANG, R.-P. & LU, J.-P. 2010. Characterization of chemosynthetic Al<sub>2</sub>O<sub>3</sub>–2SiO<sub>2</sub> geopolymers. *Journal of Non-Crystalline Solids*, 356, 72-76.
- CUI, X.-M., ZHENG, G.-J., HAN, Y.-C., SU, F. & ZHOU, J. 2008. A study on electrical conductivity of chemosynthetic Al<sub>2</sub>O<sub>3</sub>–2SiO<sub>2</sub> geopolymer materials. *Journal of Power Sources*, 184, 652-656.
- DAVIDOVITS, J. 1991. Geopolymers: inorganic polymeric new materials. *Journal of Thermal Analysis and calorimetry*, 37, 1633-1656.
- DAVIDOVITS, J. 1994. Properties of geopolymer cements. *Proceedings First International Conference on Alkaline Cements and Concretes*. Kiev, Ukraine: Alkaline Cements and Concretes.
- DAVIDOVITS, J. 2008. *Geopolymer chemistry and applications*, Geopolymer Institute.
- DEB, P. S., SARKER, P. K. & BARBHUIYA, S. 2016. Sorptivity and acid resistance of ambient-cured geopolymer mortars containing nano-silica. *Cement and Concrete Composites*, 72, 235-245.
- DIAMOND, S. 2000. Mercury porosimetry: An inappropriate method for the measurement of pore size distributions in cement-based materials. *Cement and Concrete Research*, 30, 1517-1525.
- DUAN, P., YAN, C., ZHOU, W., LUO, W. & SHEN, C. 2015. An investigation of the microstructure and durability of a fluidized bed fly ash–metakaolin geopolymer after heat and acid exposure. *Materials & Design*, 74, 125-137.
- DUXSON, P., FERNÁNDEZ-JIMÉNEZ, A., PROVIS, J. L., LUKEY, G. C., PALOMO, A. & VAN DEVENTER, J. S. 2007a. Geopolymer technology: the current state of the art. *Journal of materials science*, 42, 2917-2933.
- DUXSON, P., LUKEY, G. C., SEPAROVIC, F. & VAN DEVENTER, J. S. J. 2005a. Effect of Alkali Cations on Aluminum Incorporation in Geopolymeric Gels. *Industrial & Engineering Chemistry Research*, 44, 832-839.
- DUXSON, P., MALLICOAT, S. W., LUKEY, G. C., KRIVEN, W. M. & VAN DEVENTER, J. S. 2007b. The effect of alkali and Si/Al ratio on the development of mechanical properties of metakaolin-based geopolymers. *Colloids and Surfaces A: Physicochemical and Engineering Aspects*, 292, 8-20.
- DUXSON, P. & PROVIS, J. L. 2008. Designing Precursors for Geopolymer Cements. *Journal of the American Ceramic Society*, 91, 3864-3869.
- DUXSON, P., PROVIS, J. L., LUKEY, G. C., MALLICOAT, S. W., KRIVEN, W. M. & VAN DEVENTER, J. S. J. 2005b. Understanding the relationship between geopolymer composition, microstructure and mechanical properties.

- Colloids and Surfaces A: Physicochemical and Engineering Aspects*, 269, 47-58.
- DYER, T. 2017. Influence of cement type on resistance to attack from two carboxylic acids. *Cement & Concrete Composites*, 83, 20-35.
- FAN, Y. F., HU, Z. Q., ZHANG, Y. Z. & LIU, J. L. 2010. Deterioration of compressive property of concrete under simulated acid rain environment. *Construction and Building Materials*, 24, 1975-1983.
- FELICETTI, R. 2004. Digital camera colorimetry for the assessment of fire-damaged concrete. *WSp Fire design of concrete structures: what now*, 211-220.
- FENG, D., PROVIS, J. L. & VAN DEVENTER, J. S. J. 2012. Thermal Activation of Albite for the Synthesis of One-Part Mix Geopolymers. *Journal of the American Ceramic Society*, 95, 565-572.
- FERNANDEZ-JIMENEZ, A., GARCÍA-LODEIRO, I. & PALOMO, A. 2007. Durability of alkali-activated fly ash cementitious materials. *Journal of Materials Science*, 42, 3055-3065.
- FERNÁNDEZ-JIMÉNEZ, A., GARCÍA-LODEIRO, I. & PALOMO, A. 2007. Durability of alkali-activated fly ash cementitious materials. *Journal of Materials Science*, 42, 3055-3065.
- FERNÁNDEZ-JIMÉNEZ, A. & PALOMO, A. 2003. Characterisation of fly ashes. Potential reactivity as alkaline cements☆. *Fuel*, 82, 2259-2265.
- FERNÁNDEZ-JIMÉNEZ, A. & PALOMO, A. 2005. Composition and microstructure of alkali activated fly ash binder: Effect of the activator. *Cement and Concrete Research*, 35, 1984-1992.
- FERNÁNDEZ - JIMÉNEZ, A., PUERTAS, F., SOBRADOS, I. & SANZ, J. 2003. Structure of calcium silicate hydrates formed in alkaline - activated slag: influence of the type of alkaline activator. *Journal of the American Ceramic Society*, 86, 1389-1394.
- FERNANDO, P.-T. & SAID, J. 2011. Resistance to acid attack, abrasion and leaching behavior of alkali-activated mine waste binders. *Materials and Structures*, 44, 487-498.
- GAO, X., YU, Q. L. & BROUWERS, H. J. H. 2017. Apply  $^{29}\text{Si}$ ,  $^{27}\text{Al}$  MAS NMR and selective dissolution in identifying the reaction degree of alkali activated slag-fly ash composites. *Ceramics International*, 43, 12408-12419.
- GAO, X. X., MICHAUD, P., JOUSSEIN, E. & ROSSIGNOL, S. 2013. Behavior of metakaolin-based potassium geopolymers in acidic solutions. *Journal of Non-Crystalline Solids*, 380, 95-102.
- GARCÍA-LODEIRO, I., FERNÁNDEZ-JIMÉNEZ, A., BLANCO, M. T. & PALOMO, A. 2008. FTIR study of the sol-gel synthesis of cementitious gels: C-S-H and N-A-S-H. *Journal of Sol-Gel Science and Technology*, 45, 63-72.
- GARCIA-LODEIRO, I., PALOMO, A., FERNÁNDEZ-JIMÉNEZ, A. & MACPHEE, D. E. 2011. Compatibility studies between N-A-S-H and C-A-S-H gels. Study in the ternary diagram  $\text{Na}_2\text{O}-\text{CaO}-\text{Al}_2\text{O}_3-\text{SiO}_2-\text{H}_2\text{O}$ . *Cement and Concrete Research*, 41, 923-931.
- GARCÍA LODEIRO, I., MACPHEE, D. E., PALOMO, A. & FERNÁNDEZ-JIMÉNEZ, A. 2009. Effect of alkalis on fresh C-S-H gels. FTIR analysis. *Cement and Concrete Research*, 39, 147-153.
- GLASSER, F. P., MARCHAND, J. & SAMSON, E. 2008. Durability of concrete—degradation phenomena involving detrimental chemical reactions. *Cement and Concrete Research*, 38, 226-246.

- GRANDCLERC, A., DANGLA, P., GUEGUEN-MINERBE, M. & CHAUSSADENT, T. 2018. Modelling of the sulfuric acid attack on different types of cementitious materials. *Cement and Concrete Research*, 105, 126-133.
- GRAYTEE, A., SANJAYAN, J. G. & NAZARI, A. 2018. Development of a high strength fly ash-based geopolymer in short time by using microwave curing. *Ceramics International*, 44, 8216-8222.
- GRENGG, C., MITTERMAYR, F., UKRAINCZYK, N., KORAIMANN, G., KIENESBERGER, S. & DIETZEL, M. 2018. Advances in concrete materials for sewer systems affected by microbial induced concrete corrosion: A review. *Water Research*, 134, 341-352.
- GRENGG, C., UKRAINCZYK, N., KORAIMANN, G., MUELLER, B., DIETZEL, M. & MITTERMAYR, F. 2020. Long-term in situ performance of geopolymer, calcium aluminate and Portland cement-based materials exposed to microbially induced acid corrosion. *Cement and Concrete Research*, 131, 106034.
- GU, L., VISINTIN, P. & BENNETT, T. 2018. Evaluation of accelerated degradation test methods for cementitious composites subject to sulfuric acid attack; application to conventional and alkali-activated concretes. *Cement and Concrete Composites*, 87, 187-204.
- GÜLGÜN, M. A., NGUYEN, M. H. & KRIVEN, W. M. 1999. Polymerized Organic - Inorganic Synthesis of Mixed Oxides. *Journal of the American ceramic society*, 82, 556-560.
- GUO, X., SHI, H. & DICK, W. A. 2010. Compressive strength and microstructural characteristics of class C fly ash geopolymer. *Cement and Concrete Composites*, 32, 142-147.
- HAGER, I. 2014. Colour Change in Heated Concrete. *Fire Technology*, 50, 945-958.
- HASHIMOTO, S., MACHINO, T., ANDO, K., DAIKO, Y., HONDA, S. & IWAMOTO, Y. 2017. Hot sulfuric acid-resistance of fly-ash-based geopolymer paste product due to the precipitation of natroalunite crystals. *Construction and Building Materials*, 151, 714-719.
- HEMALATHA, T. & RAMASWAMY, A. 2017. A review on fly ash characteristics—Towards promoting high volume utilization in developing sustainable concrete. *Journal of cleaner production*, 147, 546-559.
- HUANG, C. & KERR, P. F. 1960. Infrared study of the carbonate minerals. *American Mineralogist: Journal of Earth and Planetary Materials*, 45, 311-324.
- HUANG, G., JI, Y., ZHANG, L., LI, J. & HOU, Z. 2018. The influence of curing methods on the strength of MSWI bottom ash-based alkali-activated mortars: The role of leaching of OH<sup>-</sup> and free alkali. *Construction and Building Materials*, 186, 978-985.
- ISLANDER, R. L., DEVINNY, J. S., MANSFELD, F., POSTYN, A. & SHIH, H. 1991. Microbial ecology of crown corrosion in sewers. *Journal of Environmental Engineering*, 117, 751-770.
- ISMAIL, I., BERNAL, S. A., PROVIS, J. L., HAMDAN, S. & VAN DEVENTER, J. S. 2013a. Drying-induced changes in the structure of alkali-activated pastes. *Journal of Materials Science*, 48, 3566-3577.
- ISMAIL, I., BERNAL, S. A., PROVIS, J. L., HAMDAN, S. & VAN DEVENTER, J. S. J. 2013b. Drying-induced changes in the structure of alkali-activated pastes. *Journal of Materials Science*, 48, 3566-3577.

- ISMAIL, I., BERNAL, S. A., PROVIS, J. L., SAN NICOLAS, R., HAMDAN, S. & VAN DEVENTER, J. S. J. 2014. Modification of phase evolution in alkali-activated blast furnace slag by the incorporation of fly ash. *Cement and Concrete Composites*, 45, 125-135.
- IZZAT, A. M., AL BAKRI, A. M. M., KAMARUDIN, H., MOGA, L. M., RUZAIDI, G. C. M., FAHEEM, M. T. M. & SANDU, A. V. 2013a. Microstructural analysis of geopolymer and ordinary Portland cement mortar exposed to sulfuric acid. *Materiale Plastice*, 50, 171-174.
- IZZAT, A. M., AL BAKRT, A. M. M., KAMARUDIN, H., SANDU, A. V., RUZAIDI, G. C. M., FAHEEM, M. T. M. & MOGA, L. M. 2013b. Sulfuric acid attack on ordinary Portland cement and geopolymer material. *Revista de Chimie*, 64, 1011-1014.
- JACQUEMET, N., PIRONON, J., LAGNEAU, V. & SAINT-MARC, J. 2012. Armouring of well cement in H<sub>2</sub>S–CO<sub>2</sub> saturated brine by calcite coating – Experiments and numerical modelling. *Applied Geochemistry*, 27, 782-795.
- JENSEN, H. S. 2009. *Hydrogen sulfide induced concrete corrosion of sewer networks*, Section of Environmental Engineering, Aalborg University.
- JIANG, G., WIGHTMAN, E., DONOSE, B. C., YUAN, Z., BOND, P. L. & KELLER, J. 2014. The role of iron in sulfide induced corrosion of sewer concrete. *Water Research*, 49, 166-174.
- JIN, M., ZHENG, Z., SUN, Y., CHEN, L. & JIN, Z. 2016. Resistance of metakaolin-MSWI fly ash based geopolymer to acid and alkaline environments. *Journal of Non-Crystalline Solids*, 450, 116-122.
- JOSEPH, A. P., KELLER, J., BUSTAMANTE, H. & BOND, P. L. 2012. Surface neutralization and H<sub>2</sub>S oxidation at early stages of sewer corrosion: Influence of temperature, relative humidity and H<sub>2</sub>S concentration. *Water research*, 46, 4235-4245.
- KHAN, H. A., CASTEL, A. & KHAN, M. S. H. 2020. Corrosion investigation of fly ash based geopolymer mortar in natural sewer environment and sulphuric acid solution. *Corrosion Science*, 168, 108586.
- KHAN, H. A., CASTEL, A., KHAN, M. S. H. & MAHMOOD, A. H. 2019. Durability of calcium aluminate and sulphate resistant Portland cement based mortars in aggressive sewer environment and sulphuric acid. *Cement and Concrete Research*, 124, 105852.
- KO, L. S.-C., BELEÑA, I., DUXSON, P., KAVALEROVA, E., KRIVENKO, P. V., ORDOÑEZ, L.-M., TAGNIT-HAMOU, A. & WINNEFELD, F. 2014. AAM Concretes: Standards for Mix Design/Formulation and Early-Age Properties. *Alkali Activated Materials*. Springer.
- KOCH, G. H., BRONGERS, M. P., THOMPSON, N. G., VIRMANI, Y. P. & PAYER, J. H. 2002. Corrosion cost and preventive strategies in the United States. United States. Federal Highway Administration.
- KOENIG, A., HERRMANN, A., OVERMANN, S. & DEHN, F. 2017. Resistance of alkali-activated binders to organic acid attack: Assessment of evaluation criteria and damage mechanisms. *Construction and Building Materials*, 151, 405-413.
- KOMLJENOVIĆ, M. M., BAŠČAREVIĆ, Z., MARJANOVIĆ, N. & NIKOLIĆ, V. 2012. Decalcification resistance of alkali-activated slag. *Journal of Hazardous Materials*, 233-234, 112-121.

- KONG, D. L. Y., SANJAYAN, J. G. & SAGOE-CRENTSIL, K. 2007. Comparative performance of geopolymers made with metakaolin and fly ash after exposure to elevated temperatures. *Cement and Concrete Research*, 37, 1583-1589.
- KRÓL, M., ROŽEK, P., CHLEBDA, D. & MOZGAWA, W. 2018. Influence of alkali metal cations/type of activator on the structure of alkali-activated fly ash – ATR-FTIR studies. *Spectrochimica Acta Part A: Molecular and Biomolecular Spectroscopy*, 198, 33-37.
- KWASNY, J., AIKEN, T. A., SOUTSOS, M. N., MCINTOSH, J. A. & CLELAND, D. J. 2018. Sulfate and acid resistance of lithomarge-based geopolymer mortars. *Construction and Building Materials*, 166, 537-553.
- LABBEZ, C., POCHARD, I., JÖNSSON, B. & NONAT, A. 2011. CSH/solution interface: Experimental and Monte Carlo studies. *Cement and Concrete research*, 41, 161-168.
- LANE, M. D. 2007. Mid-infrared emission spectroscopy of sulfate and sulfate-bearing minerals. *American Mineralogist*, 92, 1-18.
- LEE, N. K. & LEE, H. K. 2016. Influence of the slag content on the chloride and sulfuric acid resistances of alkali-activated fly ash/slag paste. *Cement & Concrete Composites*, 72, 168-179.
- LESTI, M., TIEMEYER, C. & PLANK, J. 2013. CO<sub>2</sub> stability of Portland cement based well cementing systems for use on carbon capture & storage (CCS) wells. *Cement and Concrete Research*, 45, 45-54.
- LI, N., SHI, C. & ZHANG, Z. 2019. Understanding the roles of activators towards setting and hardening control of alkali-activated slag cement. *Composites Part B: Engineering*, 171, 34-45.
- LI, N., SHI, C., ZHANG, Z., ZHU, D., HWANG, H.-J., ZHU, Y. & SUN, T. 2018. A mixture proportioning method for the development of performance-based alkali-activated slag-based concrete. *Cement and Concrete Composites*, 93, 163-174.
- LI, S. & SUN, W. 2013. Review on deterioration of concrete subjected to coupling effect of fatigue load, carbonation and chlorides. *Journal of The Chinese Ceramic Society*, 41, 1459-1464.
- LIKENS, G. E., WRIGHT, R. F., GALLOWAY, J. N. & BUTLER, T. J. 1979. Acid rain. *Scientific American*, 241, 43-51.
- LIU, B., ZHUANG, K., LI, D., FANG, Y. & PAN, G. 2020. Understanding the early reaction and structural evolution of alkali activated slag optimized using K-A-S-H nanoparticles with varying K<sub>2</sub>O/SiO<sub>2</sub> ratios. *Composites Part B: Engineering*, 200, 108311.
- LLOYD, R. R., PROVIS, J. L. & VAN DEVENTER, J. S. 2010. Pore solution composition and alkali diffusion in inorganic polymer cement. *Cement and Concrete Research*, 40, 1386-1392.
- LLOYD, R. R., PROVIS, J. L. & VAN DEVENTER, J. S. 2012a. Acid resistance of inorganic polymer binders. 1. Corrosion rate. *Materials and structures*, 45, 1-14.
- LLOYD, R. R., PROVIS, J. L. & VAN DEVENTER, J. S. J. 2012b. Acid resistance of inorganic polymer binders. 1. Corrosion rate. *Materials and Structures*, 45, 1-14.
- LONGHI, M. A., RODRÍGUEZ, E. D., WALKLEY, B., ZHANG, Z. & KIRCHHEIM, A. P. 2020. Metakaolin-based geopolymers: Relation between formulation, physicochemical properties and efflorescence formation. *Composites Part B: Engineering*, 182, 107671.

- LONGHI, M. A., WALKLEY, B., RODRÍGUEZ, E. D., KIRCHHEIM, A. P., ZHANG, Z. & WANG, H. 2019. New selective dissolution process to quantify reaction extent and product stability in metakaolin-based geopolymers. *Composites Part B: Engineering*, 176, 107172.
- LONGHI, M. A., ZHANG, Z., WALKLEY, B., RODRÍGUEZ, E. D. & KIRCHHEIM, A. P. 2021. Strategies for control and mitigation of efflorescence in metakaolin-based geopolymers. *Cement and Concrete Research*, 144, 106431.
- LOTTHENBACH, B., DURDZINSKI, P. & DE WEERDT, K. 2016. Thermogravimetric analysis. *A practical guide to microstructural analysis of cementitious materials*, 1.
- LOTTHENBACH, B., SCRIVENER, K. & HOOTON, R. D. 2011. Supplementary cementitious materials. *Cement and Concrete Research*, 41, 1244-1256.
- MA, Y., YANG, X., HU, J., ZHANG, Z. & WANG, H. 2019. Accurate determination of the “time-zero” of autogenous shrinkage in alkali-activated fly ash/slag system. *Composites Part B: Engineering*, 177, 107367.
- MARCHETTI, C. 1977. On geoengineering and the CO<sub>2</sub> problem. *Climatic change*, 1, 59-68.
- MEHTA, A. & SIDDIQUE, R. 2017. Sulfuric acid resistance of fly ash based geopolymer concrete. *Construction and Building Materials*, 146, 136-143.
- MELLADO, A., PÉREZ-RAMOS, M. I., MONZÓ, J., BORRACHERO, M. V. & PAYÁ, J. 2017. Resistance to acid attack of alkali-activated binders: Simple new techniques to measure susceptibility. *Construction & Building Materials*, 150, 355-366.
- MYERS, R. J. 2015. *Thermodynamic Modelling of CaO-Al<sub>2</sub>O<sub>3</sub>-SiO<sub>2</sub>-H<sub>2</sub>O-Based Cements*. PhD, University of Sheffield.
- MYERS, R. J., BERNAL, S. A., GEHMAN, J. D., VAN DEVENTER, J. S. J. & PROVIS, J. L. 2015a. The Role of Al in Cross-Linking of Alkali-Activated Slag Cements. *Journal of the American Ceramic Society*, 98, 996-1004.
- MYERS, R. J., BERNAL, S. A., SAN NICOLAS, R. & PROVIS, J. L. 2013. Generalized structural description of calcium–sodium aluminosilicate hydrate gels: the cross-linked substituted tobermorite model. *Langmuir*, 29, 5294-5306.
- MYERS, R. J., PROVIS, J. L. & LOTTHENBACH, B. 2015b. Composition–solubility–structure relationships in calcium (alkali) aluminosilicate hydrate (C-(N, K-) A-S-H). *Dalton Transactions*, 44, 13530-13544.
- NGUYEN, A. D. & ŠKVÁRA, F. 2016. The influence of ambient pH on fly ash-based geopolymer. *Cement and Concrete Composites*, 72, 275-283.
- NGUYEN, K. T., LEE, Y. H., LEE, J. & AHN, N. 2013. Acid Resistance and Curing Properties for Green Fly Ash-geopolymer Concrete. *Journal of Asian Architecture and Building Engineering*, 12, 6.
- OKOYE, F. N., PRAKASH, S. & SINGH, N. B. 2017. Durability of fly ash based geopolymer concrete in the presence of silica fume. *Journal of Cleaner Production*, 149, 1062-1067.
- OLIVIER, J. G. J., PETERS, J. A. H. W., JANSSENS-MAENHOUT, G. & MUNTEAN, M. 2013. Trends in global CO<sub>2</sub> emissions. 2013 Report. Netherlands.
- OURGESSA, A. W., ANILEY, A., GUDISA, A. G., NEME, I. & BEKELE, A. 2019. Effect of Alkaline Concentration and Solid Liquid Ratio on the Acid

- Resistance of Fly Ash Based Geopolymer Mortar. *American Journal of Science, Engineering and Technology*, 4, 80.
- PALOMO, A., BLANCO-VARELA, M. T., GRANIZO, M. L., PUERTAS, F., VAZQUEZ, T. & GRUTZECK, M. W. 1999a. Chemical stability of cementitious materials based on metakaolin. *Cement and Concrete Research*, 29, 997-1004.
- PALOMO, A., GRUTZECK, M. W. & BLANCO, M. T. 1999b. Alkali-activated fly ashes: A cement for the future. *Cement and Concrete Research*, 29, 1323-1329.
- PALOMO, Á., KAVALEROVA, E., FERNÁNDEZ-JIMÉNEZ, A., KRIVENKO, P., GARCÍA-LODEIRO, I. & MALTSEVA, O. 2015. A review on alkaline activation: new analytical perspectives.
- PARDAL, X., POCHARD, I. & NONAT, A. 2009. Experimental study of Si–Al substitution in calcium-silicate-hydrate (CSH) prepared under equilibrium conditions. *Cement and Concrete Research*, 39, 637-643.
- PAVLÍK, V. 1994. Corrosion of hardened cement paste by acetic and nitric acids part I: Calculation of corrosion depth. *Cement and Concrete Research*, 24, 551-562.
- PECHINI, M. P. 1967. *Method of Preparing Lead and Alkaline Earth Titanates and Niobates and Coating Method Using the Same to Form a Capacitor*. United States patent application.
- PHUNG, Q. T., MAES, N. & SEETHARAM, S. 2019. Pitfalls in the use and interpretation of TGA and MIP techniques for Ca-leached cementitious materials. *Materials & Design*, 182, 108041.
- PRAMANIK, P. & PATHAK, A. 1994. A new chemical route for the preparation of fine ferrite powders. *Bulletin of Materials Science*, 17, 967-975.
- PROVIS, J. & VAN DEVENTER, J. 2007. Geopolymerisation kinetics. 2. Reaction kinetic modelling. *Chemical Engineering Science*, 62, 2318-2329.
- PROVIS, J. L. 2018. Alkali-activated materials. *Cement and Concrete Research*, 114, 40-48.
- PROVIS, J. L. & BERNAL, S. A. 2014a. Geopolymers and Related Alkali-Activated Materials. *Annual Review of Materials Research*, 44, 299-327.
- PROVIS, J. L. & BERNAL, S. A. 2014b. Geopolymers and related alkali-activated materials. *Annual Review of Materials Research*, 44, 299-327.
- PROVIS, J. L., LUKEY, G. C. & VAN DEVENTER, J. S. 2005a. Do geopolymers actually contain nanocrystalline zeolites? A reexamination of existing results. *Chemistry of Materials*, 17, 3075-3085.
- PROVIS, J. L., LUKEY, G. C. & VAN DEVENTER, J. S. J. 2005b. Do Geopolymers Actually Contain Nanocrystalline Zeolites? A Reexamination of Existing Results. *Chemistry of Materials*, 17, 3075-3085.
- PROVIS, J. L., MYERS, R. J., WHITE, C. E., ROSE, V. & VAN DEVENTER, J. S. J. 2012. X-ray microtomography shows pore structure and tortuosity in alkali-activated binders. *Cement and Concrete Research*, 42, 855-864.
- PROVIS, J. L., PALOMO, A. & SHI, C. 2015. Advances in understanding alkali-activated materials. *Cement and Concrete Research*, 78, 110-125.
- PROVIS, J. L., VAN DEVENTER JANNIE S. J. (ed.) 2014. *Alkali Activated Materials: State-of-the-Art Report, RILEM TC 224-AAM*, Dordrecht: Springer/RILEM.
- PROVIS, J. L. & VAN DEVENTER, J. S. 2014. *State of the art report, RILEM TC 224-AAM*, Springer, Springer Science & Business Media.

- PROVIS, J. L. & VAN DEVENTER, J. S. J. 2009. *Geopolymers: structures, processing, properties and industrial applications*, Elsevier.
- PYATINA, T. & SUGAMA, T. 2016. Acid resistance of calcium aluminate cement–fly ash F blends. *Advances in Cement Research*, 28, 433-457.
- QING, H. & YANXIA, Z. 2009. An Analysis on Characteristics of Regional Acid Rain over China in 2007 [J]. *Advances in Climate Change Research*, 1.
- RAFEET, A., VINAI, R., SOUTSOS, M. & SHA, W. 2019. Effects of slag substitution on physical and mechanical properties of fly ash-based alkali activated binders (AABs). *Cement and Concrete Research*, 122, 118-135.
- RANJBAR, N., KASHEFI, A. & MAHERI, M. R. 2018. Hot-pressed geopolymer: Dual effects of heat and curing time. *Cement and Concrete Composites*, 86, 1-8.
- REES, C. A., PROVIS, J. L., LUKEY, G. C. & VAN DEVENTER, J. S. J. 2007. Attenuated Total Reflectance Fourier Transform Infrared Analysis of Fly Ash Geopolymer Gel Aging. *Langmuir*, 23, 8170-8179.
- REN, J., ZHANG, L. & SAN NICOLAS, R. 2020. Degradation process of alkali-activated slag/fly ash and Portland cement-based pastes exposed to phosphoric acid. *Construction and Building Materials*, 232, 117209.
- SAND, W. & BOCK, E. 1984. Concrete corrosion in the Hamburg Sewer system. *Environmental Technology Letters*, 5, 517-528.
- SATA, V., SATHONSAOWAPHAK, A. & CHINDAPRASIRT, P. 2012. Resistance of lignite bottom ash geopolymer mortar to sulfate and sulfuric acid attack. *Cement and Concrete Composites*, 34, 700-708.
- SCHILLING, P. J., BUTLER, L. G., ROY, A. & EATON, H. C. 1994.  $^{29}\text{Si}$  and  $^{27}\text{Al}$  MAS - NMR of NaOH - activated blast - furnace slag. *Journal of the American Ceramic Society*, 77, 2363-2368.
- SHARMA, H. D. & REDDY, K. R. 2004. *Geoenvironmental engineering: site remediation, waste containment, and emerging waste management technologies*, John Wiley & Sons.
- SHI, C. 2003. Corrosion resistance of alkali-activated slag cement. *Advances in Cement Research*, 15, 5.
- SHI, C., JIMÉNEZ, A. F. & PALOMO, A. 2011. New cements for the 21st century: The pursuit of an alternative to Portland cement. *Cement and Concrete Research*, 41, 750-763.
- SHI, C., QU, B. & PROVIS, J. L. 2019. Recent progress in low-carbon binders. *Cement and Concrete Research*, 122, 227-250.
- SHI, C., ROY, D. & KRIVENKO, P. 2003. *Alkali-activated cements and concretes*, CRC press.
- SHI, C. & STEGEMANN, J. 2000a. Acid corrosion resistance of different cementing materials. *Cement and Concrete Research*, 30, 803-808.
- SHI, C. & STEGEMANN, J. A. 2000b. Acid corrosion resistance of different cementing materials. *Cement and Concrete Research*, 30, 803-808.
- SHI, C. & STEGEMANN, J. A. 2000c. Acid corrosion resistance of different cementing materials. *Cement and Concrete Research*, 30, 6.
- SHI, Z., SHI, C., ZHANG, J., WAN, S., ZHANG, Z. & OU, Z. 2018. Alkali-silica reaction in waterglass-activated slag mortars incorporating fly ash and metakaolin. *Cement and Concrete Research*, 108, 10-19.
- SHOOK, W. E. & BELL, L. W. 1998. Corrosion control in concrete pipe and manholes. *Technical Presentation, Water Environmental Federation, Florida*.

- SINGH, M. & GARG, M. 2000. Making of anhydrite cement from waste gypsum. *Cement and Concrete Research*, 30, 571-577.
- SKIBSTED, J. & ANDERSEN, M. D. 2013. The Effect of Alkali Ions on the Incorporation of Aluminum in the Calcium Silicate Hydrate (C–S–H) Phase Resulting from Portland Cement Hydration Studied by <sup>29</sup>Si MAS NMR. *Journal of the American Ceramic Society*, 96, 651-656.
- SMITH, B. C. 2011. *Fundamentals of Fourier transform infrared spectroscopy*, CRC press.
- SONG, X., MAROSSZEKY, M., BRUNGS, M. & MUNN, R. Durability of fly ash based geopolymer concrete against sulphuric acid attack. Proceedings of the international conference on durability of building materials and components, Lyon, France, 2005. 369-375.
- SONG, Y., TIAN, Y., LI, X., WEI, J., ZHANG, H., BOND, P. L., YUAN, Z. & JIANG, G. 2019. Distinct microbially induced concrete corrosion at the tidal region of reinforced concrete sewers. *Water Research*, 150, 392-402.
- SREEVIDYA, V., ANURADHA, R., DINAKAR, D. & VENKATASUBRAMANI, R. 2012. Acid resistance of flyash based geopolymer mortar under ambient curing and heat curing. *International journal of engineering science and technology*, 4, 681-684.
- STANDARD, A. Supplementary cementitious materials Part 2: Slag—Ground granulated blast-furnace (AS 3582.2: 2016). *no*, 1, 21.
- STERLING, R., SIMICEVIC, J., ALLOUCHE, E., CONDIT, W. & WANG, L. 2010. State of technology for rehabilitation of wastewater collection systems. *Rep. EPA/600/R-10/078*, US Environmental Protection Agency, Washington, DC. <<http://nepis.epa.gov/Exe/ZyPURL.cgi>.
- STRYDOM, C. A., HUDSON-LAMB, D. L., POTGIETER, J. H. & DAGG, E. 1995. The thermal dehydration of synthetic gypsum. *Thermochimica Acta*, 269-270, 631-638.
- SUN, G., YOUNG, J. F. & KIRKPATRICK, R. J. 2006. The role of Al in C–S–H: NMR, XRD, and compositional results for precipitated samples. *Cement and Concrete Research*, 36, 18-29.
- SVINNING, K., HØSKULDSSON, A. & JUSTNES, H. 2008. Prediction of compressive strength up to 28days from microstructure of Portland cement. *Cement and Concrete Composites*, 30, 138-151.
- TAHERI, S., AMS, M., BUSTAMANTE, H., VORREITER, L., BEVITT, J. J., WITHFORD, M. & CLARK, S. M. 2020. Characterizing concrete corrosion below sewer tidal levels at chemically dosed locations. *Water Research*, 185, 116245.
- TAYLOR, H. F. 1997. *Cement chemistry*, Thomas Telford London.
- TEMUJIN, J., MINJIGMAA, A., LEE, M., CHEN-TAN, N. & VAN RIESSEN, A. 2011. Characterisation of class F fly ash geopolymer pastes immersed in acid and alkaline solutions. *Cement and Concrete Composites*, 33, 1086-1091.
- THOKCHOM, S., GHOSH, P. & GHOSH, S. 2009. Resistance of fly ash based geopolymer mortars in sulfuric acid. *ARPJ Journal of Engineering and Applied Sciences*, 4, 6.
- TOGNONVI, M. T., SORO, J. & ROSSIGNOL, S. 2012. Durability of Tubular Geopolymer Reinforced with Silica Sand. *New Journal of Glass and Ceramics*, 02, 85-90.
- UNDERDAL, A. & HANF, K. 2019. *International environmental agreements and domestic politics: The case of acid rain*, Routledge.

- VAFAEI, M., ALLAHVERDI, A., DONG, P. & BASSIM, N. 2018. Acid attack on geopolymer cement mortar based on waste-glass powder and calcium aluminate cement at mild concentration. *Construction and Building Materials*, 193, 363-372.
- VAN DEVENTER, J. S. J., SAN NICOLAS, R., ISMAIL, I., BERNAL, S. A., BRICE, D. G. & PROVIS, J. L. 2015. Microstructure and durability of alkali-activated materials as key parameters for standardization. *Journal of Sustainable Cement-Based Materials*, 4, 116-128.
- VEDALAKSHMI, R., SUNDARA RAJ, A., SRINIVASAN, S. & GANESH BABU, K. 2003. Quantification of hydrated cement products of blended cements in low and medium strength concrete using TG and DTA technique. *Thermochimica Acta*, 407, 49-60.
- VET, R., ARTZ, R. S., CAROU, S., SHAW, M., RO, C.-U., AAS, W., BAKER, A., BOWERSOX, V. C., DENTENER, F., GALY-LACAUX, C., HOU, A., PIENAAR, J. J., GILLETT, R., FORTI, M. C., GROMOV, S., HARA, H., KHODZHER, T., MAHOWALD, N. M., NICKOVIC, S., RAO, P. S. P. & REID, N. W. 2014. A global assessment of precipitation chemistry and deposition of sulfur, nitrogen, sea salt, base cations, organic acids, acidity and pH, and phosphorus. *Atmospheric Environment*, 93, 3-100.
- WALKLEY, B. 2016. *Understanding geopolymers through synthetic gel systems*. PhD Dissertation, University of Melbourne University.
- WALKLEY, B., PROVIS, J., SAN NICOLAS, R., SANI, M.-A. & VAN DEVENTER, J. 2015. Stoichiometrically controlled C-(A)-S-H/N-A-S-H gel blends via alkali-activation of synthetic precursors. *Advances in Applied Ceramics*, 114, 372-377.
- WALKLEY, B. & PROVIS, J. L. 2019. Solid-state nuclear magnetic resonance spectroscopy of cements. *Materials Today Advances*, 1, 100007.
- WALKLEY, B., SAN NICOLAS, R., SANI, M.-A., GEHMAN, J. D., VAN DEVENTER, J. S. J. & PROVIS, J. L. 2016a. Phase evolution of Na<sub>2</sub>O-Al<sub>2</sub>O<sub>3</sub>-SiO<sub>2</sub>-H<sub>2</sub>O gels in synthetic aluminosilicate binders. *Dalton Transactions: An International Journal of Inorganic Chemistry*, 45, 5521-5535.
- WALKLEY, B., SAN NICOLAS, R., SANI, M.-A., GEHMAN, J. D., VAN DEVENTER, J. S. J. & PROVIS, J. L. 2016b. Synthesis of stoichiometrically controlled reactive aluminosilicate and calcium-aluminosilicate powders. *Powder Technology*, 297, 17-33.
- WALKLEY, B., SAN NICOLAS, R., SANI, M.-A., REES, G. J., HANNA, J. V., VAN DEVENTER, J. S. J. & PROVIS, J. L. 2016c. Phase evolution of C-(N)-A-S-H/N-A-S-H gel blends investigated via alkali-activation of synthetic calcium aluminosilicate precursors. *Cement and Concrete Research*, 89, 120-135.
- WANG, S.-D. & SCRIVENER, K. L. 2003. <sup>29</sup>Si and <sup>27</sup>Al NMR study of alkali-activated slag. *Cement and Concrete Research*, 33, 769-774.
- WANG, Y., CAO, Y., MA, Y., XIAO, S., HU, J. & WANG, H. 2021a. Fresh and hardened properties of alkali-activated fly ash/slag binders: effect of fly ash source, surface area, and additives. *Journal of Sustainable Cement-Based Materials*, 1-24.
- WANG, Y., CAO, Y., ZHANG, Z., HUANG, J., ZHANG, P., MA, Y. & WANG, H. 2021b. Study of acidic degradation of alkali-activated materials using synthetic C-(N)-A-S-H and N-A-S-H gels. *Composites Part B: Engineering*, 109510.

- WINNEFELD, F., LEEMANN, A., LUCUK, M., SVOBODA, P. & NEUROTH, M. 2010. Assessment of phase formation in alkali activated low and high calcium fly ashes in building materials. *Construction and Building Materials*, 24, 1086-1093.
- XUE, Z., HAO, J., CHAI, F., DUAN, N., CHEN, Y., LI, J., CHEN, F., LIU, S. & PU, W. 2005. Air quality impact of the coal-fired power plants in the northern passageway of the China west-east power transmission project. *Journal of the Air & Waste Management Association*, 55, 1816-1826.
- YANG, S., DU, W., SHI, P., SHANGGUAN, J., LIU, S., ZHOU, C., CHEN, P., ZHANG, Q. & FAN, H. 2016. Mechanistic and kinetic analysis of Na<sub>2</sub>SO<sub>4</sub>-modified laterite decomposition by thermogravimetry coupled with mass spectrometry. *PloS one*, 11, e0157369.
- YANKWA DJOBO, J. N., ELIMBI, A., TCHAKOUTÉ, H. K. & KUMAR, S. 2016. Mechanical properties and durability of volcanic ash based geopolymer mortars. *Construction and Building Materials*, 124, 606-614.
- YE, H. & HUANG, L. 2020. Degradation mechanisms of alkali-activated binders in sulfuric acid: The role of calcium and aluminum availability. *Construction and Building Materials*, 246, 118477.
- YU, P., KIRKPATRICK, R. J., POE, B., MCMILLAN, P. F. & CONG, X. 1999. Structure of Calcium Silicate Hydrate (C-S-H): Near-, Mid-, and Far-Infrared Spectroscopy. *Journal of the American Ceramic Society*, 82, 742-748.
- YUAN, H., DANGLA, P., CHATELLIER, P. & CHAUSSADENT, T. 2013. Degradation modelling of concrete submitted to sulfuric acid attack. *Cement and Concrete Research*, 53, 267-277.
- ZENG, X., LI, Y., RAN, Y., YANG, K., QU, F. & WANG, P. 2018. Deterioration mechanism of CA mortar due to simulated acid rain. *Construction and Building Materials*, 168, 1008-1015.
- ZHANG, J., SHI, C., ZHANG, Z. & OU, Z. 2017. Durability of alkali-activated materials in aggressive environments: A review on recent studies. *Construction & Building Materials*, 152, 598-613.
- ZHANG, M., ZHAO, M., ZHANG, G., MANN, D., LUMSDEN, K. & TAO, M. 2016a. Durability of red mud-fly ash based geopolymer and leaching behavior of heavy metals in sulfuric acid solutions and deionized water. *Construction and Building Materials*, 124, 373-382.
- ZHANG, M., ZHAO, M., ZHANG, G., SIETINS, J. M., GRANADOS-FOCIL, S., PEPI, M. S., XU, Y. & TAO, M. 2018a. Reaction kinetics of red mud-fly ash based geopolymers: Effects of curing temperature on chemical bonding, porosity, and mechanical strength. *Cement and Concrete Composites*, 93, 175-185.
- ZHANG, W., YAO, X., YANG, T., LIU, C. & ZHANG, Z. 2018b. Increasing mechanical strength and acid resistance of geopolymers by incorporating different siliceous materials. *Construction and Building Materials*, 175, 411-421.
- ZHANG, W., YAO, X., YANG, T. & ZHANG, Z. 2018c. The degradation mechanisms of alkali-activated fly ash/slag blend cements exposed to sulphuric acid. *Construction and Building Materials*, 186, 1177-1187.
- ZHANG, Y., GU, L., LI, W. & ZHANG, Q. 2019. Effect of acid rain on economic loss of concrete structures in Hangzhou, China. *International Journal of Low-Carbon Technologies*, 14, 89-94.

- ZHANG, Z., PROVIS, J. L., REID, A. & WANG, H. 2014. Geopolymer foam concrete: An emerging material for sustainable construction. *Construction and Building Materials*, 56, 113-127.
- ZHANG, Z., PROVIS, J. L., WANG, H., BULLEN, F. & REID, A. 2013. Quantitative kinetic and structural analysis of geopolymers. Part 2. Thermodynamics of sodium silicate activation of metakaolin. *Thermochimica Acta*, 565, 163-171.
- ZHANG, Z., PROVIS, J. L., ZOU, J., REID, A. & WANG, H. 2016b. Toward an indexing approach to evaluate fly ashes for geopolymer manufacture. *Cement and Concrete Research*, 85, 163-173.
- ZHANG, Z., WANG, H., PROVIS, J. L., BULLEN, F., REID, A. & ZHU, Y. 2012. Quantitative kinetic and structural analysis of geopolymers. Part 1. The activation of metakaolin with sodium hydroxide. *Thermochimica Acta*, 539, 23-33.
- ZHAO, M., ZHANG, G., HTET, K. W., KWON, M., LIU, C., XU, Y. & TAO, M. 2019. Freeze-thaw durability of red mud slurry-class F fly ash-based geopolymer: Effect of curing conditions. *Construction and Building Materials*, 215, 381-390.
- ZHUANG, H. J., ZHANG, H. Y. & XU, H. 2017. Resistance of geopolymer mortar to acid and chloride attacks. *Procedia Engineering*, 210, 126-131.
- ŽIVICA, V. & KRIZMA, M. 2013. Acidic-resistant slag cement. *Magazine of Concrete Research*, 65, 1073-1080.
- ŽIVICA, V. R. 2004. Acidic attack of cement based materials - a review Part 3: research and test methods. *Construction and Building Materials*, 18, 683-688.
- ZIVICA, V. R. & BAJZA, A. 2001a. Acidic attack of cement based materials - a review. Part 1. Principle of acidic attack. *Construction and Building Materials*, 15, 331-340.
- ZIVICA, V. R. & BAJZA, A. 2001b. Acidic attack of cement based materials - a review: Part 1. Principle of acidic attack. *Construction and Building Materials*, 15, 331-340.
- ZIVICA, V. R. & BAJZA, A. 2002. Acidic attack of cement-based materials—a review Part 2. Factors of rate of acidic attack and protective measures. *Construction and building materials*, 16, 215-222.
- ZRIBI, M., SAMET, B. & BAKLOUTI, S. 2019. Effect of curing temperature on the synthesis, structure and mechanical properties of phosphate-based geopolymers. *Journal of Non-Crystalline Solids*, 511, 62-67.

## PUBLICATIONS

### Journal papers

1. **Yanru Wang**, Yubin Cao, Zuhua Zhang, Jizhong Huang, Peng Zhang, Yuwei Ma and Hao Wang. (2021) " Study of acidic degradation of alkali-activated materials using synthetic C-(N)-A-S-H and N-A-S-H gels." *Composites Part B: Engineering*. 230, 109510.
2. **Yanru Wang**, Yubin Cao, Zuhua Zhang, Peng Zhang, Yuwei Ma, Aiguo Wang and Hao Wang. " Intrinsic sulphuric acid resistance of C-(N)-A-S-H and N-A-S-H gels produced by alkali-activation of synthetic calcium aluminosilicate precursors." *Cement and Concrete Research*. Under review.
3. **Yanru Wang**, Yubin Cao, Zuhua Zhang, Peng Zhang, and Hao Wang. " The degradation mechanisms of different cementitious materials to sulphuric acid." *Construction and Building Materials*. Submitted.
4. **Yanru Wang**, Yubin Cao, Yuwei Ma, Shanshan Xiao, Jie Hu and Hao Wang. (2021). "Fresh and hardened properties of alkali-activated fly ash/slag binders: effect of fly ash source, surface area, and additives." *Journal of Sustainable Cement-Based Materials*: 1-24.
5. **Yanru Wang**, Yubin Cao, Zuhua Zhang and Yuwei Ma. (2020). "Effective Utilization of Waste Glass as Cementitious Powder and Construction Sand in Mortar." *Materials* 13(3): 707.
6. **Yanru Wang**, Yubin Cao, Peng Zhang, Yuwei Ma, Tiejun Zhao, Hao Wang and Zuhua Zhang. (2019). "Water absorption and chloride diffusivity of concrete under the coupling effect of uniaxial compressive load and freeze–thaw cycles." *Construction and Building Materials* 209: 566-576
7. Yubin Cao, **Yanru Wang**, Zuhua Zhang, Yuwei Ma and Hao Wang., (2021). "Recent progress of utilization of activated kaolinitic clay in cementitious construction materials." *Composites Part B: Engineering* 211: 108636.
8. Yubin Cao, **Yanru Wang**, Zuhua Zhang, Yuwei Ma and Hao Wang. (2021). "Turning sandstone clay into supplementary cementitious material: activation and pozzolanic reactivity evaluation." *Composites Part B: Engineering* 223: 109137.
9. Yubin Cao, Zuhua Zhang, **Yanru Wang**, Hao Wang. (2021). "Recycled sand from sandstone waste: a new source of high quality fine aggregate." *Resources, Conservation & Recycling* 179: 106116.
10. Rui Mo, Penggang Wang, **Yanru Wang**, Yubin Cao. " Influence of elevated temperatures and cooling regimes on the microstructure development and phases evolution of sodium silicate-activated slag." *Materials* 2022, 15(6), 2022.

## Refereed conference papers

11. **Yanru Wang**, Peng Zhang, Zuhua Zhang, Yubin Cao, Hao Wang, “The coupling effect of pressure and freeze-thaw cycles on the durability of concrete,” 15th International Congress on the Chemistry of Cement (ICCC 2019), Sep. 16-20, 2019, 510, pp. 370.
12. **Yanru Wang**, Peng Zhang, Zuhua Zhang, Yubin Cao, Hao Wang. and Tiejun Zhao, “Capillary water absorption of loading concrete under freezing-thawing circumstance,” 11th Asian-Australasian Conference on Composite Materials (ACCM-11) , Sep. 29th - Aug. 1st, 2018, Comp-3-2-O3, pp. 64.
13. **Yanru Wang**, Yubin Cao, Zuhua Zhang and Hao Wang, “Understand the intrinsic structure of geopolymer gels of N-A-S-H and C-(N)-A-S-H by synthetic pure precursors,” International Union of Laboratories and Experts in Construction Materials, Systems and Structures (RILEM 2019), Aug. 25-30, 2019.
14. Yubin Cao, Qiuyi Li, Zuhua Zhang, **Yanru Wang**, “Features of multiple interface structures in recycled aggregate concrete (RAC),” 15th International Congress on the Chemistry of Cement (ICCC 2019), Sep. 16-20, 2019, 514.

## APPENDIX

A1. The FTIR spectrum of synthesized precursors exposed to thermal treatment at 400, 600, 800, and 1000 °C

